Interfacial behaviour in stratified and stratifying annular flows

Nora Lecoeur

A thesis submitted in partial fulfillment of the requirements for the degree
of
Doctor of Philosophy of Imperial College London

Department of Chemical Engineering and Chemical Technology
Imperial College of Science, Technology and Medicine
London SW7 2BY

January 2013

To Oscar

Abstract

This thesis describes work which was focused on *stratifying annular flow* in horizontal tubes. Stratifying-annular flows in horizontal tubes are characterized by the tube being wetted with liquid over its whole periphery but with a tendency for more of the liquid to be present in the layer at the bottom of the tube. For such a condition to exist, there have to be some mechanisms by which the liquid is transported at the top of the pipe in opposition to the influence of gravity. Such flows are typically experienced in hydrocarbon recovery and in many other applications as for instance in gas-condensate lines. Unless the liquid phase (to which a corrosion inhibitor is often added) can adequately wet the top of the pipe, corrosion and ultimate pipe failure may occur in this region; this is a crucial problem for the petroleum industry. Three physical mechanisms have been identified for the transport of the liquid phase to the top of the tube, namely: droplet transport, wave spreading and mixing, and secondary flow. The secondary flow mechanism seems unlikely to contribute significantly and the wave spreading mechanism is only significant in smaller diameter tubes (typically 25 mm). For larger pipes, it is the droplet transport mechanism which is likely to occur; in this mechanism, droplets are entrained from the liquid layer at the bottom of the pipe and transported in the gas core at the top where they deposit to form a liquid film. Two mechanisms of droplet transport seem to be significant, namely *ballistic* transport in which larger droplets move in a direction governed by their initial release velocity and *diffusional* transport in which droplets move randomly under the influence of the gas flow turbulence. For pipes of medium diameter (for example in the 78 mm diameter pipe used in the experiments described here), ballistic droplet transport is likely to be the dominant mechanism but diffusional transport is expected to be dominant for large diameter pipes.

The work described in the thesis comprised both experimental and computational studies. In the experimental work, a special visualization method (namely axial view photography) was employed to study the droplet entrainment and transport mechanisms. The distribution of liquid film flow rate around the pipe was determined using a film extractor device. The axial viewing system was used to investigate droplet entrainment in stratifying-annular air-water flows in a 0.078 m diameter horizontal pipe. The process of droplet entrainment was captured using a high speed cine camera. Both ligament and bag breakup mechanisms leading to droplet entrainment were identified. The creation of a ballistic droplet from a ligament was clearly observed. The film flow rate measurements were used in conjunction with previous measurements of droplet mass flux in the core in comparisons with a computational model which aimed to predict the transport of droplets using Reynolds Averaged Navier Stokes (RANS) modelling embodied in a commercial CFD code (CFX). In this model, the turbulent gas core was modelled and the motion of droplets emitted from the liquid layer at the bottom of the pipe was tracked in this turbulent field. Ultimately, the droplets are deposited on the tube wall and the film flow rate may be calculated using the predicted deposition rates as input data. The thesis closes with a description of a numerical experiment aimed at investigating the influence of the turbulence model on droplet transport. Specifically, comparisons were made between RANS and Large Eddy Simulation (LES) models.

Acknowledgements

I would like to thank my supervisor Prof. Geoff. Hewitt for his guidance, enthusiasm, support, patience and encouragement and for his help in finalising this thesis. I also thank my supervisor Dr Peter Spelt for his guidance and support. I thank my collaborator academic Prof. Omar Matar.

I wish to express my gratitude to Terrence Crombie, Prash Valluri and Ryo Torii for their assistance for the modelling work. I also thank TransAT Ascomp (Djamel Lakehal, Chidu Narayanan) and Hu Bin.

I thank Colin Hale, Jessy Zheng, Jerzy Pental, Ivan Zadrazil and Daniel Parsonage for their assistance in the experimental work on the WASP facility.

I thank my colleagues within the Multiphase Fluid Systems Group: Kabir Abdullahi, Deng Jr Peng, Rhys Morgan, Lennon O'Narraigh, Min Lu and Paul Pickering.

I also thank Markus Schmuck, Dan Liu, Chiara Corrao, Matthias Kwaterski, Livio Ruffine, Gianluca Memoli, Anthony Abbott, Evgeniy Burlutskiy, Antonio Pereira, Harrison Shumba and Mike.

A great deal of thanks to the department of Humanity, John Hugues, Robin, Sharon Smith and Hilary Glasmann Deal for their precious advices.

I would like to mention the following people within the Chemical Engineering Department: The academic staff, Prof. Alexander Bismarck, Prof. Felix Weinberg; Susi Underwood; Rayner Simpson; Sarah Paynes; Aleksandra Szymanska; the workshop (Tony Meredith, Paul Crudge, Richard Wallington); the computing services (Graham Stuart, Terrence Crombie), The electronic workshop (Chin Lang), The Chemical Engineering Stores (Keith Walker), the catering (Anna Dowden); Pim Amrit and Severine Toson.

I would like to thank Prof. Michel Belorgey, Prof. Alain Campbell and Prof. Taoufik Sassi.

This work has been undertaken within the Joint Project on Transient Multiphase Flows and Flow Assurance. The Author(s) wish to acknowledge the contributions made to this project by the UK Engineering and Physical Sciences Research Council (EPSRC) and the following: -ASCOMP, GL Noble Denton; BP Exploration; CD-adapco; Chevron; ConocoPhillips; ENI; ExxonMobil; FEESA; IFP Energies nouvelles; Institutt for Energiteknikk; PDVSA (INTEVEP); Petrobras; PETRONAS; SPT Group; Shell; SINTEF; Statoil and TOTAL. This work was supported further by the EPSRC under grant number EP/E021468/1. The Author(s) wish to express their sincere gratitude for this support.

In closing, I would like to thank my mother and my partner Dan for their support and patience.

Table of Contents

List of Figures

Chapter 1. Introduction

Chapter 2. Literature review

Chapter 3. Literature review on axial view technique

Chapter 4. Experimental facilities and methods

Chapter 5. Experimental results

Chapter 6. Modelling of liquid transport in stratifying annular flow

Chapter 8. Droplet transport in a tube: A numerical experiment to compare the RANS and LES turbulence models

List of Tables

Nomenclature

Main Roman Symbols

D	inner tube diameter
Q	volumetric flow rate of water
$\dot{m}$	total droplet mass flux in the gas core
r	radius
U_{SG}	superficial gas velocity
U_{SL}	superficial liquid velocity
k	turbulence kinetic energy
g	acceleration due to gravity
(dp_F / dz)	frictional pressure gradient
$(dp_F / dz)_L$	pressure gradient for the liquid phase
$(dp_F / dz)_G$	pressure gradient for the gas phase
x	flow quality
f_I^*	interfacial friction factor
f_s	smooth pipe friction factor
Q	volumetric flow of the liquid in the film
P	tube periphery
k	apparent roughness of the liquid film
E	entrained fraction
W_{LFC}	critical liquid flow rate (kg/s)
W_L	total liquid flow rate
W_{LE}	mass rates of flow of liquid as droplets
W_{LF}	mass rates of flow of liquid as film
W_G	mass rate of flow of the gas phase
k_A	constant
k_D	droplet transport coefficient
R_A	atomisation rate
R_D	deposition rate
C_D	concentration of the droplets
C_B	droplet concentration in the gas core
u_T	terminal settling velocity of the droplets.
G_{LE}	average entrained liquid mass flux
f_v	normalised volume distribution function
d_P	droplet diameter
d_t	tube diameter
d_{50}	volume medium diameter
d_{32}	Sauter mean diameter
d_{max}	maximum drop diameter
u_L	liquid phase velocity
f_L	friction factor
R	radius
k	circumferential transport coefficient
y	radial distance
f_{TP}	overall two-phase friction factor

$\dot{M}_{LP}$	mass flow rate of liquid phase in the stratified layer.
$\dot{m}_G$	gas mass flux
$\dot{m}_{LF}$	liquid film flow rate
$\dot{m}_{LFC}$	flow rate required for the onset of entrainment
$C(\mathrm{j})$	number of droplets deposited at partition j
S_I	width of the interface
j	number of partitions
R	pipe radius
C_i	number of drops with a diameter di emitted from the source plane
A(j,k)	areas of the elements
P_i(j,k)	cumulative probability of a droplet emitted at z=0 passing through the sum of areas A(j,k) of each plane p of the group of parallel plane pn
$\dot{V}_i$	volumetric emission rate of droplets of diameter di
L_p	length of the periodic elements
$n_{d_i}(j,k)$	total number of droplets of diameter di passing through the sum of parallel areas A(j,k) per unit time
C	concentration
N	segments number
D_{drop}	drop diameter
u_{drop}	droplet velocity,
C_D	drag coefficient,
u_{purge}	purge velocity
L_S	stopping distance

Main Greek Symbols

σ	surface tension
θ	circumferential coordinate angle
μ	dynamic viscosity
ρ_G	gas density
ρ_L	liquid density
η_G	gas dynamic viscosity
η_L	liquid dynamic viscosity
δ	liquid film thickness
$\bar{x}$	angle from the bottom of the tube
ε	turbulent diffusivity of the droplets
ρ_L	liquid density,
ρ_G	liquid density,
ε_f	gas diffusivity
a	residual constant
β	reciprocal time constant of the particle
τ_f	time constant
x	circumferential distance from the bottom of the tube
ϕ_L^2	pressure gradient multiplier
τ_{WL}	liquid wall shear stress
ε_L	total liquid hold-up
ε	turbulence eddy dissipation
ε_L	hold-up

μ_L	liquid kinematic viscosity
Γ_θ	peripheral mass flow rates in the circumferential direction
Γ_z	mass flow rates in the axial direction
δ	film thickness
τ_i	interfacial shear stress
τ_{yx}	interfacial shear in the circumferential direction
$\tau_o(\theta)$	local shear rate
τ_{xx}	liquid Reynolds stress (normal stress).
τ_I	mean axial interfacial shear
τ_w	wall shear stress
v	kinematic viscosity of the gas phase
$\tau_i(\theta)$	interfacial shear stress at location θ
τ_0	wall shear stress for the gas phase flowing alone in the channel
α_0, β_0	maximum vertical and horizontal emission angles of emission
α , β	emission angles
ε_{NL}	non-slip liquid hold-up.
λ	Taylor wave length

Relevant Dimensionless Number Symbols

Re	Reynolds number	$\frac{\rho UD}{\mu}$
Re_{LF}	liquid film Reynolds number $=4Q/P\mu_L$	
Fr_L	Liquid Froude number	$\frac{U_L}{(gD)^{1/2}}$
X	Martinelli parameter	
$g+$	ratio of the atomization rate at the top and the bottom	

Acronyms

CFD	Computational Fluid Dynamics
WASP	Water Air Sand and Petroleum
LOTUS	Long Tube System
LOWPRESS	Low Pressure System
RANS	Reynolds-averaged Navier-Stokes equations
LES	Large Eddy Simulation
VOF	Volume of Fluid
SGS	Sub-grid scale Model
DNS	Direct Numerical Simulation
RSM	Reynolds Stress Model
A	annular
F	frothy slug
Sp	separated or stratified
ULLN	upper-limit-log–normal
UV	ultra violet

FEP	fluorinated ethylene propylene
PBCs	Periodic boundary conditions

CHAPTER 1

Introduction

The Ph.D. study described in this thesis is focused on stratifying-annular flows in horizontal pipelines. Such flows are encountered widely in hydrocarbon recovery systems and the work described here has been carried out under the umbrella of TMF4* which is a Joint Industrial Project supported by the oil industry. In what follows, Section 1.1 states the aims of the study, Section 1.2 gives a brief overall introduction to horizontal two-phase flows, Section 1.3 discusses the specific regimes which were dealt with in the current work (stratified and stratifying annular flows) and Section 1.4 discusses atomization processes (which are at the heart of the work described). Section 1.5 gives a brief description of the processes by which the liquid film can be maintained at the top of the tube in annular flow in horizontal tubes and, finally, Section 1.6 outlines the content of the remaining Chapters in this thesis.

1.1. Aims of study

In stratifying-annular flows in horizontal pipes, the liquid film is thicker at the bottom of the pipe than at the top due to the influence of gravity. In some cases, the liquid may fail to wet the top of the pipe. This may lead to corrosion of the top of the pipe which, in turn, may lead to pipe failure.

The overall aim of the present study is to gain a better understanding of liquid transport mechanisms in stratifying-annular flows. Liquid may be transferred towards the top of the pipe by wave action in the liquid film or by the entrainment of droplets in the lower part of the pipe and the subsequent transport of these droplets through the gas core to deposit on the upper part of the pipe surface. Typically, in stratifying annular flow, droplet entrainment occurs principally from the layer of liquid at the bottom of the pipe (the “pool”). Though wave action is an important mechanism for maintaining annular flow in small diameter pipes, the focus here has been on the droplet transport mechanism which is dominant for medium and large diameter pipes.

* TMF4 is the fourth in a series of projects on Transient Multiphase Flow (TMF) which is supported by a group of oil and service companies.

The objective of this work has been the development of a fundamental insight into the physical processes that determine droplet entrainment and transport in stratifying annular flow. The work has included both experimental and computational studies.

1.2. Two-phase gas-liquid flow in a horizontal pipe

1.2.1. Standard flow patterns

Several flow regimes may be observed in horizontal gas-liquid flow. These regimes depend on flow rates of the two phases, the fluid properties and the configuration of the pipeline system. Hubbard and Dukler (1966) divided those regimes into three groups, namely separated, intermittent and dispersed flows (see Figure 1.1).

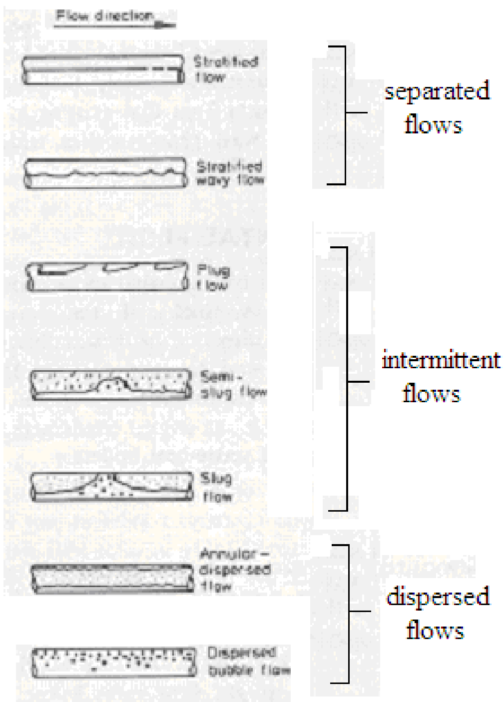

Figure 1.1. Flow regimes in horizontal flows.

In separated flows, there is a continuous gas phase at the top of the pipe and a continuous liquid phase at the bottom. They are split into two groups: stratified flows which are characterized by a smooth interface and stratified wavy flows characterized by wave formation at the interface.

Intermittent flows are characterised by discontinuities in the gas and/or liquid flows. This category of flow includes: plug flows characterized by bullet shaped bubbles moving along the top of the tube, semi slug flow characterized by waves developing on top of a stratified layer but which not bridge the top of the tube and finally slug flow characterized by waves bridging the top of the pipe and aeration taking place at the slug front.

Dispersed flows are characterized by the dispersion of one of the phases in the other. This group includes dispersed bubble flow where the gas is dispersed in the liquid phase in the form of bubbles and dispersed annular flow where part of the liquid phase is dispersed in the gas core as liquid droplets. In horizontal flows, gravitational separation occurs in these regimes. Thus, the bubbles in dispersed bubble flow tend to congregate at the top of the tube and the liquid film in dispersed annular flow tends to be much thicker at the bottom of the tube than it is at the top (hence the name stratifying-annular flow given to this regime).

1.2.2. Flow pattern maps

In order to predict the conditions at which each of the above flow regimes occurs, a large amount of data has been collected and these data have been mapped using a wide variety of empirical and semi-empirical representations. However, most of the data are for air-water flows in tubes of fixed diameters. In order to widen their applications, continuous efforts have been made to generalize the flow pattern maps.

One of the earliest attempts was made by Baker (1954) who took into account the physical properties by introducing the Baker physical property parameters λ_B and ψ_B .

$$\lambda_B = \sqrt{\left(\frac{\rho_G \rho_L}{\rho_A \rho_W}\right)} \tag{1.1}$$

$$\varphi_B = \left[\frac{\sigma_w}{\sigma}\right]\left[\frac{\mu_L}{\mu_W}\right]^{1/3}\left[\frac{\rho_W}{\rho_L}\right]^{2/3} \tag{1.2}$$

Where σ is the surface tension, ρ the density and μ the viscosity. The subscripts $_W$ and $_A$ indicate respectively water and air at atmospheric conditions, $_L$ and $_G$ are the liquid and gas values.

The map (cf. Figure 1.2) was a plot of $\dot{m}_G/\lambda_B$versus $\dot{m}_L\lambda_B\psi_B/\dot{m}_G$ (where $\dot{m}_G/\lambda_B$ and $\dot{m}_L\lambda_B\psi_B/\dot{m}_G$ are generalized coordinate parameters) and was divided into seven regions. Scott (1963) has later modified the map and introduced transition regions between neighbouring regimes. Although the map was extremely useful, the choice of a dimensional y-axis limits its results to condition close to those of the original experiments.

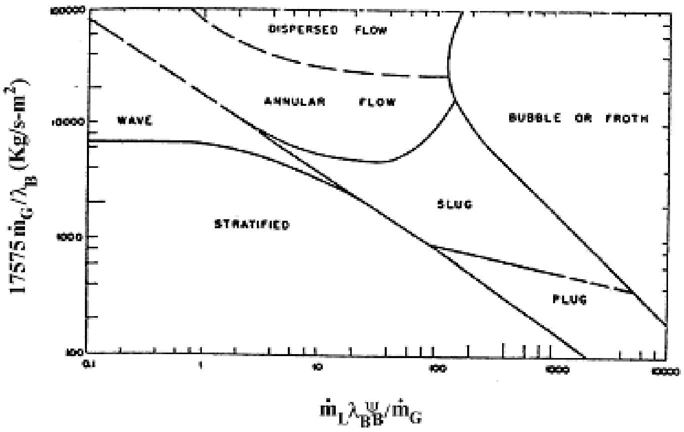

Figure 1.2. Flow pattern map of Baker (1954), modified by Scott (1963).

Later studies showed that the Baker map was deficient in representing the effects of various parameters. This had led to the development of alternative transition maps. Beggs & Brill (1973) tried to simplify their map by considering only three regimes: separated (stratified, wavy and annular), intermittent (plug and slug) and dispersed (bubbly flow). However, it was based on a system of fixed properties and failed to account for density, viscosity and interfacial tension variation. Moreover, their transition lines are 'best-fit' and are only applicable to systems similar to those on which they were obtained.

Mandhane et al (1974) used the flow pattern observations from the University of Calgary Multiphase Pipe Flow Data Bank to generate a basic flow pattern map of superficial gas velocity (U_{SG}) versus superficial liquid velocity (U_{SL}), see Figure 1.3. The map was based on air-water flow data and was divided into five regimes: stratified wavy, elongated bubble, slug, dispersed and annular. Despite its limitation in being a purely correlational approach, it was constructed using a comparatively large database and should provide a better prediction over a wider range of conditions compared to the map of Beggs & Brill (1973). Taitel and Dukler (1976) developed semi-analytical models for flow regime transitions in horizontal flow and fitted models to the Mandhane et al (1994) map as shown in Figure 1.3.

In the present work, experiments are being conducted primarily on the Imperial College WASP facility. This is described in more detail in Section 6.2. The WASP facility has a bore horizontal test section and data obtained by Jamari (2006) for flow patterns in the facility are shown in Figure 1.4.

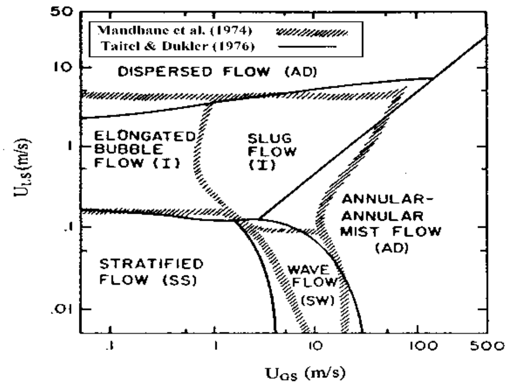

Figure 1.3. Flow pattern maps of Mandhane (1974) and Taitel & Dukler (1976).

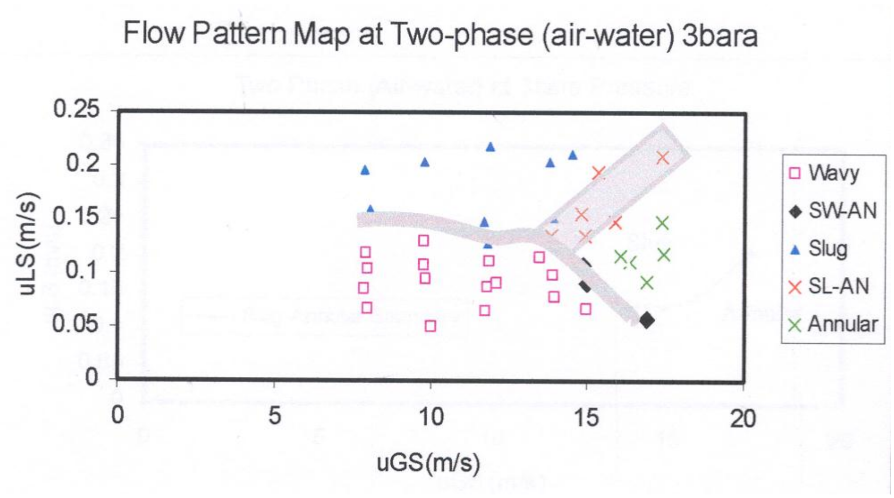

Figure 1.4. Stratified and stratifying-annular flow: flow pattern map from WASP facility (Jamari, 2006).

1.3. Stratified and stratifying annular flows

The present study is focused on the following regimes:

- Stratified flow: the liquid flows in the lower part of the pipe, the gas flows above the liquid. The gas-liquid interface is smooth.

- Wavy-stratified flows: an increase of gas causes the formation of waves at the gas-liquid interface.

- Stratifying-annular flows: it is a transition regime between stratified flow and annular flow. It is characterized by a liquid film around the pipe but not at the top, the liquid film at the bottom of the pipe is thicker than this in the case of an annular flow and liquid droplets are entrained in the gas core.

- Annular flows: this flow regime is characterized by a liquid film around the wall of the tube (thicker at the bottom of the tube because of the gravity) and droplets entrained from the liquid film in the gas core.

The regions of occurrence of these regimes are dictated by the superficial liquid and gas velocities.

We shall be concerned specifically with stratified and stratifying/annular flows. In Figure 1.5 video snapshots are shown of the side view in a 32.8 mm diameter pipe in the LOTUS facility which illustrates the transition between stratified and annular flows.

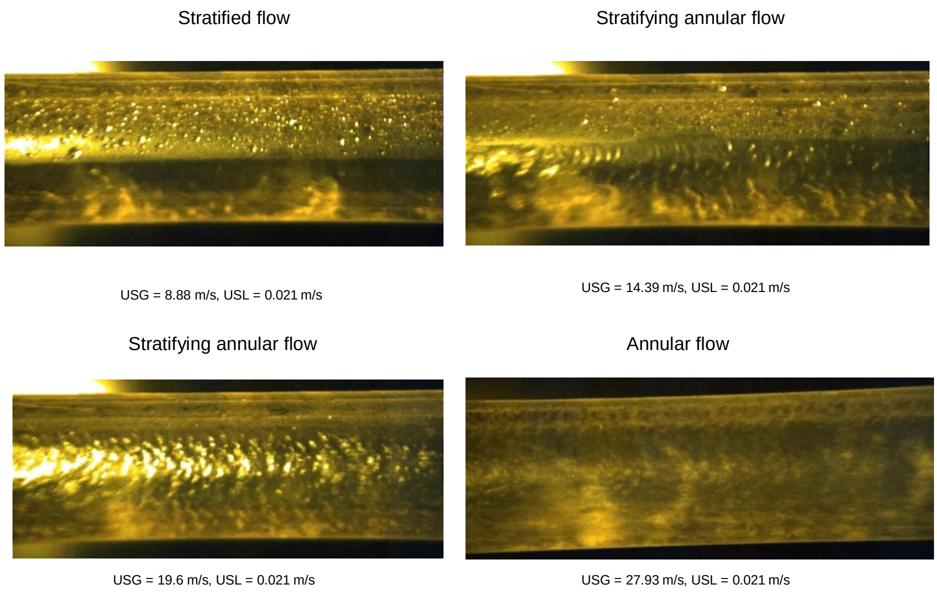

Figure 1.5. Videos of 32.8 mm experiments: Stratified and stratifying-annular flow. Side view.

Figure 1.6 presents a schematic of the cross sectional view of each flow pattern (stratified, annular and the transition stratifying-annular flow).

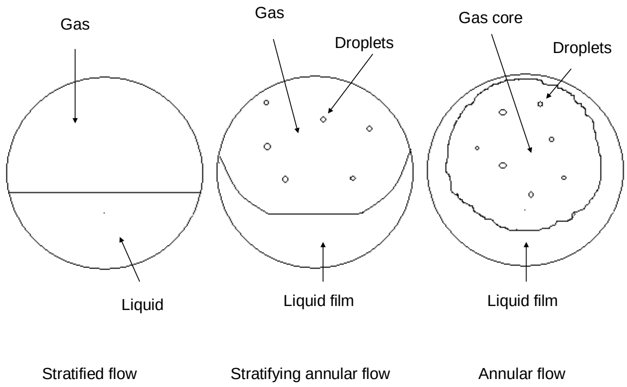

Figure 1.6. Schematic of the cross sectional view of the transition between stratified and annular flows.

1.4. Atomization processes

The formation of droplets from a liquid layer is a highly complex process and may occur by a variety of mechanisms. Azzopardi (1983) suggested that the principal mechanisms are “bag breakup” and “ligament breakup” as illustrated in Figure 1.7, bag breakup occuring at lower flow rates and ligament break up occurring at higher flow rates.

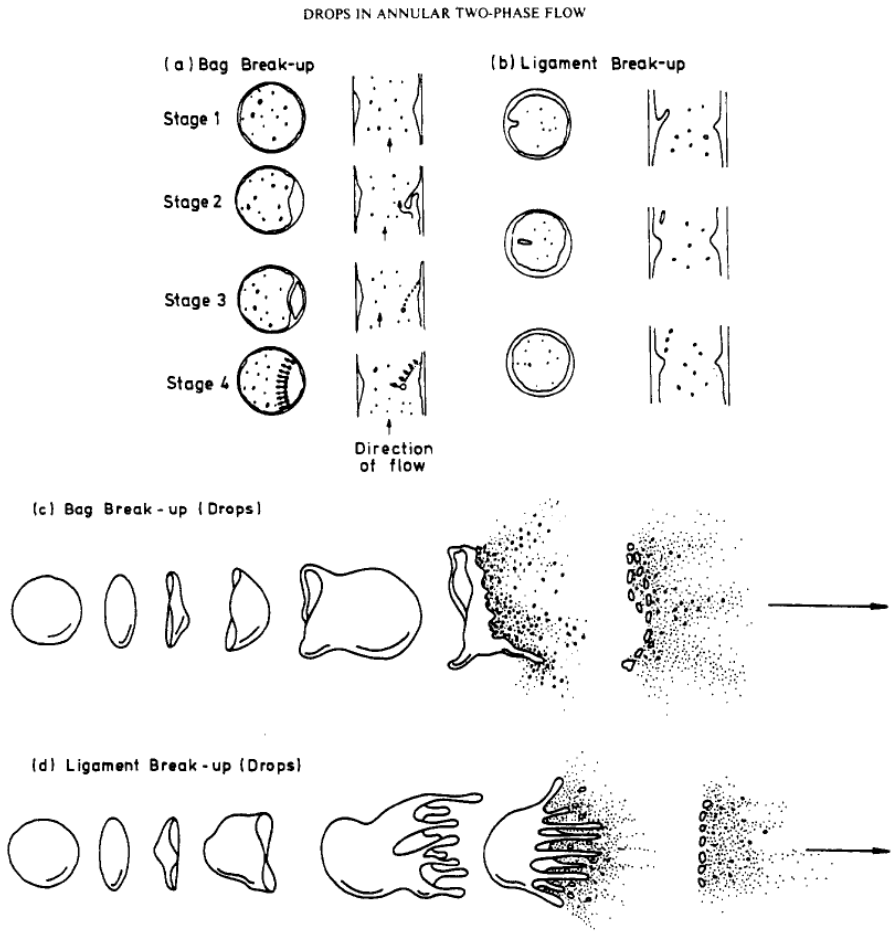

Figure 1.7. Mechanisms of atomization and drop breakup (Azzopardi, 1997).

1.5. Mechanisms responsible for maintaining a liquid film around the wall of the pipe in annular flow, and drop size

In stratifying-annular flow in horizontal pipes, some mechanism must exist to transport the liquid phase towards the top of the pipe, this mechanism counteracting the gravitational force which tends to move the liquid towards the bottom of the pipe. Three mechanisms have been suggested for maintaining a liquid film around the pipe, namely droplet entrainment, wave spreading (dominant in small diameter pipes) and secondary flow. A detailed review of these mechanisms is given in Chapter 2. Here, a brief statement is given on each mechanism with the objective of explaining the context of the present work.

Droplet transport

Droplets are entrained from the liquid layer at the bottom of the pipe and are deposited at the top to form a liquid film. This liquid film drains then towards the bottom. Two classes of droplets are identified: large droplets emitted from the bottom passing ballistically to the upper surfaces (dominant in pipes of medium diameter eg. the 78 mm tube in the WASP facility) and small diameter droplets moving by turbulent diffusion to the upper part of the pipe (dominant mechanism in large diameter pipes).

Wave spreading

The transport of liquid around the circumference may be due to the influence of waves. Waves, being thicker at the bottom of the pipe than at the top, sweep the liquid towards the top.

Secondary flow

This is created by the differences in, for instance, the wave height around the periphery of the pipe which induces differences in the apparent roughness of the gas-liquid interface as seen by the phase gas. This secondary flow corresponds to gas moving upwards near the interface and downwards in the centre of the pipe. Secondary flow can transport the liquid upwards by creating a circumferential interfacial shear stress which opposes gravity.

1.6. Structure of thesis

In what follows in this thesis, the following Chapters are presented:

Chapter 2 gives an exhaustive review of the literature on horizontal annular and stratifying annular flows.

Chapter 3 presents a review on axial view photography. In this technique (which has been used extensively in the experimental studies described here), the oncoming flow is viewed along the axis of the pipe.

Chapter 4 describes the experimental facilities used in the present work including two low-pressure air-water flow facilities (LOTUS and LOWPRESS) and a high pressure multiphase flow facility (WASP). This chapter also describes the measurement methods employed with an emphasis on axial view photography and on new apparatus for the measurement of local film flow rate.

Chapter 5 presents the results from the experiments, again with an emphasis on axial view photography and film flow rate measurement.

Chapter 6 describes the bases of the model used to calculate droplet transport and deposition in stratifying annular flow. This model was based on Lagrangian tracking of droplets in the gas core using a commercial code (CFX) based on a Reynolds Averaged Navier Stokes (RANS) representation of the turbulence.

Chapter 7 presents the results of the CFX-RANS calculations and gives comparisons between these calculations and experimental results for local droplet mass flux in the core and for liquid film flow rate.

Chapter 8 presents the results of a numerical experiment aimed at comparing calculations of droplet transport using RANS and Large Eddy Simulation (LES) representations of turbulence in the gas phase.

Chapter 9 summarizes the main conclusions from the work and presents recommendations for further studies.

CHAPTER 2

Literature review

2.1. Introduction

This document aims to present a review of the literature relevant to stratified annular flow in horizontal tubes. In what follows below, Section 2.2 deals with pipe-averaged information and includes a discussion of flow pattern (Section 2.2.1), pressure gradient (Section 2.2.2), liquid hold-up (Section 2.2.3), entrained fraction (Section 2.2.4) and drop size (Section 2.2.5). By definition, there is concern also about the *distribution* of time averaged quantities and Section 2.3 presents a discussion of such distributions for liquid film thickness (Section 2.3.1), liquid film flow rate (Section 2.3.2) and entrained droplet mass flux (Section 2.3.3). In Section 2.4, studies of time-varying phenomena are discussed, and in particular time-varying film thickness (interfacial waves) in Section 2.4.1 and photographic studies of flow structures in Section 2.4.2.

It is obvious that there will be a tendency, in horizontal flows, for the liquid phase to flow downwards towards the bottom of the tube under the influence of gravity. Thus, if annular flows with the tube completely wetted are to exist, then there must be some mechanism by which the liquid is transported upwards in opposition to the influence of gravity. Basically, there have been three classes of models to address this problem:

(1) *Wave spreading and mixing.* In this class of models, it is suggested that the influence of interfacial waves on the liquid film is such as to cause transport around the circumference. The film on the bottom surface has a much greater thickness than that on the top and, consequently, has larger waves. The basis of the wave spreading/mixing mechanism is that these waves act to sweep the liquid towards the top of the pipe. Models based on this hypothesis are discussed in Section 2.5.1.

(2) *Droplet transport.* In this mechanism, droplets are entrained from the film at the bottom of the pipe and are transported towards the upper part of the pipe where they deposit and form a liquid film which drains downwards towards the bottom. Thus, there is a process of

continuous renewal and drainage of the film in the upper part of the pipe. Work related to this mechanism is summarised in Section 2.5.2.

(3) *Secondary flow*. In this mechanism, a secondary flow in the gas phase is created as a result of the variation of wave height on the liquid film around the periphery. The differences in wave height give differences in the apparent roughness of the interface as seen by the gas phase and this creates a secondary flow with the gas moving upwards near the interface and downwards in the centre of the pipe. This secondary flow can create a circumferential interfacial shear stress which can oppose gravity and transport the liquid upwards. The work on this mechanism is discussed in Section 2.5.3.

In Section 2.6, some brief conclusions are drawn from the literature appraisal.

2.2. Quantities averaged over time and cross section

Here, we consider quantities which represent averages of measurements or observations which are averaged over time and over the cross sectional area of the pipe. The *flow pattern* or *flow regime* has been traditionally based on visual observations (aided by, for instance, high speed cine or video images) which attempt to classify the types of interfacial distribution observed in a two-phase flow. Thus, though the determination of flow pattern represents an interpretation of instantaneous events, the flow pattern itself can be regarded as a time and space averaged parameter and is discussed in Section 2.2.1. Other time and spaced averaged quantities discussed here are pressure gradient (Section 2.2.2), liquid hold-up (Section 2.2.3), entrained fraction (Section 2.2.4) and drop size (Section 2.2.5).

2.2.1. Flow Pattern

The principal flow patterns in horizontal two-phase flows are stratified (where the gas and liquid flow in separate layers), slug (where regions of liquid-continuous flows pass down the pipe separated by regions of relatively stratified flow) and annular (where the liquid flows partly as a film around the periphery of the tube and, usually, partly as entrained liquid droplets in the gas core). There has been an enormous amount of work on flow patterns in horizontal tubes and a whole range of methods have been developed to predict the transitions. These ranges from the classical empirical flow maps (such as those of Baker, 1954 and Mandhane et al 1974) to more analytical approaches such as that of Taitel

& Dukler (1976). A general review of the slug-annular and stratified-annular transitions has been prepared by Jamari (2005).

The unfortunate fact is that the empirical flow pattern maps are based on data often well removed from the conditions of interest and the fundamental bases of the semi-theoretical maps (such as that of Taitel & Dukler, 1976) are not totally secure. However, it is worth mentioning four papers which address the flow pattern transition question as follows:

1- Kadambi (1982) suggests "global" transition criteria, based upon a momentum balance and energy transfer between the two phases. The criteria require that the mechanical energy change experienced by the gas be greater than the work done by the interfacial forces in bringing about the transition. It is not clear how general this criterion is, though it did appear to fit available data.

2- Fukano et al (1985) presents an interesting flow pattern map in terms of the liquid Froude number (Fr_L) and the Martinelli parameter X as shown in Figure 2.1. Here, Fr_L and X are defined as:

$$Fr_L = \frac{U_L}{(g\,D)^{1/2}} \tag{2.1}$$

$$X = \left[\frac{(dp_F/dz)_L}{(dp_F/dz)_G}\right]^{1/2} \approx \left(\frac{1-x}{x}\right)^{0.9}\left(\frac{\rho_G}{\rho_L}\right)^{0.5}\left(\frac{\eta_L}{\eta_G}\right)^{0.1} \tag{2.2}$$

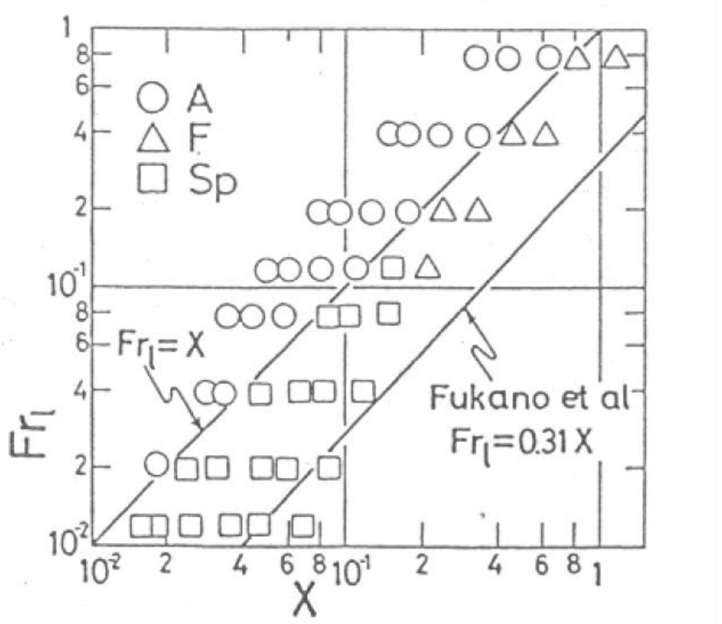

Figure 2.1. Horizontal two-phase flow pattern map of Fukano et al (1985).

In Equations 2.1 and 2.2, U_L is the superficial velocity of the liquid phase, g the acceleration due to gravity, D the tube diameter, where $(dp_F/dz)_L$ and $(dp_F/dz)_G$ are the pressure gradients for the liquid and gas phases flowing along in the channel, x the quality (fraction of the mass flow which is gas), ρ_L and ρ_G the liquid and gas densities and η_L and η_G the liquid and gas viscosities. The regimes shown in Figure 2.1 are annular (A) frothy slug (F) and separated or stratified (Sp). The transition between the annular and the other flow regimes is expressed as $Fr_L = X$ and Fukano et al suggest a line corresponding to $Fr_L = 0.31X$ as a line above which disturbance waves occur. Thus, they claim that disturbance waves are a *necessary* condition for the existence of annular flow (we shall return to this point further in Section 2.5.1 below).

3- Baik & Hanratty (2003) present the flow pattern map shown in Figure 2.2. The numbers associated with each point in this diagram indicate the calculated film thickness (in micrometers) and Baik and Hanratty suggest that a film thickness of greater than 20 micrometers in required to maintain a wetted condition. Baik and Hanratty cite a Private Communication from G. Zabaras (2002) giving the natural gas transition to annular flow as shown in the diagram. This seems to occur at film thicknesses calculated for the top of the tube, which are in excess of the 20 micrometers suggested by Baik and Hanratty. This emphasises the fact that *wetting* of the upper surface is important and may represent a limiting condition for corrosion. Surface wetting in annular flow was studied by Hewitt & Lacey (1965). The liquid flow rate required to wet the surface (the "minimum wetting rate") was found to decrease with increasing gas velocity changing from around 0.02 kg/ms (i.e. mass flow rate per unit perimeter) at around 30 m.s^{-1} gas velocity to around 0.01 kg/ms at around 80 m.s^{-1} gas velocity. The work of Hewitt and Lacey (1965) is cited by Baik & Hanratty (2003) who note that the film thicknesses estimated for the Hewitt and Lacey experiments were much greater than the 20 micrometers suggested by Baik & Hanratty and this may be consistent with the observations by Zabaras (2002).

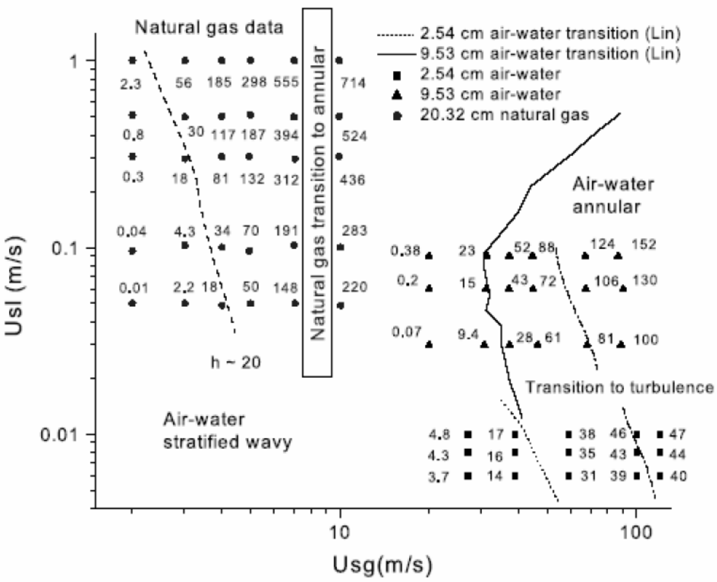

Figure 2.2. Map for transition for stratified to annular flow (Baik & Hanratty, 2003).

4- The characteristics of an oil-gas flow in a horizontal 125 mm diameter pipe were investigated both experimentally and numerically by Lu et al (2007). Only stratified flow, wavy flow and slug flow were observed in the experiments. The flow patterns obtained in this study are shown in Figure 2.3.

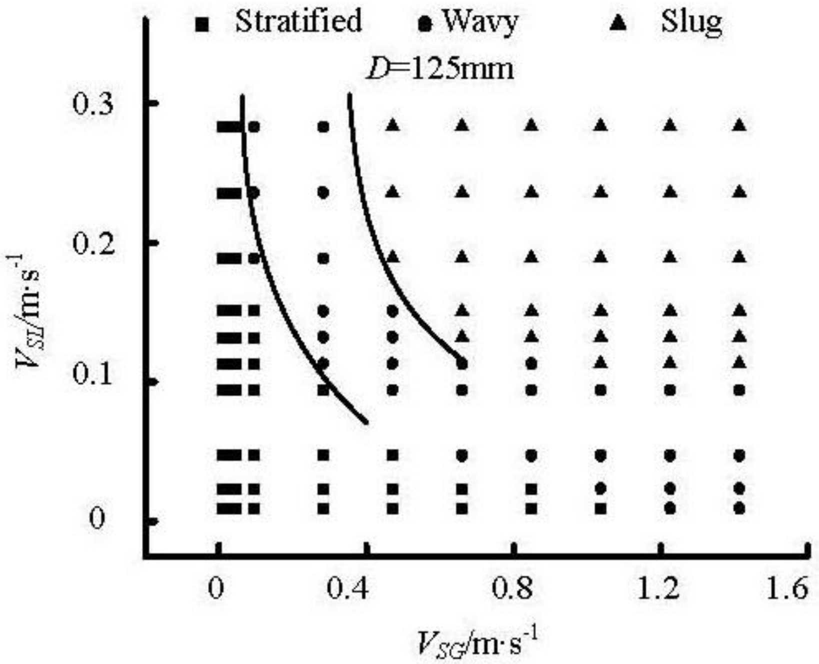

Figure 2.3. Flow patterns of oil-gas two-phase flow in a 125 mm diameter horizontal pipe.

A critical superficial liquid velocity (above which the superficial liquid velocity has to be in order the slug flow to appear) for the transition from stratified flow to slug flow was found to be equal to V_{SL} =0.113 m.s^{-1}. This critical value was independent of an increase of the superficial gas velocity. An increase in the superficial liquid velocity for the transition from stratified flow to slug flow led to a decrease in the corresponding superficial gas velocity.

Numerical simulations of different flow patterns and their transitions were performed with the Computational Fluid Dynamics (CFD) using the Volume Of Fluid (VOF) technique and the results of the computations were in agreement with the experimental data.

Zhang and Sarica (2011) presented a review on low liquid loading gas-liquid flow giving descriptions of the typical flow phenomena. These descriptions were based on the experimental data gathered by various authors. The models used to predict flow pattern, pressure gradient and liquid holdup were listed, as well as the closure relationships developed in the previous literature. It was concluded that almost all empirical correlations were inadequate for the predictions of low liquid loading flow behaviour. It was also shown that for the different mechanistic models developed, their performance depended on the accuracies of the closure relationships (interfacial shear, liquid entrainment fraction, wetted wall fraction). Zhang and Sarica suggest improvements to the closure relationships based on new experimental and modelling studies.

2.2.2. Pressure Gradient

Pressure gradients for horizontal flows have been extensively investigated. The approach has been mainly one of the use of empirical correlations, typified by the early correlation of Lockhart & Martinelli (1949) and later correlations such as those of Chisholm (1973) and Friedel (1979). A systematic evaluation of horizontal flow pressure drop correlations against a large data base is presented by Hewitt (2000). Not surprisingly, it is found that the empirical correlations show considerable scatter compared to the data which is, of course, a reflection of the complexities of the flows as discussed here.

Laurinat et al (1984) correlated frictional pressure gradients for the specific case of horizontal annular flow and present a number of alternative correlations. The simplest of these is as follows:

$$\left({dp_F}\big/{dz} \right) = \frac{2 f_I^*}{d_t} \rho_G U_{SG}^2 \tag{2.3}$$

where (dp_F / dz) is the frictional pressure gradient, f_I^* the interfacial friction factor, d_t the tube diameter and U_{SG} the superficial gas velocity. f_I^* is given by:

$$\frac{f_I^*}{f_s} = 2 + 2.5 \times 10^{-5} \frac{\mathrm{Re}_{LF}}{d_t} \tag{2.4}$$

where f_s is the smooth pipe friction factor for the same gas velocity and Re_{LF} is the liquid film Reynolds number ($= 4Q / P\mu_L$, where Q is the volumetric flow of the liquid in the film, P the tube periphery and μ_L the liquid kinematic viscosity).

Building on earlier work by Hamersma & Hart (1987), Hart et al developed an interesting model for pressure drop and hold-up in stratifying annular flow. The basis of the model is shown in Figure 2.4. The flow is represented notionally as being one in which a fraction θ of the perimeter of the tube is wetted by a liquid layer of constant thickness. The pressure gradient is given by:

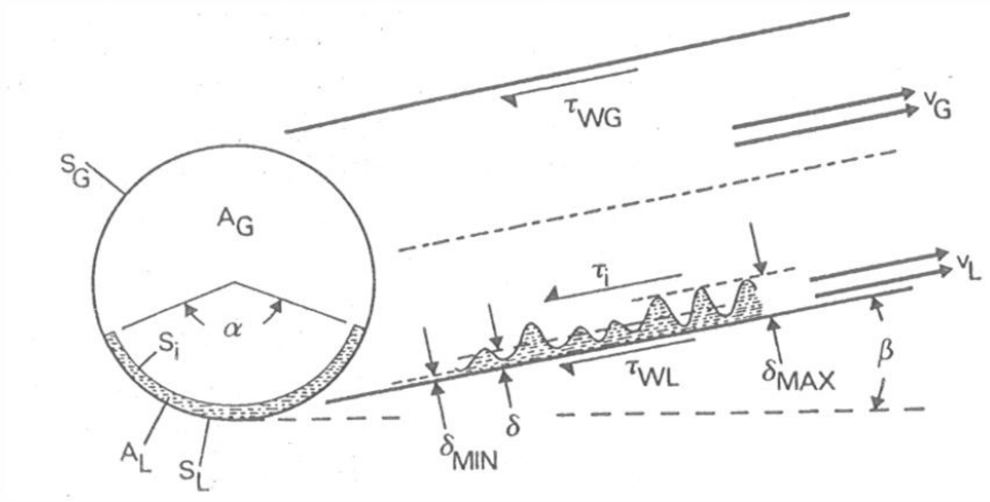

Figure 2.4. Basis of the model of Hart et al (1989).

$$\frac{dp_F}{dz} = \frac{2 f_{TP}}{d_t} \rho_G U_{SG}^2 \tag{2.5}$$

where f_{TP} is given by:

$$f_{TP} = (1-\theta) f_s + \theta f_i \tag{2.6}$$

where f_i is the interfacial friction factor which is obtained from the Equation of Eck (1973) as follows:

$$f_i = \frac{0.0625}{\left[\log_{10}\left(\frac{15}{\mathrm{Re}_G} + \frac{k}{3.715 d_t}\right)\right]^2} \tag{2.7}$$

where k is the apparent roughness of the liquid film which is approximated by:

$$k \approx 2.3\delta \tag{2.8}$$

where δ is the thickness of the liquid film. Hart et al give the following correlation for θ:

$$\theta = \theta_0 + 0.26 Fr^{0.58} \tag{2.9}$$

where Fr is given by:

$$Fr = \left(\frac{\rho_L}{\rho_L - \rho_G}\right) \frac{U_{SL}^2}{g\, d_t} \tag{2.10}$$

and θ_0 is related to liquid hold-up ε_L by the expression:

$$\theta_0 = 0.52\varepsilon_L^{0.374} \qquad (2.11)$$

The film thickness δ may be calculated from the hold-up ε_L by the expression:

$$\delta = \frac{\varepsilon_L d_t}{4\theta} \qquad (2.12)$$

Equations 2.11 and 2.12 require values of ε_L and Hart et al. suggest the following correlation in order to calculate this:

$$\frac{\varepsilon_L}{1-\varepsilon_L} = \frac{U_{SL}}{U_{SG}}\left\{1+\left[10.4\,\mathrm{Re}_{SL}^{-0.363}\left(\frac{\rho_L}{\rho_G}\right)^{\frac{1}{2}}\right]\right\} \qquad (2.13)$$

The above equations were found to give good agreement with a wide range of experimental pressure gradient and hold-up data.

Badie proposed a new analysis in predicting pressure gradient in two-phase gas-liquid flows. This analysis is able to capture the effect of liquid viscosity and produces reasonable estimates for air-water and air-oil flows. The estimates are compared with experimental data and results from other prediction techniques (Hart et al, 1989), Chen et al (1995), and Vlachos et al (1999).

The flow geometry proposed by Badie is illustrated in Figure 2.5. In this geometry, the main liquid layer is at the bottom of the pipe and the side and upper walls of the pipe are covered with a thin liquid film.

The pipe used in Badie’s experiments was 78 mm internal diameter tube which is typical of industrial applications.

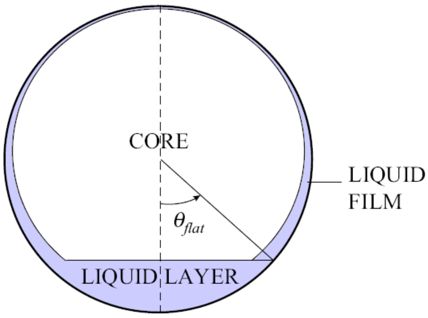

Figure 2.5. Proposed flow geometry.

It is assumed in this analysis that the liquid film is produced by deposition of entrained droplets present in the gas core as shown in Figure 2.6. This phenomenon is assumed to be dominant in high diameter pipe in comparison with the wave transport mechanism which is dominant in smaller diameter pipe.

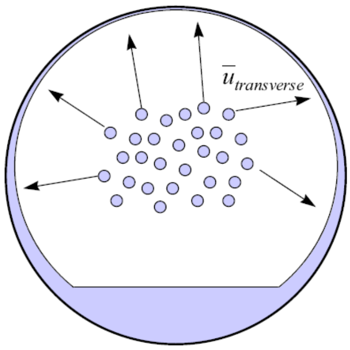

Figure 2.6. Liquid film replenishment.

The total liquid hold-up is obtained from the correlation by Hart et al (1984) (Equation 2.13).

Where the total liquid hold-up ε_L has contribution from the liquid in the layer flowing along the bottom $\varepsilon_{L,film}$, the film at the sides and the top and the entrained droplets $\varepsilon_{L,drop}$.

The liquid hold-up is therefore defined by:

$$\varepsilon_L = \varepsilon_{L,layer} + \varepsilon_{L,film} + \varepsilon_{L,drop} \quad (2.14)$$

However, $\varepsilon_{L,film} + \varepsilon_{L,drop} << \varepsilon_{L,layer}$

It is therefore assumed that

$$\varepsilon_L \approx \varepsilon_{L,layer} \quad (2.15)$$

The angle $\theta_{flat,}$ (see Figure 2.5), formed at the centre of the pipe, between the vertical diameter and the edge of the flat liquid layer, shown in Figure 2.7, is evaluated by solving the geometrical relationships:

$$\varepsilon_{L,layer} = \frac{\theta_{flat} - \cos\theta_{flat}\sin\theta_{flat}}{\pi} \tag{2.16}$$

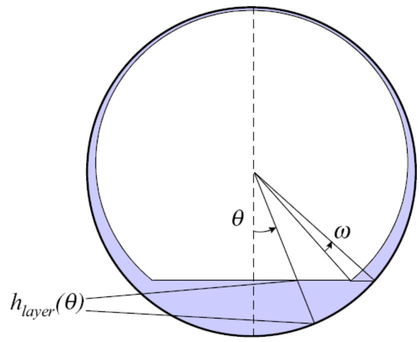

Figure 2.7. Liquid layer analysis.

The height of the liquid layer at a position θ, h_{layer} is defined as:

$$h_{layer}(\theta) = \left(\frac{D}{2}\right)\left(1 - \frac{\cos\theta_{flat}}{\cos\theta}\right) \quad \text{for} \quad 0 \le \theta \le \theta_{flat} - \omega \tag{2.17}$$

The height of the liquid film h_{film} illustrated in Figure 2.8 is obtained from the Nusselt analysis of a draining film in a tube:

$$h_{film}(\theta) = \left(\frac{3\eta_L\,\dot{m}_D R(\pi-\theta)}{\rho_L(\rho_L-\rho_G)g\sin\theta}\right)^{\frac{1}{3}} \quad \text{for} \quad \theta_{flat} - \omega \le \theta \le \pi \tag{2.18}$$

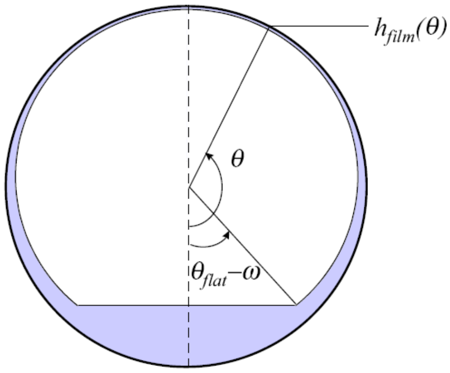

Figure 2.8. Liquid film analysis.

The rate of mass deposited per unit area on the walls or mass flux, $\dot{m}_D$ is given by:

$$\dot{m}_D = \varepsilon_{L,drop}\rho_L\bar{u}_{transverse} \tag{2.19}$$

Where $\varepsilon_{L,drop}$ is the droplet hold-up, ρ_L the density of the liquid phase and $\bar{u}_{transverse}$ the average velocity of droplets.

Badie used sampling probes (see Chapter 4) to give data on local droplet flow rate value $\dot{M}_c$ (kg.s^{-1}) at the tube axis. It allows the mass flux to be calculated from:

$$\dot{m}_c \approx \frac{\dot{M}_c}{S_{tube}} \tag{2.20}$$

where S_{tube} is the sampling probe cross sectional area. The relationships for $\varepsilon_{L,drop}$ is given by:

$$\varepsilon_{L,drop} = \frac{\dot{m}_C}{\bar{u}_{axial}\rho_L} \tag{2.21}$$

The average axial velocity of the droplets at the centre of the pipe $\bar{u}_{axial}$ is approximated by:

$$\bar{u}_{axial} \approx u_G \tag{2.22}$$

where u_G is the gas velocity.

Badie uses the experimental result of Hart et al. (1989) to evaluate the roughness k for the liquid layer and the liquid film:

$$k_{layer} = 2.3\bar{h}_{layer} \tag{2.23}$$

$$k_{film} = 2.3\bar{h}_{film} \tag{2.24}$$

$\bar{h}_{layer}$ and $\bar{h}_{film}$ are the average heights, respectively of the liquid film and the liquid layer. They are defined by:

$$\bar{h}_{layer} = \frac{\int_0^{\theta_{flat}-\varpi} h_{layer}(\theta)d\theta}{\int_0^{\theta_{flat}-\varpi} d\theta} \tag{2.25}$$

$$\bar{h}_{film} = \frac{\int_{\theta_{flat}-\varpi}^{\pi} h_{film}(\theta)d\theta}{\int_{\theta_{flat}-\varpi}^{\pi} d\theta} \tag{2.26}$$

The roughness k is used in the correlation developed by Eck (1973) (Equation 2.7) to evaluate the interfacial friction factor f_i for the layer and the film portions of the pipe.

The overall two-phase friction factor f_{TP} is obtained from:

$$f_{TP} = \left(\frac{\theta_{flat} - \omega}{\pi}\right) f_{i,layer} + \left(1 - \frac{\theta_{flat} - \omega}{\pi}\right) f_{i,film} \qquad (2.27)$$

This leads to the expression of the pressure gradient given by:

$$\frac{dP}{dz} = \frac{2 f_{TP} \rho_G u_G^2}{D} \qquad (2.28)$$

where f_{TP} is the overall two-phase friction factor.

The results obtained by Badie (2000) for air-water and air-oil stratifying-annular flows are shown in Figures 2.9 and 2.10.

The pressure gradient obtained from Badie's analysis is compared with experimental data from Badie's experiments and also compared to previous analytical studies carried out by Hart et al. (1989), Chen et al. (1995) and Vlachos et al. (1999).

For the air-water case, the model and the experimental data from Badie are in close agreement. Moreover, the prediction by Badie is in agreement with the other predictions.

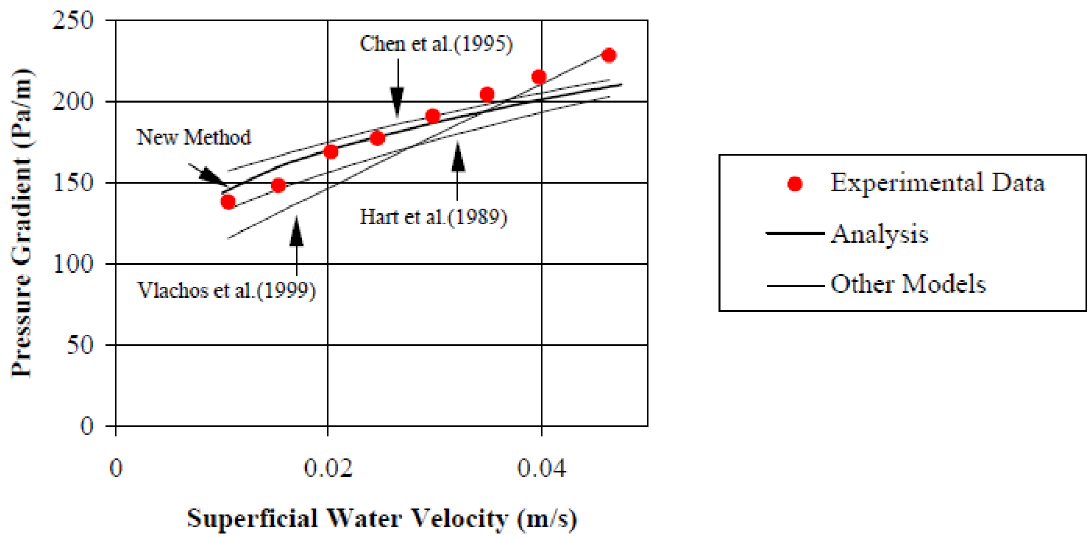

Figure 2.9. Pressure gradient comparison for air-water flows (superficial air velocity =25m.s^{-1}).

For the air-oil case, the Badie model also gives good predictions for pressure gradient the prediction technique being able to capture the effect of viscosity. However, the other models (developed using air-oil data) perform less well.

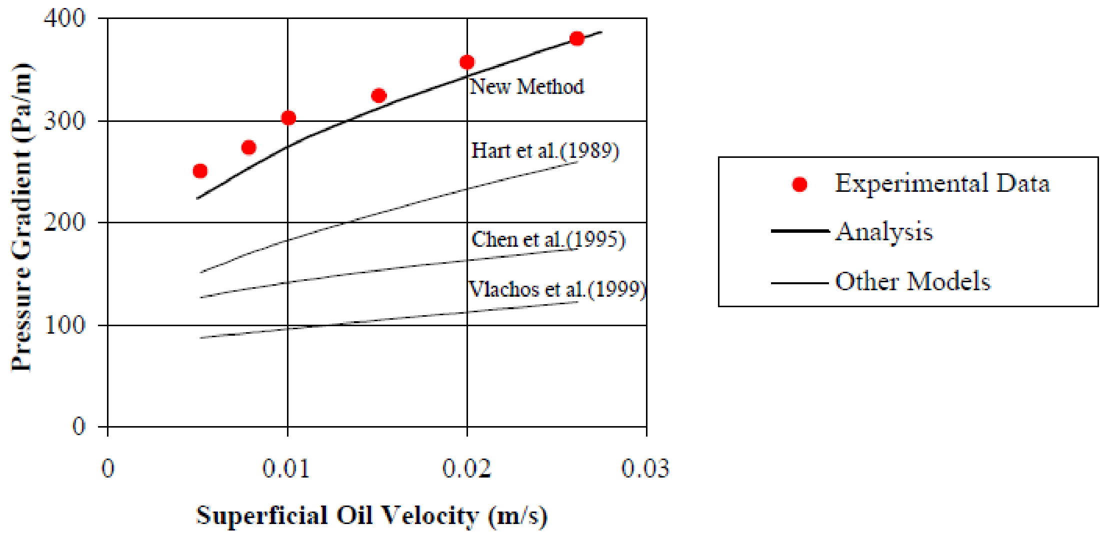

Figure 2.10. Pressure gradient comparison for air-oil flows (superficial air velocity =25m.s^{-1}).

Badie (2000) also measured (using a hot film probe) the wall shear stress at the bottom of the pipe and compared this with the average wall shear stress calculated from the pressure gradient. Typical results are shown in Figure 2.11; the wall shear stress at the bottom of the pipe is seen to be many times the average value as would have been expected.

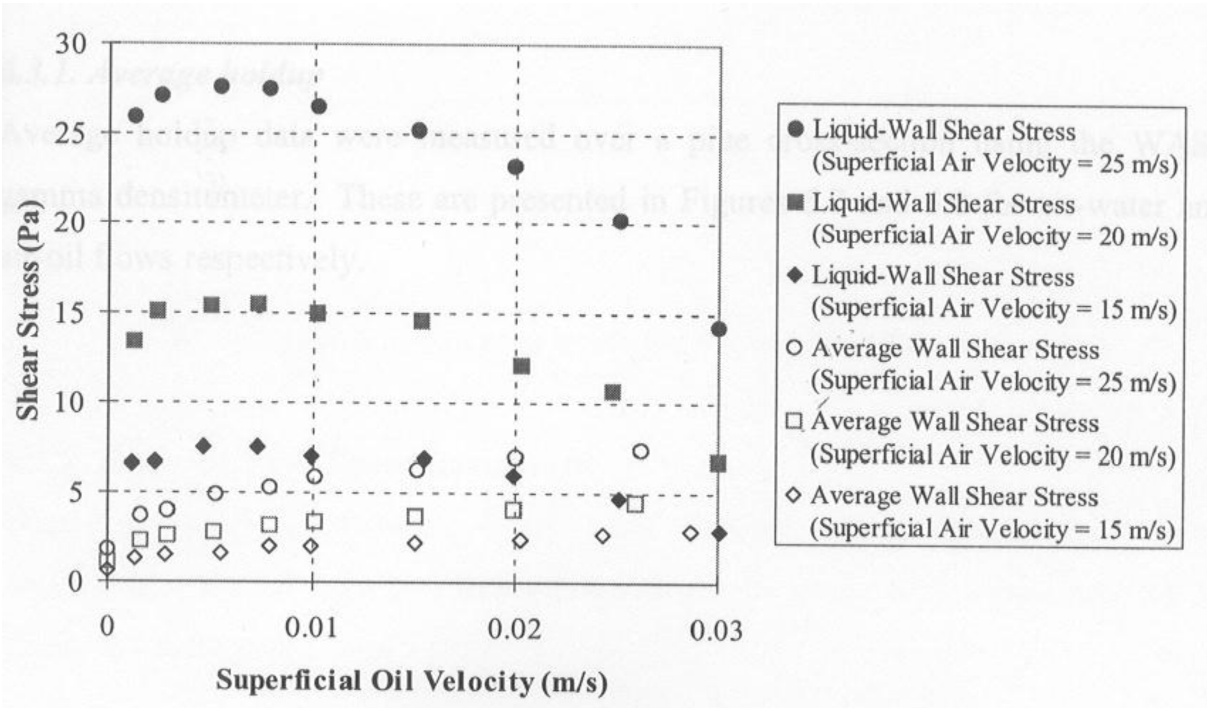

Figure 2.11. Comparison of liquid wall shear stress at the bottom of the pipe with the average wall shear stress in stratifying annular air-oil flow (Badie, 2000).

Schubring and Shedd (2009) predicted the wall shear for horizontal annular air-water flow in 8.8, 15.1, and 26.3 mm diameter tubes. In this study, non-intrusive pressure drop, liquid base film thickness distribution, and wave behaviour measurements were also obtained. The correlation used to predict wall shear was a friction factor involving flow quality and gas Reynolds number (see Paragraph 2.5.1) and it was found to perform better than the correlated shear stress found in the literature such as film roughness correlations or two-phase multiplier methods, and pure data fits. The most accurate correlation in the literature were found to be the Müller-Steinhagen and Heck correlation. A modified version of the Lockhart-Martinelli correlation provided reasonable results. It is important to note that the gas friction velocity is found to be similar to the disturbance wave velocity suggesting that waves are important sources of shear.

Sidi-Ali and Gatignol (2010) studied a simplified version of the shear stresses at the wall and gas–liquid interface in stratified two-phase gas–liquid flow in three-dimensional (3D) considering only the gas–liquid interface. The gas-liquid interface was seen as a wall moving at a fixed liquid velocity on which the gas was flowing. The velocity profiles of the gas were determined by transposition of the geometry of a gas-liquid stratified flow using the CFD code Fluent. The simulation of experiments done by Strand (1993) for a horizontal stratified gas-liquid flow was carried out. The simulation results were in agreement with experimental results, and also to the numerical results of Meknassi et al. (2000). The correlations used to calculate gas-wall friction factor and the gas-liquid interface friction factor in order to evaluate the shear stresses were derived from this approach. These correlations were found to agree with the experimental values better that the value by Taitel and Duckler (1976a, b).

A recent work by Schubring et al (2011) presents a model for film thicknesses, pressure gradient, film flow rates and wave velocities in gas-liquid annular flow. This model requires flow rates, absolute pressure, temperature, and pipeline diameter as input.
Film thicknesses, which correspond in this work to the base film and the wave height, are predicted from a modified critical friction factor model. Three sources of interfacial shear are used to estimate pressure gradient which are base film roughness, enhanced wave roughness, and a term linked to the wave intermittency (sudden transitions between base film and waves). The universal velocity profile in the waves and a linear profile in the base film are used to calculate film flow rate and wave velocity. Comparisons of the predicted

pressure gradient, film thickness and wave velocity with literature data agrees within 17%, 10% and 14%.

2.2.3. Liquid Hold-up

As in the case of pressure gradient, there exists in the literature a wide variety of relationships for liquid hold-up in horizontal pipes. A relationship which is particularly relevant to the annular flow case is that of Hart et al (1989) as given in Equation 2.13 above. Badie (2000) reports measurements of average hold-up and distribution of chordal mean hold-up for air-water and air-oil flows in a 78 mm diameter pipe. These data were compared with a drop transport model (see Section 2.5.2 below) which predicted the hold-up values reasonably accurately.

2.2.4. Entrained Fraction

The fraction E of the liquid phase which is entrained as droplets in annular flows is an important parameter and substantial efforts have been made to measure and correlate it. Measurements of entrained fraction are reported by Dallman et al (1984), Williams et al (1996) and Meng et al (1999). Dallman et al (1984) and Meng et al (1999) measured the entrained fraction by extracting the liquid film through porous wall sections and determining the entrained fraction by the difference between the input liquid flow rate and the extract rate. Williams et al (1996) determined entrained fraction by integrating the droplet mass flux measured by sampling probes (see Section 2.3.3 below) which were traversed across the gas core.

Dallman et al (1984) give the following empirical equation for entrained fraction:

$$\frac{E}{\left(1-W_{LFC}/W_L\right)} = \frac{d_t \rho_G^{1/2} \rho_L^{1/2} U_{SG}^3 \left(k_A/4k_D\right)}{1+d_t \rho_G^{1/2} \rho_L^{1/2} U_{SG}^3 \left(k_A/4k_D\right)} \qquad (2.29)$$

where W_{LFC} is the critical liquid flow rate (kg/s) for the onset of entrainment and W_L is the total liquid flow rate. k_A and k_D are constants in the following equations for droplet deposition rate R_D and atomisation rate R_A:

$$R_D = k_D C_D = \frac{k_D \rho_G W_{LE}}{W_G} \qquad (2.30)$$

$$R_A = k_A \left(W_{LF} - W_{LFC}\right) U_{SG}^2 \, \rho_G^{1/2} \, \rho_L^{1/2} \qquad (2.31)$$

where W_{LE} and W_{LF} are the mass rates of flow of liquid as droplets and film respectively, W_G is the mass rate of flow of the gas phase and C_D is equal to the concentration of the droplets (kg/m^3) calculated on a homogeneous flow basis. Equation 2.29 can be used to correlate both vertical and horizontal entrained fraction data; for the vertical case, $(k_A / 4k_D) = 4.9 \times 10^{-6} s^3 / kgm$ and for the horizontal case, $(k_A / 4k_D) = 3 \times 10^{-6} s^3 / kgm$, the lower value reflecting the fact that the entrained fraction is lower in horizontal flows due to the influence of gravity.

Williams et al (1996) and Pan & Hanratty (2002) present and correlate data in terms of $\left(E / E_M\right) / \left(1 - E / E_M\right)$ where E_M is defined as:

$$E_M = 1 - \left(\frac{W_{LFC}}{W_L}\right) \qquad (2.32)$$

Figure 2.12 shows the results of Williams et al (1996) for $\left(E / E_M\right) / \left(1 - E / E_M\right)$ as a function of superficial gas velocity. The data for a range of pipe diameters are reasonably well correlated.

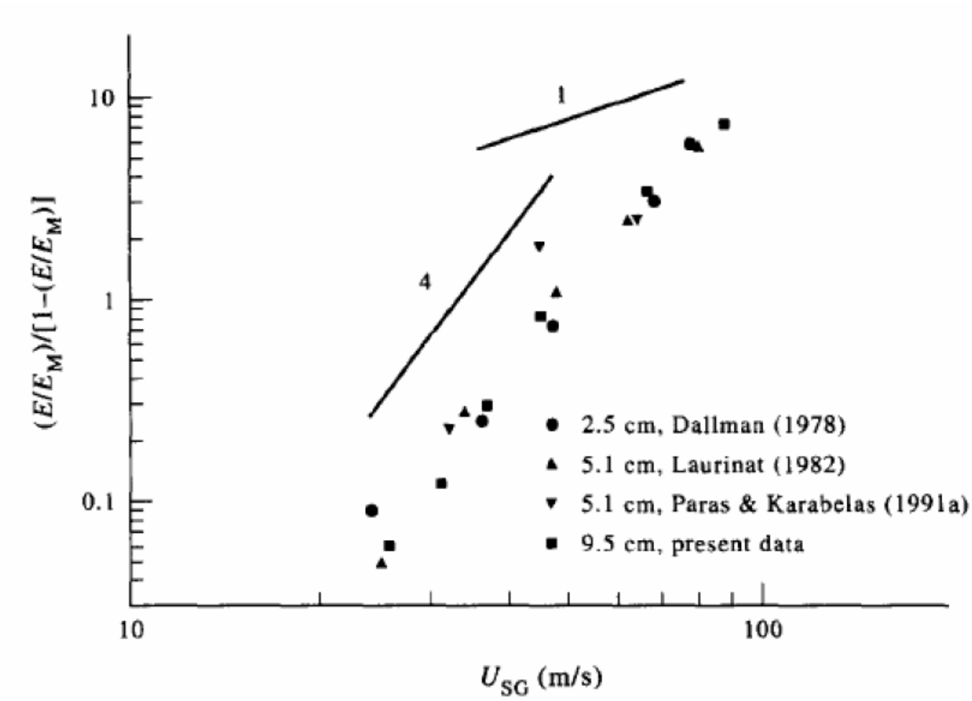

Figure 2.12. Effect of gas velocity on entrainment in horizontal pipes (Williams et al, 1996).

Williams et al compared the results for horizontal pipes with those for vertical pipes by plotting the latter in the same parameters as shown in Figure 2.13.

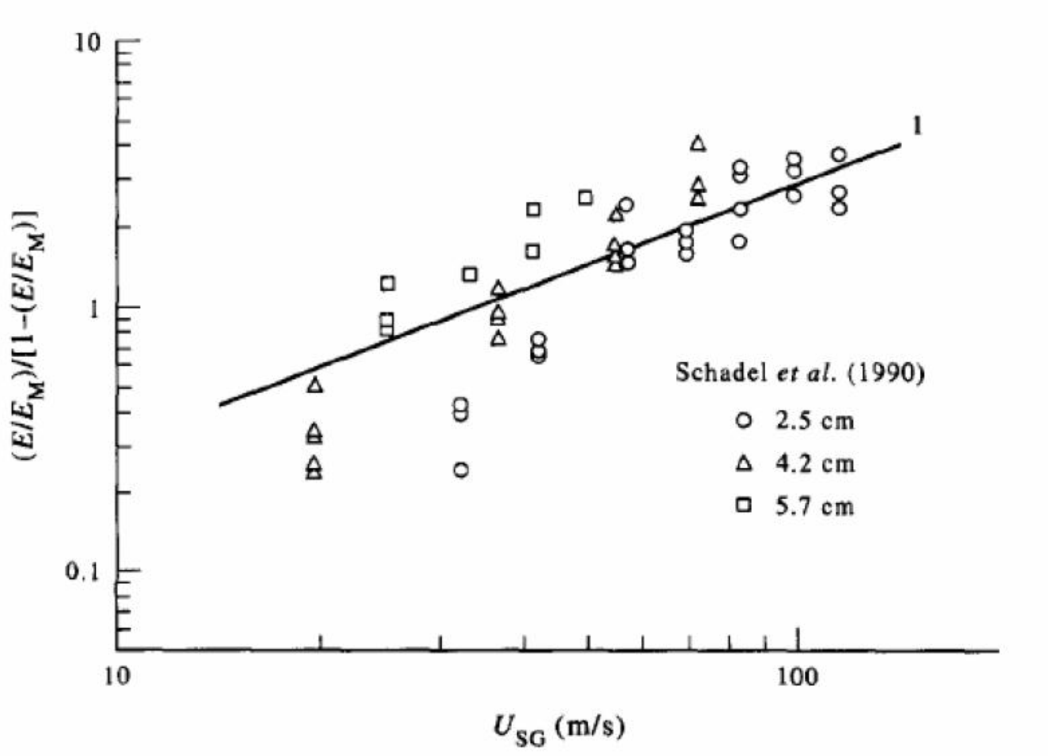

Figure 2.13. The effect of gas velocity in entrainment in vertical pipes (Williams et al, 1996).

As will be seen, entrained fraction in horizontal pipes is lower at low gas velocities (as noted above) but may be higher at high gas velocities.

Pan & Hanratty (2002) explore a number of empirically-based correlations and also a more analytical model for entrained fraction in horizontal pipes. For instance, they suggest the following equation for lower gas velocities (where deposition is dominated by gravity):

$$\frac{E/E_M}{1-(E/E_M)} = 9\times10^8\left(\frac{d_t U_G^3 \rho_G^{1/2} \rho_L^{1/2}}{\sigma u_T}\right) \tag{2.33}$$

where σ is the surface tension and u_T is the terminal settling velocity of the droplets.

2.2.5. Drop Size

A knowledge of the size of the entrained droplets is important in modelling liquid transport in horizontal annular flows but, until recently, there has been a dearth of measurements in such flows and analytical studies (Paras & Karabelas, 1991b, Binder & Hanratty, 1992) used data for drop size obtained for vertical flows, and specifically the correlation of Azzopardi (1988) which as follows:

$$\frac{d_{32}}{\lambda} = \frac{15.4}{We^{0.58}} + \frac{3.5 G_{LE}}{\rho_L U_G} \tag{2.34}$$

where d_{32} is the Sauter mean diameter, G_{LE} the average entrained liquid mass flux and λ the Taylor wave length defined as:

$$\lambda = \sqrt{\frac{\sigma}{\rho_L g}} \tag{2.35}$$

The Weber number in Equation 2.19 is defined as:

$$We = \frac{\rho_L U_G^2 \lambda}{\sigma} \tag{2.36}$$

New data measured for horizontal annular flows are now available; Simmons & Hanratty (2001) and Al-Sarkhi & Hanratty (2002) used a Malvern Spraytec RTS 5008 analyser (based on laser defraction) and Hurlburt & Hanratty (2002) used an immersion method. Ribeiro et al (2001) also used the defraction method to study the effect of a bend on drop size in horizontal annular flow (they found that a 90º horizontal bend increased the diameter of the drops, possibly due to drop coalescence and secondary flows).

The method used by Simmons & Hanratty (2001) and by Al-Sarkhi & Hanratty (2002) is illustrated in Figure 2.14. The liquid film is removed using a porous wall section and the droplet-laden gas core passes on through the laser beam, the diffracted light being collected on a multiple-annular ring detector.

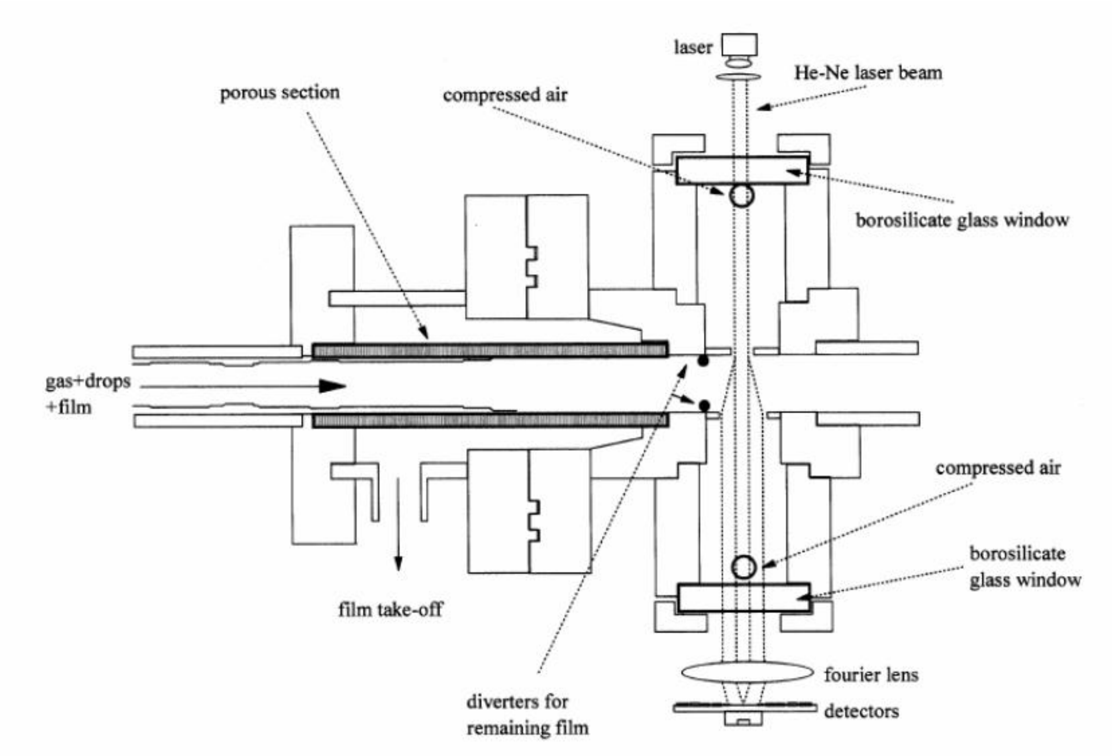

Figure 2.14. Experimental arrangement for measurement of drop size in horizontal annular flow (Simmons & Hanratty, 2001).

In the measurements of Simmons & Hanratty (2001), air-water horizontal annular flows were studied in a 95.3 mm pipe, with measurements being made with the laser beam in the horizontal orientation passing through the centre line and through chords 19 mm above and 19 mm below the centre line. Figure 2.15 shows typical results for Sauter mean diameter for a fixed gas velocity and varying liquid velocity.

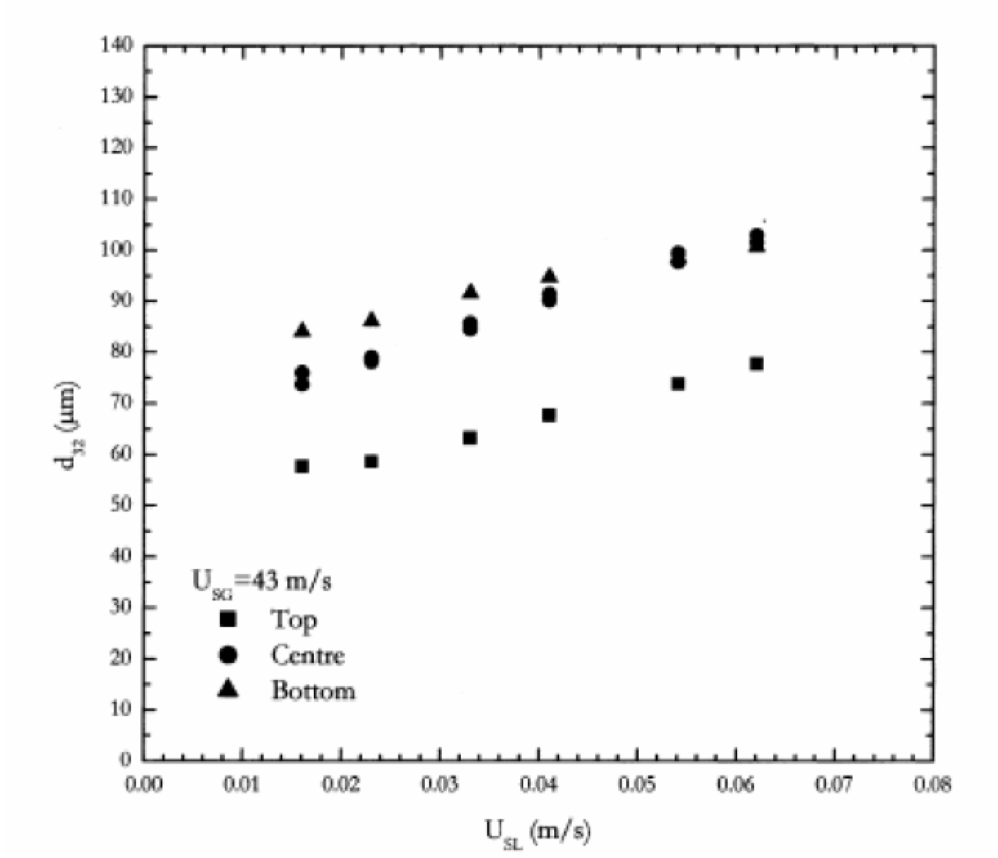

Figure 2.15. Measurements of Sauter mean diameter across the centre line and at positions 19 mm above ("top") and 19 mm below ("bottom") below the centre line in a 95.3 mm tube (Simmons and Hanratty, 2001).

As will be seen from Figure 2.15, the Sauter mean diameter at the centre line and in the lower part of the tube is much greater than the value in the upper part of the tube, reflecting the separation by gravity of the larger droplets. Typical drop size distribution data obtained by Simmons & Hanratty (2001) is shown in Figure 2.16.

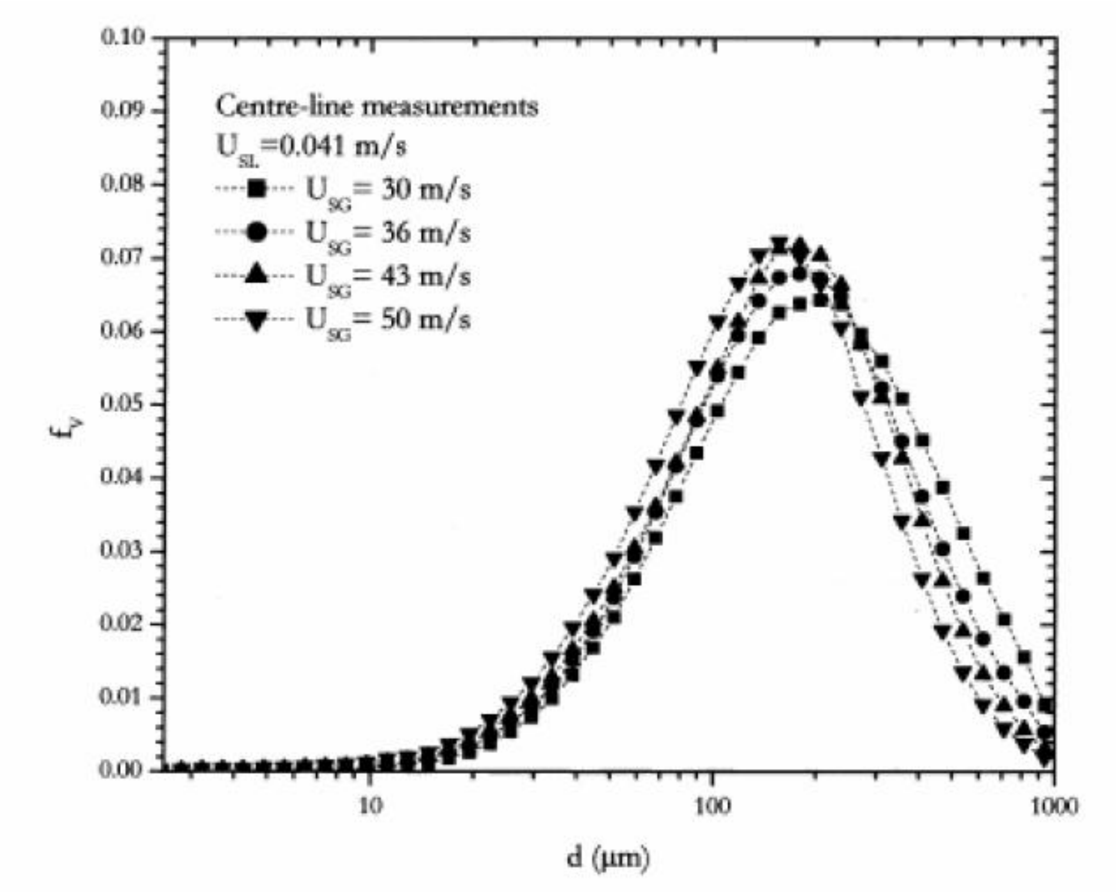

Figure 2.16. Drop size distribution data obtained by Simmons & Hanratty (2001).

In Figure 2.15, f_v is the normalised volume distribution function defined as:

$$f_v = \frac{d\nu}{dd_p} \tag{2.37}$$

and it follows that:

$$\int_o^\infty f_v(d_p)dd_p = 1 \tag{2.38}$$

where d_p is the droplet diameter. The Sauter mean diameter is related to f_v by the expression:

$$d_{32} = \frac{\int_o^{d_{max}} f_v(d_p)ddp}{\int_o^{d_{max}} d_p^{-1} f_v(d_p)ddp} \tag{2.39}$$

Simmons & Hanratty (2001) correlate their data for mean drop size by two alternative non-dimensional equations:

$$\left(\frac{d_{32} U_G^2 \rho_G}{\sigma}\right)^{0.55} \left(\frac{d_{32}}{\lambda}\right)^{0.45} = 332.9 \frac{G_{LE}}{\rho_L U_G} + 0.261 \quad (2.40)$$

$$\left(\frac{d_{32} U_G^2 \rho_G}{\sigma}\right)^{0.55} \left(\frac{d_{32}}{d_t}\right)^{0.45} = 66.5 \frac{G_{LE}}{\rho_L U_G} + 0.052 \quad (2.41)$$

These equations use either the Taylor wave length (Equation 2.35) or the tube diameter (d_t) as a scaling parameter. Since the experiments were carried out at a constant diameter, it was not possible to determine which is the correct scaling length.

The experiments of Al-Sarkhi & Hanratty (2002) were carried out for a 25.4 mm horizontal pipe, the main aim being to investigate the effect of tube diameter. Results for volume medium diameter (d_{50}) are compared with the Simmons & Hanratty (2001) data for the 95.3 mm diameter tube in Figure 2.17.

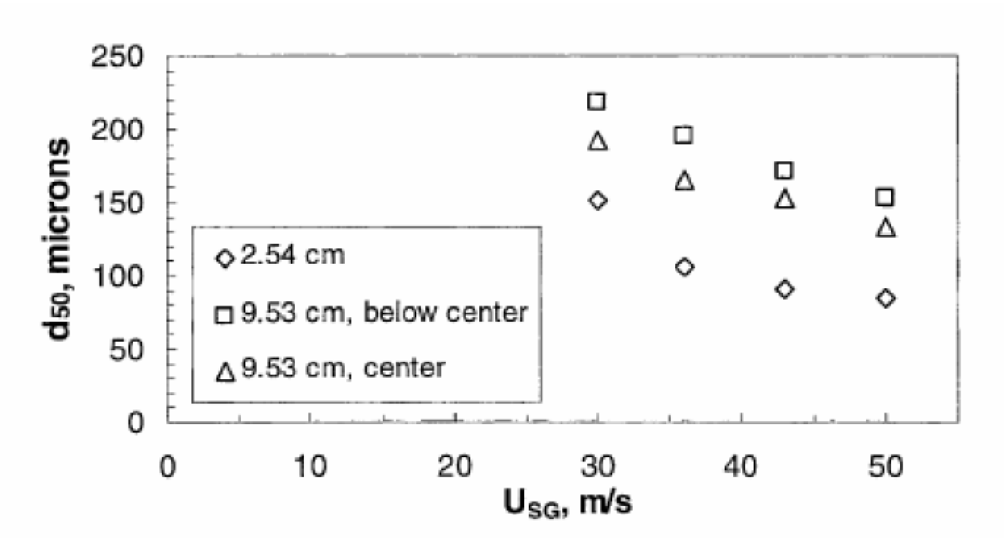

Figure 2.17. Effect of gas velocity on volume medium drop diameter (Al-Sarkhi & Hanratty, 2002).

As will be seen, the centre line values for d_{50} are significantly lower than the centre line values for the 95.3 mm tube, but are rather similar to the results obtained at a position 19 mm below the centre line for the latter tube. This leads to the conclusion that there is a significant effect of tube diameter and Al-Sarkhi & Hanratty (2002) suggest the following equation (which includes their data) as an alternative to Equation 2.41:

$$\left(\frac{d_{32}U_G^2\,\rho_G}{\sigma}\right)^{0.55}\left(\frac{d_{32}}{d_t}\right)^{0.45} = 29.5\,\frac{G_{LE}}{\rho_L U_G} + 0.072 \tag{2.42}$$

Equation 2.27 is somewhat difficult to use because data on entrained mass flux are needed and Al-Sarkhi & Hanratty suggest the following simplified equation which gives a reasonable fit to the data:

$$\left(\frac{d_{32}U_G^2\,\rho_G}{\sigma}\right)^{0.55}\left(\frac{d_{32}}{d_t}\right)^{0.45} = 0.154 \tag{2.43}$$

The distribution of drop sizes is also an important piece of information in modelling horizontal annular flows. Simmons & Hanratty (2001) investigated a number of fits to their drop size distribution data as shown in Figure 2.18. They concluded that the upper-limit-log-normal (ULLN) distribution was the most appropriate. This is given as:

$$f_v\left(d_p\right) = \frac{\delta\, d_{\max}}{\sqrt{\pi}\, d_p\left(d_{\max} - d_p\right)}\,\exp\left(-\delta^2 z^2\right) \tag{2.44}$$

where z is given by:

$$z = \ln\left[\frac{a\,dp}{d_{\max} - d_p}\right] \tag{2.45}$$

where $d_{\max}$ is the maximum drop diameter and a is given by:

$$a = \frac{d_{\max} - d_{v50}}{d_{v50}} \tag{2.46}$$

where d_{v50} is the volume medium diameter. Thus, to characterise a drop size distribution using Equation 2.44, parameter $d_{\max}, d_{v50}$ and δ are required. In the experiments of Simmons and Hanratty, these parameters had the following ranges:

d_{v50} : $106-222\,\mu m$

d_{max} : $1350-1700\,\mu m$

δ : $0.67-0.85$

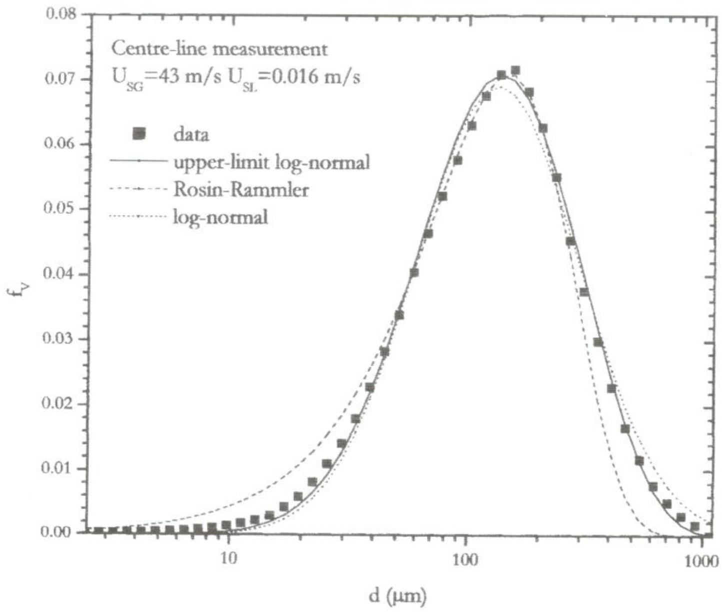

Figure 2.18. Comparison of data for drop size distribution data in horizontal annular flow with various fitting equations (Simmons & Hanratty, 2001).

An alternative method for measuring drop size was used by Hurlburt & Hanratty (2002) as illustrated in Figure 2.19. A sample of the droplets is obtained by operating a shutter and the droplets impinge on bins filled with high viscosity oil. After sampling, the bins are removed from the apparatus and the droplets are photographed.

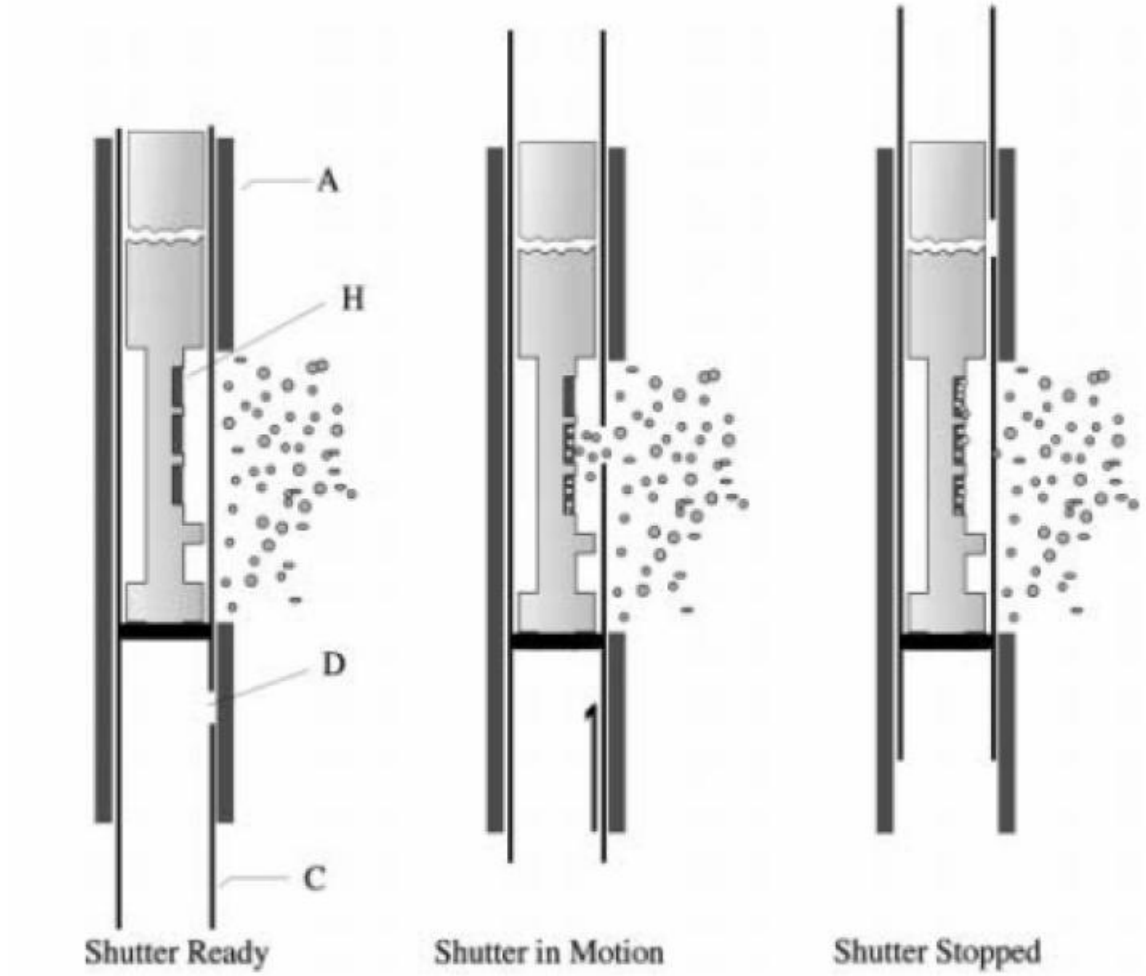

Figure 2.19. Oil immersion method for measuring drop size (Hurlburt & Hanratty, 2002).

Figure 2.20 shows a comparison of drop size distribution obtained by this method with results obtained by the diffraction method by Simmons & Hanratty (2001). The immersion method shows significantly less droplets at the larger size though the Sauter mean diameters were in better agreement. A possible explanation for the discrepancy shown in Figure 2.20 may be that the larger droplets may not enter the collection bins since they have a significant radial velocity (see Section 2.4.2 below).

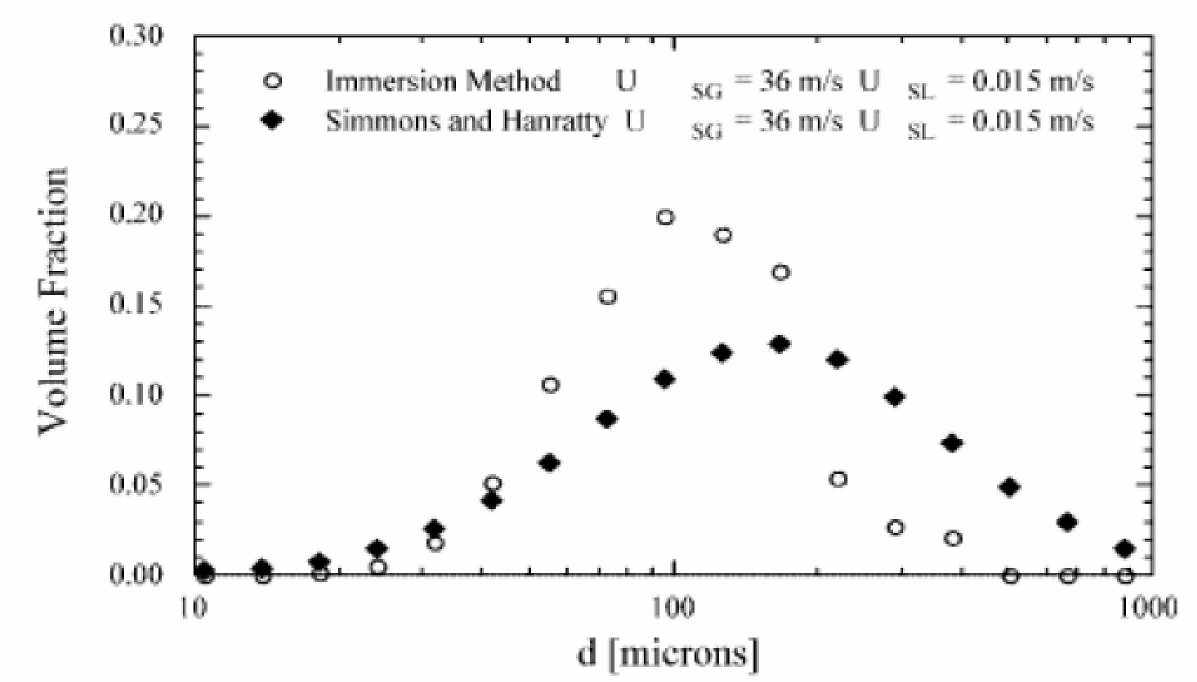

Figure 2.20. Comparison of results obtained with the immersion method of Hurlburt & Hanratty (2002) with those obtained with the diffraction method by Simmons & Hanratty (2001).

2.3. Spatial distribution of parameters in horizontal annular flows

In Section 2.2, we were concerned primarily with values of parameters averaged over the flow field. In this Section, we discuss distributions of parameters around the tube periphery (film thickness and local fluid flow rate) and within the gas core (droplet mass flux).

2.3.1. Film Thickness Distribution.

There have been a surprisingly large number of experiments in which film thickness distribution was measured or estimated in horizontal annular flow. It is convenient to summarise these measurements in terms of the experimental technique used as follows:

(1) *Needle contact method.* In this technique, a needle is moved in a direction normal to the film surface and the time it spends in contact with the film is noted. The device gives a distribution of film thickness between the maximum value (wave tips) to the minimum value (wave troughs) and the mean film thickness is normally defined as that which corresponds to the needle being in contact for 50% of time with the film. Detailed investigations of this technique for vertical flows are described by Hewitt et al (1962) and

its application to horizontal annular flows is reported by Butterworth (1969), Sekoguchi et al (1982), Fukano et al (1983) and Lin et al (1985).

(2) *Flush-mounted conductance probes*. Here, two probes are mounted flush with the tube surface and the conductance between them is a measure of the film thickness. This technique has been used for horizontal annular flows by Laurinat et al (1984), Jayanti et al (1989), Zimmerman et al (2006) and Pearce & Fisher (1976).

(3) *Parallel wire conductance method*. Here, two adjacent wires are mounted normal to the surface and the conductance between them measured to give an indication of the film thickness. This technique has been used by Laurinat et al (1984), Paras & Karabelas (1991a), Williams et al (1996) and Paz & Shoham (1999) for measurements in horizontal annular flows.

To exemplify the type of results obtained, two examples are presented as shown in Figures 2.21 and 2.22, taken from the work of Butterworth (1969) and Lin et al (1985) respectively.

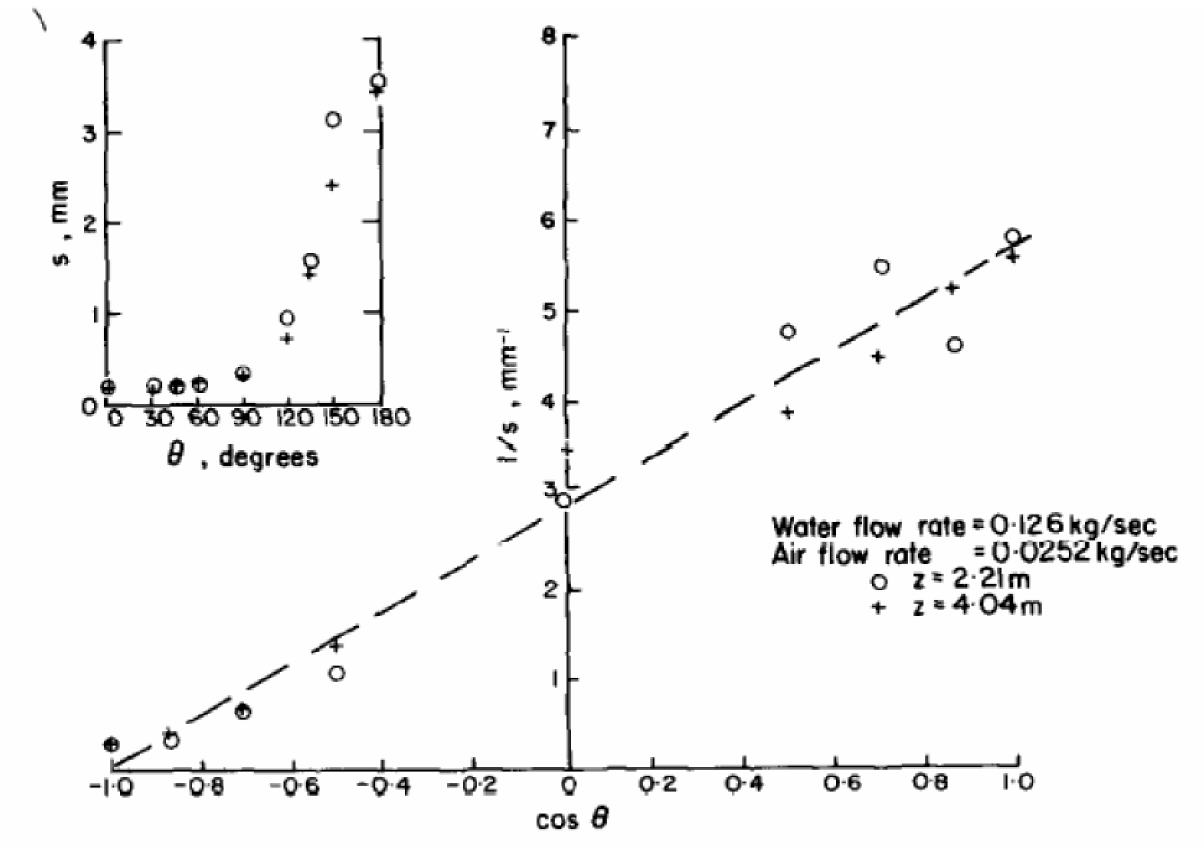

Figure 2.21. Circumferential variation of time averaged film thickness (Butterworth, 1969).

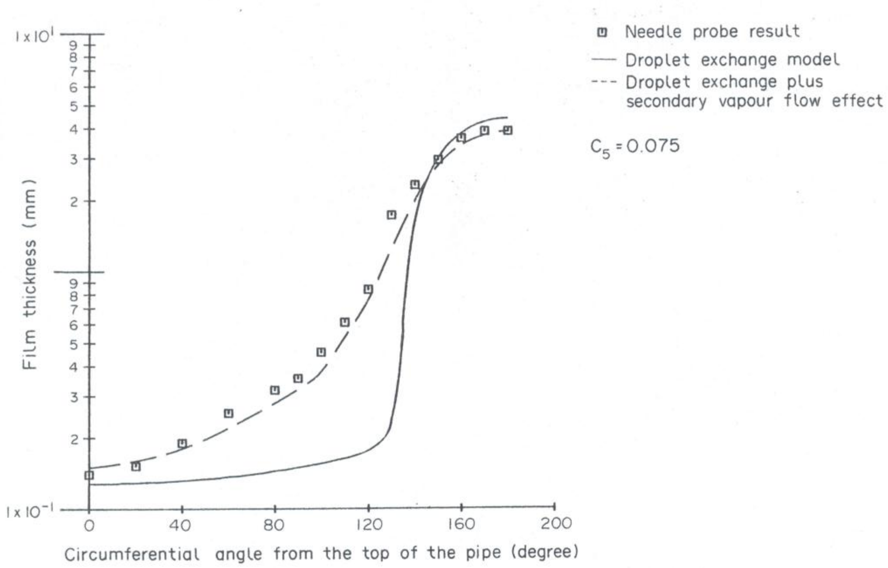

Figure 2.22. Time averaged circumferential distribution of mean film thickness (Lin et al, 1985).

As will be seen from the data presented in Figure 2.21 and 2.22, the film thickness may vary by an order of magnitude or more from the bottom to the top of the pipe. This reflects the effect of gravity. Also shown in these Figures are predictions from models; we shall return to discuss these in more detail in Section 2.2.5.

It is also interesting to mention the work by Schubring and Shedd (2009). They used a critical friction factor to model horizontal annular base film thickness. Measurements of liquid base film thickness distribution were obtained for several horizontal annular two-phase air-water flow conditions in 8.8 mm, 15.1 mm, and 26.3 mm diameter tubes. It was found that the base film thickness measurements did not agree with the data from the literature for average film thickness which includes both waves and base film. The circumferentially averaged base film thickness was modelled using an iterative critical friction factor model and an empirical correlation was also used. Asymmetry was correlated by a modified Froude number based on the correlated base film thickness and the gas mass flux. Asymmetry was well predicted by the modified Froude number. It was also possible to determine the critical film flow rate via the use of this iterative model, the results obtained being in agreement with those using entrainment measurements. It was concluded that base film thickness was inversely related to gas flow and increased with increasing liquid flow, but at high gas flow rates, the dependency on liquid flow became small. Finally, film thickness and asymmetry both increased with increasing diameter, though the dependencies were not clearly linear.

2.3.2. Film Flow rate Distribution

It is clearly more difficult to measure the local axial film flow rate in annular flow than it is to measure local film thickness and this is reflected in the relatively small number of studies which have been reported in the literature. Butterworth & Pulling (1973) used the method illustrated in Figure 2.23 to measure local film flow rate as a function of circumferential position. A porous window in the tube wall was used to extract a segment of liquid film, with ingress of adjacent film being prevented by using fins as shown. Figure 2.24 shows results obtained with this method; as will be expected, the liquid film flow rate varies from a high value at the bottom of the tube to a lower value at the top of the tube, consistent with the results for film thickness distribution.

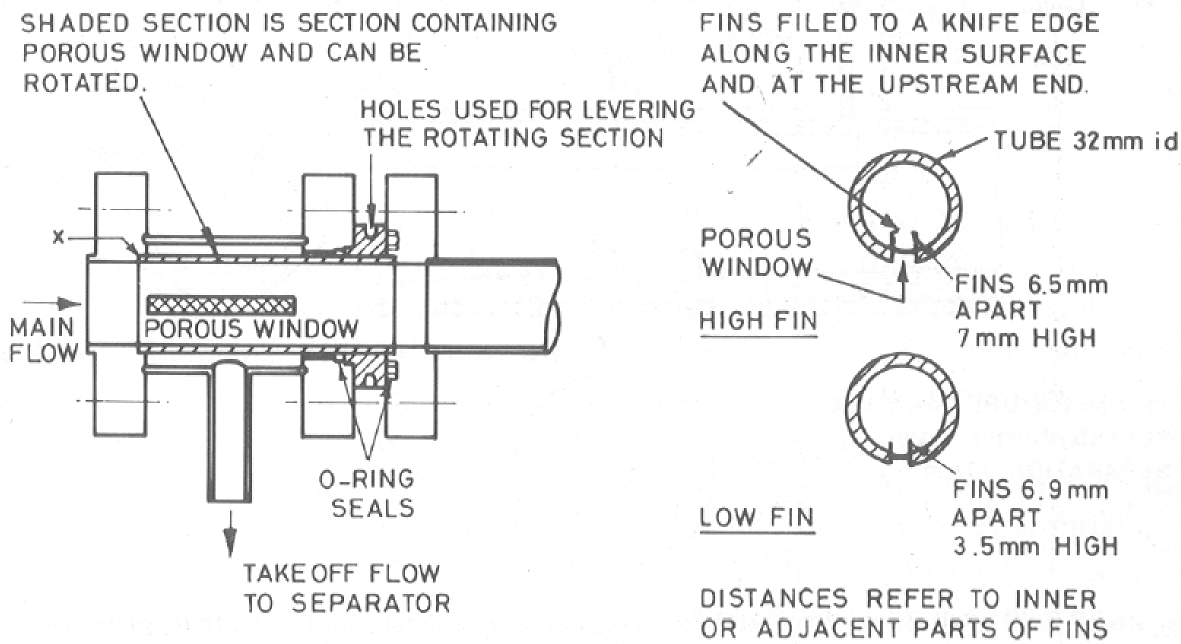

Figure 2.23. Film extraction method for measuring local film flow rate (Butterworth and Pulling, 1973).

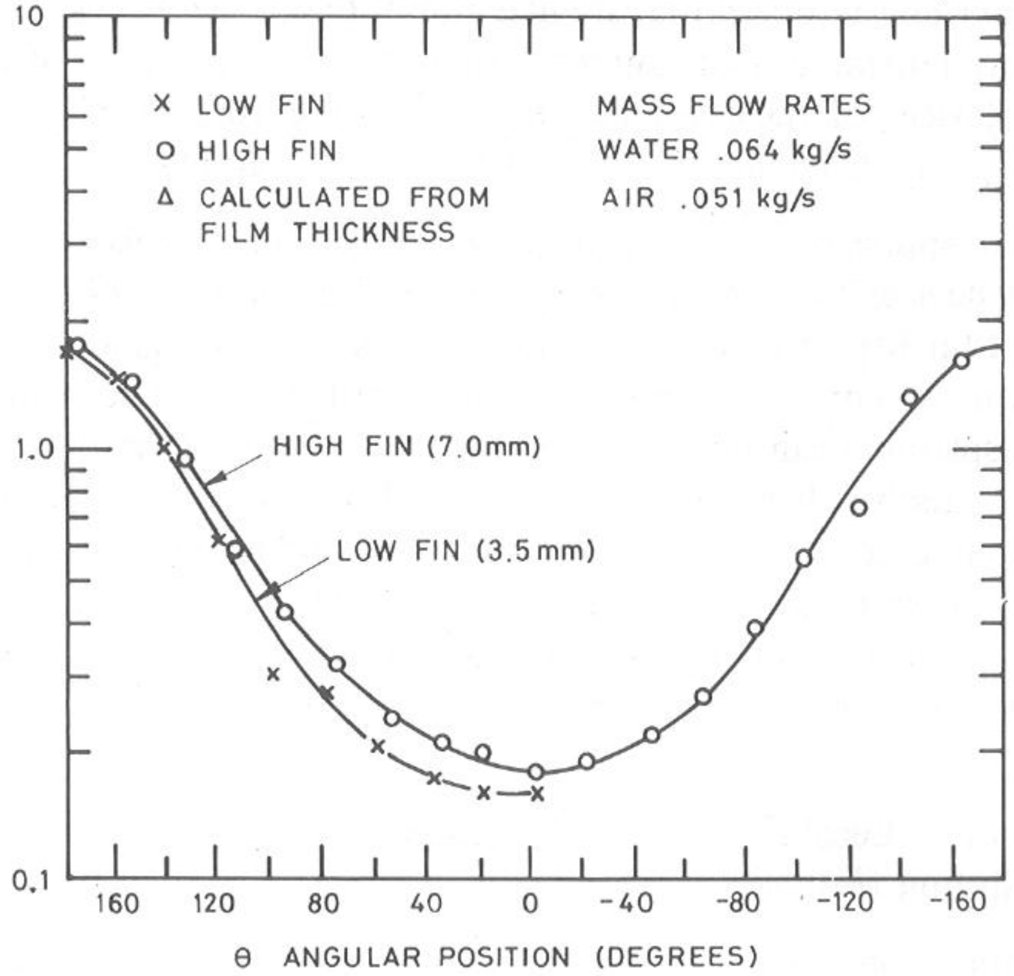

Figure 2.24. Results obtained using the film extraction method for horizontal air-water annular flow in a 32 mm tube (Butterworth & Pulling, 1973).

An alternative method of measuring film flow rate was used by Pearce & Fisher (1976) as illustrated in Figure 2.25. Potassium chloride solution is pumped at a constant rate into the sector of liquid film, with which it mixes. The mixed concentration is measured with a miniature conductivity probe that is small enough so that its response depends only on the solution conductivity. The flow rate in the film sector can be determined from the mass balance, since the flow rate and Potassium Chloride concentration of the injected stream are known.

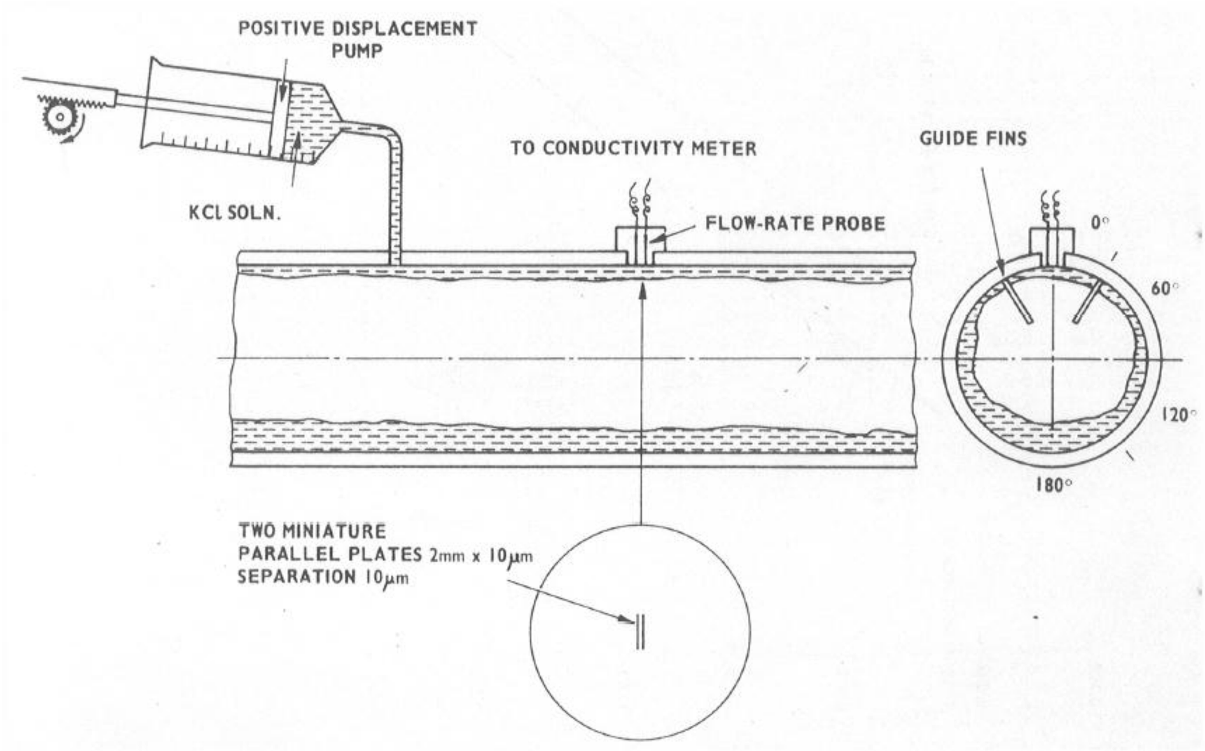

Figure 2.25. Salt dilution method for measurement of local film flow rate (Pearce & Fisher, 1976).

The results obtained by Pearce and Fisher are exemplified by those shown in Figures 2.26 and 2.27. Figure 2.27 shows the measured film flow rate at the top of the 32 mm tube as a function of liquid and gas flow rates. As will be seen, the (critically important) flow rate at the top of the tube increases with increasing gas velocity and with increasing liquid velocity. Figure 2.27 shows flow rate distribution data. As will be expected, the flow rate (as in the results shown in Figure 2.24) changes markedly from the bottom to the top of the tube. The results obtained by Pierce and Fisher showed that the flow rate at the bottom of the tube decreased with increasing gas flow rate in contrast to the results for the top of the tube as shown in Figure 2.26.

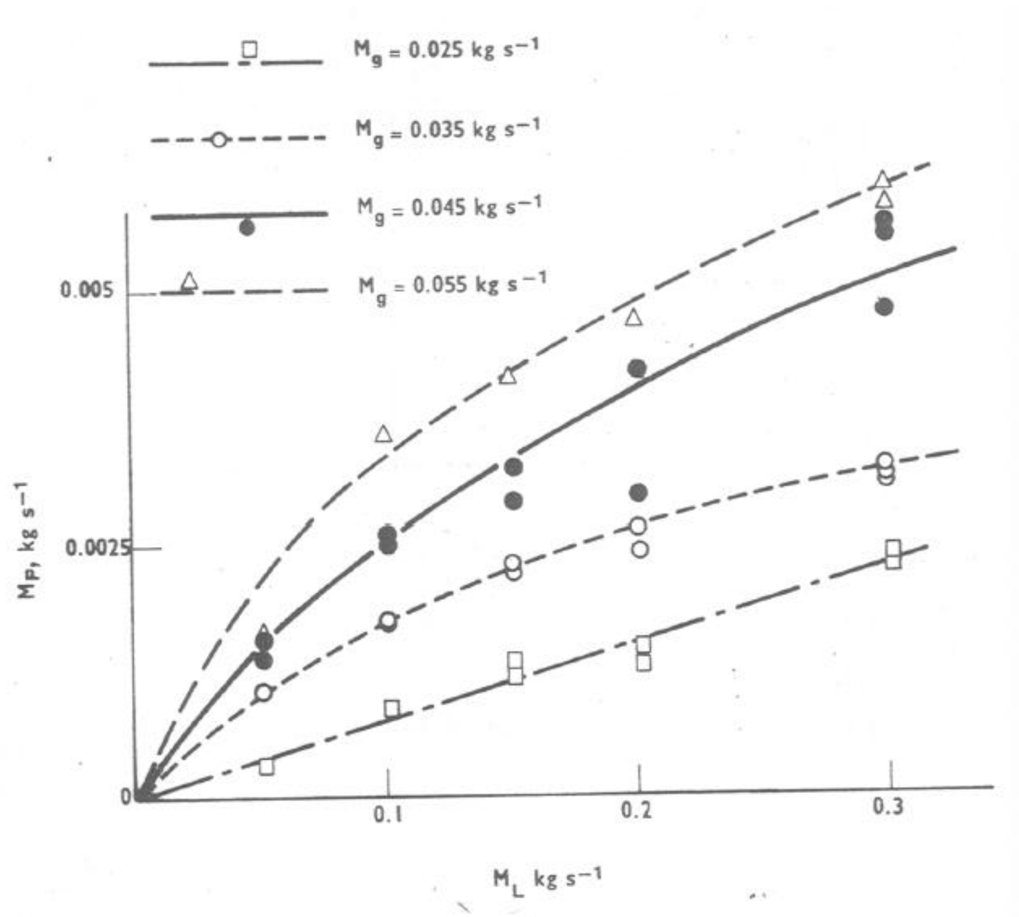

Figure 2.26. Film flow rates measured at the top of a 32 mm diameter tube with air-water annular flow (Pearce & Fisher, 1976).

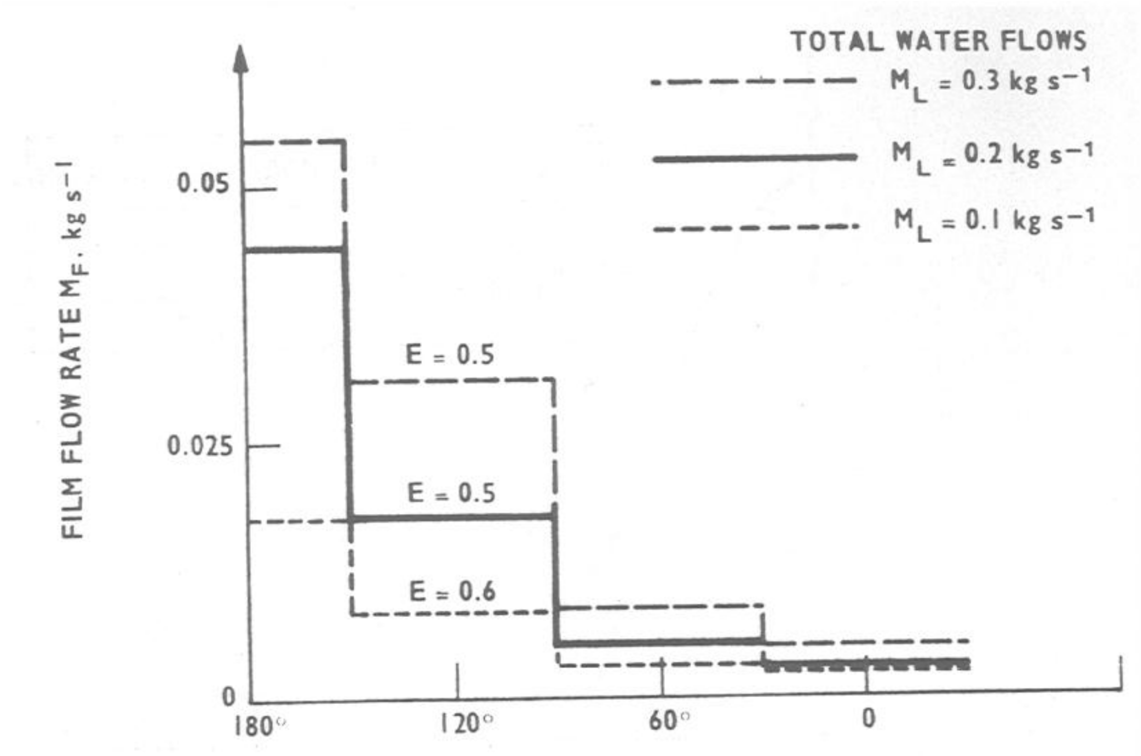

Figure 2.27. Distribution of film flow rate in air-water horizontal annular flow in a 32 mm tube (Pearce & Fisher, 1976).

Lin et al (1983) studied liquid flow rates in horizontal annular flow using a pulsed proton activation technique. Here, a linear accelerator source was used to activate the liquid phase in air-water flow in a 27 mm diameter pipe. A detector placed 1.2 m downstream of the target gave peaks of radiation characteristic of the velocity of the liquid. The results showed two peaks, one corresponding to the lower and one corresponding to the upper film; Lin et al concluded that there was little mixing between the lower and upper films in these flows.

2.3.3. Droplet Mass Flux Distribution

The transport of droplets may be an important factor in maintaining the upper film in horizontal annular flows. Thus, measurements of the distribution of droplet mass flux across the pipe are of potentially great significance. The droplet mass flux can be measured by using an upstream facing tubular probe which collects the droplets. This collection can be done *isokinetically* by adjusting the flow through the probe to give zero impact pressure, or can be done non-isokinetically where the air flow rate through the probe is not necessarily equal to the local flow rate in the absence of the probe. The success of the nonisokinetic (droplet sampling) method depends on the fact that the droplet mass flux collected is relatively insensitive to the air flow through the probe over quite a wide range.

Data for droplet mass flux were obtained for a 50.8 mm diameter tube by Paras & Karabelas (1991b) and their data is illustrated in Figure 2.28. As would be expected, the droplet mass flux decreases from the bottom of the tube. However, at any given vertical position, Paras & Karabelas found that the droplet mass flux was relatively constant across the tube (as also indicated in Figure 2.28).

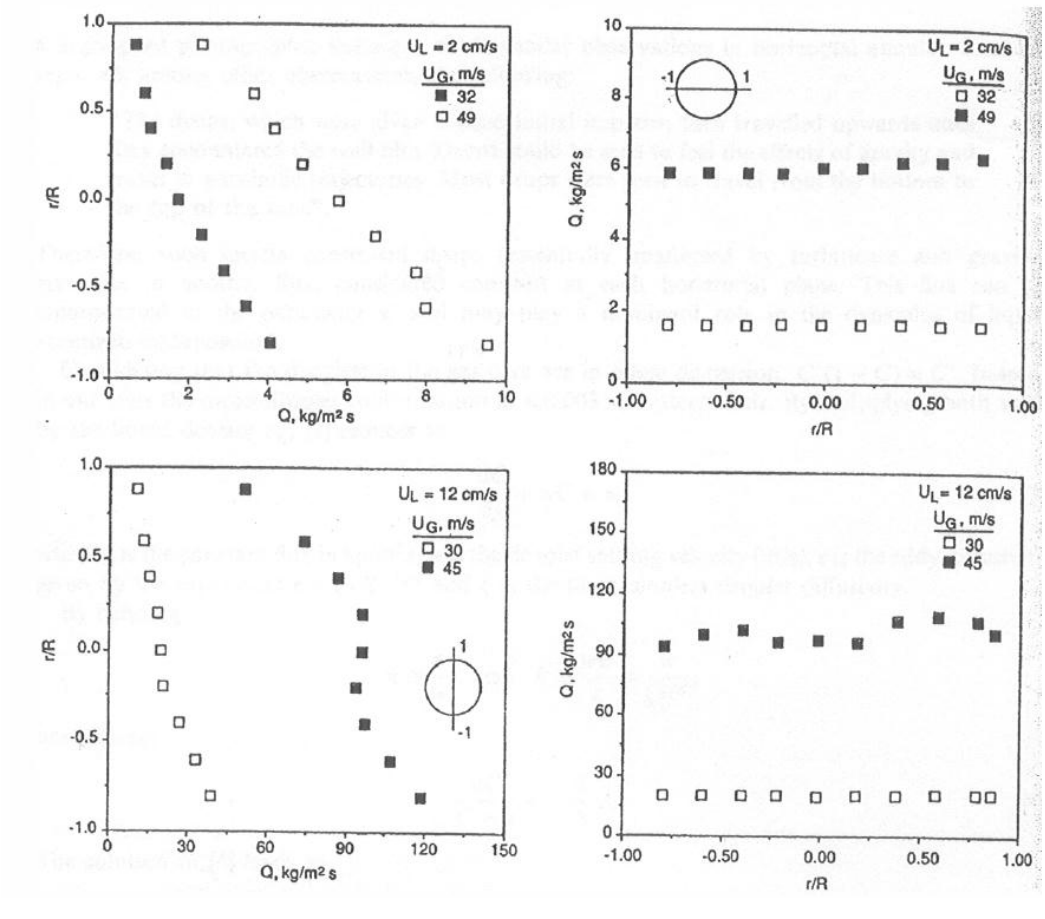

Figure 2.28. Droplet mass flux distributions in a 50.8 mm diameter tube with air-water horizontal annular flow (Paras & Karabelas, 1991b).

More detailed data was obtained by Williams et al (1996) as illustrated in Figure 2.29. Again, the variations in the vertical direction are much greater than those in the horizontal direction, though the mass fluxes are by no means as constant in the horizontal direction as those observed by Paras & Karabelas.

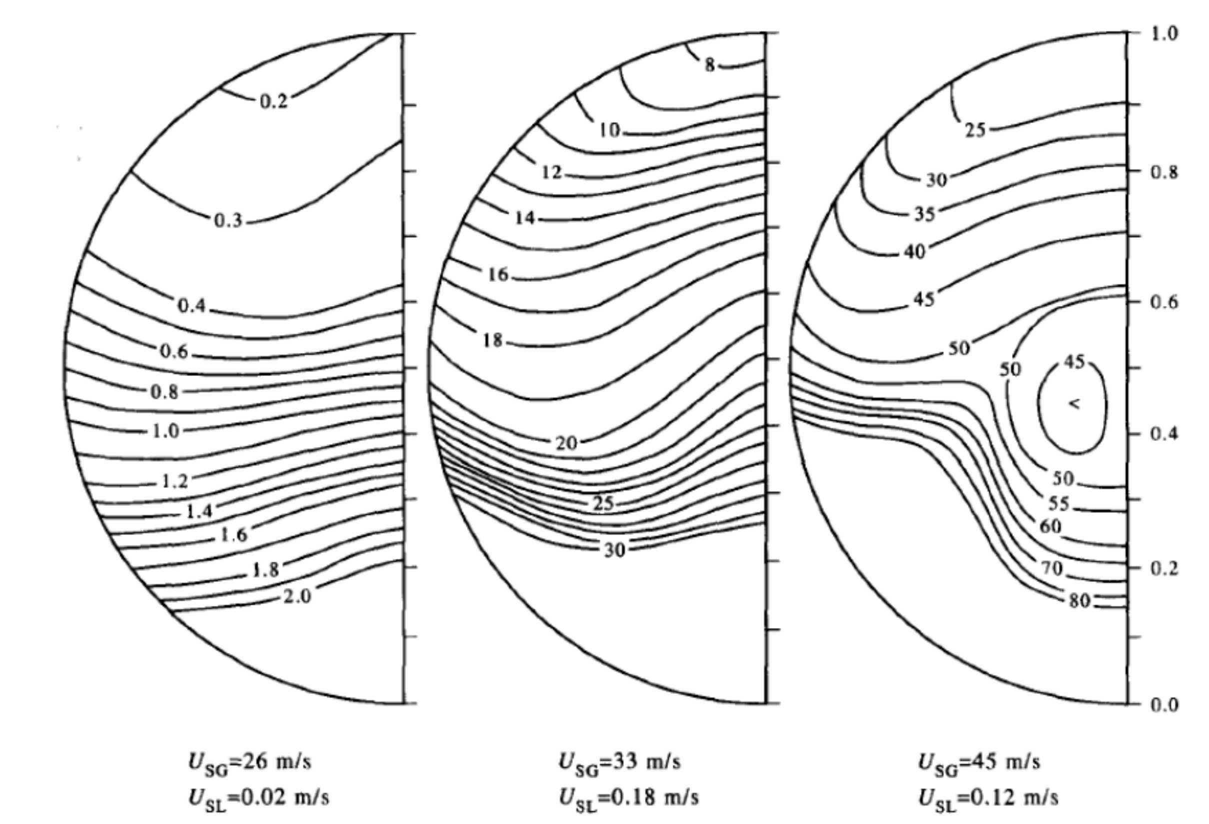

Figure 2.29. Contours of drop flux at various gas and liquid velocities (kg/m^{2}s) (Williams et al, 1996).

Most of the data available is for air-water flows. A limited set of experiments are described by Badie (2000) in which both air-water and air-oil flows were studied. The oil was a lubricating oil with a viscosity of 4.8×10^{-2} Pa.s at 20ºC. Results from these experiments are shown in Figures 2.30 and 2.31. Figure 2.32 shows the distribution of droplet flow (measured through the 2.8 mm sampling probe) across the diameter of the pipe. As will be seen, the droplet flows for air-oil flow are significantly higher than those for air-water flow and peak at the centre of the tube. Figure 2.31 shows the flow rate at the centre of the tube as a function of liquid velocity at a superficial gas velocity of 25 m.s^{-1}. It will be seen that the droplet flow rates are very much higher in the case of air-oil than in the case of air-water flows.

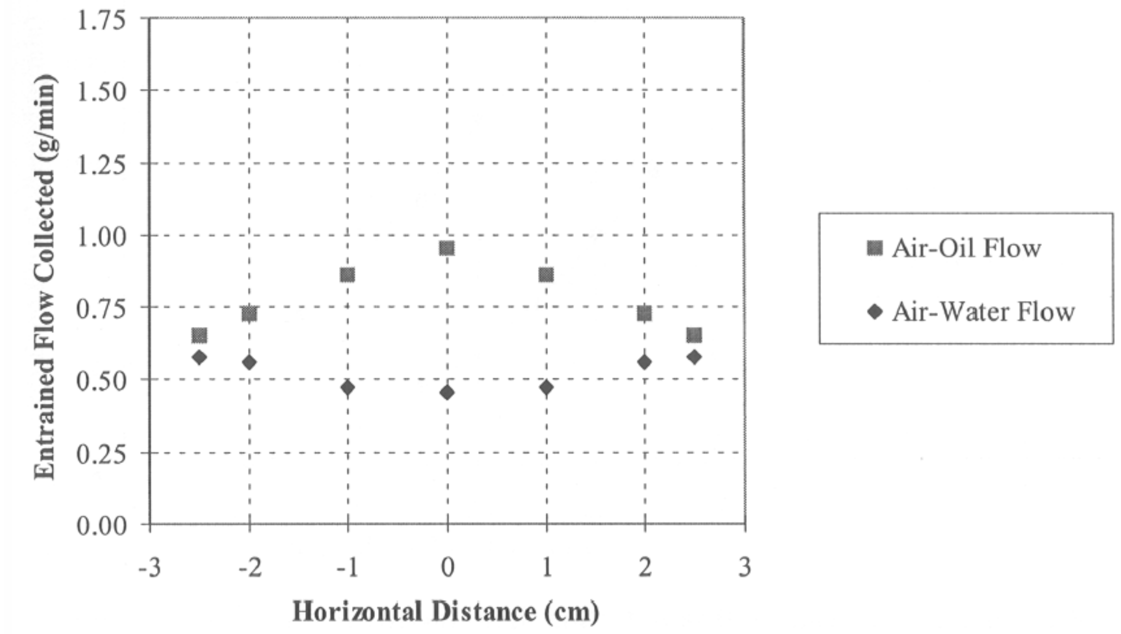

Figure 2.30. Profile of entrained drop flow across the horizontal pipe diameter. Superficial gas velocity: 25 $m.s^{-1}$, superficial liquid velocity: 0.02 $m.s^{-1}$. Sampling tube diameter: 2.8 mm (Badie, 2000).

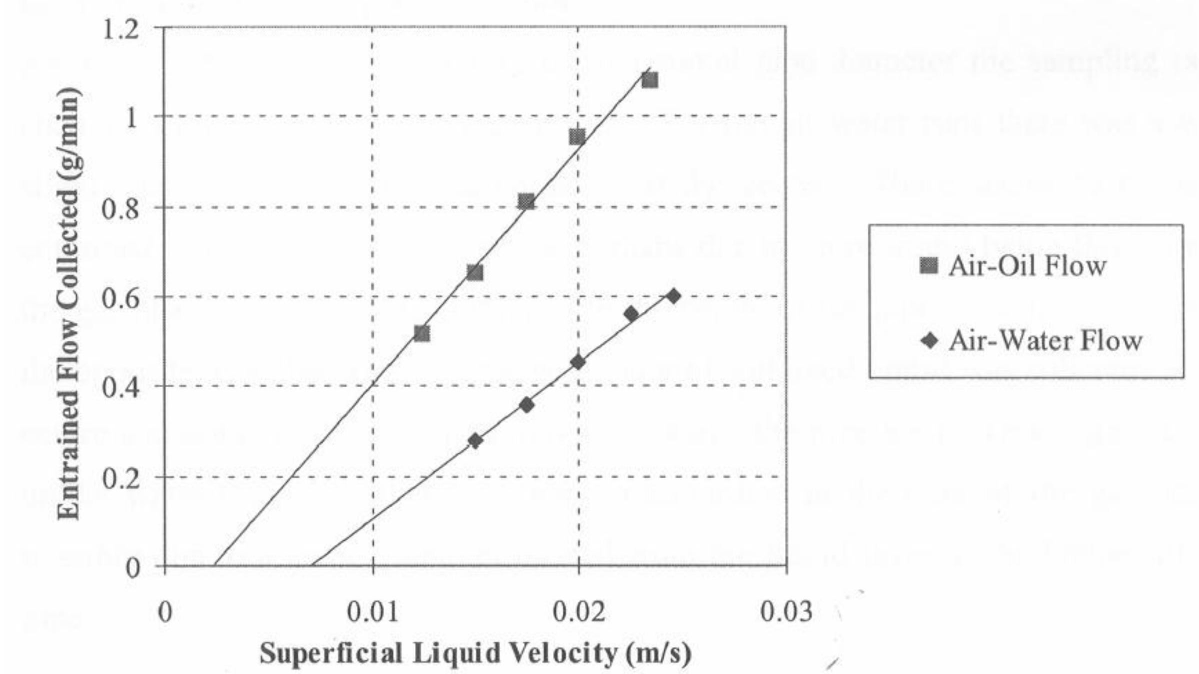

Figure 2.31. Variation of droplet flow rate collected in a 2.8 mm sampling tube at the centre of a 78 mm tube with liquid superficial velocity for a superficial gas velocity of 25 $m.s^{-1}$ (Badie, 2000).

In further (and as yet unpublished) work at Imperial College, measurements have been made of liquid flow rates (again through a 2.8 mm diameter sampling tube) for three-phase (air-oil-water) flows and results from these investigations are shown in Figure 2.32.

In the measurements, as indicated, the water cut (WC) varies from zero to unity; the water cut represents the fraction of the input liquid volumetric flow rate which is in the form of water. In these measurements, the oil fraction in the extracted sample can be measured and results for this are shown in Figure 2.32. The oil fraction in the extracted droplet flow over the gas core region and is higher than the oil fraction (1-WC) in the inlet flow. This reflects preferential entrainment of the oil which would tend to segregate from the water in the liquid layer at the bottom of the pipe.

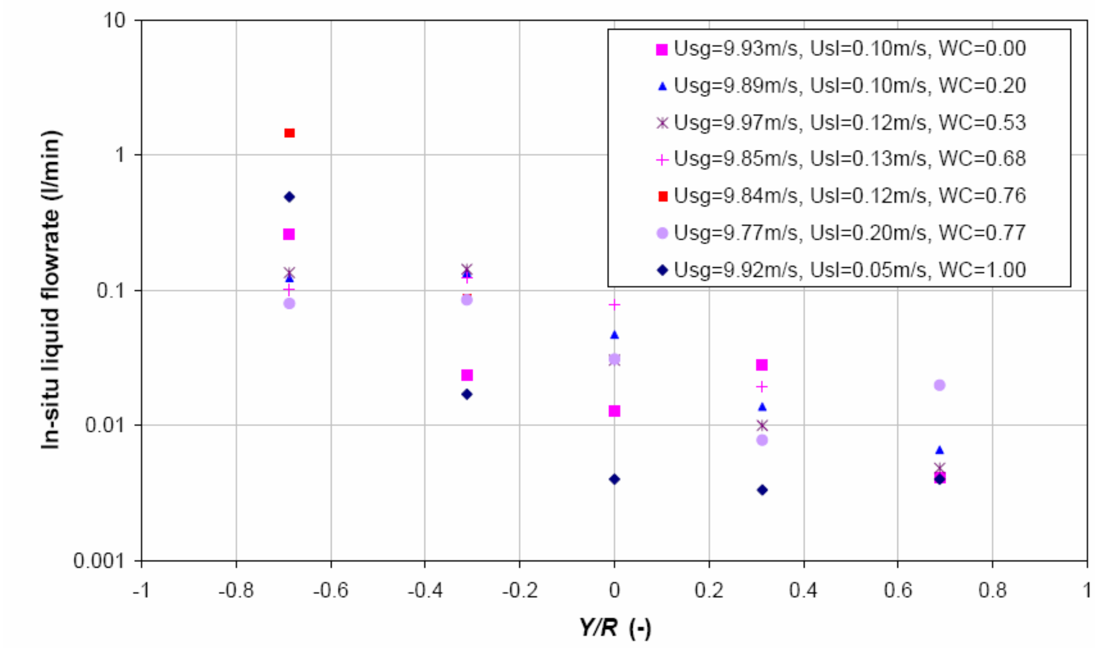

Figure 2.32. Imperial College data for droplet mass flux distribution in three-phase air-oil-water flows in a 78 mm diameter tube.

2.4. Time varying phenomena

In the previous sections, we have been concerned with channel average quantities (Section 2.2) and with the time-averaged values of spatially varying parameters (Section 2.3). However, much information can be gleaned about horizontally annular flow by considering time varying phenomena. Here, we consider time varying film thickness (reflecting the presence of interfacial waves) in Section 2.4.1 and photographic observations of transient phenomena in Section 2.4.2.

2.4.1. Time Varying Film Thickness (Interfacial Waves)

An early study of time varying film thicknesses using flush-mounted conductance probes is reported by Pearce (1979). Figure 2.33 typifies the results obtained. As will be seen, the film is much thinner and less wavy at the top of the tube than at the bottom (as would be expected) but cross correlation of the traces showed that the wave speeds were similar at the top and bottom of the tube, being about one tenth of the vapour core velocity. Jayanti et al (1989, 1990a, 1990b) also report studies of the time varying film thickness (interfacial waves) in air-water flow in a 32 mm diameter tube; they also used the flush-mounted conductance probe method. Two characteristic wave types were observed; the first was a low frequency high speed wave travelling at around 3 m.s^{-1} which was coherent around the tube periphery. A second (higher frequency) type of wave was observed near the bottom of the tube which travelled at a lower speed (around 2 m.s^{-1}). Jayanti et al (1990a) used cross correlation between the film thickness at the bottom and the side of the tube to give information on the distributed wave shapes of disturbance waves which are formed in horizontal annular flow. The results are illustrated in Figure 2.34. The circumferential spreading by distortion is illustrated and is an important feature of the flow.

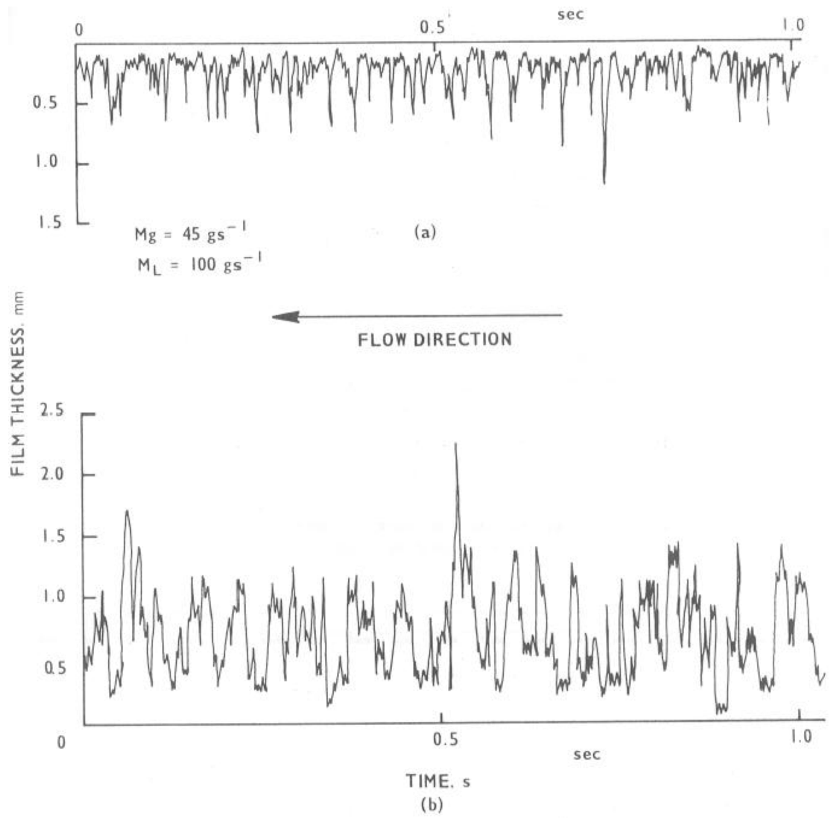

Figure 2.33. Typical film thickness traces for (a) top and (b) bottom of a 32 mm tube with horizontal annular air-water flow (Pierce, 1979).

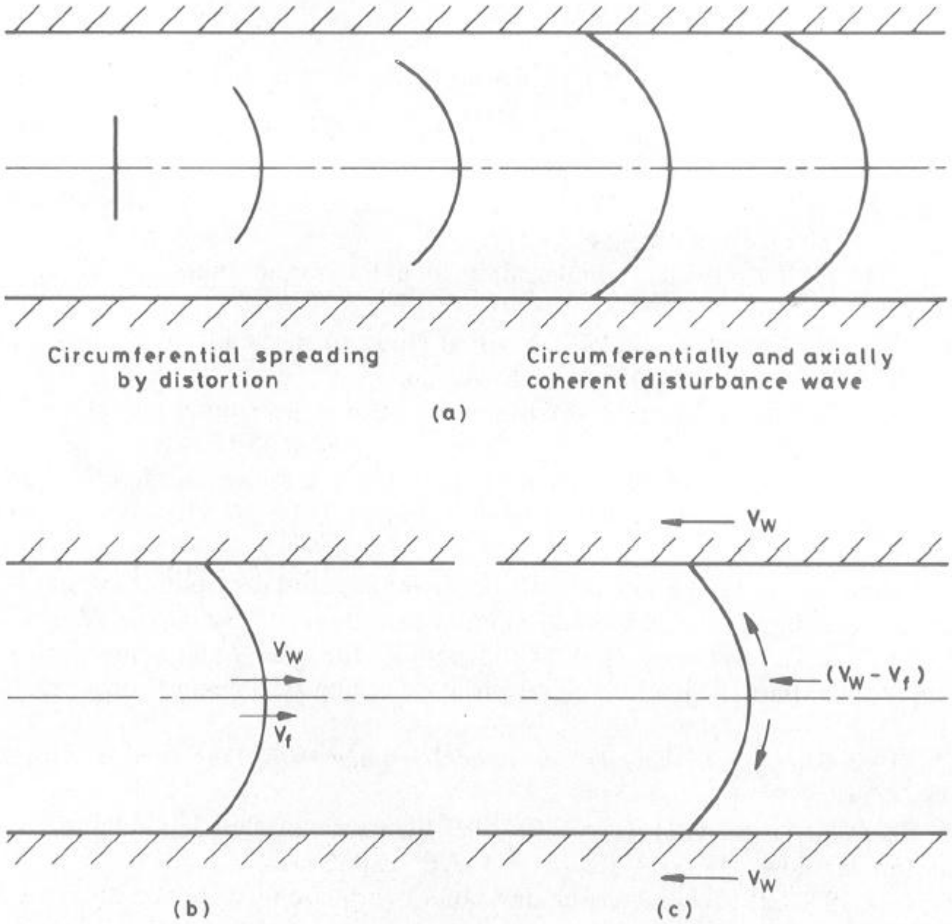

Figure 2.34. Circumferential spreading of a disturbance wave after inception (a), fully developed disturbance waves (b) and secondary motion in the liquid due to a disturbance wave moving faster than the film (c). Jayanti et al (1990a).

Measurements of the angle of disturbance waves were carried out also by Paras & Karabelas (1991a) for circular tubes and by Fukano (1997) for both rectangular and circular tubes. Figure 2.35 shows the data obtained by Paras and Karabelas for the angle to the vertical subtended by the disturbance waves as a function of gas velocity at various liquid velocities. As will be seen, the disturbance waves tend to become vertically orientated at high gas velocities. The measurements of Fukano et al (1997) of fluctuations of local film thickness at a given cross section confirmed the structure of disturbance waves to be consistent with the suggestions by Fukano and co-workers on the wave transport mechanisms (see Section 2.2.5.1). Figure 2.36 shows a sketch of the structure of disturbance waves in the rectangular channel system investigated by Fukano et al (1997) who also studied the drainage of the base film between the disturbance waves; they calculated the change of film thickness with time using a laminar drainage model and obtained good agreement with this model as shown in Figure 2.37.

There is still some controversy about the nature of disturbance waves both in vertical upwards and horizontal flows; a case can be made that they represent regions of turbulence passing over a laminar substrate. Jayanti & Hewitt (1997) calculated the profiles of velocity and turbulent viscosity using a low-Reynolds number $k-\varepsilon$ model for a vertical flow in which the flow is approximately two dimensional. Similar calculations might be done for the horizontal case where the disturbance waves are three-dimensional in nature. Measurements of the three-dimensional waves on the bottom part of a 78 mm diameter in horizontal annular flow are reported by Badie (2000) who used multiple parallel wire conductance probes to obtain the interfacial structure. Typical results from the work are shown in Figure 2.38.

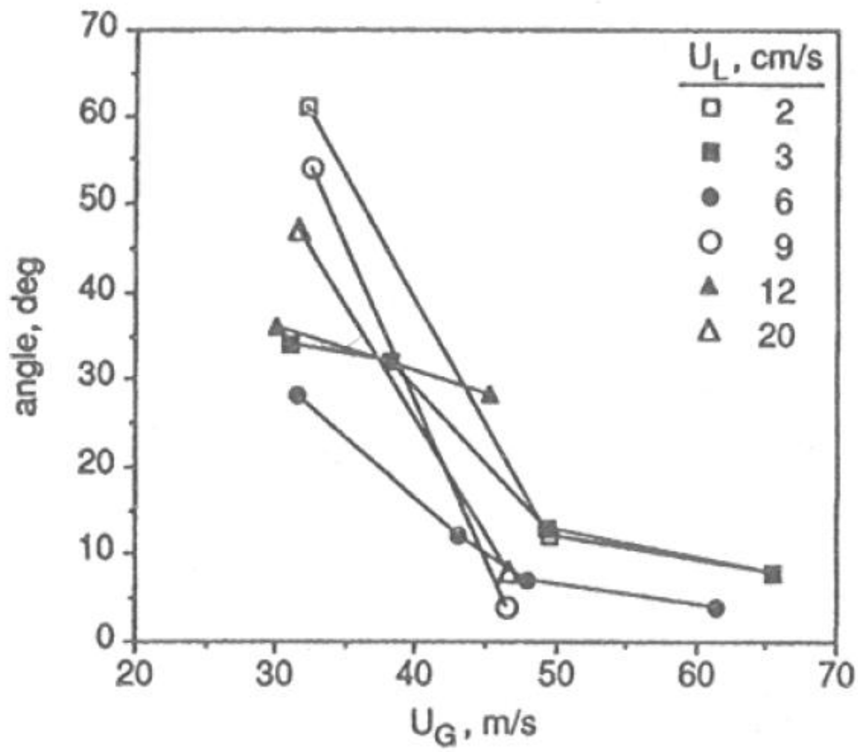

Figure 2.35. Influence of superficial liquid and gas velocity on the deviation of disturbance waves from the vertical orientation (Paras & Karabelas, 1991a).

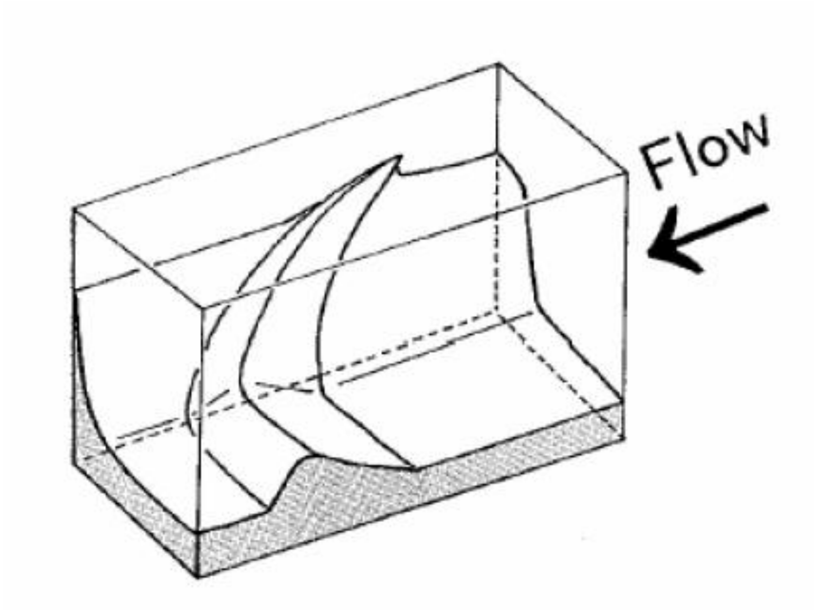

Figure 2.36. Observed shape of disturbance wave in flow in a rectangular channel (Fukano et al, 1997).

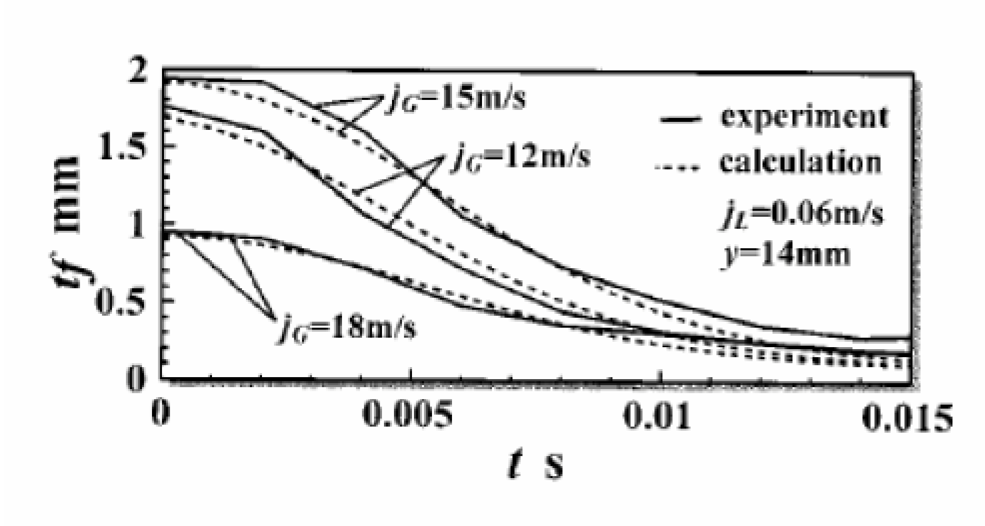

Figure 2.37. Time variation of liquid film thickness at the top of a circular tube during the period of film drainage following the passage of a disturbance wave (Fukano et al, 1997).

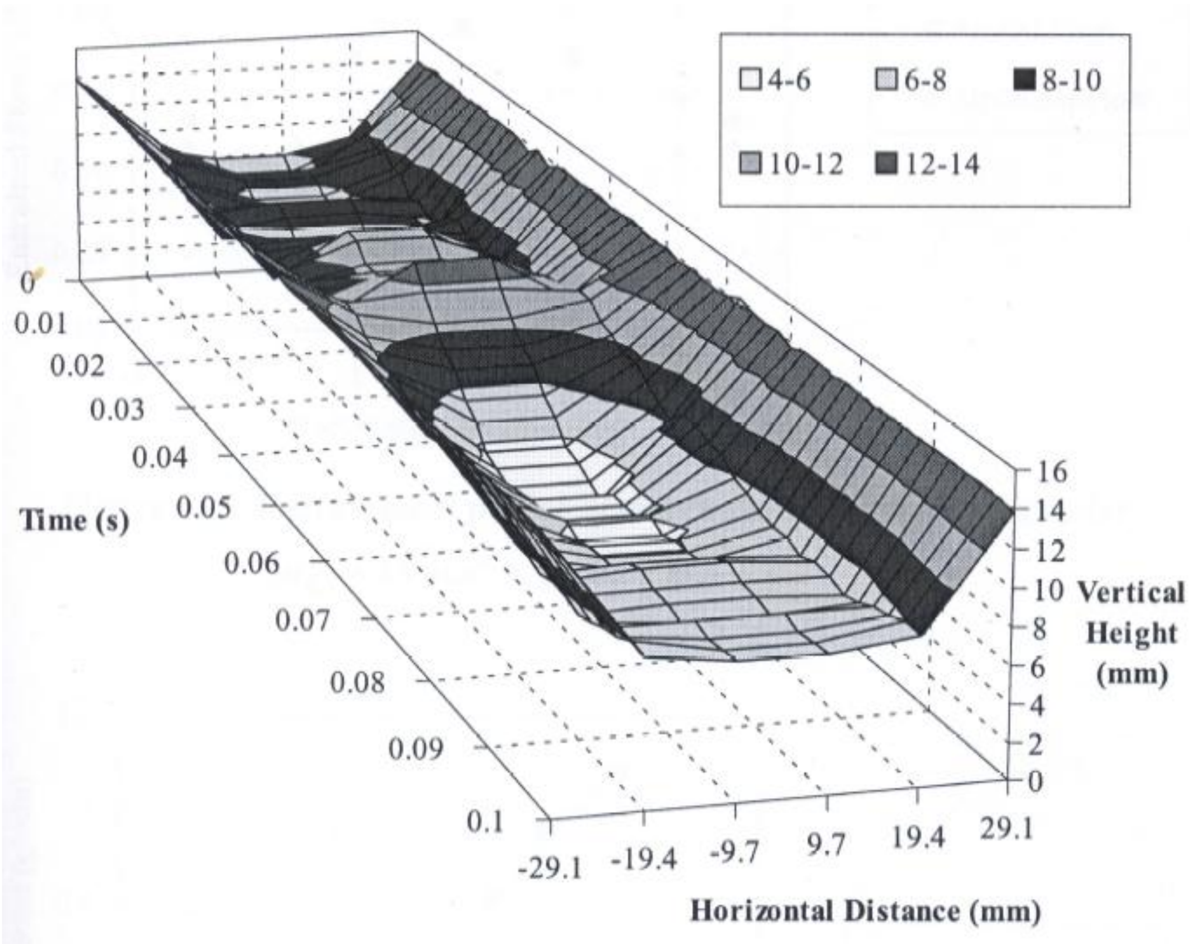

Figure 2.38. Film structure at the bottom of the pipe in horizontal annular flow (Badie, 2000).

Sampaio et al. (2008) present a numerical and experimental investigation of stratified gas-liquid two-phase flow in horizontal circular pipes. The finite element method is used to solve the Reynolds averaged Navier-Stokes equations with the k-ω turbulence model for a fully developed stratified gas-liquid two-phase flow. The effect of the interfacial waves are neglected thus a smooth interface surface is used. The continuity of the shear stress across the interface is reached when the continuity of the velocity is satisfied by the variational formulation. The numerical results are in agreement with experimental data.

The numerical results have also been compared with those obtained using the model of Taitel and Dukler and they matched positively showing that the k-ω model is suitable for the numerical simulation of such flows. Nevertheless, for the modelling of stratified wavy two-phase flow, a better understanding is required on how to choose interfacial values for k and ω in order to obtain a better agreement with experimental data.

2.4.2. Photographic Studies of Flow Structure

Traditionally, photographic methods have been of great importance in clarifying issues in multiphase flow. In the case of horizontal annular flow, there have been two main areas of study, namely investigations of the liquid film and investigations of the gas core.

Photographic studies of liquid film behaviour. Butterworth & Pulling (1972, 1974) reported a study of dye tracing which was aimed at adding understanding of circumferential transport mechanisms. A dyestuff was injected at the side of the tube and its movement followed using high speed photography. Two types of behaviour were noted:
(a) the dye trace moves generally downwards from the point of injection except when disturbance waves passed periodically which mix the dye circumferentially. Some time elapsed before the trace settled down to its normal downward flow again.
(b) in the second type of behaviour, the dye trace was dispersed rapidly and chaotically by a continuous passage of waves with the dye trace moving somewhere randomly both upwards and downwards, with the downwards motion being dominant.

These observations lead to the wave mixing/spreading mechanism for maintaining horizontal annular flow which will be discussed further in Section 5.1 below.

Studies of liquid film behaviour using the technique in which the refractive indices of the channel wall, its surroundings and liquid flow in the channel were matched were reported by Hewitt et al. (1989, 1990) and Jayanti & Hewitt (1991). The matching refractive indices method allowed focusing on the bottom film cross-section in a vertical plane passing through the tube axes (in principle, the same technique could be used for any other cross section but this was not explored). Figure 2.39 shows a cross-sectional picture of the bottom liquid film and two principal features emerged, namely the highly wavy nature of the interface and the existence of the entrained bubbles in the liquid layer. More recently, this observation has been confirmed by Rodriguez & Shedd (2004) who made much more detailed measurements, for instance determining the bubble size distribution in the bottom liquid film. Typical bubble size distributions obtained by Rodriguez & Shedd (2004) are shown in Figure 2.40 where the bubble sizes are normalized to the liquid film thickness δ. Note that bubbles of larger size than the mean film thickness are possible. The average bubble diameter was of the order of 20-30% of the film thickness as illustrated in Figure

2.41. The existence of bubbles of diameter much greater than the liquid film has certainly been observed in boiling (where the bubbles grow until they burst with diameters of several times the film thickness, Sun et al., 1995) and bubble transport/bursting may play a significant role in entrainment from the bottom liquid layer.

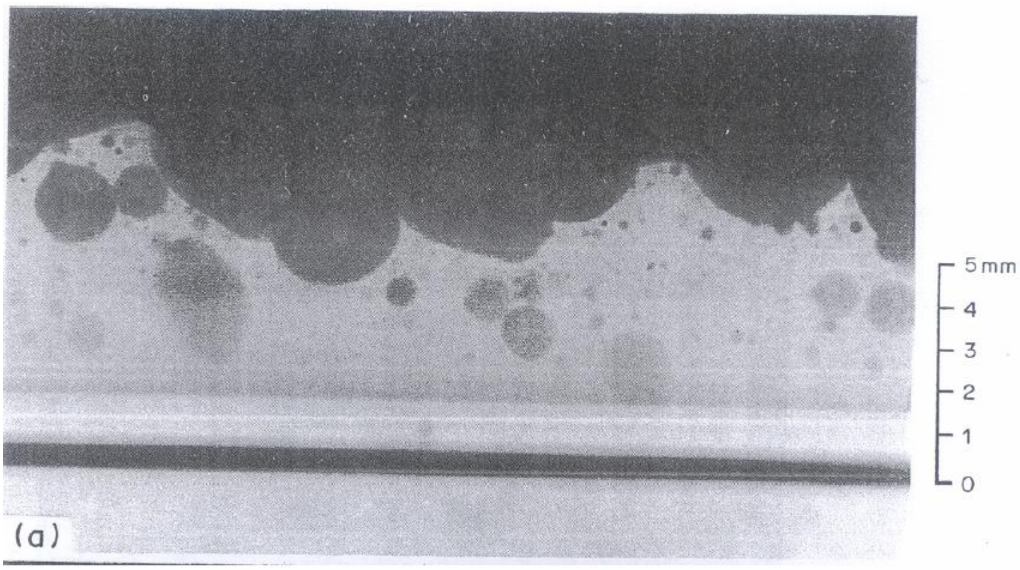

Figure 2.39. Instantaneous structure of the liquid film at the bottom part of tube in air-water annular flow (Hewitt et al., 1990).

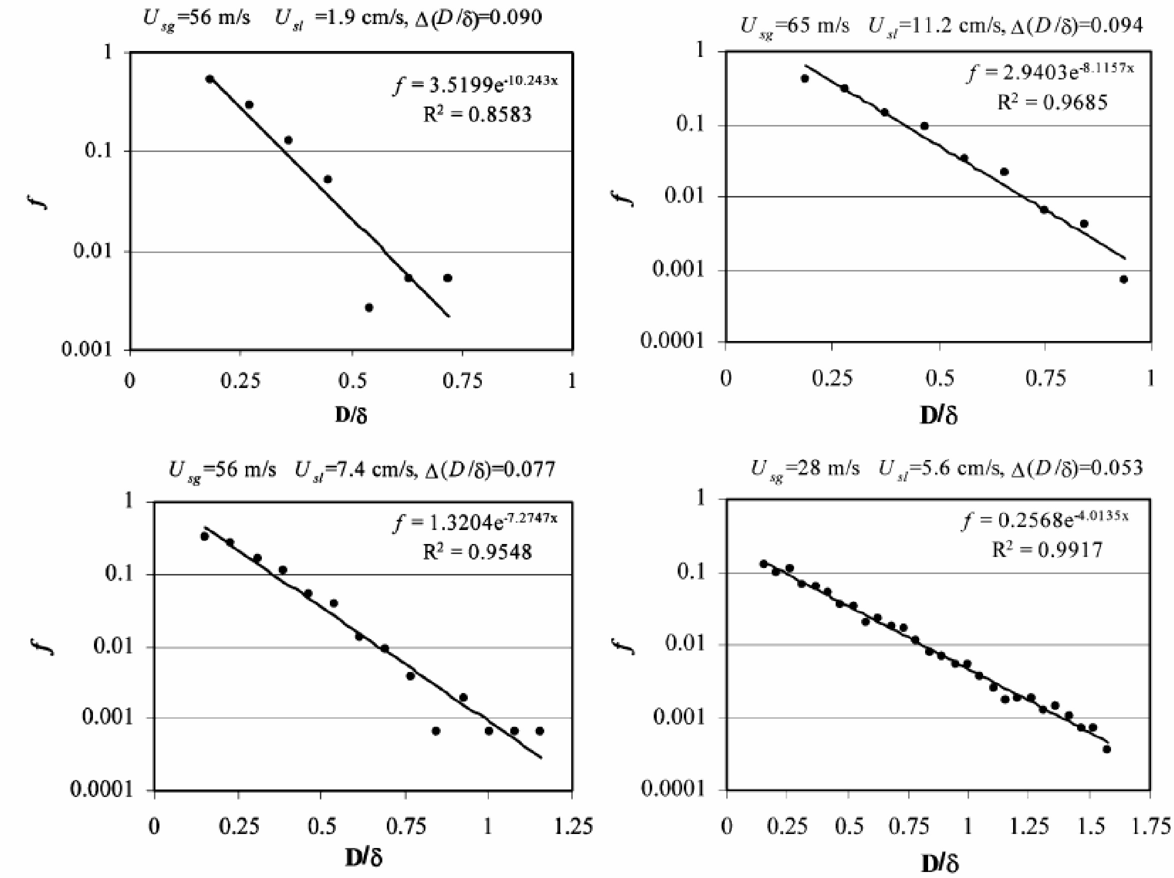

Figure 2.40. Distribution of ratio of bubble diameter to film thickness in the bottom film of a horizontal annular flow (Rodriguez & Shedd, 2004).

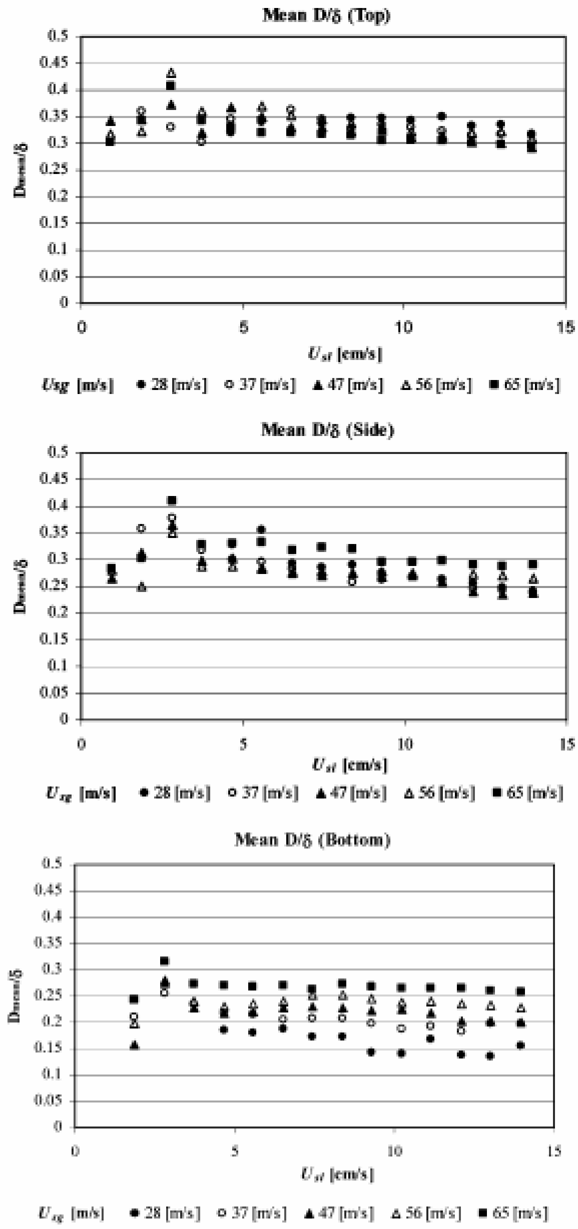

Figure 2.41. Ratio of mean bubble diameter to film thickness in the bottom film of a horizontal annular flow (Rodriguez & Shedd, 2004).

In the experiments reported by Hewitt et al. (1989, 1990) and Jayanti & Hewitt (1991), a photochromic dyestuff was used in the liquid phase such that pulses of UV laser light could be used to excite lines in the flow which were convected downstream and gave an indication of the film velocity profiles. These were extremely complex as exemplified in Figure 2.42. In a smooth film there was a distorted S-shaped profile and under a wave, the profile is parabolic as shown.

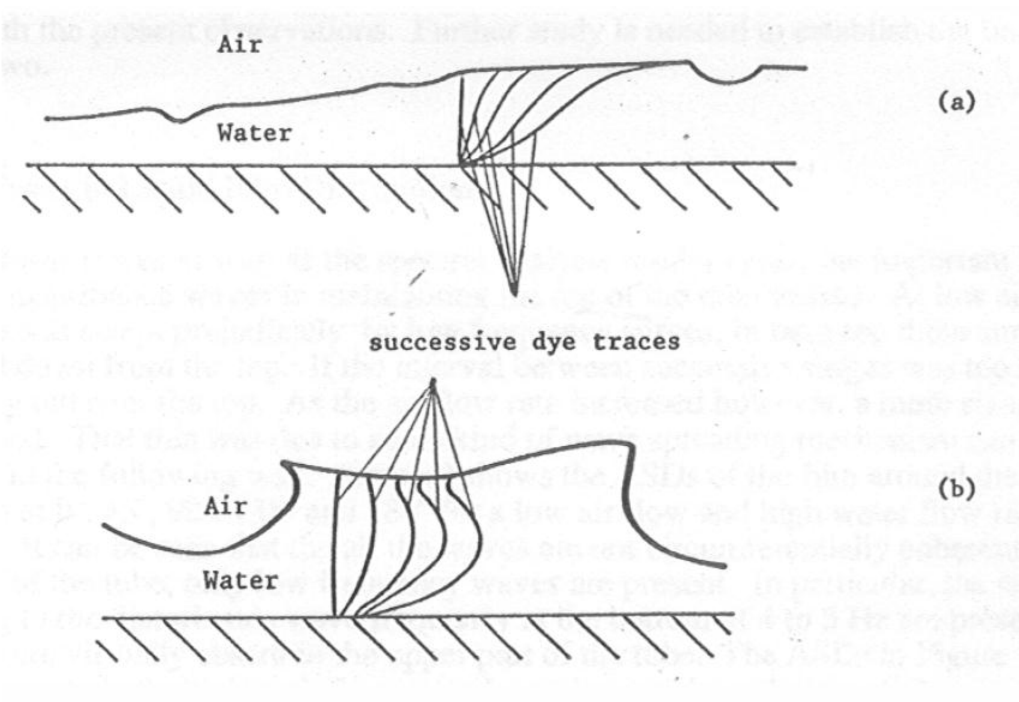

Figure 2.42. Evolution of photochromic dye traces in a bottom film of a horizontal annular flow indicating (a) a distorted S-shaped profile in the thin film and (b) a parabolic profile under a wave (Jayanti & Hewitt, 1991).

A much more comprehensive study of liquid film behaviour using photochromic dye tracing was carried out by Sutharshan et al. (1995). The optical arrangement is illustrated in Figure 2.43. Spots of photochromic dye were introduced at the pipeline centre in an air-kerosene horizontal annular flow. The subsequent behaviour of the spots was then observed using a video camera. The key role of the disturbance waves in promoting circumferential transport of the liquid was clearly demonstrated. During the passage of each disturbance wave, the dye trace was usually seen to move upwards; whereas it sometimes moves in a purely axial direction, it never moves downwards. This demonstrates conclusively the transport of the liquid around the periphery of the tube as a result of wave action. The behaviour of the base film which existed between the disturbance waves are also very interesting as illustrated in Figure 2.44. Just after the disturbance wave, the base film still continues to move upwards but then it begins to move downwards, resuming an upward motion just before the next disturbance wave. However, Sutharshan et al. (1995) concluded that it was unlikely that the base film, though covered with ripples that could move upwards, would contribute significantly to circumferential transport; such transport is nearly all associated with the disturbance waves. It may be possible that transient upwards transport of the base film may be associated with transient secondary flows as discussed in Section 2.5.3 below.

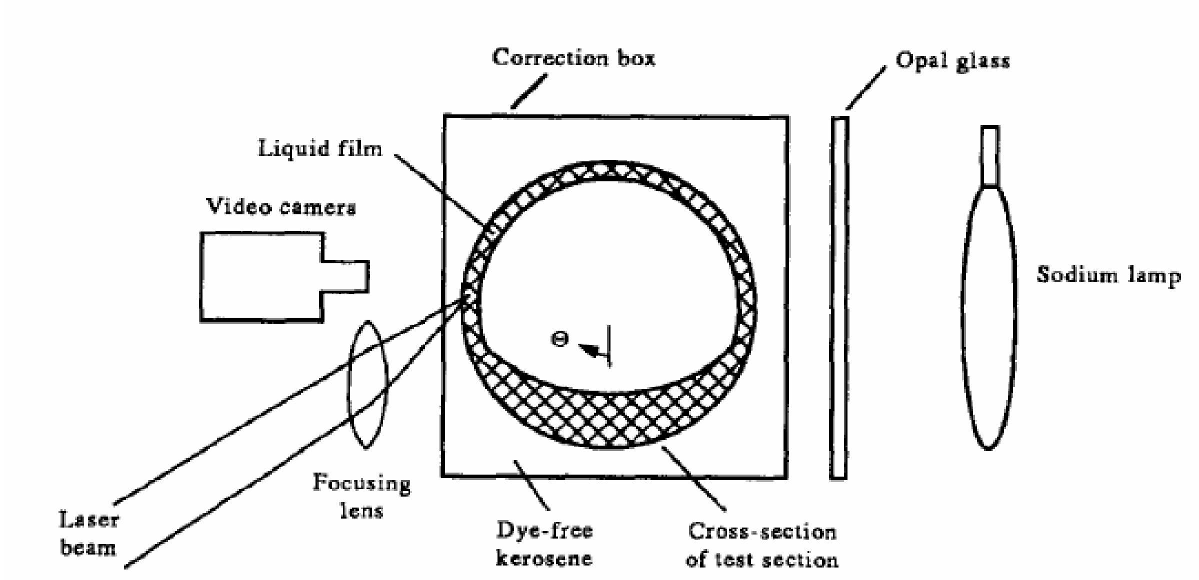

Figure 2.43. Optical arrangement for photochromic dye tracing in air-kerosene horizontal annular flow (Sutharshan et al., 1995).

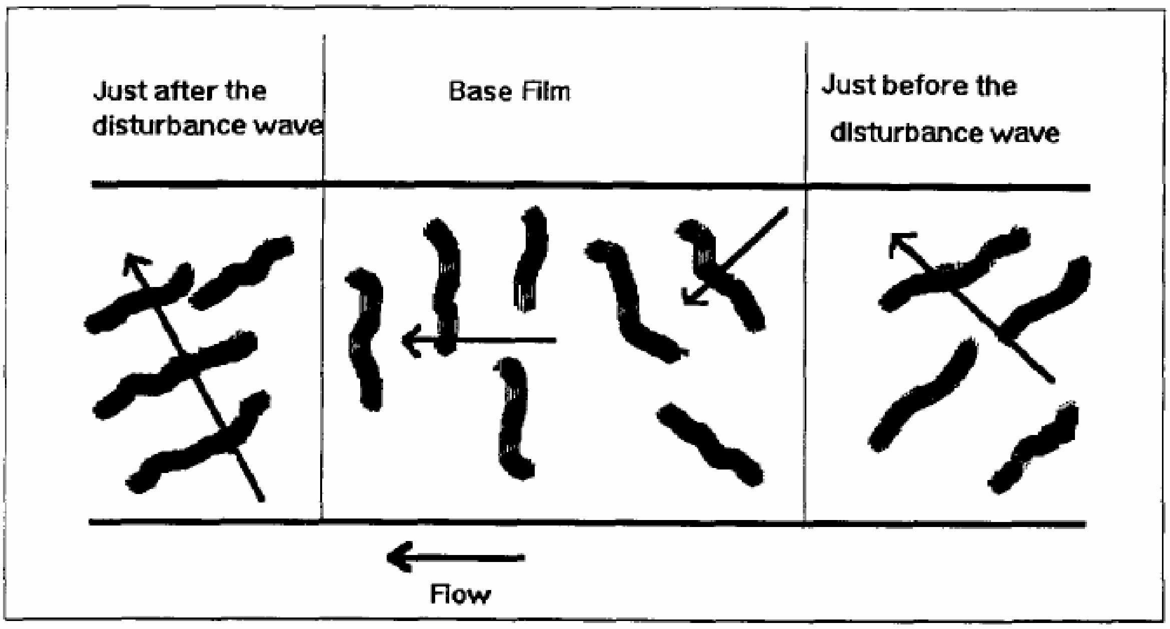

Figure 2.44. Motion of ripples propagating over the base film in a horizontal annular flow (Sutharshan et al., 1995).

Axial view photography of droplet motion. Axial view photography has been a useful tool in understanding annular flows and has been widely applied in the vertical flow case (Arnold & Hewitt, 1967; Hewitt & Roberts, 1969; Hewitt & Whalley, 1980). The first axial view technique to be applied involved illuminating the flows at a given cross-section and focusing a camera onto the cross-section through an aspirated viewing tube. This gives the information on the time varying structure of the flow at a given location but it is also interesting to use a parallel light beam passing down the axis of the tube (usually provided with a laser). In this case, the motion of the drops could be observed over their full lifetime in the channel (Hewitt & Whalley, 1980). Compared to the extensive application of the technique in vertical flows, there has been relatively little work on horizontal annular flow with observations using the parallel light beam approach being reported by Azzopardi (1987) and observations using the plane focusing approach being reported by Badie (2000). The results obtained by Azzopardi (1987) are illustrated in Figure 2.45. Following their creation, the observed droplets follow a continuous path to the opposite wall with little deviation from a straight line. The range of the diameters observed in these experiments is shown in Figure 2.46; droplets moving in the manner shown were relatively large size (typically, 1-5 mm) and the translation velocity observed were in the range of 1.2-2.1 $m.s^{-1}$.

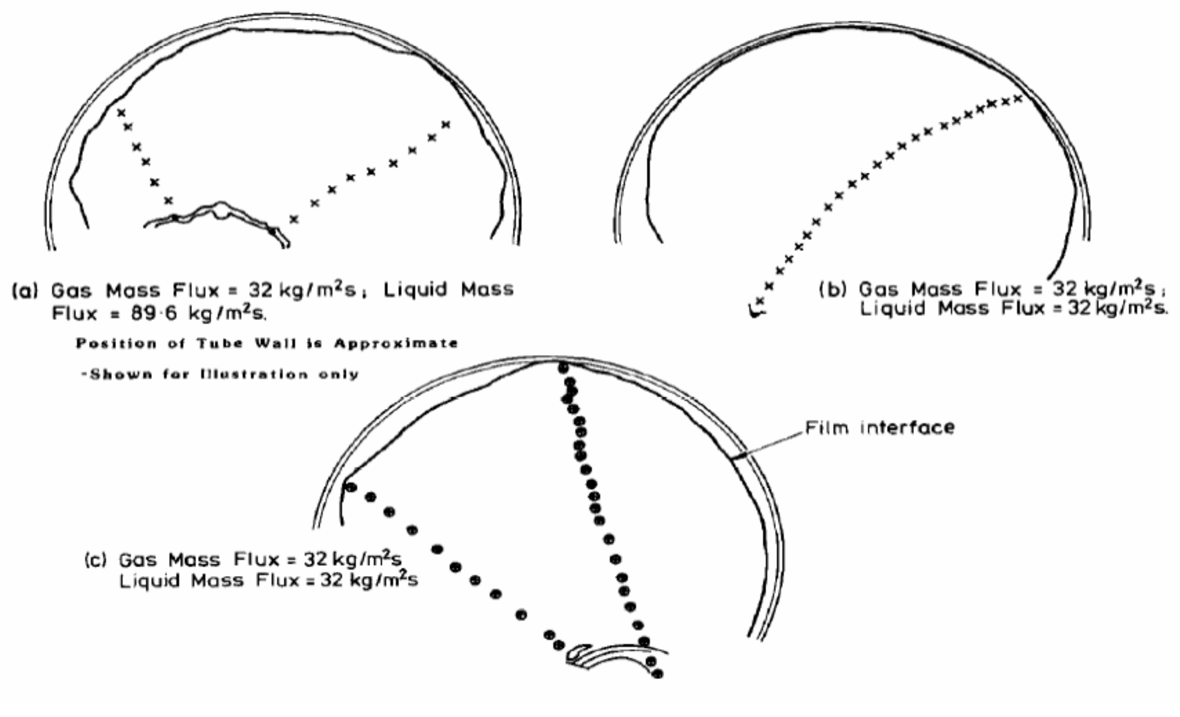

Figure 2.45. Droplet trajectories observed in horizontal annular flow in a 32 mm diameter tube (Azzopardi, 1987).

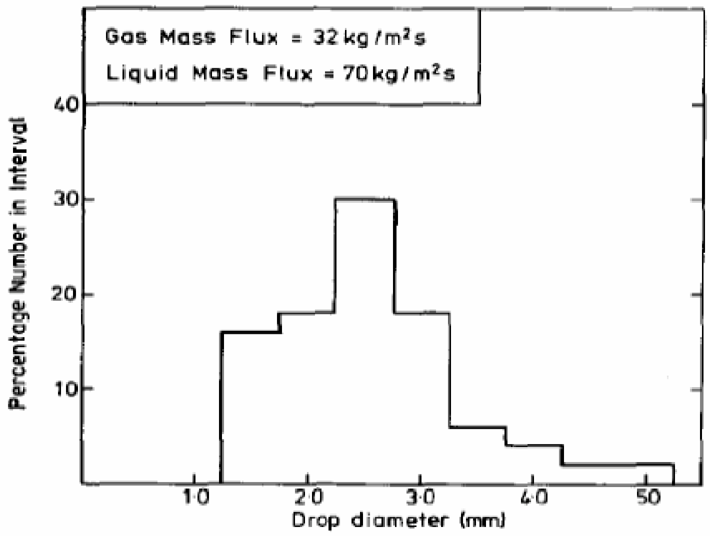

Figure 2.46. Distribution of sizes of analysed droplets in experiments of Azzopardi (1987).

Figure 2.47 shows a typical sequence of several frames obtained by Badie (2000) for a horizontal annular flow with a superficial gas velocity of 15 m.s^{-1} and a superficial liquid velocity of 0.01 m.s^{-1}. The motion of the droplets and breakup can be observed in these pictures and by superimposing several successive frames, it can be seen that the droplets continue in straight lines (see Figure 2.48) ; the velocity of the droplets can be determined and was found to be in the range of 1.0-1.5 m.s^{-1} in these experiments on a 78 mm tube which were therefore consistent with the measurements of Azzopardi (1987) for a smaller diameter tube. Badie (2000) used the data gleaned from pictures such as Figure 2.48 in developing a closure for his droplet transport model for horizontal annular flow (see Section 2.5.2 below).

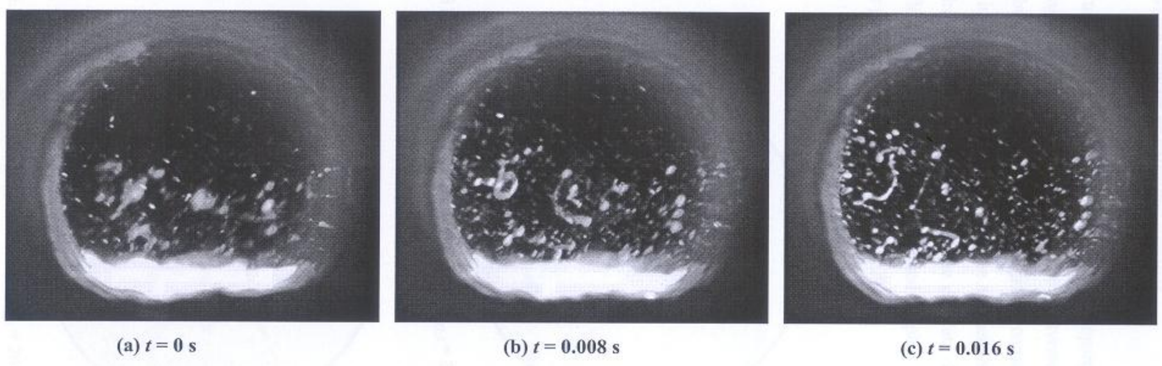

Figure 2.47. Successive frames taken using axial view photography with a given plane of focus for air-oil flow in a 78 mm diameter tube (Badie, 2000).

Figure 2.48. Droplet motion observed by superimposing four successive frames of the axial view video sequences (Badie, 2000).

Axial view photography of stratifying annular flow formed an important part of the work described in this thesis and a more detailed review of the topic is given in Chapter 3. The methodology used in the present work is described in Chapter 4 and the results obtained are presented in Chapter 5.

2.5. Mechanisms for maintaining horizontal annular flow

2.5.1. Wave Spreading and Mixing

Experiments carried out by Butterworth (1968) on vertical annular flow in an eccentric annulus showed that the film tended to become uniform around the inner surface and he postulated that this was due to wave action. He suggested the following equation to describe the process of achieving a uniform liquid film:

$$\Gamma_\theta = -\frac{k}{R}\frac{\partial \Gamma_z}{\partial \theta} \tag{2.47}$$

where Γ_θ and Γ_z are the peripheral mass flow rates (flow rate per unit width of surface) in the circumferential and axial directions, respectively, R is the radius of the surface on which the film is flowing and θ is the circumferential coordinate angle. Butterworth found that the circumferential transport coefficient (k) was estimated to have a value in a range 3-

20 mm in the eccentric annular experiments. In the case of a horizontal annular flow, this wave spreading effect is opposed by the drainage of the film under gravity and Butterworth (1969) wrote the following equation (which assumes laminar film drainage around the periphery).

$$\Gamma_\theta = \frac{(\rho_L - \rho_G)\rho_L g \delta^3 \sin\theta}{3\mu_L} - \frac{k}{R}\frac{\partial \Gamma_z}{\partial \theta} \tag{2.48}$$

In Equation (2.48), δ is the film thickness and g is the acceleration due to gravity. For a fully developed flow, where Γ_θ and δ change only with θ, it follows that:

$$\frac{d\Gamma_z}{d\theta} = \frac{R(\rho_L - \rho_G)\rho_L g \delta^3 \sin\theta}{3\mu_L k} \tag{2.49}$$

For a thin laminar flow, Γ_z can be expressed as:

$$\Gamma_z = \frac{\rho_L \tau_i \delta^2}{2\mu_L} \tag{2.50}$$

where τ_i is the interfacial shear stress. For this case, Equation (2.49) can be solved to give following results:

$$\frac{1}{\delta} = a\cos\theta + C \tag{2.51}$$

where C is the a constant of integration and a is given by:

$$a = \frac{R(\rho_L - \rho_G)g}{3k\tau_i} \tag{2.52}$$

Thus, a can be estimated from a plot of $1/\delta$ against $\cos\theta$; such a plot did, in fact, yield a straight line as expected from Equation (2.51) and typical results in this form are shown in Figure 2.21. Butterworth estimated k from such plots and found values in a range of 2 to 8 mm which were similar magnitude to those obtained for the eccentric annular case. In later work, Butterworth (1972, 1974) elaborated this concept to include turbulent flow in the liquid films (assuming an isotropic turbulent viscosity which governs both axial and circumferential flows, notwithstanding the fact that the Reynolds number for the circumferential flows was rather low). This methodology as been used in the modelling studies reported in this thesis as is described in more detail in Chapter 6.

A more formal structure for considering the circumferential and axial flows was developed by Laurinat et al. (1985). A simplified version of the circumferential momentum equation was derived as follows:

$$\frac{\partial \tau_{yx}}{\partial y} + \frac{1}{R}\frac{\partial \tau_{xx}}{\partial \bar{x}} - \rho_L g \sin \bar{x} - \frac{\rho_L g}{R} \cos \bar{x} \frac{d\delta}{d\bar{x}} = 0 \qquad (2.53)$$

where y is the radial distance, $\bar{x}$ the angle from the bottom of the tube (= x/r where x is the circumferential distance from the bottom of the tube), τ_{yx} is the interfacial shear in the circumferential direction and τ_{xx} the liquid Reynolds stress (normal stress). Laurinat et al. (1985) modelled τ_{yx} by the following expression based on the experiments of Darling & McManus (1969) as follows:

$$\tau_{yx} = C_5 \bar{\tau}_I \sin \bar{x} \qquad (2.54)$$

where τ_I is the mean axial interfacial shear and C_5 a constant which was selected to give good agreement between the calculations and the experiments (Laurinat et al. suggested a value of 0.004).

The τ_{xx} was modelled by the expression:

$$\tau_{xx} = -C_1 \overline{w}^2 \qquad (2.55)$$

where:

$$\overline{w} = \frac{\Gamma_z}{\delta} \qquad (2.56)$$

Thus, it will be seen that this term is rather analogous to that used in the analysis of Butterworth (1969). Laurinat et al. suggested a value of C_1=0.28.

The Laurinat et al. (1985) analysis was adopted by Hurlburt & Newell (2000) who used the experimental data to develop an improved expression for τ_{xx}. Hurlburt & Newell (2000) did not take into account of the circumferential shear stress term τ_{yx} in analysing their data.

Transport of the liquid to the upper surface as a result of wave action has also been extensively investigated by Prof. T. Fukano (Kyushu University, Japan) and co-workers (Fukano et al., 1985; Fukano & Ousaka, 1989; Fukano et al., 1997 and Fukano & Inatomi, 2003). The basis of the suggested model is illustrated in Figure 2.49. A change of pressure occurs across the disturbance wave, this change being highest at the bottom of the tube and lowest at the top. This generates a circumferential pressure gradient which transports the liquid upwards as illustrated. In between the disturbance waves, the liquid film drains as shown. Fukano & Ousaka (1989) developed an analysis analogous to that of Laurinat et al. (1985) but related τ_{xx} directly to the difference in pressure around the wave (bottom to top) which was calculated using a drag law expression. Numerical calculations supporting the idea of circumferential pumping of the fluid in the wave due to the circumferential pressure gradient are described by Fukano & Inatomi (2003). The model captures the annular flow formation process and also predicts the transport as a result of circumferential pressure gradients. Results from this numerical simulation are shown in Figure 2.50.

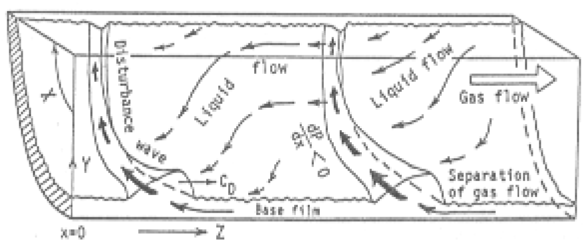

Figure 2.49. Pumping action of a disturbance wave giving rise to circumferential liquid transport (Fukano & Ousaka, 1989).

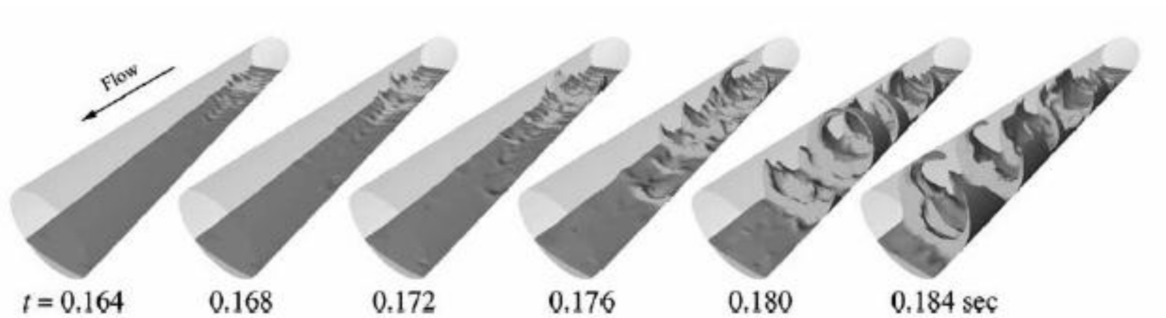

Figure 2.50. Numerical simulation of annular flow formation (Fukano & Inatomi, 2003).

Wave behaviour in horizontal annular air-water flow was investigated by Schubring et al (2008). Pipelines with internal diameter of respectively 8.8, 15.1, and 26.3 mm were used in this study. Prediction methods for wave velocity and wave frequency based on correlations and experimental measurements (pressure drop, liquid film thickness distribution) were given. The correlated values were in agreement with the measured values of wave velocity and frequency for the same flow conditions available in the literature. The wave velocity was related to the gas friction velocity defined as follows:

$$v_{fric,g} = \frac{\tau_w}{\rho_g} \tag{2.57}$$

where τ_w is the wall shear stress. Schubring et al used published correlations for wall shear stress to close the above relationship. It should be noted that Swanson (1966), found that the gas friction velocity, defined by Eq. (2.57) was equal to the wave velocity for his databank:

The wave frequency measurements by Schubring et al (2008) showed a different behaviour between the annular and wavy-annular/wavy flow regimes. Moreover the wave frequency was found to be dependent on gas and liquid flow rates. Wave velocity measurements in wavy-annular flow were found to have similar trends to that in fully annular flow.

2.5.2. Droplet Transport

In the droplet transport model for the formation of the film in annular two-phase flow, droplets entrained from the lower part of the pipe move upwards and deposit on the upper part, forming a film which drains downwards. Replenishment of the film by droplet deposition is then equal, in fully developed flow, to the deposition of the droplets on the surface. This model was first described by Anderson & Russell (1970) and has attracted a great deal of work since. Basically, the transport of the droplets from the lower to the upper part of the tube can occur by two mechanisms:

(1) Interaction between the droplets and the turbulent gas flow field in the core leading to turbulent diffusion of the droplets towards the upper surface and their ultimate deposition.

(2) A 'droplet ballistics' effect arising from the surprisingly large initial injection velocity of the droplets (typically in a order of 1 m.s^{-1}) which cause them to proceed directly to the upper surfaces from the point at which they are created in the bottom part of the tube.

In both mechanisms, the upwards motion of the droplets is opposed by the influence of gravity. Of course, both mechanisms can occur at the same time and this presents unique difficulties in interpretation of droplet transport behaviour.

Interpretation of droplet deposition in terms of a pure diffusion model is discussed by Lee and Hanratty (1988). The deposition rate (mass flow per unit peripheral area), R_D, is classically given by:

$$R_D = k_D C_B \tag{2.58}$$

where C_B is the droplet concentration in the gas core (kg/m^3, calculated on the basis of a homogeneous mixture in the core) and k_D is the droplet transport coefficient (m.s-1). Lee & Hanratty related k_D to the friction velocity u^* given by:

$$u^* = \sqrt{\frac{\tau_w}{\rho_G}} \tag{2.59}$$

where τ_w is the wall shear stress and ρ_G the gas density. A surprisingly wide range of data for vertical annular flows is represented by k_D/u^*=0.15-0.17. For a horizontal pipe, diffusional transport of the droplets is opposed by gravity and Paras & Karabelas (1991b) write the following equation for droplet transport in this case:

$$\varepsilon \frac{dC}{dy} + u_t C = a \tag{2.60}$$

where ε is the turbulent diffusivity of the droplets, u_t the terminal settling velocity and a is residual constant introduced to account for inertial transport of the droplets which are unaffected by turbulence and gravity. Paras and Karabelas (1991b) assumed that $\varepsilon = \varepsilon_f$, where ε_f is the gas diffusivity which was calculated from the expression (due to Vames and Hanratty, 1988):

$$\frac{\varepsilon_f}{Ru^*} = 0.074 \tag{2.61}$$

The settling velocities of the droplets were calculated using a method proposed by Wallis (1975). Paras & Karabelas (1991b) obtained an empirical correlation for the parameter *a* in Equation (2.60) and their model provides a relatively simple approach to calculating droplet flux distribution and deposition.

Binder & Hanratty (1992) consider Lagrangian simulation of the motion of droplets injected at the point source in a horizontal flow. Some of their results are shown in Figure 2.51. The effect of gravity is characterised by the product $\beta\tau_f$ where β is the reciprocal time constant of the particle representing its ability to respond to fluid turbulence, the latter having a time constant τ_f. For $\beta\tau_f$ =1 (small droplets) almost all the depositions are associated with turbulent transport. When $\beta\tau_f$ =0.01 (large droplets), then settling is dominant as shown in Figure 2.51. Mols & Oliemans (1998) present Lagrangian calculations of droplet motion a two-dimensional channel. The distribution of droplet concentration was determined as a function of the position in the channel and distance from the point of introduction of the particles. They concluded that, for a 5 cm height channel, particles larger than 70 μm are not able to reach top of the tube without having an initial radial entrainment velocity. Mols et al. (2000) extended this model to horizontal annular dispersed flow and obtained the droplet concentration profiles illustrated in Figure 2.52. These were in qualitative agreement with the results of Williams et al. (1996). The model also predicted the concentration profiles observed by Paras & Karabelas (1991b).

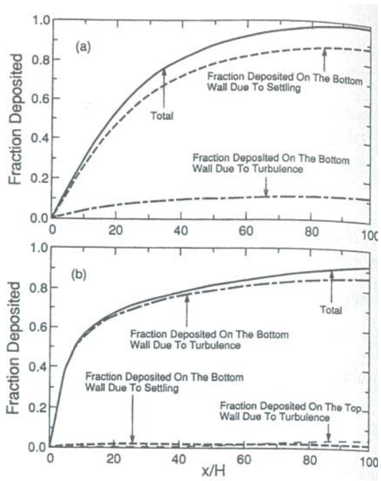

Figure 2.51. Influence of $\beta\tau_f$ on distribution of deposition between turbulence and settling: (a) $\beta\tau_f$ =0.01, (b) $\beta\tau_f$ =1.0 (Binder & Hanratty, 1992).

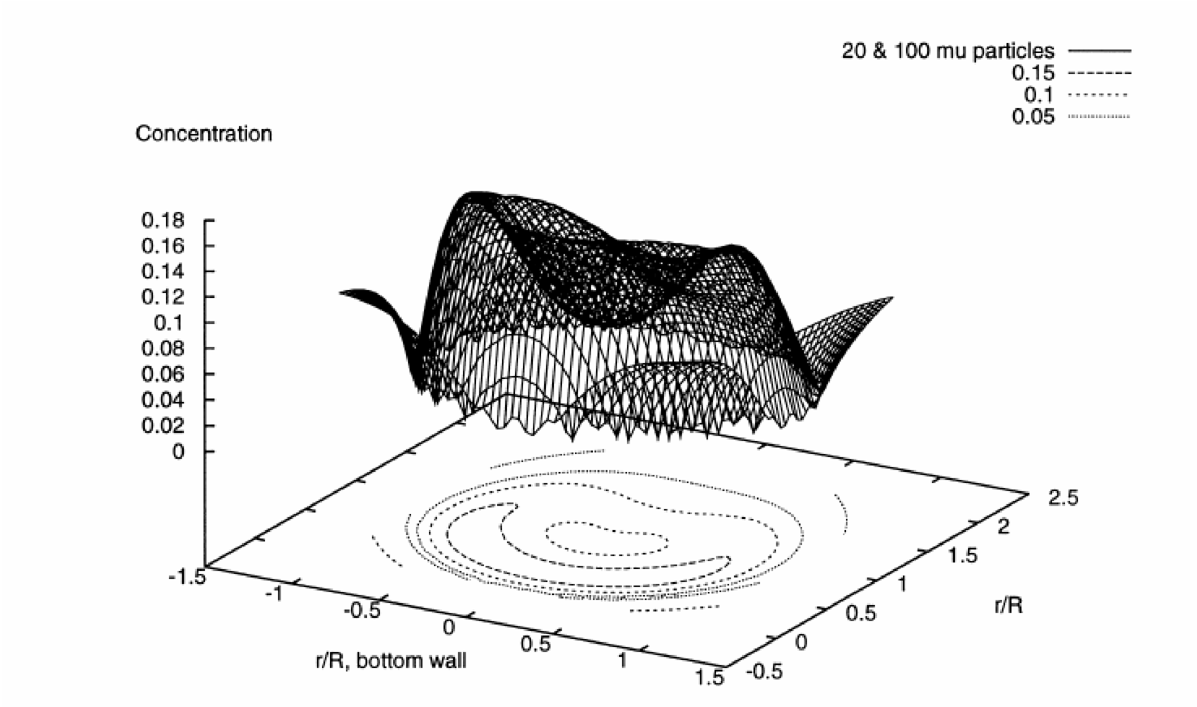

Figure 2.52. Three-dimensional concentration profiles in a horizontal annular flow (Mols et al., 2000).

Mito & Hanratty (2003) also use Lagrangian simulation methods to describe particle motion; they used a simplified turbulence model and obtained good agreement with results obtained using Direct Numerical Simulation (DNS) for the small Reynolds number range which is feasible with DNS. This led Mito & Hanratty (2004) to apply the model to horizontal annular flow case as illustrated in Figure 2.53. For fully developed flow, the rates of entrainment and deposition will be equal for both the top and the bottom surfaces of the two-dimensional channel illustrated, though the rates at the bottom and the top of the tube would clearly be very different if gravity is significant. Figure 2.54 shows results obtained by Mito & Hanratty for the ratio of the atomization rate at the top and the bottom as a function of a non-dimensional parameter g^+ defined as:

$$g^+ = \frac{g\nu}{u^{*3}} \qquad (2.62)$$

where ν is the kinematic viscosity of the gas phase. At high values of g^+, then the atomization rate at the top of the tube decreases rapidly, as will be expected. However, for low values of g^+ (corresponding to high gas velocities) then the rates become equal.

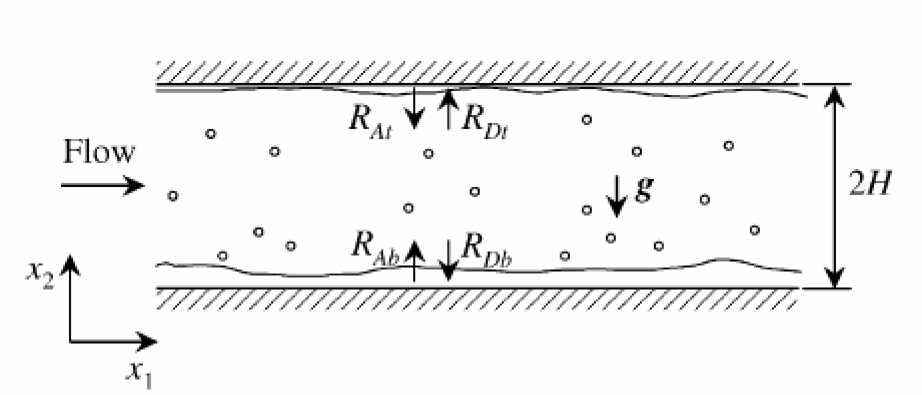

Figure 2.53. Two-dimensional model for liquid mass transfer in annular flow in horizontal channel (Mito & Hanratty, 2004).

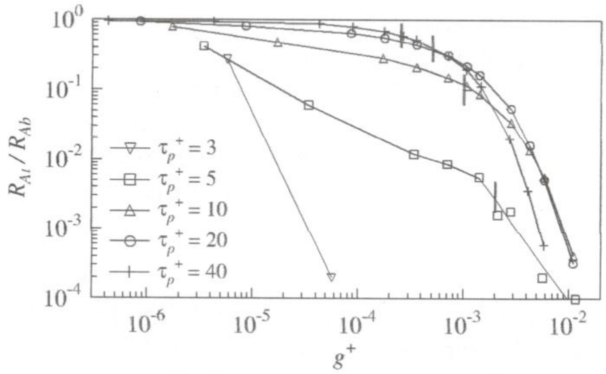

Figure 2.54. Ratio of rates of atomization at the top and bottom walls of a horizontal channel predicted by the model of Mito & Hanratty (2004).

Simulations of annular flow based on the use of a commercial CFD code (STAR-CD) are described by Adechy & Issa (2004). Their model was a comprehensive one including both droplet entrainment and deposition and wave transport. However, the model of Adechy & Issa contains a number of fairly arbitrary closure models and this means it should be used with caution. Furthermore, the *k*-*ε* model is used to describe the turbulent field and this may not be adequate in view of the variable surface roughness around the pipe (see Section 2.5.3 below).

As was mentioned above, droplets may be emitted from the film surfaces with significant radial velocity and it is obviously of interest to consider whether results obtained from horizontal annular flow could be explained entirely in terms of the emission, ballistics and deposition of such droplets. A treatment of the problems in these terms was presented by Wilkes et al. (1980) (with a more complete description of the model being given by James et al., 1987). Droplets are considered to be emitted from a continuous distribution of line sources around the tube periphery (see Figure 2.55). The droplets are emitted with a consistent distribution of angles in the axial and radial directions and the entrainment rate at any location is calculated from an approximation by Fisher & Pearce (1978) to the correlation of the Whalley & Hutchinson (1973) as follows:

$$R_A(\theta) = \frac{52.2\tau_i^2(\theta)\delta^2(\theta)}{\sigma^2} \tag{2.63}$$

where $\tau_i(\theta)$ is the interfacial shear stress at location θ. $\tau_i(\theta)$ was calculated from the expression:

$$\tau_i(\theta) = \tau_0\left[1 + \frac{90\delta(\theta)}{R}\right] \qquad \text{for } \delta(\theta) \leq 280\ \mu m$$

$$\tau_i(\theta) = 2.6\tau_0 \qquad \text{for } \delta(\theta) > 280\ \mu m \tag{2.64}$$

where τ_0 is the wall shear stress for the gas phase flowing alone in the channel (calculated from conventional single phase flow friction factor relationships).

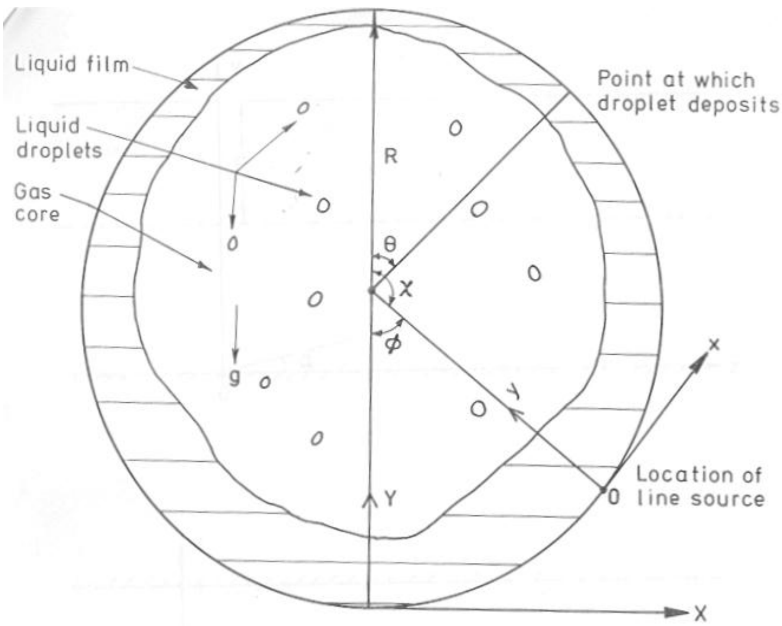

Figure 2.55. Basis of drop ballistics model (Wilkes et al., 1980).

The equations for droplet transport, deposition and film drainage were solved and this led to good predictions of the distribution of film thickness around the periphery as exemplified by that shown in Figure 2.56.

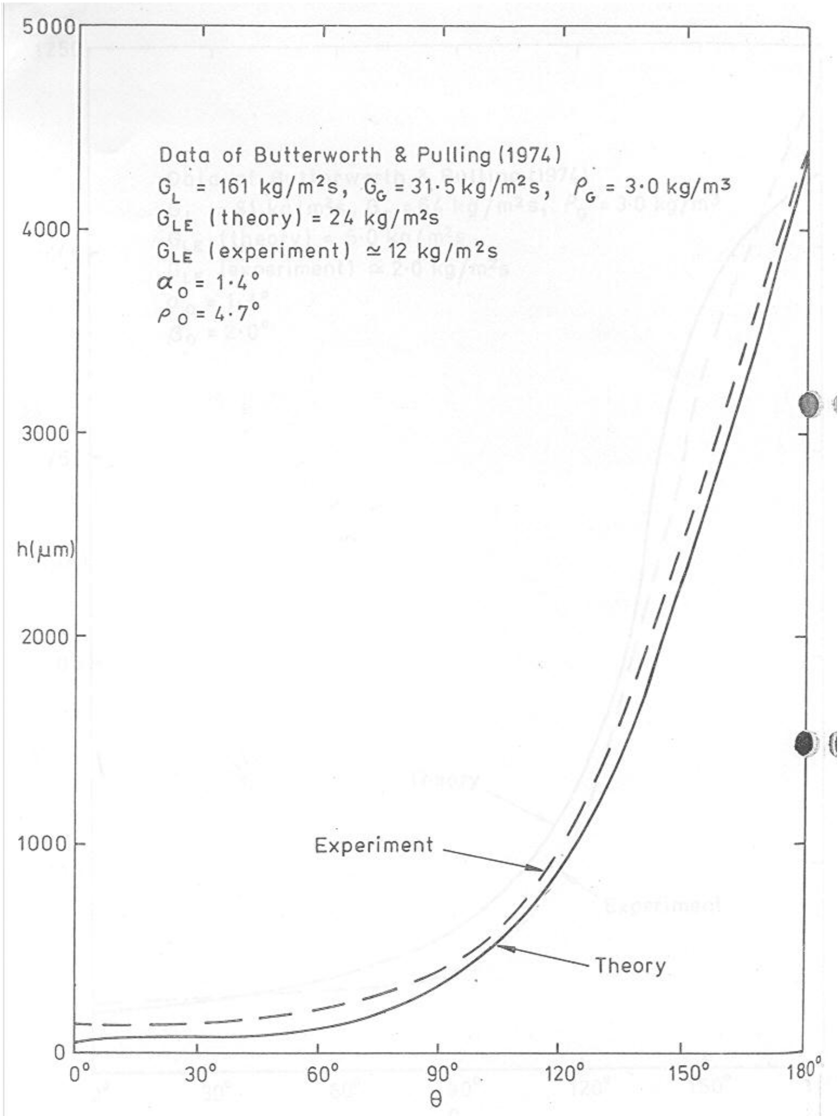

Figure 2.56. Comparison of film thickness distribution predicted by the droplet ballistics model with measurements (Wilkes et al., 1980).

Badie (2000) also developed a droplet ballistics model. In contrast to the work of Wilkes et al. (1980), he did not take account of the effect of gravity, considering that the droplets continue in a straight trajectory within the confines of the 78 mm diameter channel he used. Also, Badie did not attempt to calculate the entrainment rate; rather, he used the measured droplet fluxes at the centreline to give an indication of the number of droplets which were being transmitted through to the upper surfaces of the tube. This approach gives rather good predictions of the pressure gradient as shown in Figures 2.9 and 2.10.

Most models for droplet transport and deposition assumed relatively low concentration of droplets. However, at higher concentration of droplets two effects can occur:

(1) The turbulence in the gas phase can be suppressed as a result of the presence of the droplets leading to lower droplet transport rates.

(2) The emission of the droplets into a fast-moving droplet stream can give rise to droplet-droplet collisions which may inhibit the deposition. The net result is that, except at low concentrations, the deposition coefficient k_D decreases with increasing concentration. This effect was noticed in an early analysis of steam-water data by Bennett et al. (1967) as illustrated in Figure 2.57. It was initially thought that the effect is due to the low surface tension in the high pressure water data being examined but later study showed that this effect occurred also in air-water systems and this led to a correlation for deposition coefficient in the following form (see Hewitt & Govan, 1990):

$$k_D\sqrt{\frac{\rho_G d_t}{\sigma}} = 0.18 \qquad \text{for } C/\rho_G < 0.3 \tag{2.65}$$

$$k_D\sqrt{\frac{\rho_G d_t}{\sigma}} = 0.83(C/\rho_G)^{-0.65} \tag{2.66}$$

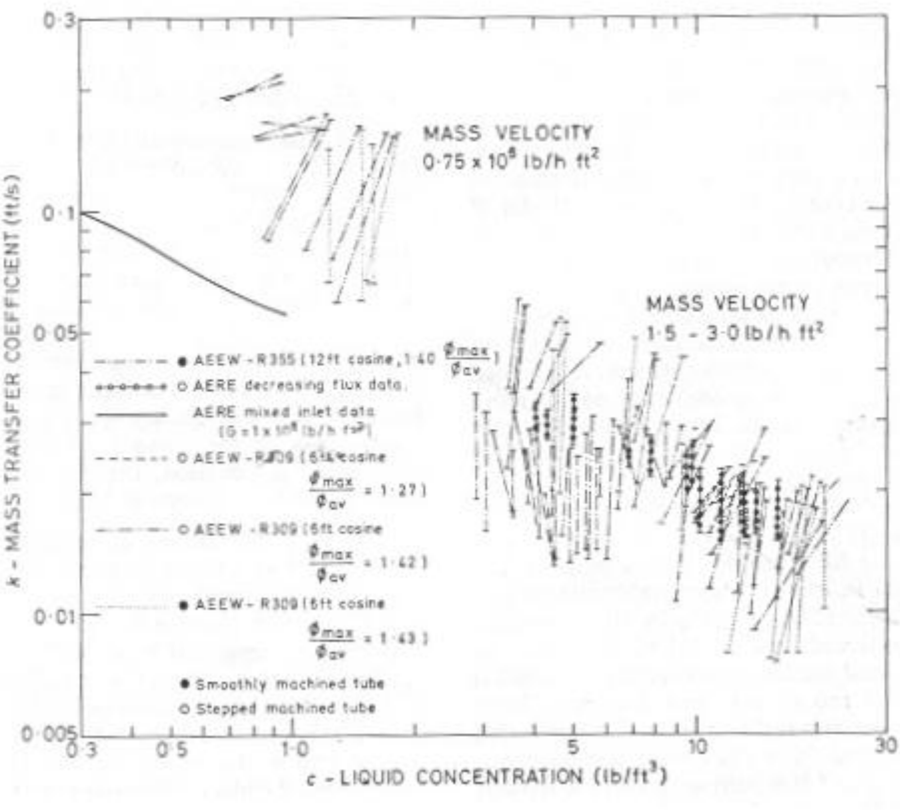

Figure 2.57. Effect of droplet concentration on droplet deposition coefficient (Bennett et al., 1967).

This correlation was compared with data in Figure 2.58. Only when the effect of droplet concentration was recognized did a reasonably successful correlation for entrainment rate emerge as follows:

$$\frac{R_A}{\dot{m}_G} = 5.75 \times 10^{-5} \left[(\dot{m}_{LF} - \dot{m}_{LFC})^2 \frac{d_t \rho_L}{\sigma \rho_G} \right]^{0.316} \tag{2.67}$$

where $\dot{m}_G$ is the gas mass flux, $\dot{m}_{LF}$ the liquid film flow rate and $\dot{m}_{LFC}$ is the flow rate required for the onset of entrainment which was estimated from:

$$\frac{\dot{m}_{LFC} d_t}{\mu_L} = exp\left(5.804 + 0.4249 \frac{\mu_G}{\rho_L} \sqrt{\frac{\rho_L}{\rho_G}}\right) \tag{2.68}$$

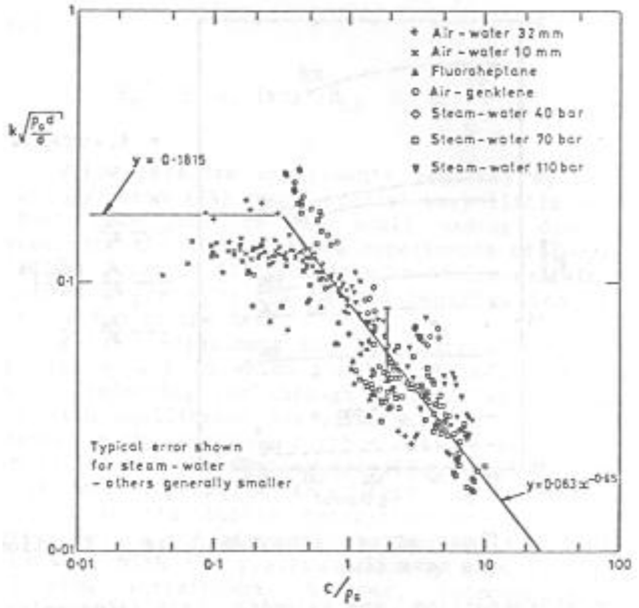

Figure 2.58. Correlation for droplet deposition coefficient (Hewitt & Govan, 1990).

Equation (2.66) is compared with the data for entrainment rate in Figure 2.59. Again, the scatter compared to the data is very large (reflecting the fact that the processes occurring are very complex) but Equations (2.65), (2.66) and (2.67) have proved very useful in calculations of entrainment and depositions in situations ranging from industrial evaporators and condensers to nuclear reactors.

The suppression of the deposition illustrated in Figure 2.58 may be connected to an observation made of pressure gradient in annular flow at very high mass fluxes. The pressure gradient may pass through a maximum as gas mass flux increases for a given liquid mass flux as illustrated in Figure 2.60. Owen & Hewitt (1987) attributed this effect to the suppression of the turbulence at high liquid mass fluxes in the gas core, as was evidenced also by a reduction in the von Karman constant from its classical value around 0.4 to values as low as around 0.15 as the concentration of the droplets increased. This concept of the suppression of turbulence is consistent with the behaviour of the deposition coefficient.

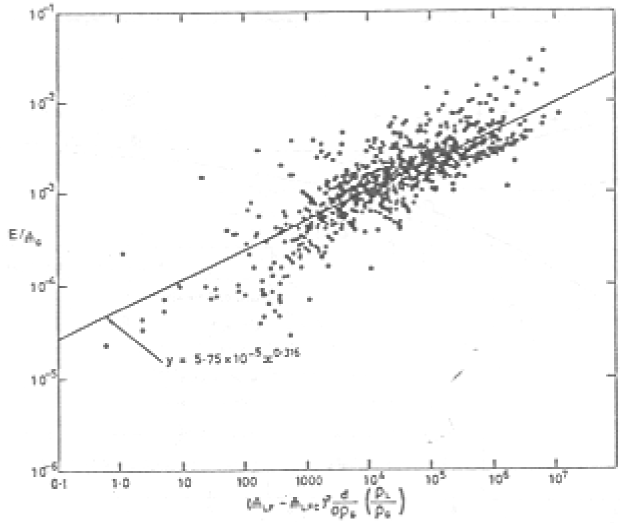

Figure 2.59. Correlation for entrainment rate (Hewitt & Govan, 1990).

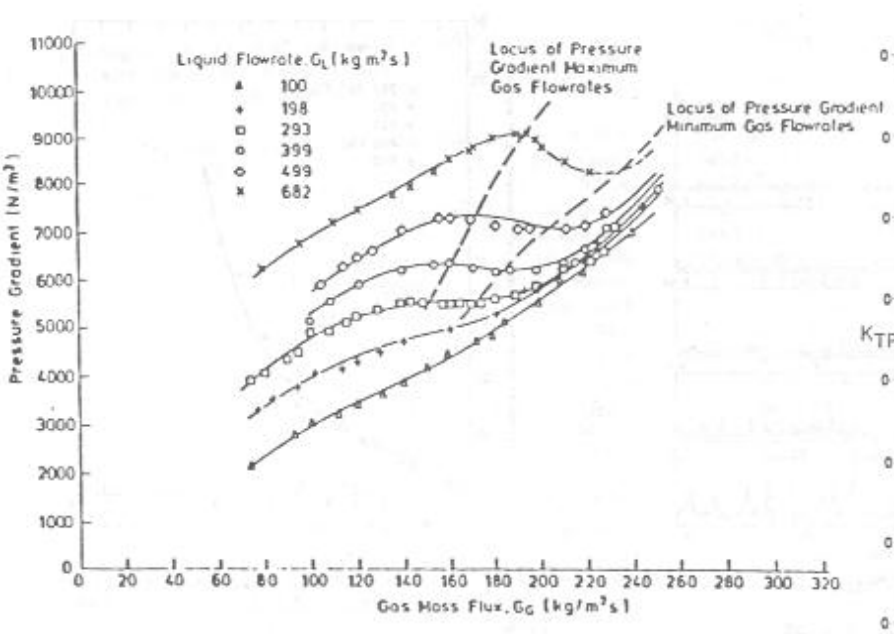

Figure 2.60. Pressure gradient for a fully developed air-water annular two-phase flow at high mass fluxes (Owen & Hewitt, 1987).

A study on effect of feedback and inter-particle collisions on deposition in gas-liquid annular flow is reported by Mito & Hanratty (2006). They used direct numerical simulation to show that significant attenuation of the fluid turbulence occurred.

Skartlien (2009) presented a CFD model for droplet transport in turbulent gas-liquid flow. The droplet concentration profiles were estimated using a simplified ‘‘first order model” in which a diameter-averaged eddy diffusivity from the full turbulence model was employed and the variation of the turbulence over the cross section was neglected. In this model, the droplet concentration in the upper half of the flow volume was dominated by the smaller droplets which are subject to a diffusivity that is close to the eddy diffusivity. The concentration near the large scale gas/fluid interface was dominated by the larger droplets.

Skartlien (2009) suggests that varying diffusivity and turbophoresis may lead to an accumulation of the droplets near the gas core region of the flow (where the turbulent kinetic energy of the gas reaches a minimum). In the low velocity cases, the measured droplet concentration was increasing towards the upper pipe wall. It was demonstrated that when a compressible double-vortex secondary flow was included in the model, a good agreement was obtained to the data by van’t Westende et al. (2007) showing that the smaller droplets are influenced by a secondary flow, leading to an increased droplet density near the upper pipe wall.

Droplet entrainment and deposition have a strong influence on the droplet size and the liquid film formation. Dorao et al. (2009) presented a macroscopic description of droplet-film interaction for the gas-liquid annular flows. This model was based on a statistical approach resembling the population balance equation. The droplet phase and the film were described by two different density functions. The modelling framework was solved by using a least squares spectral method in which a detailed description of the evolution of the droplet size distribution is allowed. However, the application of this concept to real cases would demand further research.

Of course, droplet transport in stratifying annular flows can occur by a combination of droplet movement under the influence of the initial velocity of release from the lower stratified region (the “pool”) and droplet diffusion in the gas core turbulent field. It would be expected that larger droplets (*“ballistic droplets”*) would demonstrate the first type of behaviour and smaller droplets (*“diffusional droplets”*) the second. In a joint project for ConocoPhillips, Cranfield University and Imperial College London have been pursuing predictions of droplet transport in pipelines which is based on this “two-group” concept. A non-proprietary description of some of this work is given by Brown et al (2009) and this paper represents a starting point for some of the work in this thesis (as described in Chapter

6). Basically, the Brown et al (2009) paper describes two approaches to the solution of the problem:

1. An *analytical* approach in which solutions are obtained and applied to the cases of larger droplets (the *ballistic* droplets) which move under the influence of their initial velocity (at the time of entrainment) and gravity, and smaller droplets (the *diffusional* droplets) which diffuse as a result of interactions with the turbulent field.

2. A *Computational Fluid Dynamics (CFD)* approach in which the motion of all sizes of droplets in the turbulent gas core are tracked using a Lagrangian tracking method within the calculated gas core turbulent field. The turbulent core field was calculated using the FLUENT code. Here, the larger droplets have a lasting memory of their initial conditions of release whereas the smaller droplets do not. However, it is not necessary to make a formal difference between ballistic and diffusional droplets - the spectrum of behaviour is continuous.

3. It was concluded that deposition of droplets at the top of large (typically 38 inch) pipes was governed by the transport of diffusional droplets. In the present work, a CFD approach analogous to that used by Brown et al (2009) was followed (though CFX rather than FLUENT was employed). However, the target case was predictions for a 78 mm tube where the ballistic (large droplet) mechanism is dominant.

2.5.3. Secondary Flow

The idea that secondary flow in the gas phase and the resultant circumferential shear stresses, might be responsible for upwards transport of droplet in horizontal annular flow arose from earlier experiments such as those of Darling & McManus (1969) who investigated single-phase flows in a channel with variable roughness around the periphery. Secondary flows of the type suggested were confirmed to exist and more recent experiments by Flores et al. (1995) on actual annular flows (where rotating vanes were used to detect the secondary flows) seemed to confirm this. The observations of Darling and McManus (1969) led Laurinat et al. (1985) to include such secondary flows in their model for film distribution in horizontal annular flow described above. The shear stress (τ_{yx}) induced by secondary flow was modelled using Equation (2.54) and inclusion of this term gives better predictions of the film thickness distribution. This was confirmed in calculations by Lin et al. (1985) who showed the prediction of the film thickness was greatly improved by including this effect (see Figure 2.22).

Using the Reynolds Stress model for turbulence in the gas core, it is possible to take account of the effect of variable roughness. Jayanti et al. (1989, 1990a) carried out such calculations for a typical case and, indeed, showed the existence of secondary flows as indicated in Figure 2.61. Secondary flows result in a lowering of the position of the maximum axial velocity.

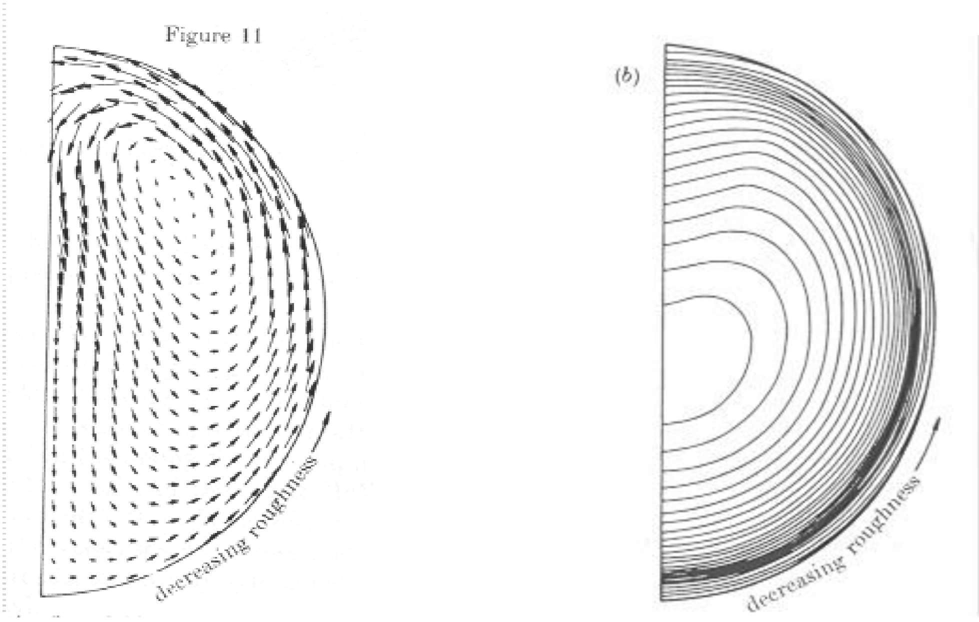

(a) (b)

Figure 2.61. Cross-sectional secondary flow (a) and axial velocity distribution (b) in a pipe with wall roughness simulating that of an annular flow (Jayanti et al., 1989, 1990).

Circumferential shear stresses calculated from the results shown in Figure 2.61 were found to be an order of magnitude less than required to support the liquid film observed in the experiments of Jayanti et al. (1989). Thus, it seems unlikely that secondary flows were important in these cases and the temptation is to reject this mechanism as being insignificant. Further evidence supporting that conclusion is provided by the photochromic dye trace experiments of Sutharshan et al. (1995); no part of the base film moves up in the absence of disturbance waves which implies the influence of secondary flow on film thickness distribution is not significant.

The above conclusions apply only to the relevance of secondary flow in transporting the liquid film around the pipe circumference. However, the existence of these secondary currents in the gas core could lead to the transport of small droplets to the upper part of the pipe where they might deposit to form a liquid film. Thus, the secondary flows could be an important factor in the upwards transport of the liquid for larger diameter pipes where other mechanisms become less significant.

The calculations such as leading to the results shown in Figure 2.61 are based on the assumption that the effective roughness (related to the interfacial roughness of the film) varies around the circumference but is *constant in the axial direction*. However, the real flow is much more complex. A major factor in creating the effective interfacial roughness is the existence of disturbance waves (see section 2.5.1). In between the disturbance waves, the film is relatively smooth. Jayanti & Hewitt (1996) have investigated the effect of having non-uniform roughness manifested by the existence of disturbance waves with a relatively smooth (base) film between them. The two systems investigated are illustrated in Figure 2.62. In the first case, an effective roughness distribution of the type investigated by Jayanti et al. (1990) is introduced at a certain position along the channel. Downstream of the start of the roughness (representing the circumferentially-non-uniform roughness characteristics of interfacial waves) the cross-sectional flow develops as shown in Figure 2.63. Ultimately, it becomes similar to the prediction shown in Figure 2.61. For the single disturbance wave, the cross-sectional flow begins to develop towards the secondary flow pattern but this becomes weaker downstream of the wave as shown in Figure 2.64 and, ultimately, disappears. It should be recalled that the interfacial roughness (probably dominated by disturbance waves) is calculated on the average basis which was used for the calculations shown in Figure 2.61. The same roughness distribution was used for the disturbance waves shown in Figure 2.62. However, since it is likely that the roughness in the wave will be much greater than the average value, the effect of the wave on the flow would be even greater. As will be seen in Figure 2.64, there is, over the wave, a rapid development of velocity vectors in the upwards direction and this could give transient transport of the droplets in the core. This effect needs to be more thoroughly investigated.

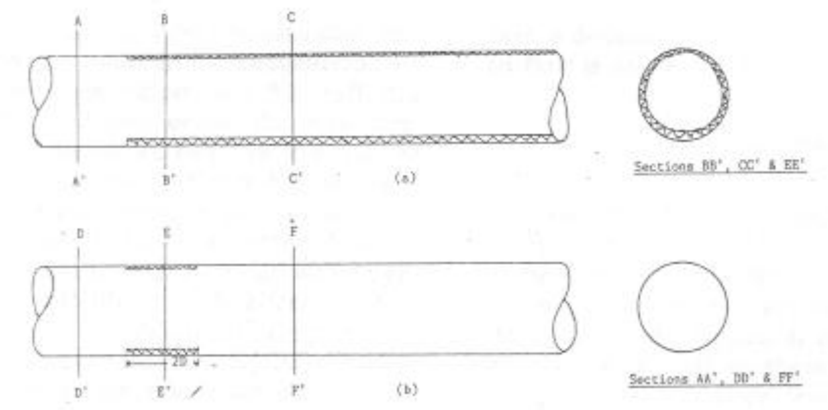

Figure 2.62. Cases investigated by Jayanti and Hewitt (1996).

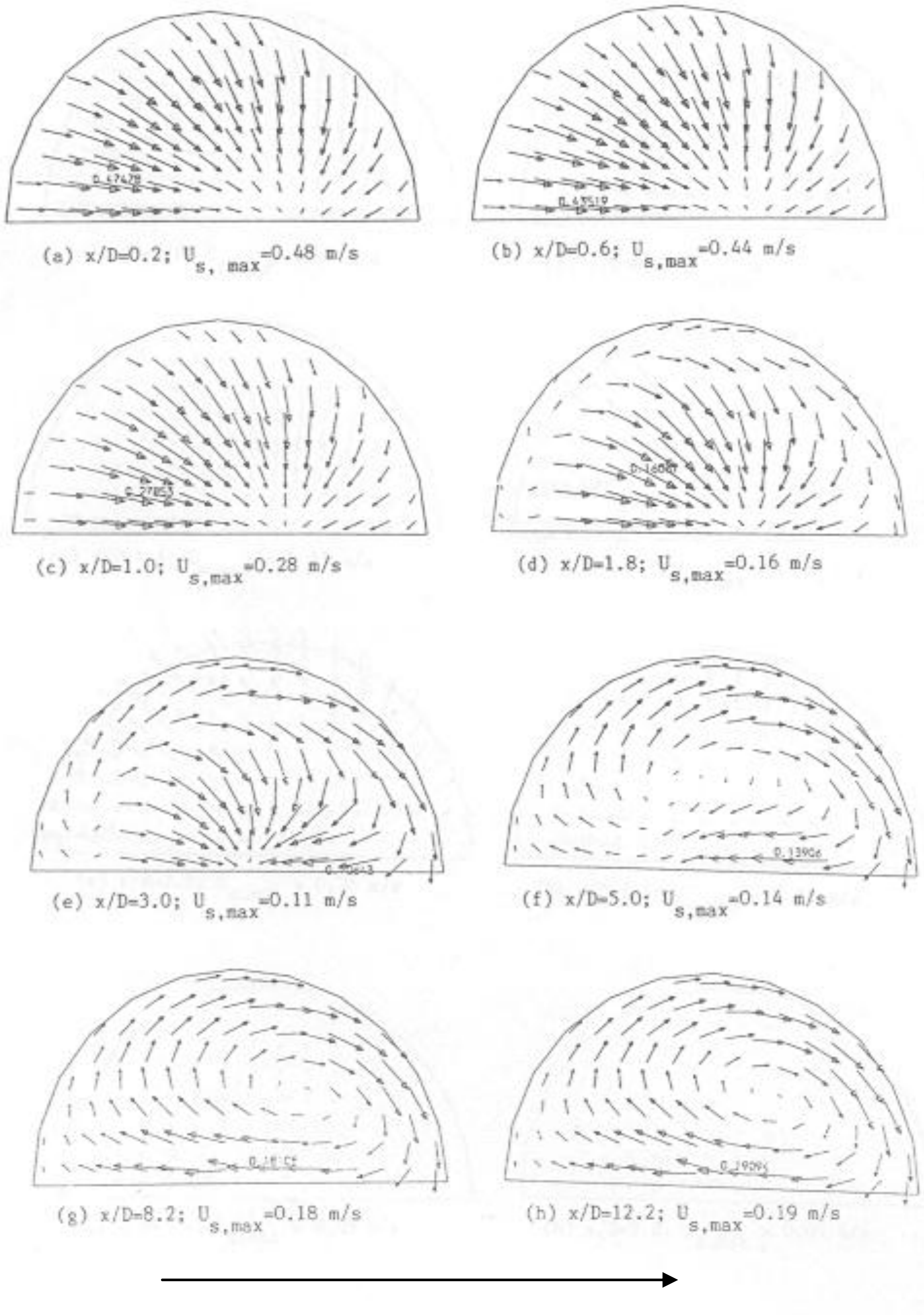

Vertical upwards direction

Figure 2.63. Development of secondary flow following a disturbance region (Jayanti & Hewitt, 1996).

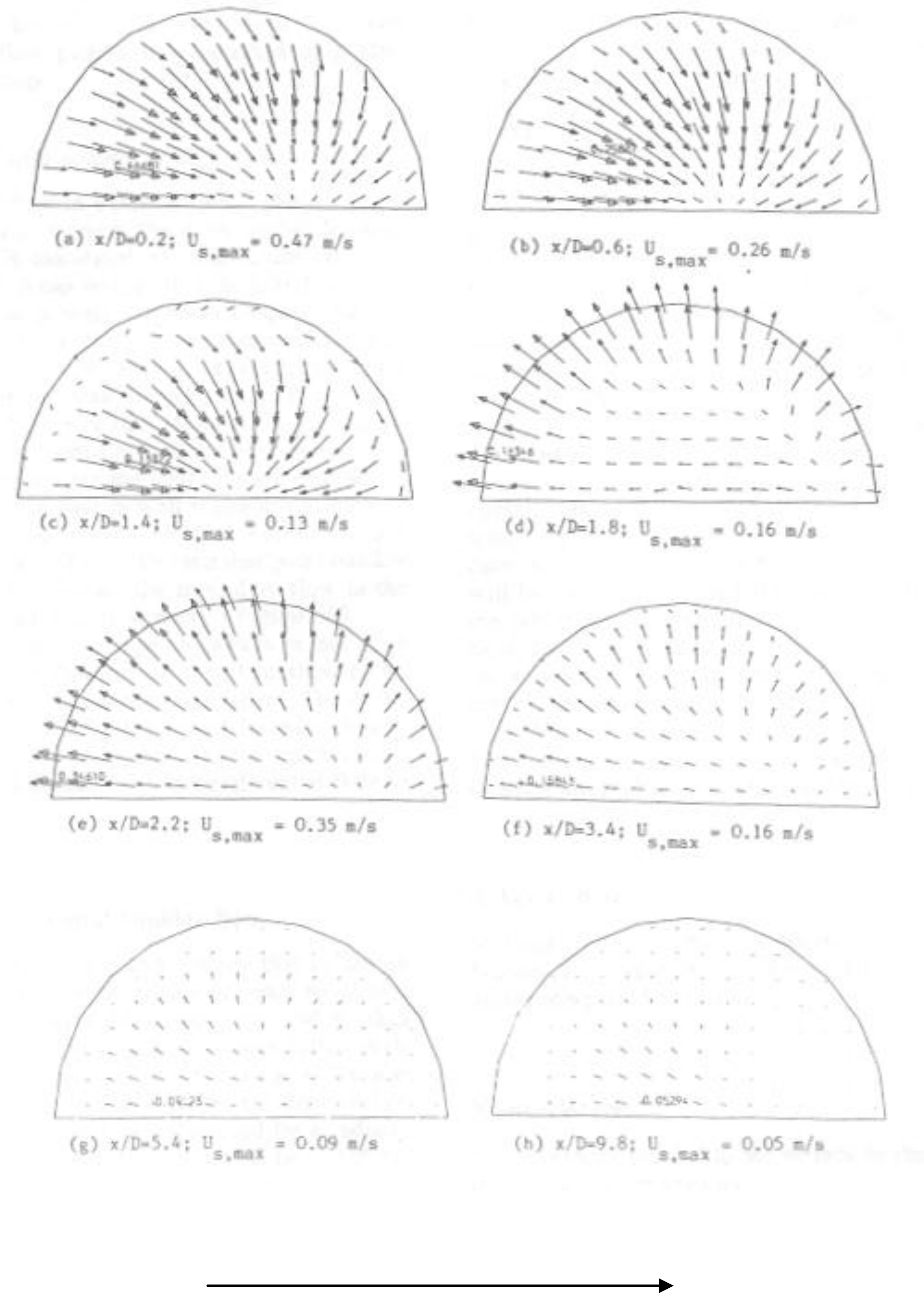

Vertical upwards direction

Figure 2.64. Development of cross-sectional velocity vectors following a short region of disturbance-wave-like roughness (Jayanti & Hewitt, 1996).

Westende et al (2007) studied the effect of secondary flow on the droplets, using a Large Eddy Simulation (LES) turbulence model. A horizontal annular air-water flow in a 5cm diameter pipe with a superficial air velocity equal to 20 $m.s^{-1}$ was simulated. The liquid film was modelled as a cylindrical wall with a varying wall roughness, the bottom wall being rough and the top wall being smooth. The Schumann wall function was used in this purpose. The secondary flow pattern agrees well with the measurements from Darling and McManus (1968) in this case.

The dispersed phase was simulated using solid spheres driven by drag and gravity. Several cases were investigated: a varying wall-roughness, a uniform roughness and a smooth wall. It was concluded that the distribution of the droplet concentration in the gas core and their deposition on the wall were increased by the presence of the secondary flow. The major global effect was the entrainment of the particles from the wall region into the gas core of the pipe, in particular, to the top part of the pipe thus bringing the stratified flow to the annular configuration. The increase in the deposition rate of the particles is a consequence of the increase in concentration of particles in the gas core. The deposition rate tends to become more uniform along the circumference of the wall under the effect of the secondary flow, the deposition at the bottom and at the top approaching the same order of magnitude.

2.6. Conclusions

The following main conclusions are drawn from this appraisal:

(1) For tubes of small to moderate diameter, the dominant mechanism leading to stratifying annular flow is likely to be wave transport.

(2) For somewhat larger tubes, the dominant mechanism is likely to be direct impaction (droplet ballistics) but gravity is likely to inhibit this mechanism for tubes greater than around 0.1 m in diameter.

(3) For larger tubes, droplet diffusion to the upper surface is likely to be the controlling mechanism, though the rates become very small for very large tubes because of the influence of gravity. In this situation, secondary flows may play a very important role in carrying small droplets to the top of the tube.

(4) If a droplet spectrum including small sizes generated at the bottom of the tube, then it seems likely that small droplets will penetrate to the top of the tube, though the rate of deposition may be low. In this case, wetting of the top of the tube may be limited by the *minimum wetting rate*.

(5) The best approach to the problem appears to be taking account of all the relevant mechanisms and, despite their limitations, commercial CFD codes would appear to be promising platform for calculation. Such a generic approach was pursued in the work described by Brown et al (2009) and was also pursued in the work described in this thesis.

CHAPTER 3

Literature review on axial view technique

High speed cine and video photography have played a crucial role in the development of our understanding of two-phase flows. A particularly useful variant of these methods is *axial view photography* in which an illuminated cross section of the flow is viewed in the axial direction. Axial viewing techniques have been widely used to visualise two-phase flow systems and form an important part of the present work. In this Chapter, a review of earlier work on the development and application of the axial view technique is presented. The aim is to provide a background to its application in the present work, as described in Chapter 5. This review describes the development of axial view systems from their origin to diverse variants of the original device such as the parallel light technique, the in-line axial viewer used on the Imperial College high pressure multiphase flow rig (WASP) and the high-temperature axial viewing system used in reflood experiments. With these techniques it has been possible to visualise in detail the various flows and to identify previously unknown mechanisms. This technique shows great continuing potential in elucidating two-phase flow phenomena.

3.1. Introduction

For many years, there has been a considerable controversy about many of the physical mechanisms of flow behaviour occurring in annular flows and related flows including the dryout phenomenon, film inversion in coiled tubes (Hewitt and Jayanti, 1992), flooding in counter-current annular flow (McQuillan et al. 1985, Govan et al. 1991) and the mechanism of droplet transport for horizontal annular flow (Badie, 2000). In order to throw some light on the responsible mechanisms of these phenomena, there has been a crucial need to design a technique capable of observing them. The axial viewing technique has been developed with this need in mind and has enabled the improvement of the understanding of these phenomena.

In the axial view technique, an optical system is used which allows direct visualisation of the flow along the axis of the pipe. This has the advantage, for instance in the case of stratifying and stratifying/annular flows, of allowing one to study the circumferential distribution of liquid films, entrainment of droplets from liquid films, the radial motion of droplets in a gas core and finally the subsequent deposition of these droplets. Quantitative analysis of the photographs allows the determination of the local radial velocity of the entrained phase (Badie, 2001). This technique has been successfully applied for vertical flow (Arnold and Hewitt 1967, Hewitt and Roberts 1969, Suzuki and Ueda 1977, Whalley et al. 1977, Whalley et al. 1979) and for horizontal flows (Fisher and Yu 1975, Fisher et al. 1978, Mayinger 1981, McQuillan et al. 1985, Shibata et al. 1999 and Badie 2000). The literature relevant to axial viewing techniques is summarised in Appendix 1. The main types of axial-view optical techniques can be classified as conventional axial view photography, optical systems using a parallel-light technique, in-line axial view systems and high-temperature axial viewing systems. A number of important features that will contribute to the design of future experiments are highlighted in this Chapter.

The general principle of conventional axial viewing techniques is described in Section 3.2, as are the main modifications introduced to this technique to allow the study of the interface, the motion of droplets as well as the variation of film thickness around the circumference of the pipe in annular flow. Descriptions of the parallel light technique or laser shadowgraph method, the in-line axial viewing system and the high-temperature axial viewing system are presented in Section 3.3; these latter techniques have been applied in visualising not only annular flow but also to studies of flooding in counter-current flow and to the reflooding of hot tubes.

3.2. Development of conventional axial viewing techniques

3.2.1. Early development

The axial viewing technique was first developed for vertical annular flow at the UK Atomic Energy Research Establishment, Harwell. A schematic of the original device (Arnold and Hewitt, 1967) used to study annular two-phase flows is shown in Figure 3.1. The viewer was fitted on top of an acrylic resin tube with an internal diameter of 1 ¼ inch (32 mm). The air was introduced at the bottom of the tube and a porous wall section was used to inject water around the periphery so as to establish an air-water flow. The window of the viewing tube was kept free of liquid by passing an air purge over the window and down the viewing tube. A short section of the tube was illuminated and the plane of illumination was viewed through the window of the viewing tube. The illuminated region of the pipe was recorded using a high speed cine-camera at frame rates of 2000-4000 per second. Still photographs and films of the axial view of the flow down the inside of the tube were obtained. The fluids flowing through the pipe issuing from the top of the column were diverted into an exit chamber and returned to the separation tank via return pipes.

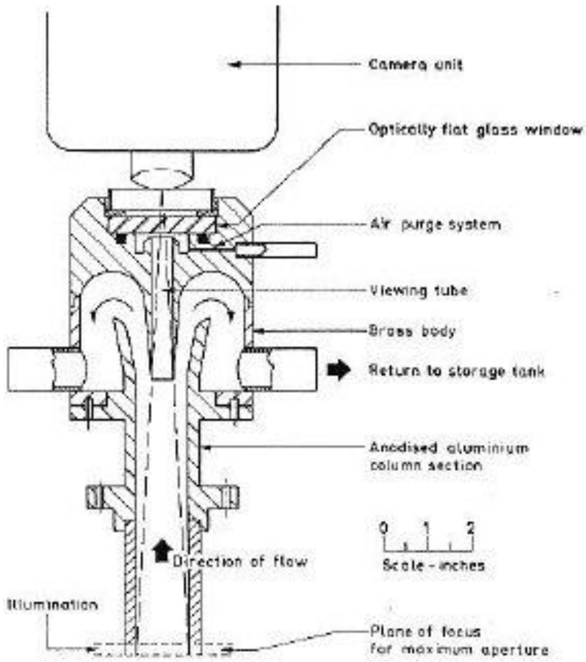

Figure 3.1. Axial viewer used by Arnold and Hewitt (1967).

The main design features of this device were to minimize the upstream disturbance of the flow during separation of the two-phase mixture issuing from the top of the column, and to keep the viewing window clear of all impinging droplets by means of a purge air system. With this technique, Arnold and Hewitt (1967) were able to observe the motion of the disturbance waves, the entrainment of droplets and the radial motion of the droplets in the gas streams. It was concluded that it was now possible to elucidate many of the unknown phenomena in annular two-phase flow using the axial view system.

The same device was utilised subsequently by Hewitt and Roberts (1969) to investigate the interface and the motion of droplets in annular two-phase flow. They were able to obtain excellent pictures using single-shot flash photography enhancing the definition of the pictures. High speed cine filming at frame rates up to 4000 per second was used to capture the details of the flow. It was possible to determine the disposition of droplets in the gas stream as well as the variation of film thickness around the circumference of the pipe. It was found that at a given flow rate, the activity of waves and the amount of droplet entrained increased with increases in liquid flow rate. At a given liquid flow rate, the quantity of droplets entrained and, the complexity and amplitude of interfacial structure were seen to decrease with increases in gas flow rate. Entrained droplets seemed to be emitted from the liquid film with a rapid motion due to their considerable initial radial velocity. A proposed mechanism for the creation of rapidly moving droplets was that the waves were undercut by the high velocity gas, forming a bubble from which filaments of liquid shattered, giving rise to droplets.

3.2.2. Main changes

Whalley et al. (1977) modified the arrangement of the viewer of the basic device to study wave phenomena in annular two-phase flows. The viewing tube previously mounted concentrically with the main flow tube was now inclined at an angle of 8° so that viewing of the surface of the liquid film was possible. The 6 mm length illuminated of the tube in the original device was increased to 100 mm that allowed droplets to be followed in a longer field and thus to obtain a better impression of the events. Still photographs and high speed cine films at 4000 frame rates per second were taken of the wavy system. In addition, a three-dimensional axial view system, a variant of the basic axial view system, was developed to observe waves and drops. The principle of this technique is illustrated in Figure 3.2. Two viewing tubes were used with viewing directions that intersected in the plane of illumination at a point close to the wall of the pipe. The three dimensional motion of the flow could be reconstructed from the stereoscopic pair of images recorded on cine-film via the two viewing tubes.

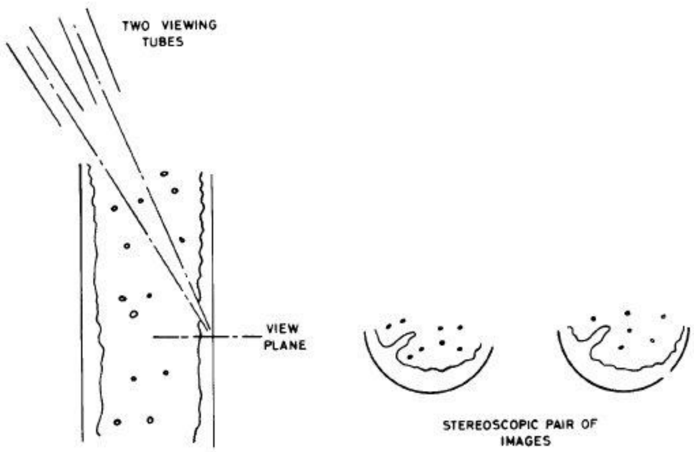

Figure 3.2. Principle of the stereoscopic axial view technique.

The viewer technique designed by Whalley et al. (1977) is shown in Figure 3.3.

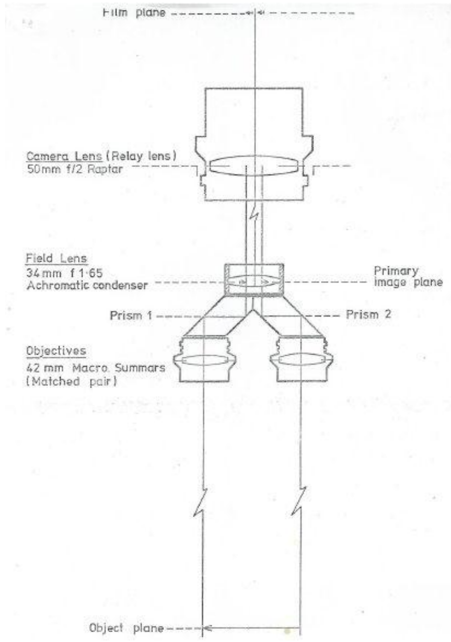

Figure 3.3. Optical system for stereo axial view photography (Whalley et al., 1977).

It was concluded that for annular flows, the role of disturbance waves in the liquid film for the formation of droplets was preponderant. Entrained droplets arose almost uniquely from disturbance waves which traversed the liquid film. At high flow rates, the number of waves and drops was too large, so it was difficult to visualise the events. At fairly modest flow rates, it was possible to distinguish a single wave and to outline the most usual mechanism of droplet formation. The study of waves was therefore easier by investigating the liquid film with only a single wave. For low liquid flow rates and at any gas flow rates, the inception of a single artificial disturbance wave occurred when the liquid flow rate was set to a critical value. To create such a wave, a pulse of liquid was injected around the periphery of the channel. This technique, described by Whalley et al. (1977), was coupled to the axial view technique and allowed one to determine the entrainment rate associated with a single wave and the source of all droplets to be seen in the viewing plane. A stereoscopic axial view photograph obtained from this coupled technique is shown in Figure 3.4.

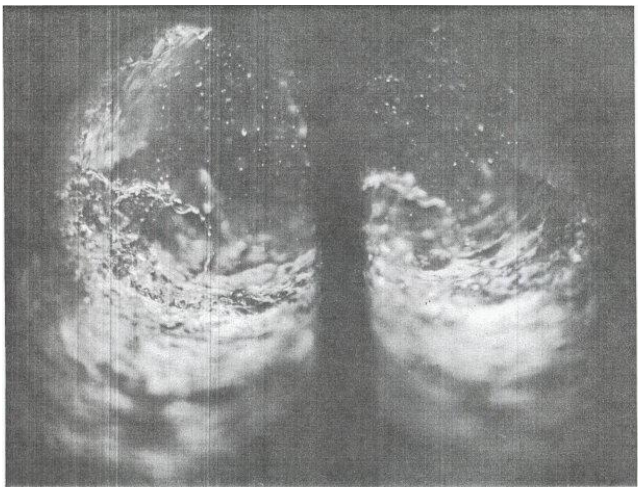

Figure 3.4. Stereo photograph of filament of liquid formed from a single injected disturbance wave (Whalley et al., 1977). Air mass flux 39 kg/m^{2}s, water mass flux 7 kg/m^{2}s, volume of water injected: 3.0 ml.

Studies of evaporating Refrigerant-12 flows in vertical tubes (Langner and Mayinger 1978 and Langner 1978) were conducted using the axial view technique and Suzuki and Ueda (1977) employed the technique with a 28.8 mm internal diameter vertical tube to study the flooding phenomena in vertical counter-current two-phase flows. The state of the wavy liquid surface during flooding was examined on the axial viewing photographs of the flow obtained using a high speed cine camera. Small amplitude ripples observed at zero gas velocity were seen to grow larger with increases in the gas flow rate. At a certain wave height, the large wave began to extend in the circumferential direction and partially broke up into liquid droplets.

Shibata et al. (1999) used axial viewing methods with a 100 mm internal diameter vertical tube to investigate the generation and behaviour of entrained droplets in counter-current flows for an air-water system. Images were recorded with the help of a high speed cine camera, and generation of droplets from the film layer and the break-up of large drops in the gas stream were identified.

3.3. Further variants of the technique

3.3.1. Parallel light technique

The limitation of the earlier development of axial view photography was the small depth of field. In a further development, Whalley et al. (1979) used a parallel light technique in their photographic studies allowing a depth of field corresponding to the full length of the tube to be obtained. The principle employed here corresponds to a shadowgraph technique: any object in a parallel light beam casts a shadow whose size is unaffected by the position of the object in the beam. This has of course the undesirable side effect that, information is lost about the axial location of the events that occur. Also, ideally, if the light beam was truly parallel, the wave nature of the light could be neglected and the object would cast a perfect in-focus shadow, but several further difficulties occur in practice, namely the fact that the light beam is never truly parallel and the fact that diffraction patterns arise from the objects in the light beam.

The new optical system for parallel light technique was created by making several modifications to the basic system shown in Figure 1 as illustrated in Figure 3.5. A He-Ne laser was used as the light source. The beam was focussed by a lens (A) onto a pinhole that was located a distance equal to the focal length from another lens (B) thus producing a parallel light beam of light. The lens (C) allowed the size of the shadow image to be diminished to fit on a 16 mm cine frame. The advantage of using a laser light was that all the energy could be focussed through the aperture, approximating to the ideal of an infinitely small source giving a true parallel beam.

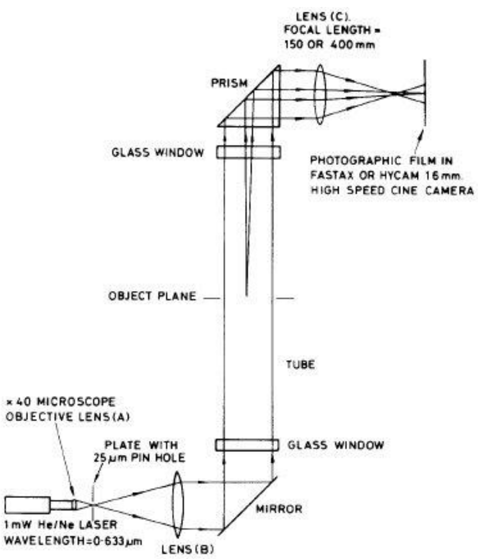

Figure 3.5. Parallel light technique-optical arrangement (Hewitt and Whalley, 1980).

In order for the parallel light technique to be employed, the original axial viewer was modified and the revised viewing section is shown in Figure 3.6. The design of both top and bottom ends of the tube was similar. The ends which contain the glass window were designed such as the liquid was diverted away from the window so as to obtain an unobstructed view of the whole tube cross section. Photographs were taken using a high speed camera at 4000 frames per second and black-and-white film.

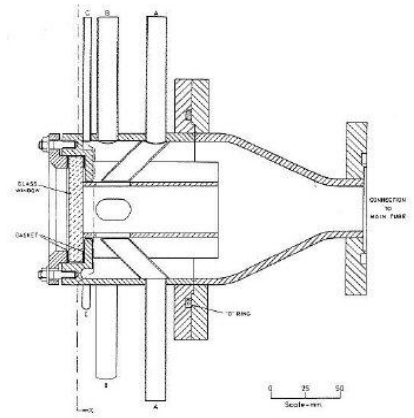

Figure 3.6. Viewer in the laser shadowgraph technique: Axial viewer used by Whalley et al. (1979).

This technique was applied to annular flow studies as well as to the flooding phenomenon in counter-current flow. For annular flow, the motion of the droplets emitted from the disturbance waves and their subsequent deposition on the liquid film downstream were studied. Drops with a diameter greater than 250 µm were mainly seen moving in a straight line subsequent to their ejection from the liquid film without being visibly affected by the gas phase eddies, except for some rare case of very slow droplets travelling with a curved trajectory. The larger droplets (i.e those with a diameter greater than 250 µm) could be not only observed but also followed frame-to-frame. The measured drop velocity was subject to large errors because of the small distance moved at the high framing rate used. It was shown that the larger droplets were entrained with significant velocity (the maximum radial velocity being around 1 m.s^{-1}) and this velocity persisted with little deceleration until the re-deposition of the drop.

A review of the optical methods developed at Harwell, including the various axial view systems, was given by Hewitt and Whalley (1980). Following the works of Whalley et al. (1979), a series of researchers have successfully applied this optical technique using parallel light (McQuillan et al., 1985; Azzopardi, 1987; Govan et al., 1989), as summarised in Appendix 1.

Observations of droplet entrainment in horizontal annular flow made with this technique were reported by Azzopardi (1987). It was found that after being created, droplets followed a continuous path to the opposite wall with little deviation from a straight line. The diameter of the droplets was relatively large, with a range of 1-5 mm. Their translation velocity was in the range of 1.2-2.1 m.s^{-1}.

Information lost about the axial location of the events occurring with the laser shadowgraph axial view method could be recovered using a parallel laser beam with a local illumination. McQuillan et al (1985) used a multiple colour side illumination technique to study flooding; successive bands of transparent plastic film of different colours were wrapped around the outside of the transparent tube, each colour indicating a range of axial location. The axial positions could be identified from the local coloration of the objects being viewed. McQuillan et al were able to demonstrate upward wave transport during the flooding process.

3.3.2. In-line Axial Viewing Systems

3.3.2.1. Axial viewer developed by Fisher and Yu

Based on the original idea reported by Hewitt and Roberts (1969), an axial viewing system was developed by Fisher and Yu (1975) in order to obtain detailed description of air-water flow patterns in horizontal flows. This system which could be placed at any point in a bank of horizontal tubes, illustrated in Figure 3.7, was fitted onto a 50 mm internal diameter experimental facility. High speed cine techniques were used to record and analyse details of the two-phase flows.

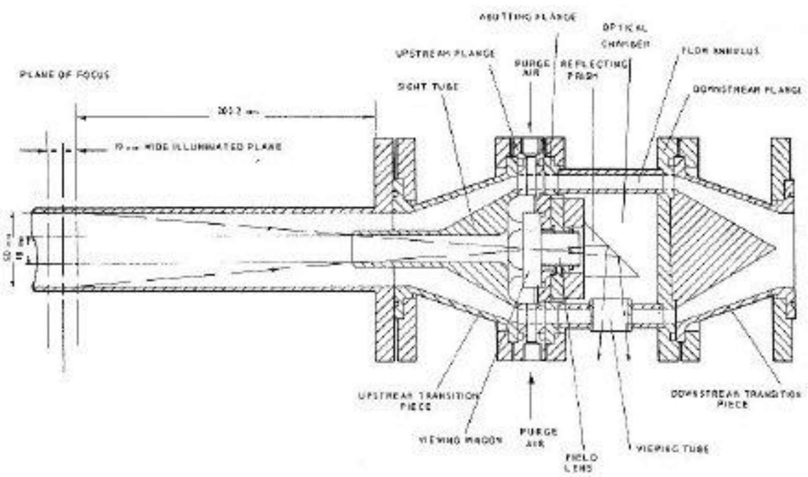

Figure 3.7. Axial viewer developed by Fisher & Yu (1975).

Coney and Fisher (1976) carried out experiments on vapour-liquid flows of Refrigerent-12 flows using the axial view technique. Continuing this work, Fisher et al. (1978) developed a new axial viewer for use with Refrigerant-12 at pressures up to 40 bar for a 32 mm internal diameter facility (see Figure 3.8). This was used in conjunction with film thickness and voidage probes to determine the boundaries between different flow patterns. High speed cine photography was used to capture images of the flow at frame rates up to 2500 per second.

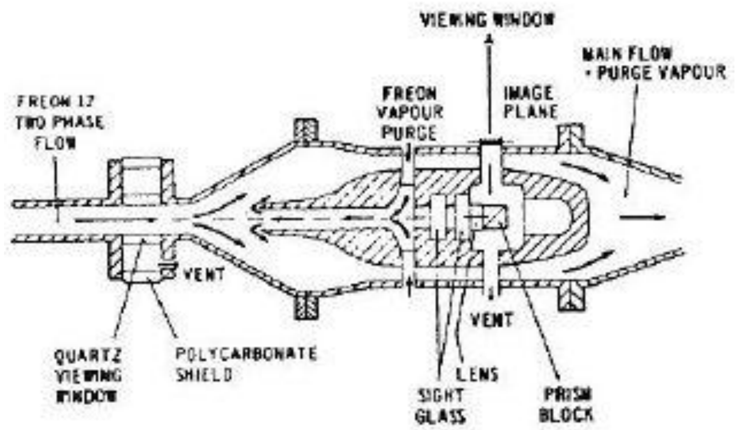

Figure 3.8. Axial viewer developed by Fisher et al. (1978).

3.3.2.2. WASP In-Line Axial Viewer

An in-line axial viewing system was developed for application on the high pressure multiphase flow WASP facility (WASP) at Imperial College London in order to investigate two-phase gas-liquid flows with low liquid loading. The axial viewer (see Figure 3.9), designed by Badie (2000), was based on the axial viewing system used by Fisher & Yu (1975) for air-water tests (see Figure 3.7). However, Fisher & Yu system was complex to machine and not very flexible, thus some alteration was needed.

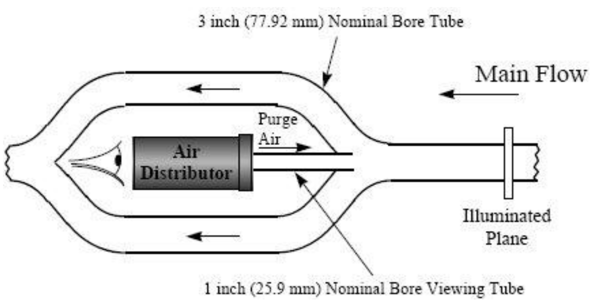

Figure 3.9. The basic design of the in-line axial viewing system (Badie, 2000).

The flow from the 3 inch (77.92 mm) nominal bore WASP test section was diverted into two three-inch tubes to leave space for the viewing and purge air systems at the junction. The 1 inch (25.4 mm) nominal bore viewing tube was welded to the main section and it protruded to about 1.5 cm into the inside of the section. The protrusion provided a platform so that any liquid on the upper wall of the main section could drain around the viewing tube, rather than into it. The air distributor was connected to the other end of the viewing tube (see Figure 3.10). The purge air flowed in a direction opposite to the direction of the flow in the main channel to maintain the window of the viewing tube free of liquid. A camera system was focussed on an illuminated plane at some distance upstream of the diverted flow. (See details in Badie, 2000).

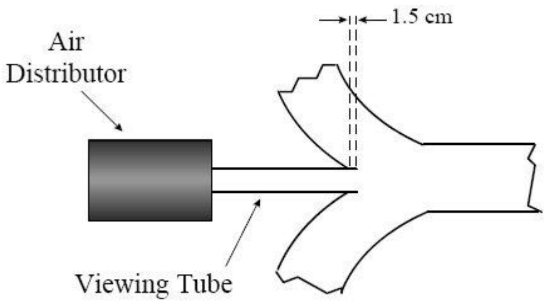

Figure 3.10. Diagram of the viewing tube. (Badie, 2000).

The main advance in design of the in-line axial view system used by Badie was a drastically improved purge air system whose role was to stop entrained drops from reaching the window on the air distributor (cf. Figure 3.11). The purge air velocity and the length of the viewing tube were chosen on the basis of the model equations governing the motion of droplets used by Fisher et al. (1978); this allowed Badie (2000) to determine stopping distances for drops travelling against purge air flow. (See details in Badie, 2000).

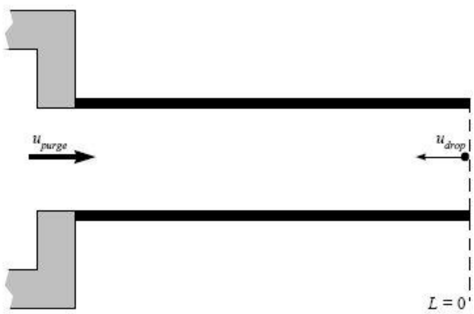

Figure 3.11. Motion of a liquid droplet in a purge stream (Badie, 2000).

A schematic diagram in Figure 3.12 shows the inside of the air distributor.

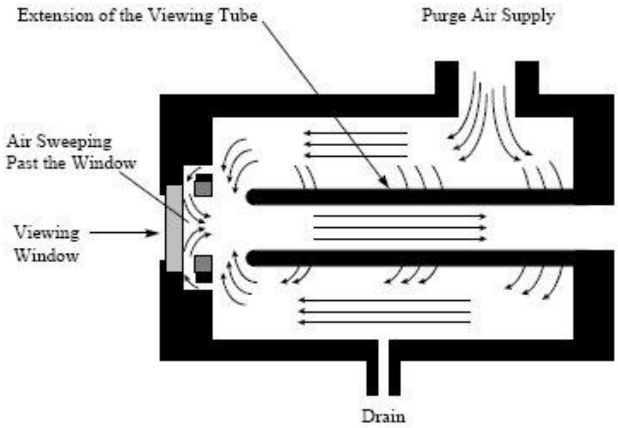

Figure 3.12. Side view of the air distributor (Badie, 2000).

Badie et al (2001) clearly identified the waves, the creation of droplets from break-up of waves or from larger droplets (secondary breakup), the radial motion of the droplets during the entrainment process and their subsequent deposition on the upper part of the film. It was possible to investigate the effects of several parameters such as the superficial gas and liquid velocities and the viscosity of the liquid phase on the amount of droplets entrained as well as on the changes in interface structure and in liquid holdup. The in-line axial view system showed the important role played by the entrained liquid. For the larger pipe diameter (78 mm) used in these experiments, it was suggested that entrained droplets were the main mechanism responsible for the transport of the liquid at the top of the pipe. A very clear observation of waves and droplets creation and entrainment was possible. Sequences of frames were extracted from the high speed video camera records for horizontal annular air-water flows and air-oil flows. A typical sequence of images for air-oil flows are shown in Figure 3.13. An increase in the liquid velocity at a given gas velocity produced an increase in the amount of entrained droplets within the gas core and in the liquid holdup.

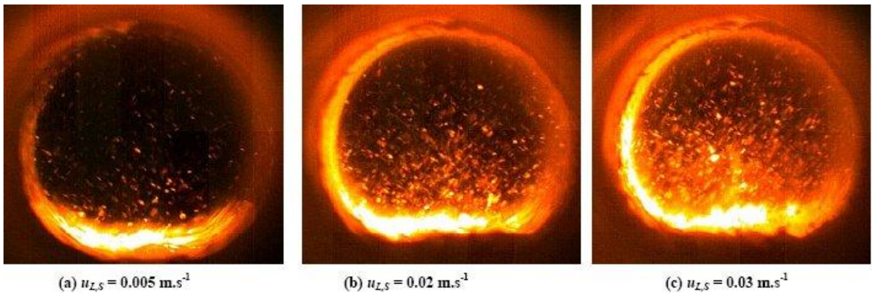

Figure 3.13. Images of air-oil flow at constant superficial gas velocity of 20 m.s^{-1}, showing the effect of superficial liquid velocity: (a) $u_{L,S}$ = 0.005 m.s^{-1}; (b) $u_{L,S}$ = 0.02 m.s^{-1}; (c) $u_{L,S}$ = 0.03 m.s^{-1} (Badie, 2001).

Comparing air-oil case and air-water cases at identical gas and liquid velocities, a much greater number of entrained droplets was found in the air-oil case. An increase in the gas velocity at a given liquid velocity produced a decrease in the liquid holdup and a decrease in the apparent concentration of entrained droplets. Moreover, the interface exhibited greater roughness as the gas velocity increased. It was possible to visualise the ballooning of a large drop (see Badie et al.,2001). Figure 3.14 shows a secondary breakup in which a large droplet took the configuration of a ring and then ruptured into smaller droplets.

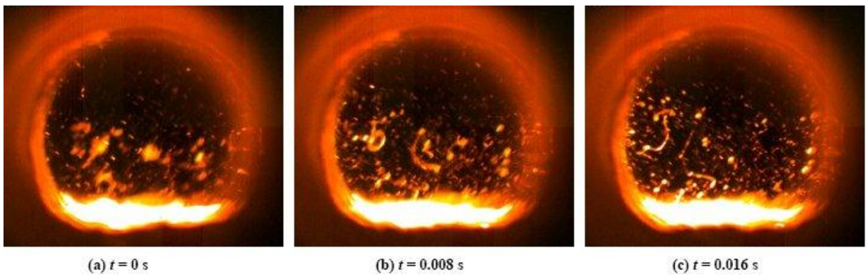

Figure 3.14. Successive frames for an air-oil flow showing secondary drop breakup (superficial gas velocity = 15 m.s^{-1}, superficial liquid velocity = 0.01 m.s^{-1}): (a) t = 0 s; (b) t = 0.008 s; (c) t = 0.016 s (Badie, 2001).

3.3.3. High-temperature axial viewing system

Rewetting of hot surfaces has applications in a number of industrial situations. An important case is that of rewetting of hot fuel elements in the reflood phase of a Loss of Coolant Accident (LOCA) in a Pressurised Water nuclear Reactor (PWR). Such rewetting can be simulated by introducing water into the bottom of a preheated tube and observing the progression of the rewetting front up the tube. Ahead of the rewetting front, water flows in the form of jets and droplets and (though direct contact between these elements of water and the hot tube wall is restricted) some cooling of the hot surface (called *precursory cooling*) occurs in this region. Work has been proceeding on the application of the axial view technique to the study the behaviour of the water phase in the region above the rewetting front and will be summarised here. Further details of this work are given by Zeng (2010) and Zeng at al (2010).

The tube used in these reflooding experiments is shown schematically in Figure 3.15. The tube is 15 mm nominal internal diameter and is made of type 316 stainless steel. In this experiment the test section is initially preheated to temperatures up to 600°C and then quenched by introducing water at the bottom of the tube at atmospheric pressure. The cooling water introduced from the bottom of the tube had a range of subcooling (at 20, 40, 60 and 80 °C respectively).

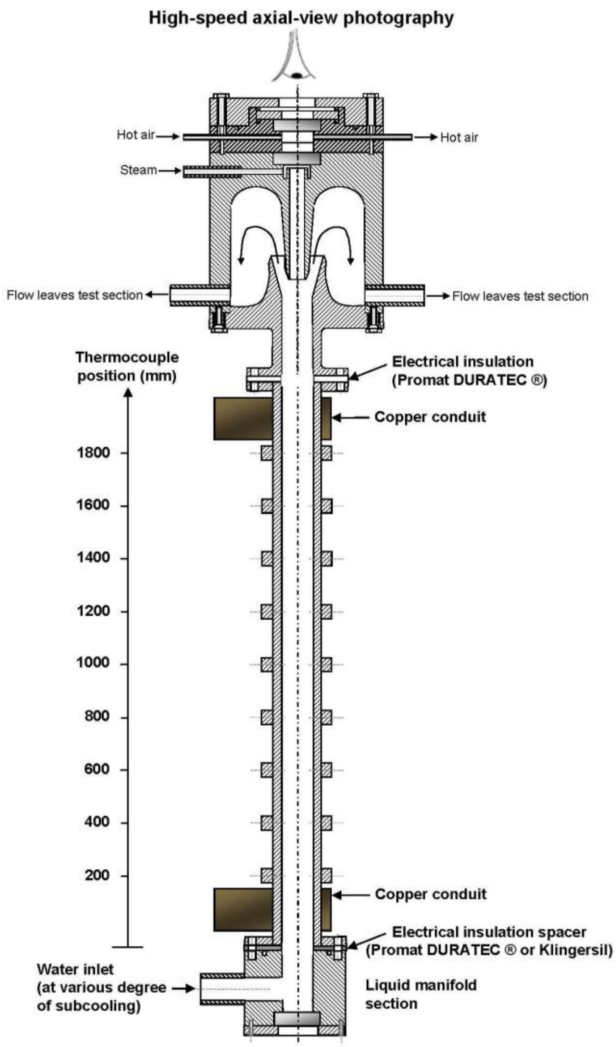

Figure 3.25. Axial-View Reflood (AVR) facility test section.

There were two main challenges in applying the axial view method to this system:

1. Introducing the light. Clearly, there are difficulties in this system in introducing a source if illumination at the side of the tube (as in the case of the conventional method - see Figure 3.1). Nor is it feasible to use the parallel beam technique (Figure 3.5). Fortunately, it was found that introducing light at the bottom of the tube and allowing it to scatter in its passage through the rewetting fluid and off the reflecting walls of the channel, produced sufficient illumination to obtain a good view of the region above the rewetting front as this region passed up the channel.

2. For the high temperatures used, the design of the axial viewer itself presented considerable challenge. The solution ultimately adopted is shown in Figure 3.16; it was

necessary to provide air cooling at the top of the unit as shown. The viewing tube and window were purged with steam.

Using the system illustrated, it has been possible to obtain much new information on the liquid behaviour in the region above the rewetting front. A typical frame from one of the video sequences is shown in Figure 3.17. This shows impingement of droplets onto the hot surface in the precursory cooling region; these droplets impinge on the surface and then rebound. Further details are given by Zeng (2010) and by Zeng et al (2010).

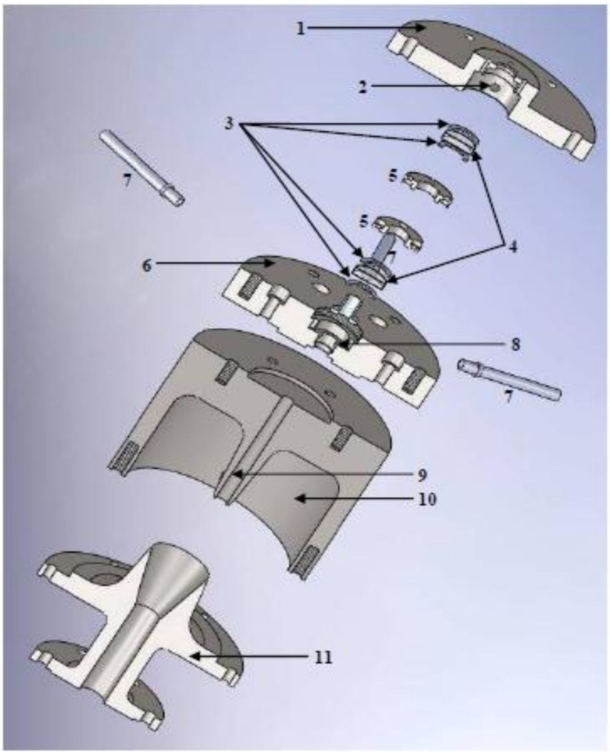

1. Secondary window section;2. Hot air inlet/outlet;3. Window gasket; 4. 18mm sapphire window;5. Window retaining ring;6. Primary window section;7. 6mm purge steam line;8. Steam inlet;9. Viewing tube;10. Axial viewer purge chamber; and 11. Flange transition section.

Figure 3.16. Axial viewing section for high temperature axial view system.

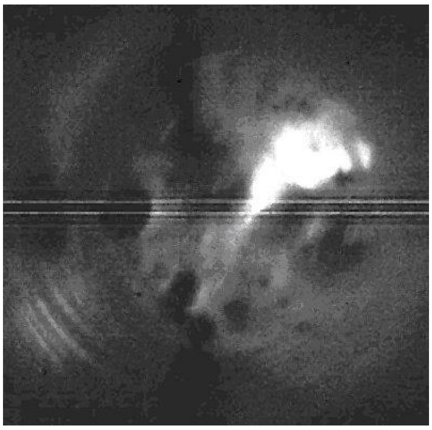

Figure 3.17. Typical frame from videos of high temperature rewetting.

3.4. Conclusions

The axial viewing technique has led to a improved interpretation of the mechanisms in two-phase annular flow allowing the resolution of controversial issues and the forming of a basis for the improved prediction. It has demonstrated its great value as a tool to investigate two-phase flow.

For the future, further developments are certainly feasible. In particular in the 3D version of the axial viewing technique, using which some studies have already been carried out, shows great development potential. Modern video cameras have the advantage of their higher frame rate and picture quality and this should allow finer details of flow behaviour in annular flow to be achieved.

A summary of the literature on axial viewing techniques is given in Appendix 1.

CHAPTER 4

Experimental facilities and methods

Three different facilities were used for the experimental investigations reported in this thesis, namely two low pressure air water facilities (LOTUS and LOWPRESS) which had test section diameters of 33 mm and 76 mm respectively and the WASP (Water Air Sand and Petroleum) high pressure facility which has a 78mm test section. In what follows, Section 4.1 introduces the work on the LOTUS facility, Section 4.2 introduces the work on the LOWPRESS facility and Section 4.3 introduces the work on the WASP facility. Each Section comprises a description of the basic facility followed by a description of the observational and parameter measurements carried out on that facility.

4.1. Work on the LOTUS facility

4.1.1. The LOTUS facility

The LOTUS (Long Tube System) facility was situated in the main pilot plant laboratory in the Department of Chemical Engineering. The main test section for this facility was an 11 m long 33 mm vertical tube but the facility also has an alternative horizontal tube test section which was also 33 mm internal diameter and was 6.3 m in length. This horizontal test section (illustrated in Figure 4.1) was constructed from flanged sections of acrylic resin tubing thus facilitating this visualisation of the flow as required in the present experiments. Unfortunately, the LOTUS facility was dismantled in 2011 due to the reconstruction of the pilot plant so the facility could not be used in the later stages of the present work.

Figure 4.1.Photograph of the horizontal pipe.

The LOTUS control panel, illustrated in Figure 4.2, was used for setting up the required flow by adjusting the air and water flow rates.

Figure 4.2. Photograph of the Lotus control.

The air used in LOTUS was derived from the Department’s main supply, available at 6.8 bar. The air was metered using a 25mm diameter orifice plate fitted to the air pipeline. The differential pressure transducer was used to measure the pressure difference across the orifice and the air flow rate is calculated from this pressure difference using the methodology specified in British Standard BS1042.

Two pumps are available to pump water through the system, one works at 1.5kW and the other is a two stage vortex pump working at 8kW. The operating ranges of the rig operating with the two pumps are shown in Figure 4.3.

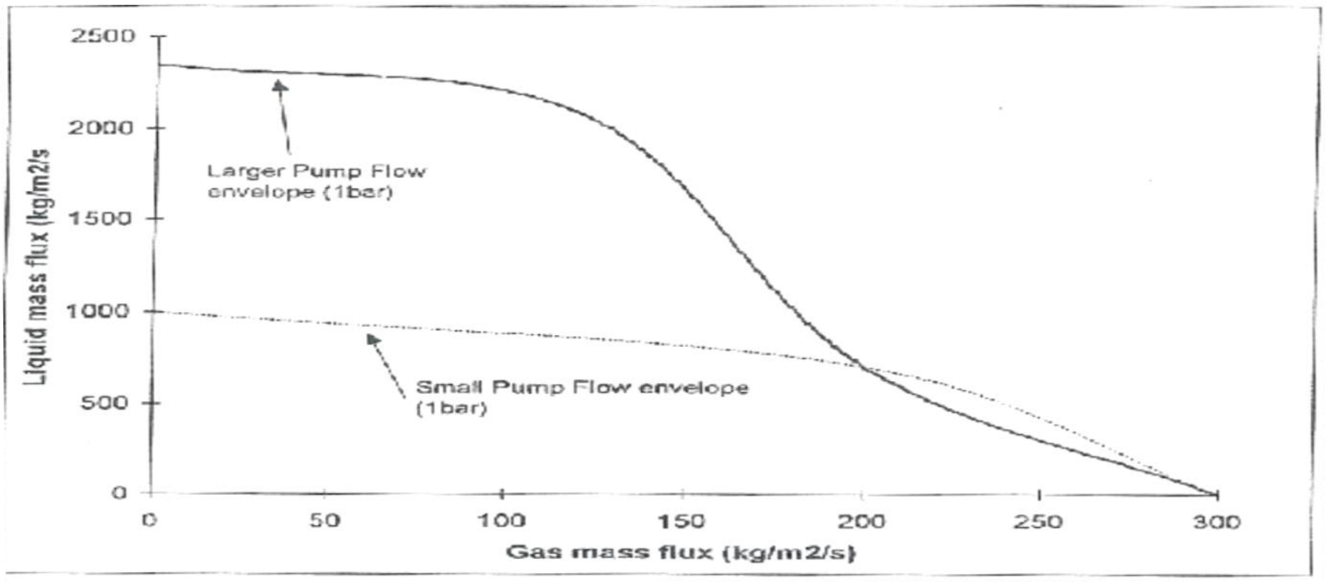

Figure 4.3. Operating range for LOTUS.

The water flow rate in LOTUS was measured by one of the 4 rotameters shown in Figure 4.4 (each rotameter operating at different flow ranges). The range of test section water mass flux for the experiments reported here was between 10 $kg.m^{-2}.s^{-1}$ and 20 $kg.m^{-2}.s^{-1}$, which can be measured by rotameter A. The height of water in the rotameter is a function of the flow rate, the relationship having previously been established by gravimetric calibrations (see Figure 4.5).

Figure 4.4. Photograph of the rotameters on LOTUS.

The calibration test correlating the rotameter reading to water flux for rotameter A is shown in Figure 4.5.

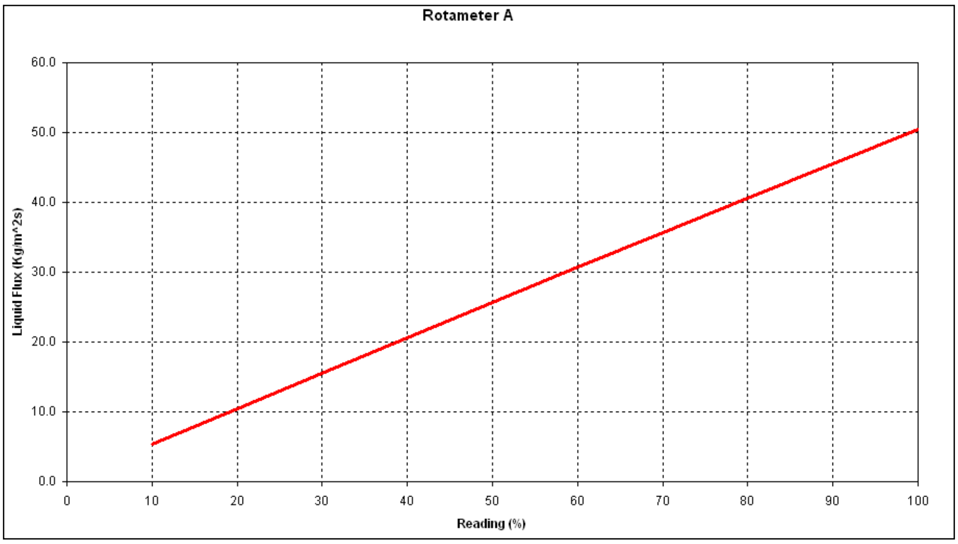

Figure 4.5. Calibration of rotameter A on LOTUS.

The present experiments were conducted at a series of fixed liquid mass fluxes. For each liquid mass flux, the gas mass flux was varied from a low value (at which stratified flow prevailed) to a high value (at which the flow was fully annular).

4.1.2. Observational and parametric studies on LOTUS

Since the horizontal section on LOTUS (Figure 4.1) was made from transparent acrylic tube, it was possible to observe (from the side of the tube) the flow pattern in the tube and, in particular, the nature of the flow in the stratifying annular regime. A large number of video recordings of the flow were made using an Olympus i-SPEED video camera. However, in the experiments on the LOTUS facility, the work was restricted to observational studies only.

4.2. Work on the LOWPRESS facility

4.2.1. The LOWPRESS facility

The LOWPRESS facility is located in Room 111 in the Department of Chemical Engineering at Imperial College. The acrylic resin test section used in the experiments which formed part of the present work was made in a 9 m long, 76 mm internal diameter horizontal pipe. The testline consists of several pipe sections joined together using tongue and groove flanges. These are machined to the exact internal diameter of the pipe to ensure geometric continuity so that disturbances to the flow are minimized.

Water is stored in the 340-litre recycle tank and it is fed into the test section using a 0.75 kW pump, which is capable of delivering a maximum flow rate of 5.7 m^3/h and the water flow is measured using a Series 2000 KDG MOBREY rotameter (range: 1.5 l/min to 16 l/min with accuracy of 0.5%).

Air is obtained from the low-pressure departmental supply (up to 7 bar g). It passes through an IMI Norgren pressure regulator and filter, enabling the upstream pressure to be fixed, before passing through a critical flow valve. This ensures a constant mass flow rate of air for a given valve setting. The air flow rate is then metered, using a D and D/2 tapping orifice plate flow meter built in accordance with BS1042:1964, before feeding into the test line.

4.2.2. Observational and parametric studies on LOWPRESS

As was the case with LOTUS, the work on LOWPRESS was restricted to recording of flows using the high speed video. However, in the case of the LOWPRESS experiments, a special technique was employed to enhance the imaging namely enhancement of the imaging using a 1 m section of FEP (fluorinated ethylene propylene) tube placed at 3 m from the inlet of the acrylic resin test line to achieve refractive index matching coupled with the addition of a fluorescent dyestuff in the liquid phase. This technique is described in more detail in Section 4.2.2.1.

4.2.2.1. FEP technique. This method is illustrated in Figure 4.6 and uses a refractive index matching technique for visualising liquid films (Hewitt et al., 1989). A 76 mm diameter tube is surrounded by a rectangular compartment filled with water.

This tube, made of FEP (fluorinated ethylene propylene), has a refractive index of 1.34 which is close to the index of water 1.33. In addition sodium fluoresceine at a concentration of c=0.01106g/l is added to the water flowing in the pipe. The pipe is illuminated with a UV light which excites the fluoresceine and leads to a better visualisation of the studied flow.

The use of this property leads to a minimisation of the distortion of the light during the video recording using an Olympus i-SPEED camera. This technique allows a much more detailed image of the liquid phase. A photograph of the setup used is shown is Figure 4.7.

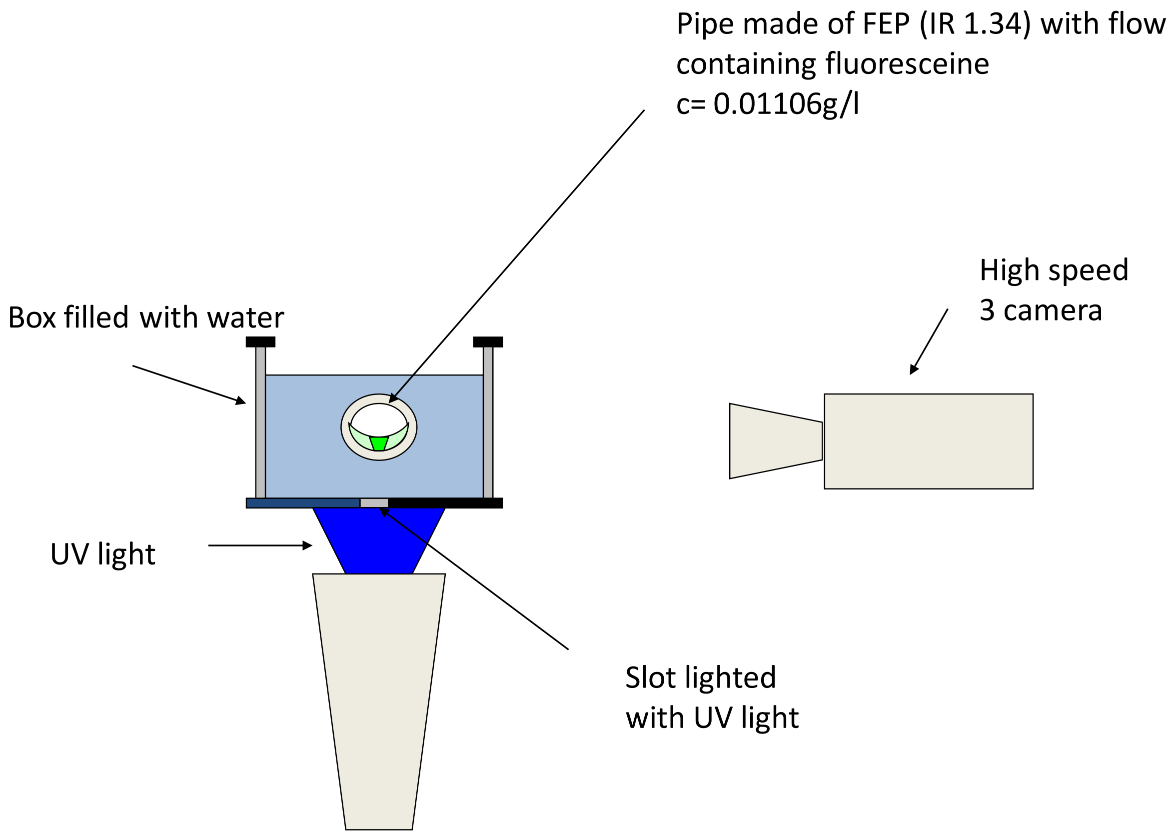

Figure 4.6. Experimental Setup: basic design UV light technique.

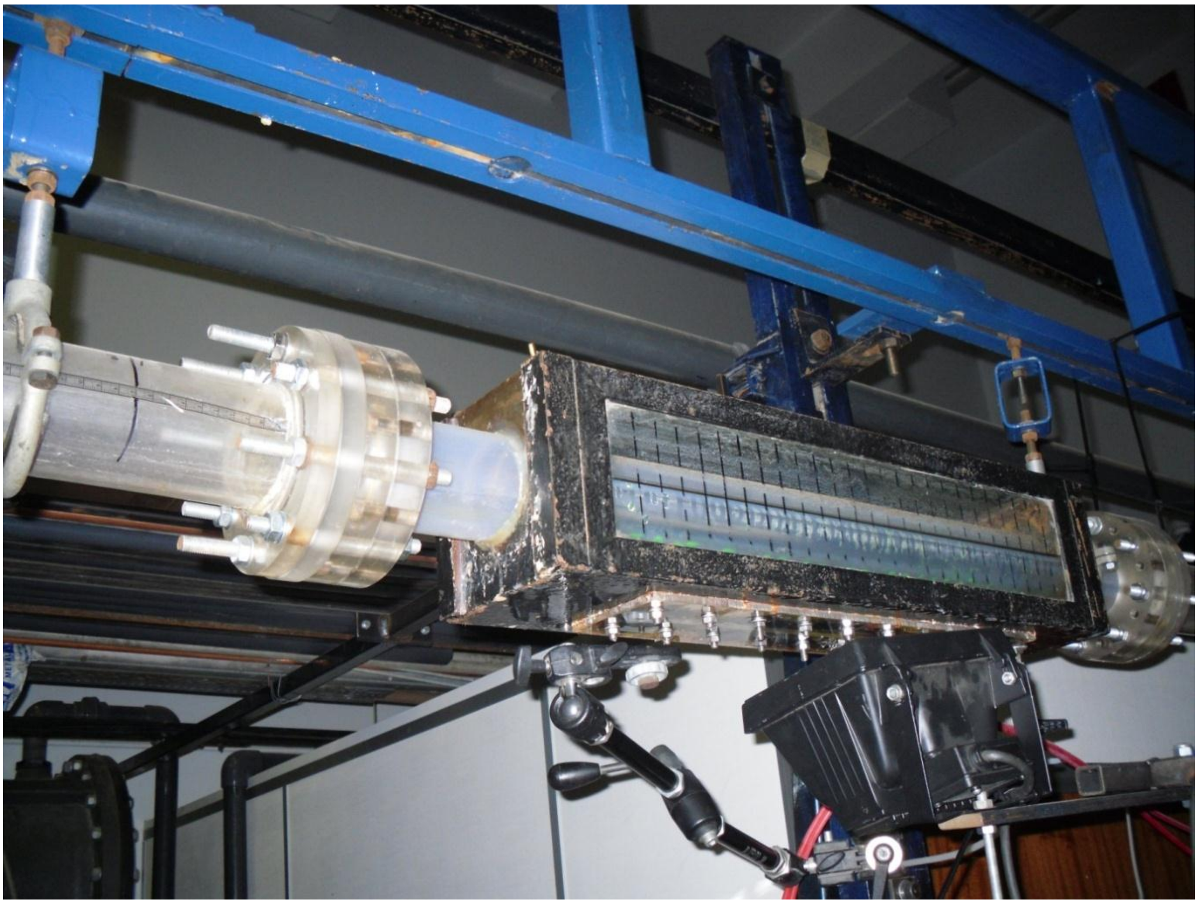

Figure 4.7. Photograph of the experimental setup: UV light technique.

4.3. Work on the WASP facility

Most of the experimental work reported in this thesis was carried out on the WASP facility and it is appropriate, therefore, to describe the facility and the experimental methods used in much more detail. Section 4.3.1 presents a description of the WASP facility and the various measurement techniques used in WASP are described in Section 4.3.2, with emphasis on those used in the present work.

4.3.1. The WASP facility

The WASP (Water, Air, Sand and Petroleum) high pressure multiphase flow facility was designed and constructed in the late 1980's and early 1990's. A schematic diagram is shown in Figure 4.8. The purpose of this facility is to provide a platform for multiphase flow studies relevant to the oil industry. The work on the facility has been supported mainly by the UK Engineering and Physical Sciences Research Council and by a consortium of oil companies. The funding for the present work was derived from this consortium. The test section on the WASP facility consists of a 37 m long, internal diameter stainless steel section that can be used in horizontal or slightly inclined (+2° to -2°) orientations. The fluids in the WASP facility are air (which may be derived from the site mains or from large pressurized tanks sited in the adjacent Department of Aeronautics), water and lubricating oil (Shell Tellus). The fluids may be used in any combination and the rig may be operated at pressures up to 42 bar (though the tests have generally been conducted at lower pressures). A general view of the facility is shown in Figure 4.9.

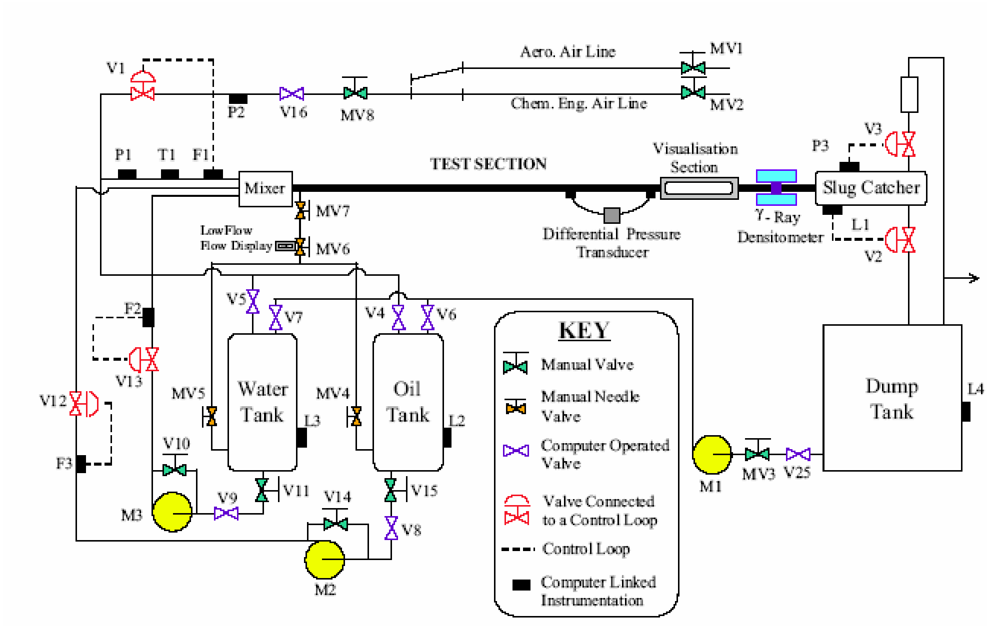

Figure 4.8. Schematic diagram of the WASP facility: the test section.

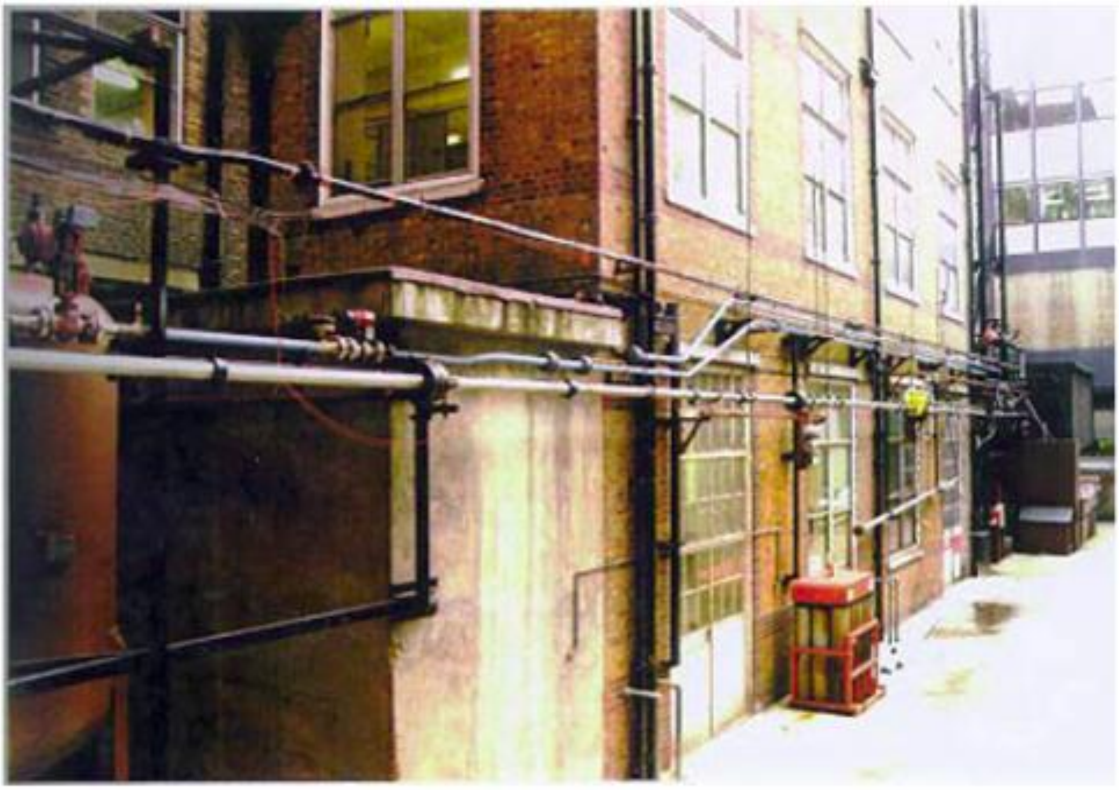

Figure 4.9. The WASP facility.

For the high gas flow rates applicable in the tests associated with the present work, the WASP facility was operated in the “blowdown“ mode using air from the 40 m^3 high pressure storage tanks located in the adjacent Aeronautics Department (see photograph in Figure 4.10). After flowing through the test section, the air is released to the atmosphere through valve V3. The tanks were pressurized (typically to around 27 bar) using a compressor and the compressor was left running during the experiments in order to have the maximum pressure available. The tank pressure from the air source of the department of Aeronautics often falls as a result of the high demand on the supply. The air supply is reduced in pressure across valve V1 and, to offset the tank pressure variations, this valve is operated in a critical flow mode; thus, the ratio between the upstream and the downstream pressures across this valve has to exceed a critical value. Manolis et al. (1995) determined this value to be 1.894. In order to be above this ratio, the experiments have to be conducted with a minimum upstream pressure of 15 bar and with atmospheric pressure at the exit.

Figure 4.10. The high pressure air supply tanks.

Orifice plates built in accordance with British Standard 1042 are used to measure the air flow rate. The air flow rate is determined from the measurement of the pressure drop across the orifice plate. Since air is compressible, the response of the orifice depends on pressure. Several diameters of orifice plate exist and each diameter corresponds to a certain range of flow rates for a given downstream pressure. Seven diameters for the orifice plates are available varying by 5mm from 10 to 40 mm. The experiments described in this work were carried out at atmospheric pressure and using the 25 mm orifice plate. Figure 4.11 shows the flow rate covered by the 25 mm orifice plate.

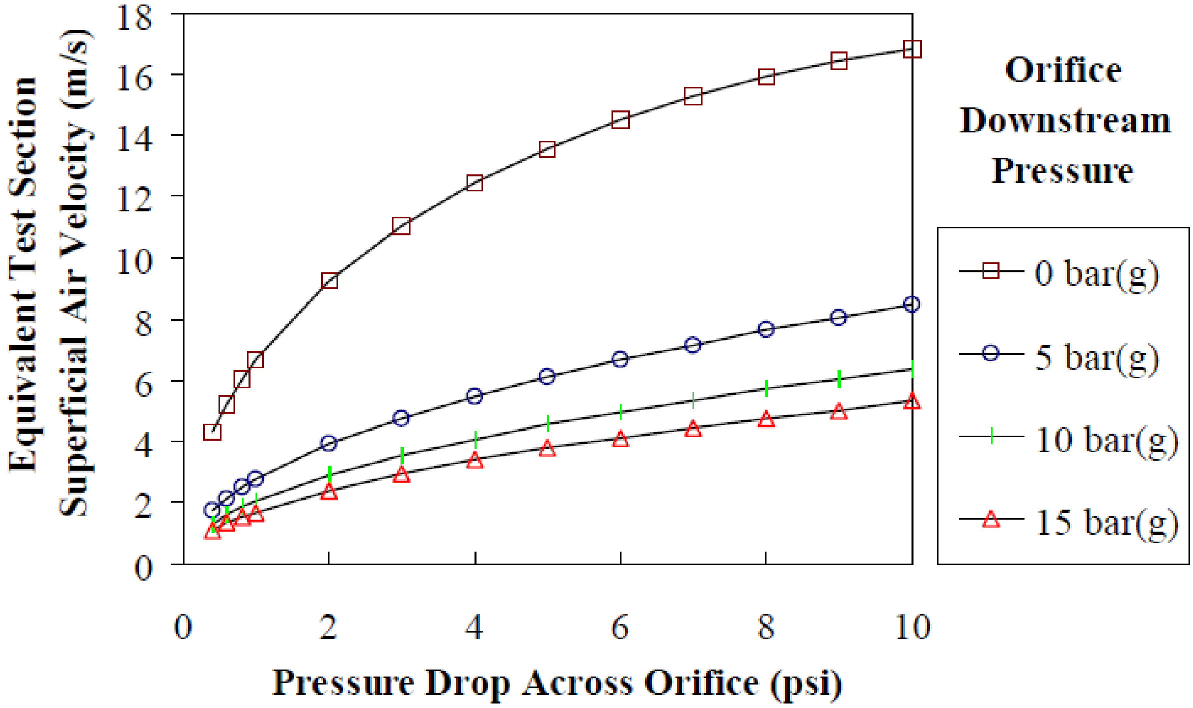

Figure 4.11. 25 mm air orifice at various orifice pressures.

The flow rates in Figure 4.11 are expressed as equivalent superficial velocity in the test section at the pressure immediately downstream the orifice plate. The air superficial velocity at the location of the axial view section is calculated from the value given in Figure 4.11 by multiplying this value by the ratio of the measurement pressure at the pressure measured at the viewing section.

The water and oil are each stored in a 5 m^3 tank. The liquid tanks are shown in Figure 4.12.

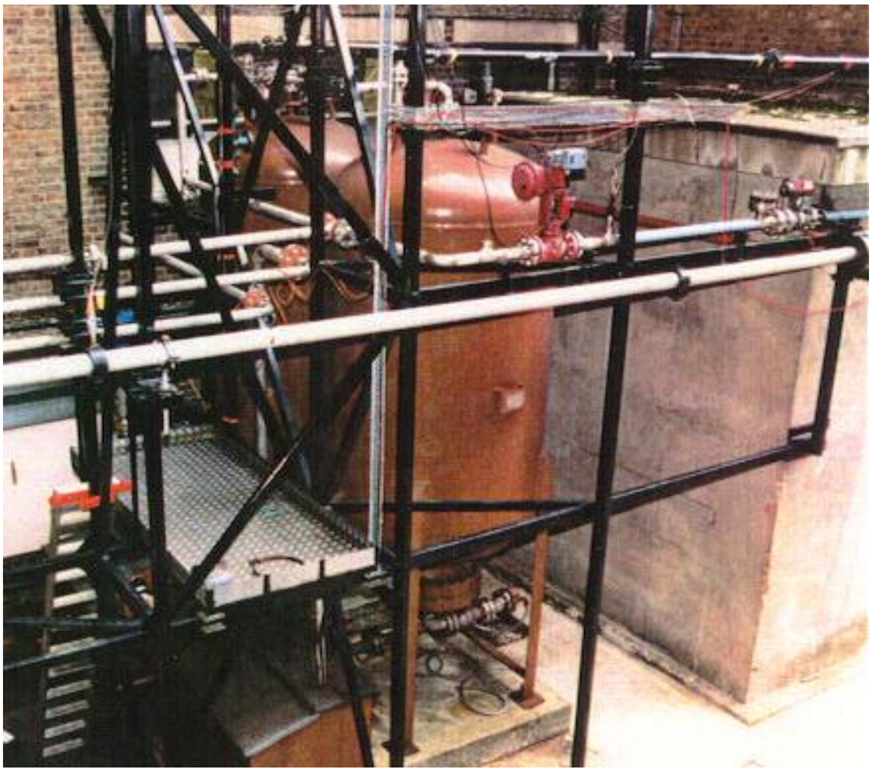

Figure 4.12. The oil and the water tanks.

The liquid tanks may be pressurized to enhance the flow through the pumps. Indeed, the tank pressure alone may be used to drive the flow through the test section with the pumps off. This option is often useful when low liquid rates are required.
The liquid flow rate was measured using two different systems: the first metering system for lower flow range i.e. for superficial liquid velocity less than 0.05 $m.s^{-1}$, the second for higher flow range i.e. for superficial liquid velocities greater than 0.05 $m.s^{-1}$.

Water or oil flows corresponding to in-pipe superficial liquid velocities over the range 0-0.05 $m.s^{-1}$ were measured with a Danfoss MASSFLOW flowmeter. The principle of the flowmeter is based on Coriolis acceleration: The liquid flows through a spiral tube which create an oscillation of the measuring pipe at a frequency which is converted into a flow rate.

For higher water flow rates, the superficial water velocity was measured with a Danfoss 381 Magnetic Flowmeter. The principle of this flowmeter is based on Faraday's law of electromagnetic induction: The water flows through the magnetic field which induced a voltage. The voltage is measured and converted in a flow rate.

For higher oil flow rates, orifice plates were used to determine the superficial oil velocity. Sizes varying by 5 mm from 15 to 40 mm are available and Figure 4.13 shows the calculated calibrations for various orifice size, showing the corresponding flow rate ranges covered.

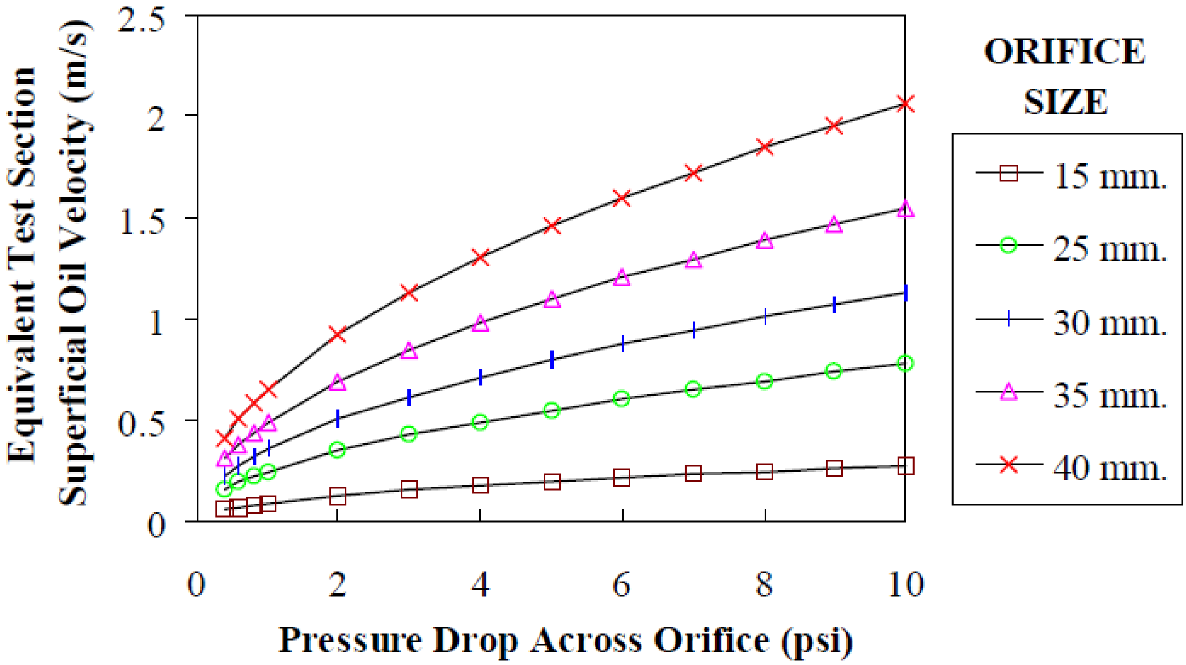

Figure 4.13. Oil orifice characteristics.

At the entrance to the test section, the fluids are introduced in a manner such that they flow in a direction parallel to the tube axis before they come into contact with the other fluids. Thus water is introduced into the bottom of the test section, oil in the middle and air at the top. A photograph of the injector system is shown in Figure 4.14.

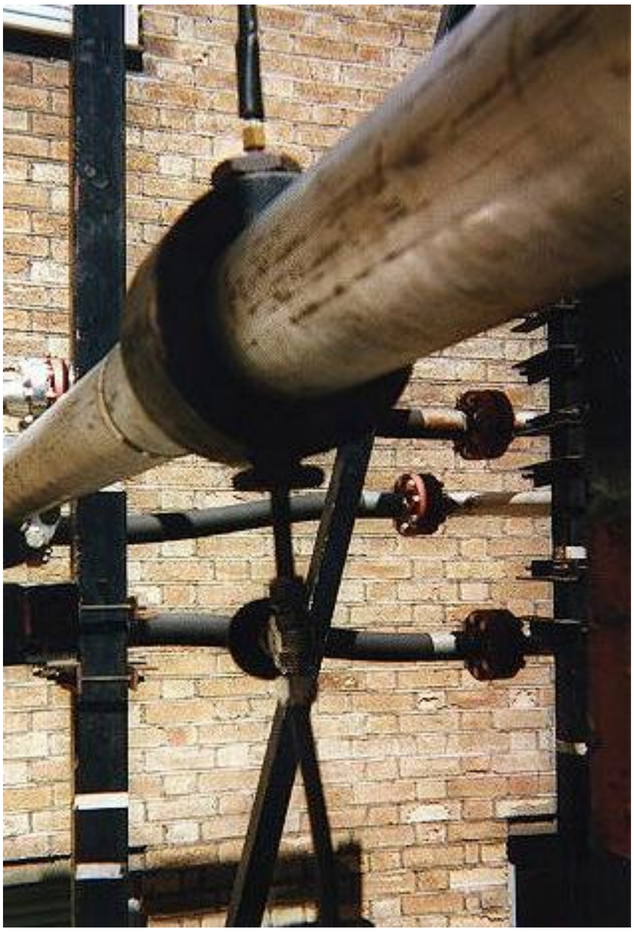

Figure 4.14. Photograph of the inlet mixing section.

A separator ("slug catcher") is placed at the exit of the test section, separates the gas and liquid phases. The slug catcher is illustrated in Figure 4.15. The air from the slug catcher discharges through a silencer (see Figure 4.16). The liquid phases (oil and water) from the slug catcher are separated in the dump tank (see Figure 4.17) under the action of gravity from which they are pumped (between experiments) to their respective tanks. Note that, in the current experiments, only water was used.

Figure 4.15. The slug catcher.

Figure 4.16. The air discharge line and silencer.

Figure 4.17. The dump tank.

The WASP high pressure facility is equipped with a computerised control system allowing the experimentalist to monitor the operations on the rig directly. A flow diagram of the rig is shown on the computer screen and this shows the valve settings, pressure, temperature, level readings from various instruments and the control loops. An example of this display is shown in Figure 4.18. The various valves are operated using solenoid switches on a control panel.

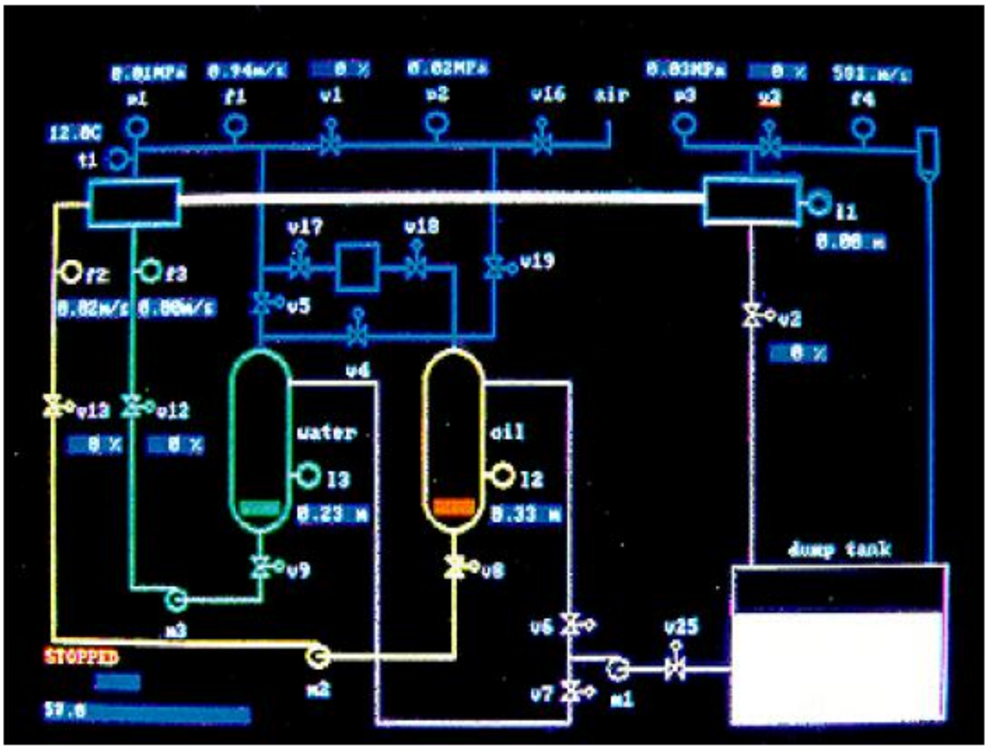

Figure 4.18. Display on the control computer.

The operator can set a flow parameter to a determined value via the control loops (see Table 4.1).

Control Parameter	Valve - Sensor Link
Air flowrate	V1 - F1
Exit pressure	V3 - P3
Water flowrate	V13 - F2
Oil flowrate	V12 - F3
Slug catcher level	V2 - L1

Table 4.1. Control loops.

The fluids used in WASP are air, water and lubricating oil (Shell Tellus 22). The viscosity of the fluids is predicted with the use of correlations. The viscosity of air is given with a correlation published by the National Research Council in the "International Critical Tables of Numerical Data" (1928).

$$\mu_A = \left[1.622\times10^{-2} + 2.708\times10^{-5}(1.8T+32)\right]\times10^{-3} \qquad (4.1)$$

The viscosity of the tap water is given by the correlation of Van Wingen (1950):

$$\mu_A = \left[\exp\left[1.003 - 1.479\times10^{-2}(1.8T+32) + 1.928\times10^{-5}(1.8T+32)^2\right]\right]\times10^{-3} \qquad (4.2)$$

The viscosity and density of the oil Shell Tellus 22, at a temperature comprise between 0^oC and 35^oC, is determined with the correlations by Hall (1992):

$$\mu_0 = \left[152.9 - 11.16T + 0.457T^2 - 0.0103T^3 + 0.0001T^4\right]\times10^{-3} \qquad (4.3)$$

$$\rho_0 = 860.5 + 4.5\left[\frac{24.7-T}{9.7}\right] \qquad (4.4)$$

To ensure the value remains constant i.e. to avoid excessive cross contamination of the liquid phases, the physical properties of the fluid on WASP undergo regular checks.

4.3.2. Observational and parametric studies on WASP

As was stated above, a wide variety of measurement and data acquisition techniques have been used on the WASP facility. In what follows, a description of the key methods is given as follows: Live imaging of the flow (Section 4.3.2.1), high speed imaging of the flow using side view photography (Section 4.3.2.2), pressure gradient measurement (Section 4.3.2.3), liquid holdup measurement (Section 4.3.2.4), entrained droplet flux (Section 4.3.2.5), axial view photography (Section 4.3.2.6) and liquid film flow rate distribution (Section 4.3.2.7). Not all of these techniques were used in the present work. The emphasis was on visualization (side view, Section 4.3.2.2 and axial view, Section 4.3.2.6) and on new technology (developed as part of the present work) for liquid film flow rate distribution around the tube periphery (Section 4.3.2.7). The accuracy of the various measurements on the WASP facility is discussed in Section 4.3.2.8. In the analytical work described in Chapters 6 and 7, extensive use was made of earlier work on droplet flux and a detailed description of this work is included in Section 4.3.2.5. A flow sheet of the WASP facility indicating the location of the various measurement devices is shown in Figure 4.19.

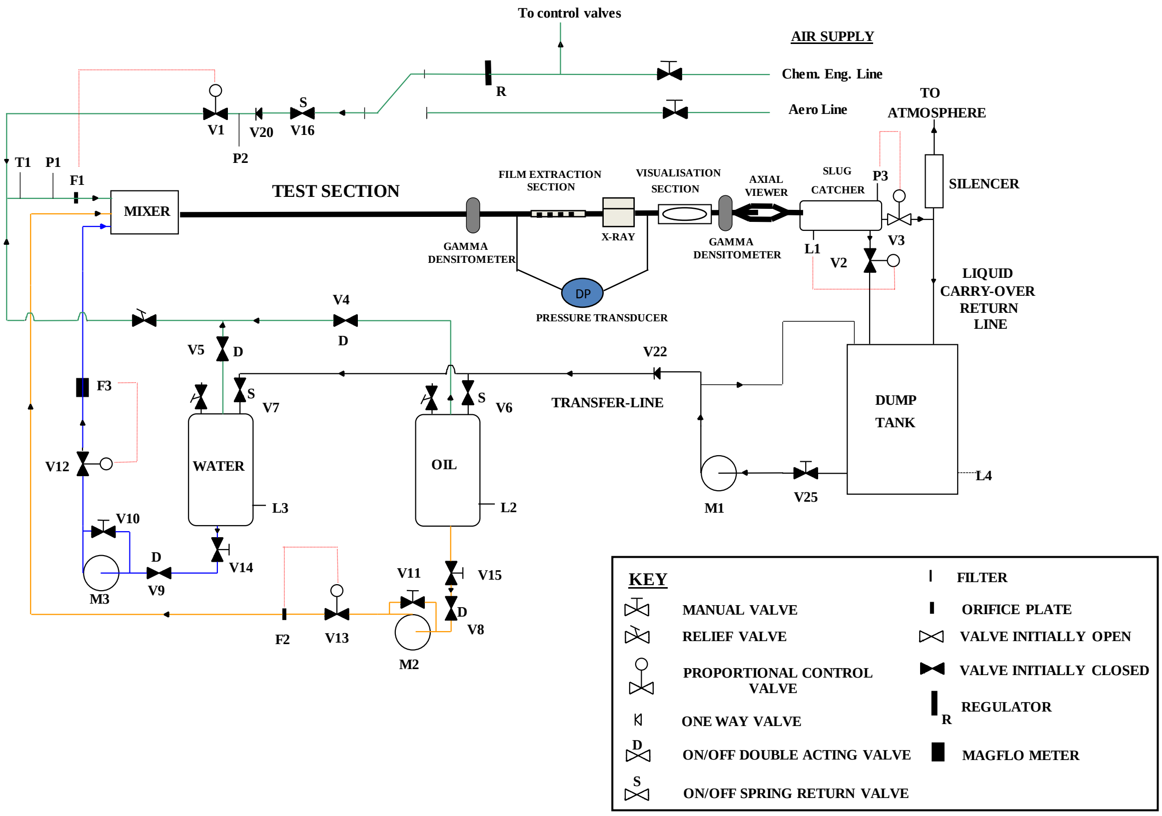

Figure 4.19. Flow sheet of the WASP facility indicating the location of the various instrumentation items.

4.3.2.1. Live imaging of the flow. A live image of the side view of the flow observed through the transparent visualization section is displayed on a screen during the experiments as illustrated in Figure 4.20. This image is accompanied with a live measurement of the experimental flow rates and pressures of the flow. A video file of the flow is recorded during the experiments and the raw data are memorized in an ASCII file. The data acquisition program, which was developed by Hall (1992), has a frequency of 10 Hz. The purpose of this system is not only to help the operator during the experiments with the possibility of visualizing the flow and knowing the live parameters of the flow but also to provide a track record of experiments done in the WASP facility.

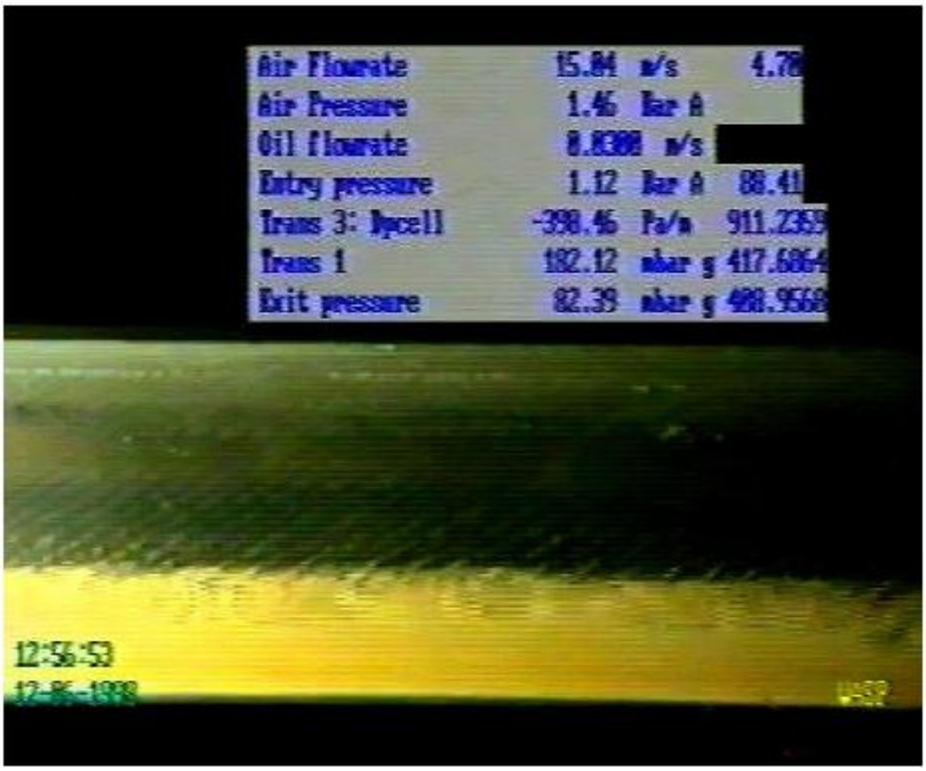

Figure 4.20. Side view of the flow and flow parameters.

4.3.2.2. High speed visualization of the flow using side view photography. The visualization section (also used in the routine live imaging described in Section 4.3.2.1) is composed of a 1m transparent acrylic resin (Polycarbonate) tube surrounded by a metal shell with side openings as shown in Figure 4.21. For the high speed visualization studies, two high intensity 1000 W halogen lamps were used to illuminate inside the visualization section. The flow was observed through the visualization section and recorded using a high speed cine camera at 500 frames per second. A high resolution recording of the flow was obtained. In some experiments simultaneous side and axial view pictures were obtained.

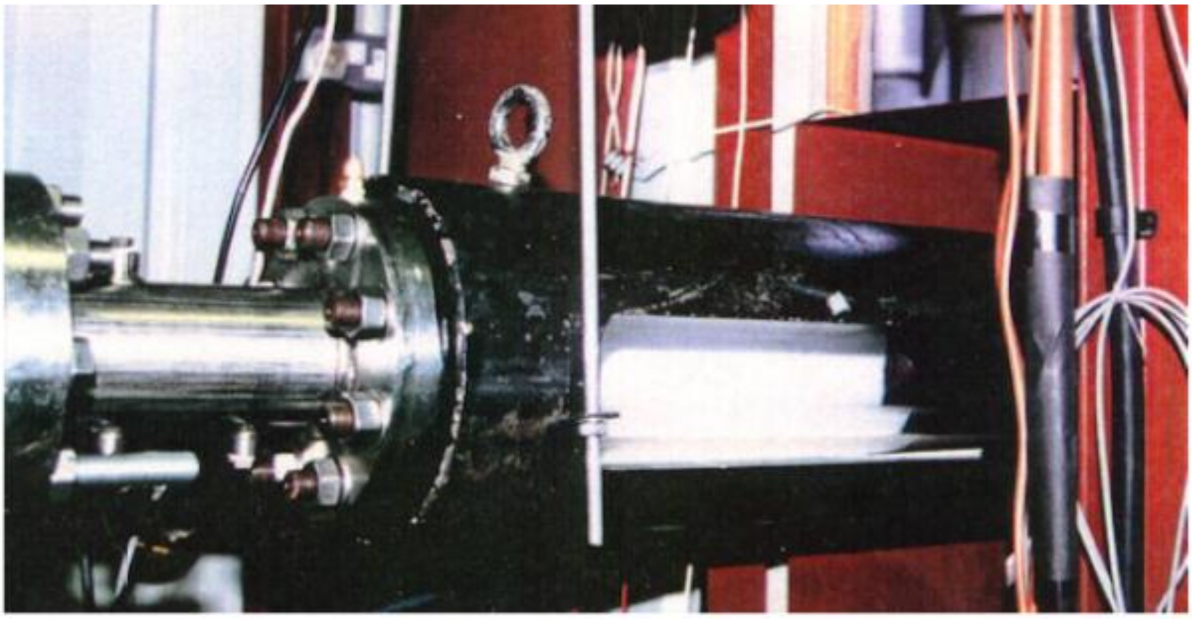

Figure 4.21. Visualisation section.

4.3.2.3. Pressure gradient measurement. The pressure gradient along the pipe was measured over a specific length set prior to the experiments, using a Rosemount 3051C differential pressure transducer. The pressure transducer is connected to the test section via lines filled with silicone fluid. The diaphragm transmits the pressure difference to the signal box. This signal is then converted to a pressure gradient measurement. The tappings are placed 3 meters apart because of the small pressure drops expected for the flow conditions in the present experiments and are flush-mounted at the bottom of the test section. The pressure is transmitted by the diaphragm to the signal box through silicone fluid filled lines (sealed by the manufacturer in order to avoid air entrapment) and converted to a pressure gradient measurement.

A diagrammatic representation of the pressure transducer system is illustrated in Figure 4.22.

A photograph of a pressure tapping and the connection to a thermally insulated silicone fluid filled line is shown in Figure 4.23.

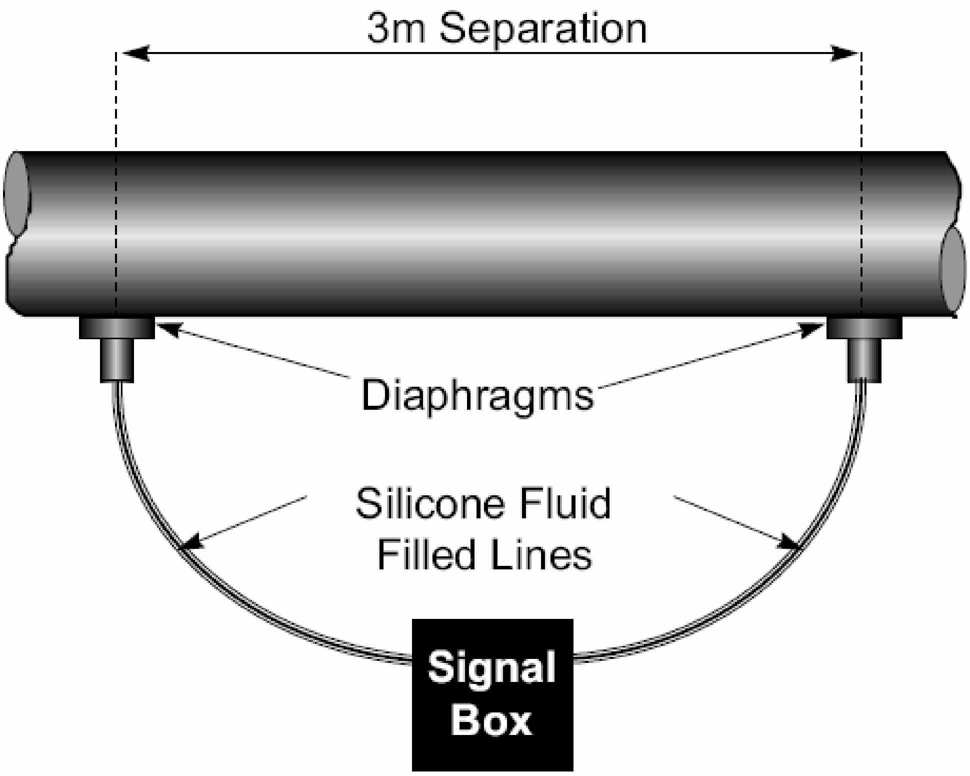

Figure 4.22. Schematic diagram of differential pressure transducer.

Figure 4.23. Photograph of a pressure tapping, diaphragm and thermally insulated silicone filled fluid line.

4.3.2.4. Liquid holdup measurement. The system most commonly used for measuring the liquid holdup on the WASP facility has been that of gamma densitometry (Pan, 1996). This system is based on attenuation of a beam of gamma photons by the flowing media. Suppose we have a beam with a initial intensity I_0. The intensity measured after the beam has passed through the medium is given by expression (4.5):

$$I = I_0 \exp(-\mu\delta) \tag{4.5}$$

Where μ is linear absorption coefficient of the medium and δ is the thickness of the medium.

The following expression by Pan (1996) gives the liquid phase fraction for a gas-liquid mixture in a pipe:

$$\varepsilon_L = \frac{\ln I - \ln I_G}{\ln I_L - \ln I_G} \tag{4.6}$$

With I_G and I_L, obtained during the calibration procedure, are the measured intensity for a pipe completely filled with respectively gas and liquid.

The traversing beam dual-energy gamma densitometer system is used to measure the holdup of the two liquid phases (oil and water) in a three-phase flow and is illustrated in Figure 4.24. It consists of a source, a detector, an electrically driven positioning system and a data acquisition system. The gamma rays were provided by the radioactive isotope Ba-133.

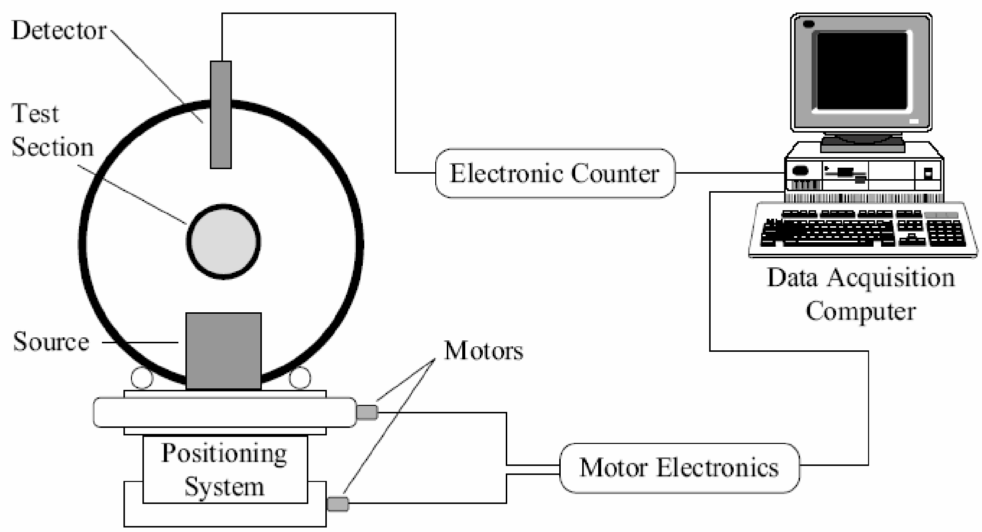

Figure 4.24. Dual-energy gamma densitometer setup.

The holdup of the two phases is determined by simultaneous solution of equations similar to Equation 4.6 for the two respective beam energies (see Pan, 1996 for details). A more recent development has been a dual energy X-ray tomography system which can give spatially and temporarily resolved parse distribution in a three-phase flow (Hu et al., 2005).

4.3.2.5. Entrained droplet flux. An important parameter in comparing the predictions of the model described in Chapter 6 with data (as reported in Chapter 7) is that of local entrained droplet mass flux in the core of the flow. Measurements of this quantity had been made previously by Badie (2000) and by Hale (2006) and their results are reproduced here for completeness. No further measurements of entrained droplet mass flux were made in the present work. Badie (2000) and Hale (2006) measured the local mass flux of entrained drops in the gas core using a sampling probe. This probe can be operated in "isokinetic" mode (the flow rate of the gas-liquid mixture is adjusted so that there is zero impact pressure at the probe mouth) or in "sampling" mode. In the isokinetic mode, both the local entrained droplet and the gas fluxes can be measured; however, the operation in this mode is much more difficult and the sampling mode is much more convenient. It is found that the liquid collection rate with the sampling probe is insensitive to the gas collection rate over a wide range of gas collection rates. A top view of the entrainment sampling apparatus is given in Figure 4.25 and a view along the pipe of the apparatus is shown in Figure 4.26. The principle behind this technique is to collect a liquid sample for a fixed period once a steady state of the liquid is achieved, to determine the mass of the liquid sample and to calculate the liquid sample flow rate.

In the earlier experiments on WASP, this system could also be manually traversed across the pipe and the variation of entrained droplet mass across the pipe diameter could thus be investigated.

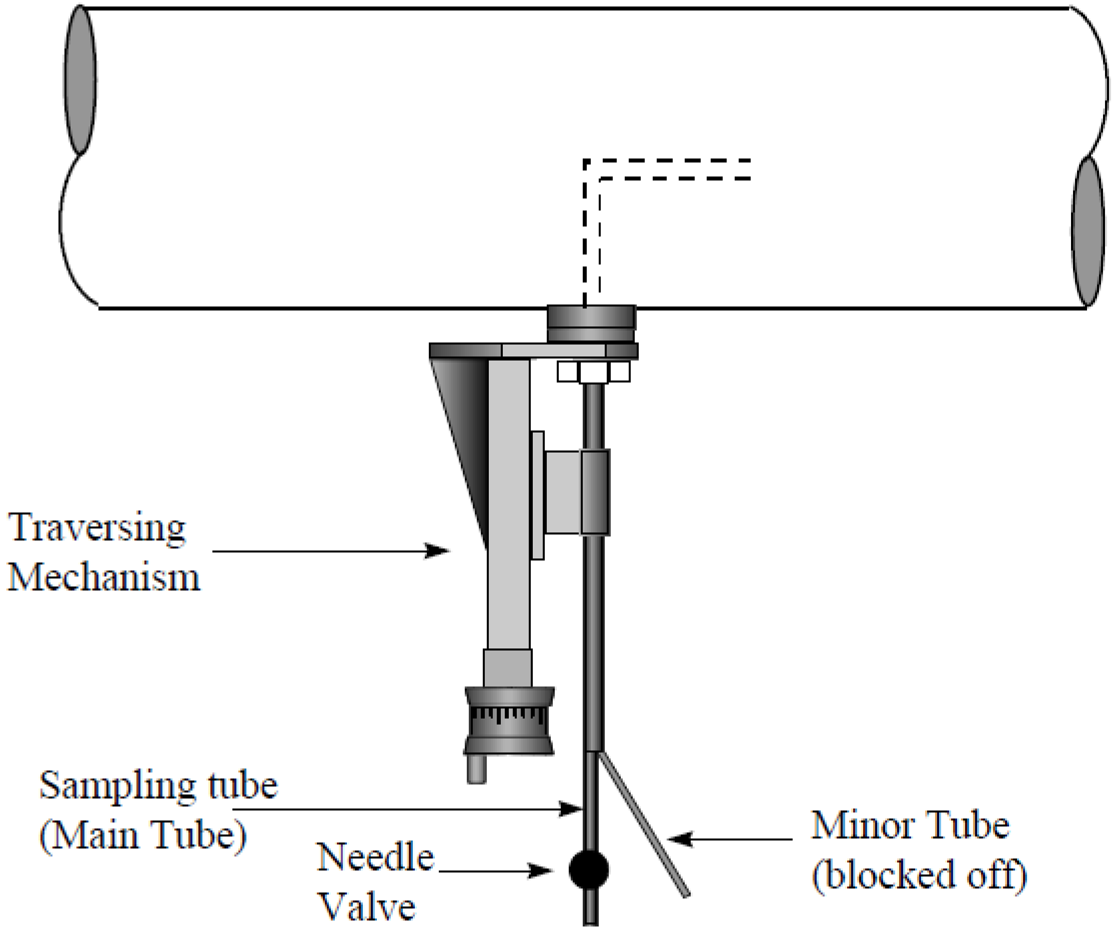

Figure 4.25. Entrainment sampling apparatus.

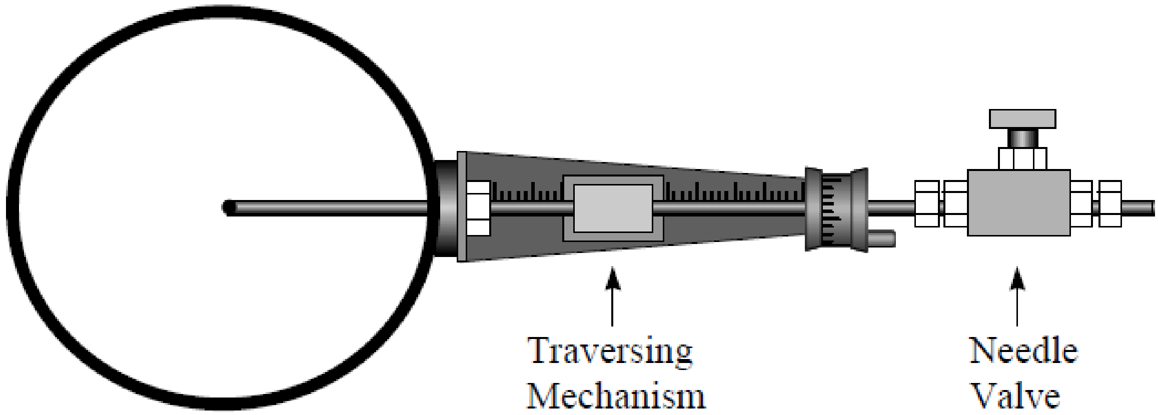

Figure 4.26. Sampling tube: View along the pipe.

As stated above, the earlier data on entrained droplet mass flux obtained in the WASP facility by Badie (2000) and Hale (2006) were used in comparisons with the calculations reported in Chapters 6 and 7. For completeness, therefore, these data are summarized here. Essentially, four Conditions were investigated as follows:

Condition 1 (Hale, 2006): Air superficial velocity: 9.92 m.s-1 and water superficial velocity: 0.05 m.s-1. The experiments by Hale (2006) were carried out with three-phase (water-oil-air) flows and the complete sets of results are plotted in Figure 4.27. Measurements of droplet flow rate were made by traversing the probe in a vertical line passing through the tube axis. The distance from the tube axis is *Y* and *R* is the tube radius (thus *Y/R= 0* is at the tube axis. For the comparisons reported in Chapters 6 and 7, only the data for air-water flow was considered (i.e. that for a water cut WC of 1.00).

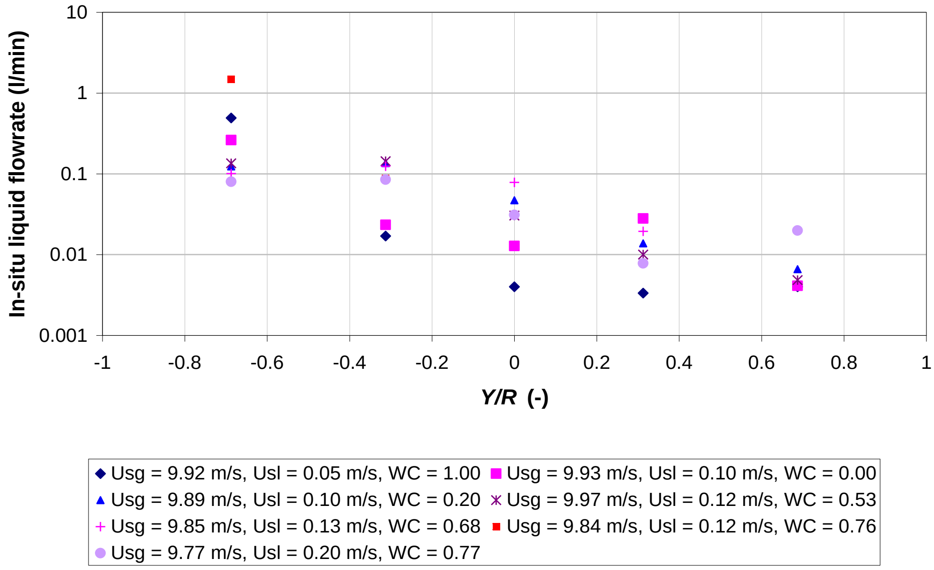

Figure 4.27. Entrained droplet sampling data obtained by Hale (2006).

Condition 2 (Hale, 2006): Air superficial velocity: 11.9 m.s^{-1} and water superficial velocity: 0.12 m.s^{-1}. This data is also taken from a series of measurements by Hale (2006) for three-phase flows the results from which are illustrated in Figure 4.28. In this case, the results used in the present analysis are for a water cut of 1.0 (i.e. for pure water flow) which were obtained for an air superficial velocity of 11.9 m.s^{-1} and a water superficial velocity of 0.12 m.s^{-1}.

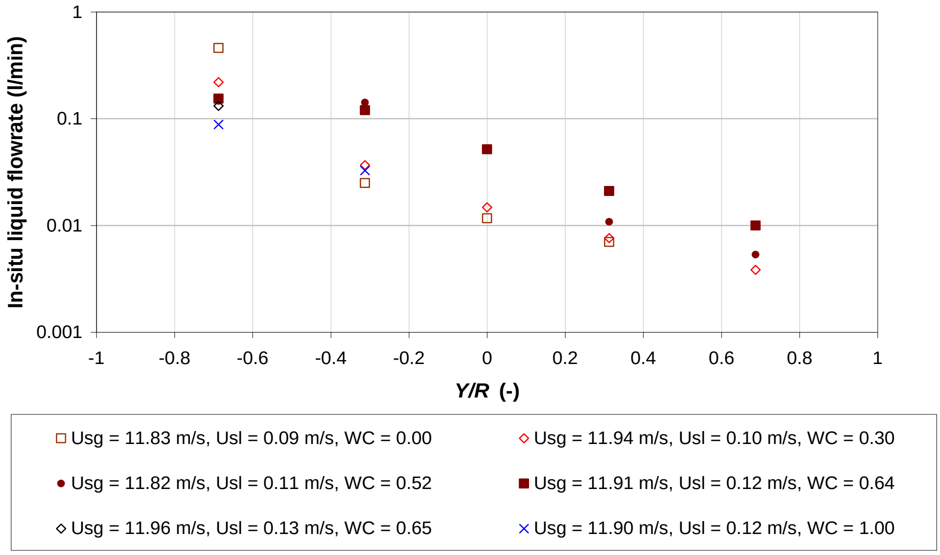

Figure 4.28. Results obtained with the sampling probe for three-phase flows (Hale, 2006).

Condition 3 (Badie, 2000) Air superficial velocity 21 m.s^{-1}, water superficial velocity 0.02 m.s^{-1}. Badie carried out droplet mass flux measurements at the centre line of the WASP pipe for both air-oil and air-water flows; the results obtained are shown in Figure 4.29. For comparison with the present analysis, the results for 21 m.s^{-1} and 0.02 m.s^{-1} air and water superficial velocities respectively were selected as Condition 3.

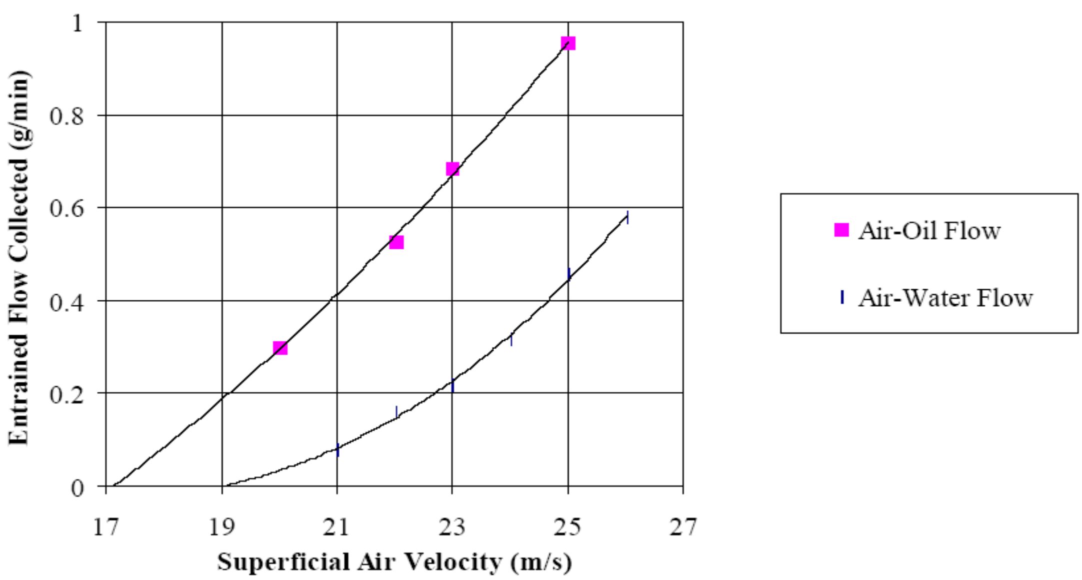

Figure 4.29. Variation of entrainment collected at the center of the pipe with superficial gas velocity for superficial liquid velocity of 0.02 m.s^{-1}.

Condition 4 (Badie, 2000) Air superficial velocity 25 m.s^{-1} and water superficial velocity 0.02 m.s^{-1}. Badie (2000) shows a set of data (taken on the WASP facility) for droplet mass flux at the centre line for oil and water flows for an air superficial velocity of 25 m.s^{-1} and for a range of superficial liquid velocities as illustrated in Figure 4.30. Condition 4 for comparison with the analysis presented in Chapters 6 and 7 was selected as that corresponding to a water superficial velocity of 0.02 m.s^{-1}.

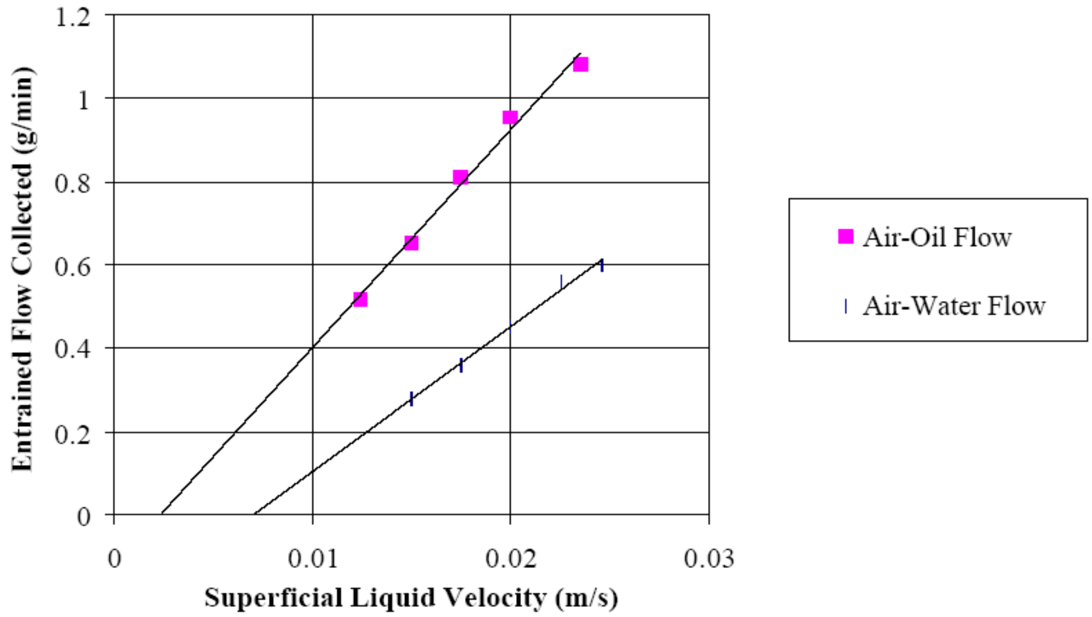

Figure 4.30. Variation of entrainment collected at the center of the pipe with superficial liquid velocity for superficial gas velocity of 25 m.s^{-1}.

4.3.2.6. Axial view photography. A systematic study of air-water stratifying annular flow using the axial viewing technique was performed as part of the present work and the results are given in Chapter 5. In the axial view photography technique, the flow is viewed along the axis of the tube through a viewing tube which is kept free of the liquid phase by blowing gas along the tube; this reverses the droplets entering the viewing tube and allows a clear view of the flow to be obtained at a plane of focus situated in a region where the flow is unaffected by the blown gas stream. Using the axial view method, it is possible to study of the behaviour at the gas-liquid interface, the entrainment of droplets from a liquid film, the radial motion of droplets in the gas core and the circumferential distribution of liquid films in stratifying-annular flows.

The axial view technique was first developed by Arnold and Hewitt (1967) and has subsequently been used by a number of researchers such as Hewitt and Roberts (1969), Fisher and Yu (1975), Suzuki and Ueda (1977), Whalley et al. (1977), Fisher et al. (1978), Whalley et al (1979), Mayinger (1981), McQuillan et al. (1985) and Shibata et al. (1999) for their visualization work on vertical and horizontal flows. A review of this technique is presented in Chapter 3.

The axial viewer used in the present work was based on a design by Badie (2000) which was, in turn, partly based on an axial viewing system used by Fisher & Yu (1975) for air-water tests. The Fisher & Yu system was complex to machine and not very flexible, thus some alteration was needed to produce an in-line axial viewing system for application on the WASP facility.
The novelty of the system used in the present work lies in the use of a new form of purge air system designed (and commissioned in the department of Chemical Engineering at Imperial College), especially to be adaptable to the WASP facility configuration.

The arrangement used is illustrated in Figure 4.31. The flow from the 3 inch (77.92 mm) nominal bore WASP test section is diverted into two three-inch bore tubes to leave space for the viewing and purge air systems at the junction. The air distributor is connected to the other end of the viewing tube. The purge air flows in a direction opposite to the direction of the flow in the main channel to maintain the window of the viewing tube free of liquid. A camera system is focussed on an illuminated plane at some distance upstream of the diverted flow.

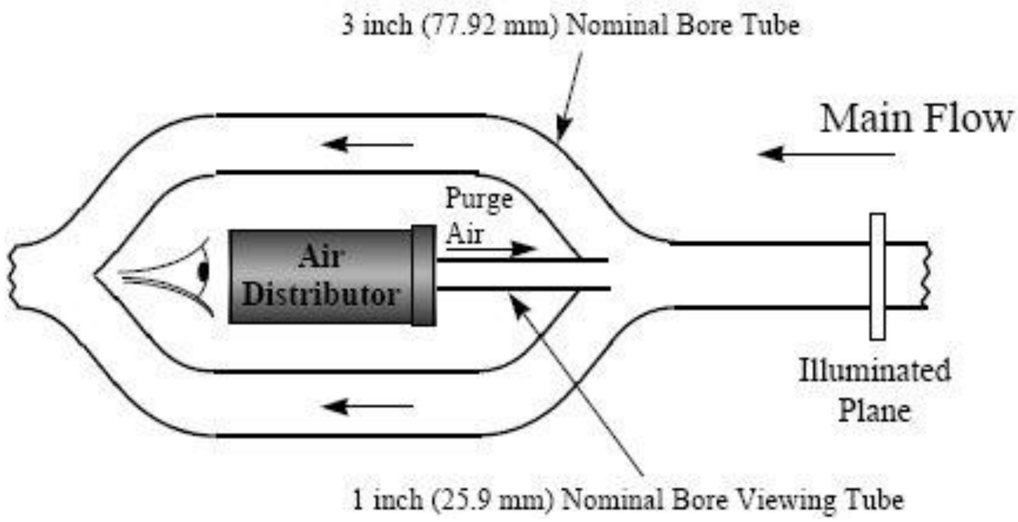

Figure 4.31. The basic design of the in-line axial viewing system (Badie, 2000).

The main body of the viewer, illustrated in Figure 4.32, is composed of 3 inch (77.92 mm) nominal bore stainless steel sections welded together with eight 45^{o} long radius elbows, four short straight pipe sections and two longer straight sections.

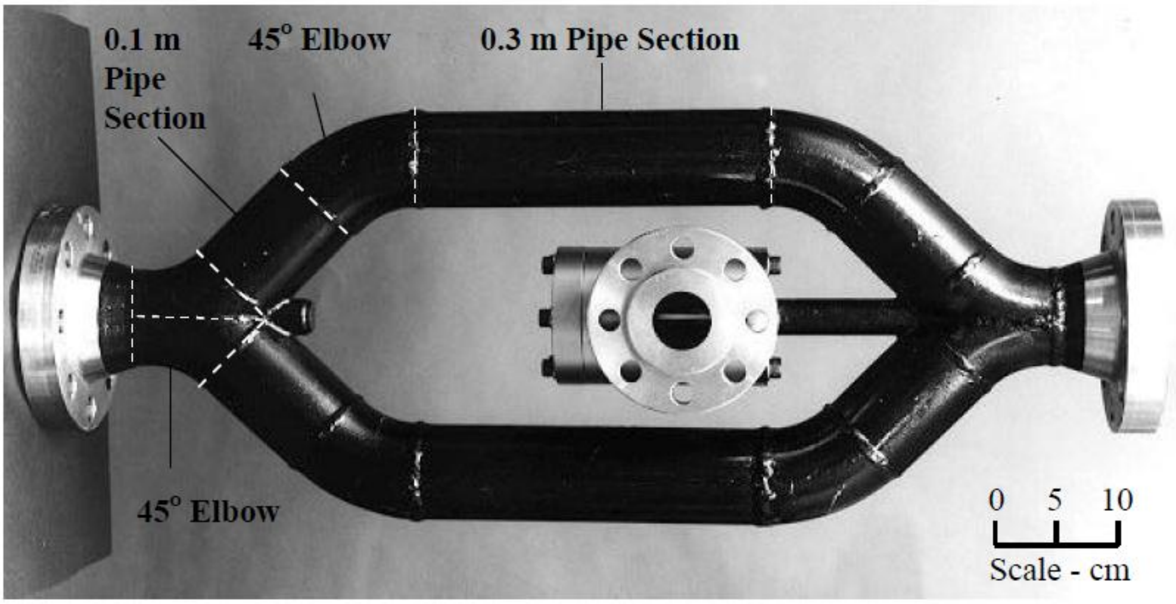

Figure 4.32. The main body of the In-Line Axial viewer.

The 1 inch (25.4 mm) nominal bore viewing tube is welded to the main section so that it protrudes of about 1.5 cm into the inside of the section as shown in Figure 4.33. The protrusion provides a platform so that any liquid on the upper wall of the main section can drain around the viewing tube, rather than into it. The air distributor is connected to the other end of the viewing tube via a flange (see Figure 4.34).

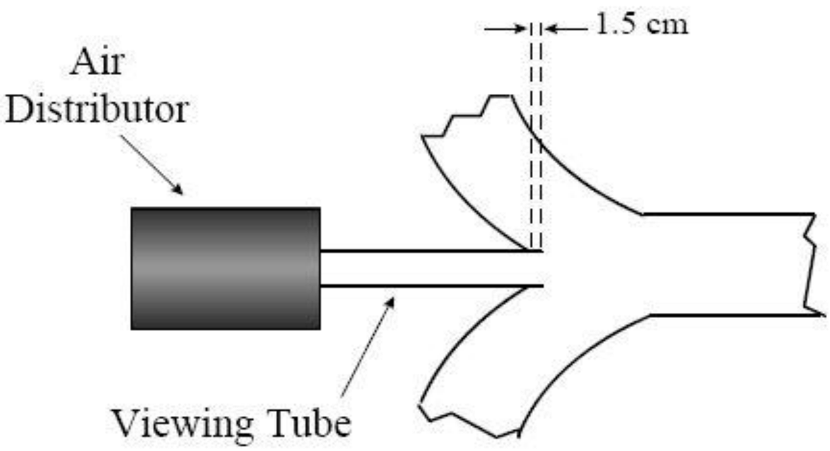

Figure 4.33. Diagram of the viewing tube.

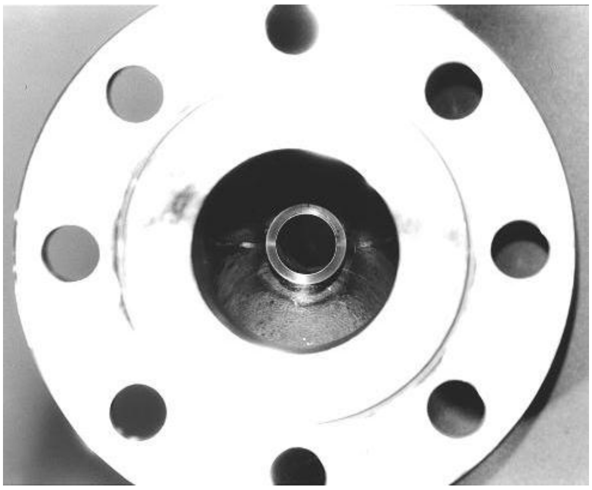

Figure 4.34. Viewing tube.

The main advance design of the in-line axial view system used here is a drastically improved purge air system whose role is to stop entrained drops from reaching the window on the air distributor (see Figure 4.35).

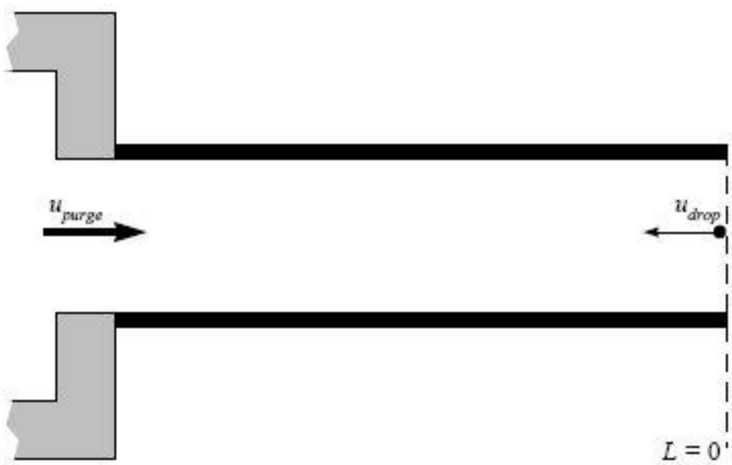

Figure 4.35. Motion of a liquid droplet in a purge stream. (Badie, 2000).

The purge air velocity and the length of the viewing tube were chosen on the basis of the model equations governing the motion of droplets used by Fisher et al. (1978) in order to determine stopping distances for drops travelling against purge air flow.

The equation of the motion is written:

$$-\frac{\pi}{6}D_{drop}^{3}\rho_{L}\frac{du_{drop}}{dt}=\frac{1}{2}C_{D}\rho_{G}(u_{purge}+u_{drop})^{2}\frac{\pi D_{drop}^{2}}{4} \tag{4.7}$$

with D_{drop} : the drop diameter
ρ_L : the liquid density,
u_{drop} : the droplet velocity,
C_D : the drag coefficient,
ρ_G : the liquid density,
u_{purge} : the purge velocity

The stopping distance L_S is then obtained assuming the drag coefficient is a constant and integrating equation (4.7).

$$\frac{L_S}{D_{drop}} = \frac{4}{3}\frac{\rho_L}{\rho_G}\frac{1}{C_D}\left[\ln\left(1+\frac{u_{drop}}{u_{purge}}\right)-\left(\frac{u_{drop}}{u_{purge}+u_{drop}}\right)\right] \qquad (4.8)$$

C_D (which is normally a function of Re), was assumed in these calculations to be a constant equal to 0.44 (Fisher et al. (1978)). This hypothesis gives an accuracy of 10% in terms of distances which were acceptable for design purposes.

The length of the viewing tube was set to 0.3 m and the average purge velocity fixed to $100 m.s^{-1}$ enabling the air purge system to stop 5 mm diameter droplets travelling at $25 m.s^{-1}$.

There were two options to feed the air purge system, namely the aeronautics high pressure supply tanks and the Imperial College main air supply; the first one was preferred to allow future tests to be carried out at higher pressure. A separate air supply line taking a portion of the air supplied from the pressurised tanks owned by the Aeronautics department was built to feed the air distributor. The air supply line within the air purge system is illustrated in Figure 4.36 and Figure 4.37. A flexible hose is connected to the flange at the top of the air distributor.

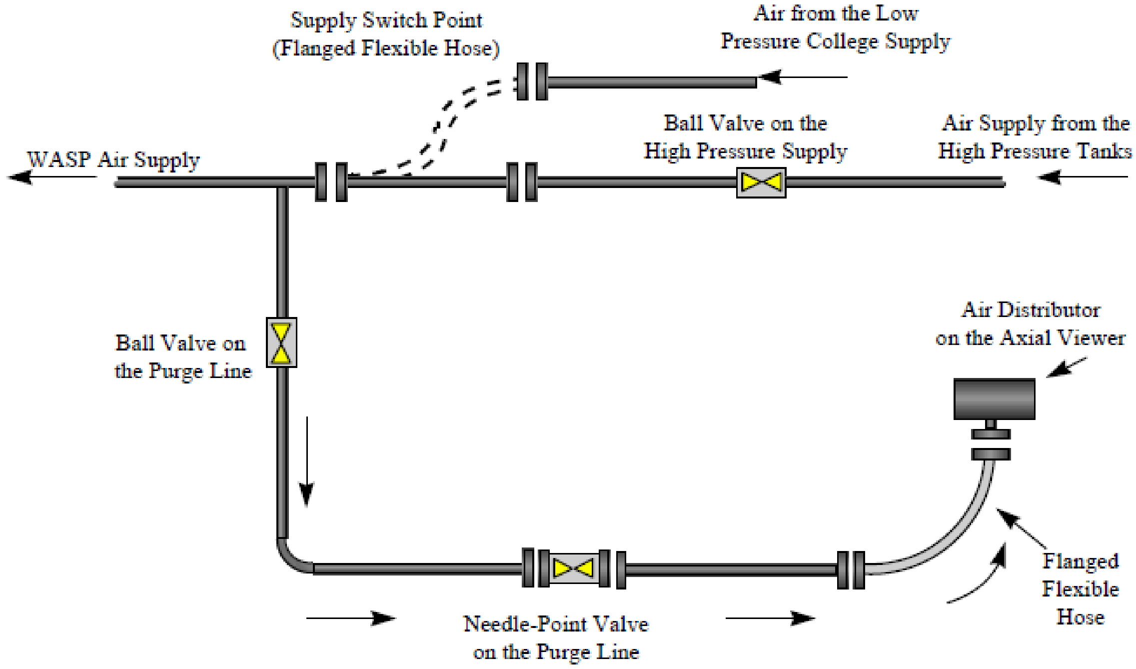

Figure 4.36. The purge air system.

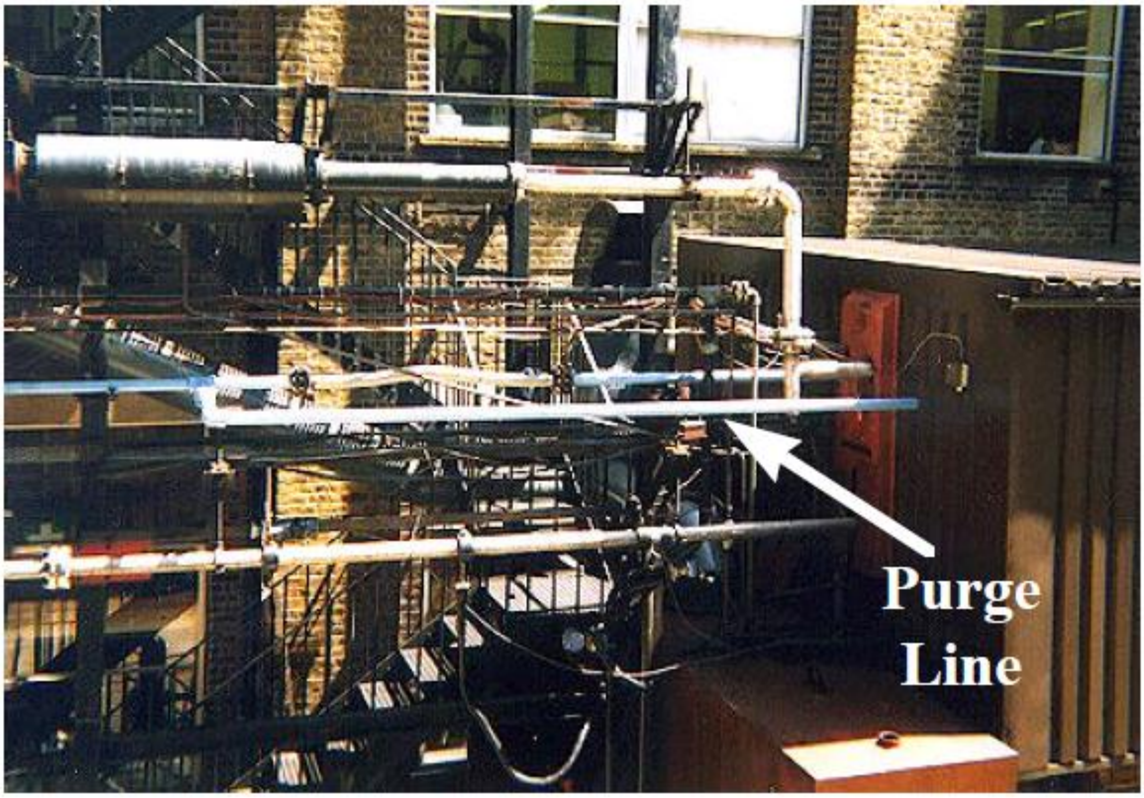

Figure 4.37. Photograph of the purge air line.

The needle valve shown in Figure 4.38 was used in order to control the purge air flow rate.

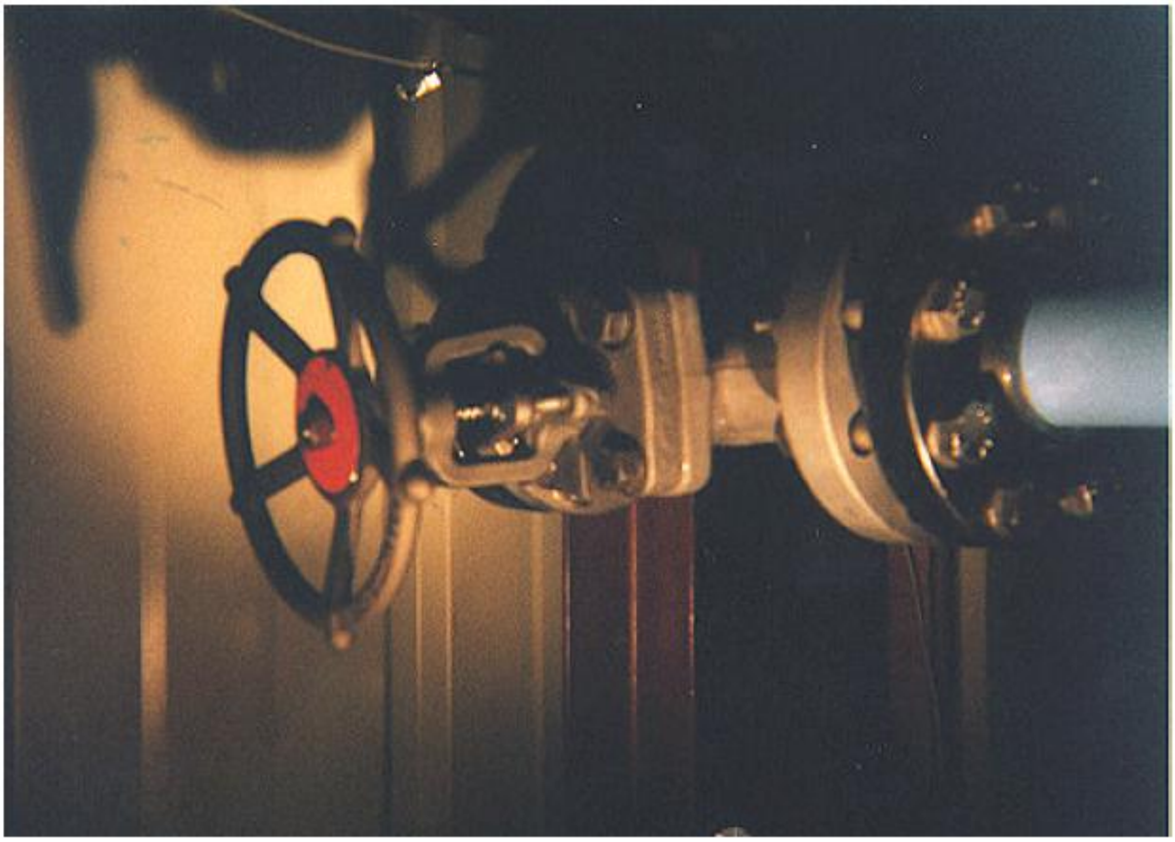

Figure 4.38. High pressure needle valve.

The viewing tube is formed by a pipe extension of the air distributor, welded to the 1 inch pipe. The air enters through the flexible hose of the air distributor, flows down on the outside of the viewing tube towards the viewing window and then flows into the viewing tube. A schematic diagram presented in Figure 4.39 shows a side view of the inside of the air distributor. The front view of the inside of the air distributor is illustrated in Figure 4.40.

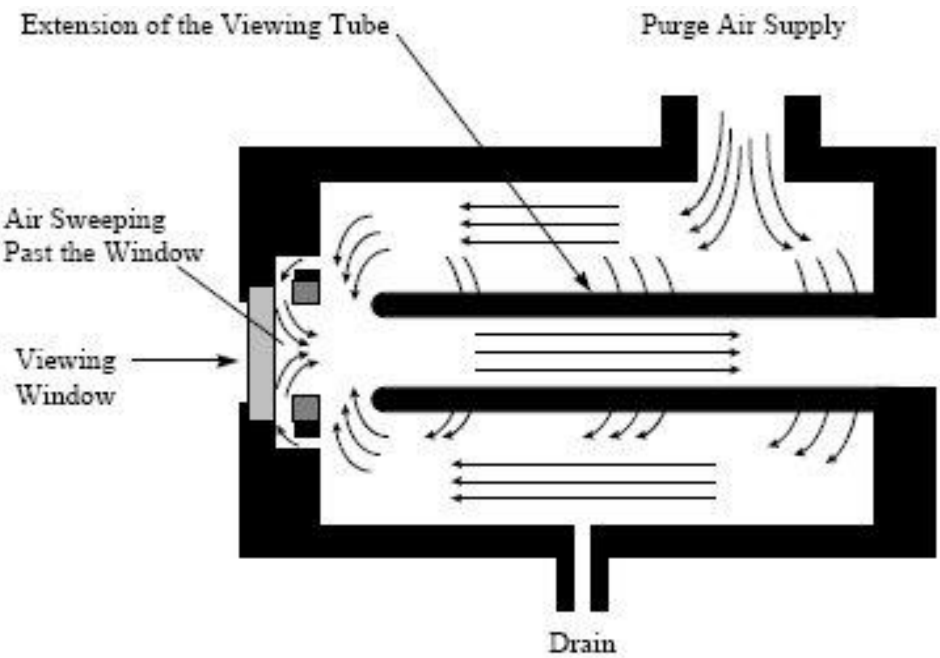

Figure 4.39. Side view of the air distributor (Badie, 2000).

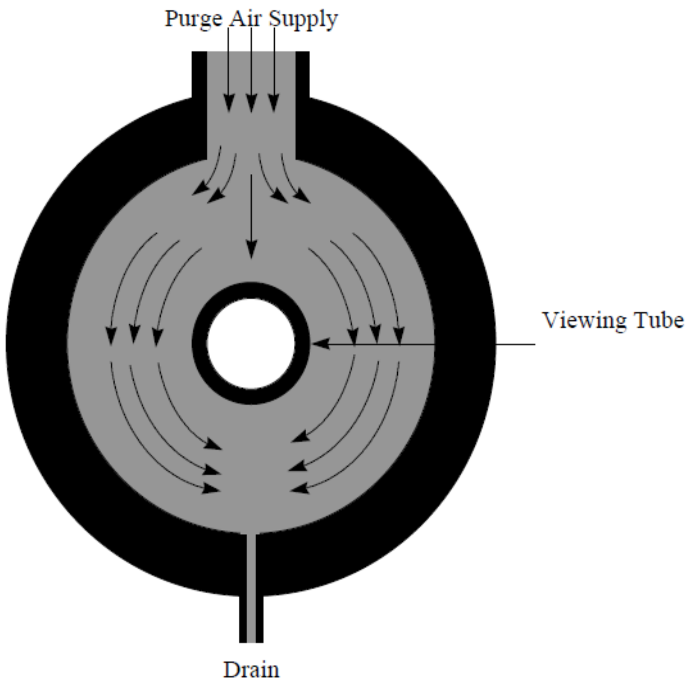

Figure 4.40. Front view of the air distributor.

Photographs (side and front views) of the air distributor are shown in Figure 4.41 and 4.42.

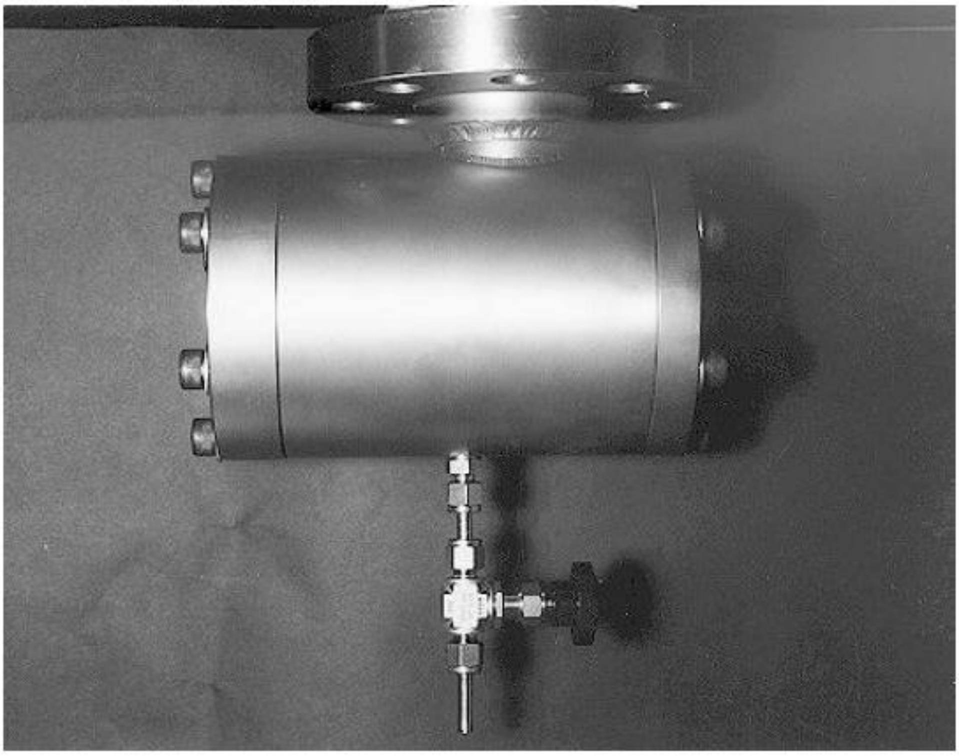

Figure 4.41. Side view of the air distributor.

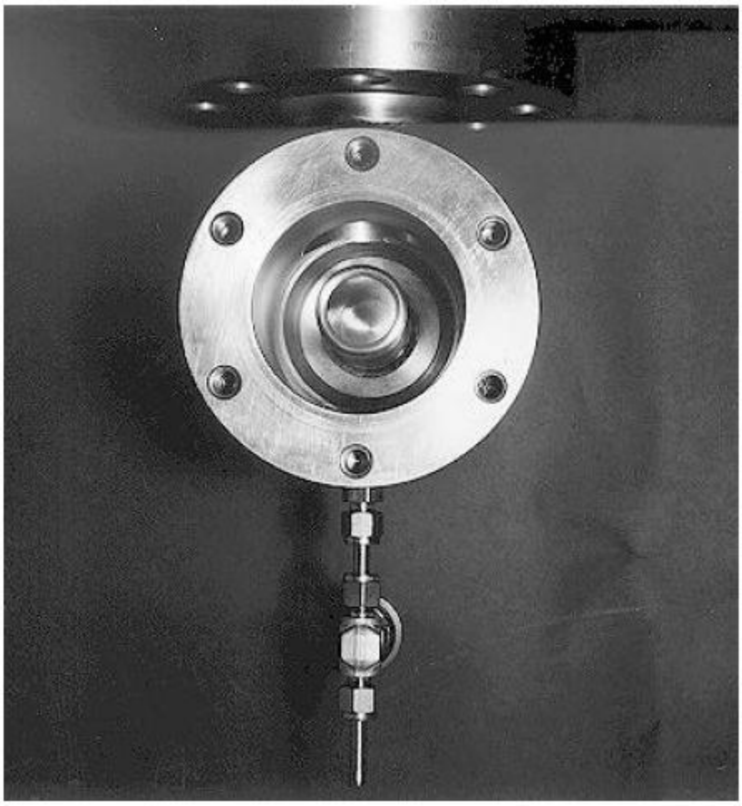

Figure 4.42. Front view of the air distributor.

The purge air sweeps across the window section through inlet and outlet passages so that the window section is kept constantly dried (see Figure 4.43).

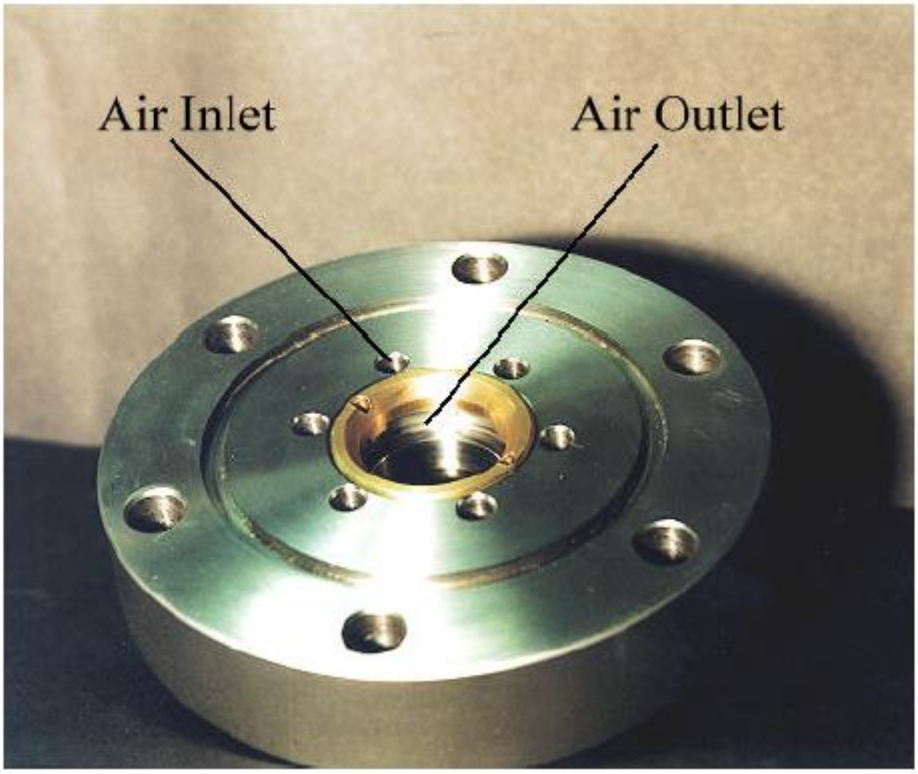

Figure 4.43. The window section.

In operating the axial view photography system, the purge air system is introduced prior to any operation involving liquids so that the air distribution section and the viewing window are kept free of impinging droplets; in addition the purge air is kept running for some time after the end of the experiments to ensure that the viewing system is cleared in preparation for the next experiment.

The lens is connected to an Olympus i-SPEED 2 video camera, shown in Figure 4.44, capturing images at a framing rate up to 2000 per second. The use of the Olympus high speed camera (CMOS 1280 x 1024 sensor) is a considerable advance since it provides a high frame rate, extreme high light sensitivity and high resolution giving an extremely detailed view of the flow. The camera is mounted on a frame onto the back plate adjustable for height and lateral position and the frame is attached to the top of the axial viewer. A schematic diagram of the high speed camera frame is presented in Figure 4.45.

Figure 4.44. The i-SPEED 2 video camera mounted on the camera frame.

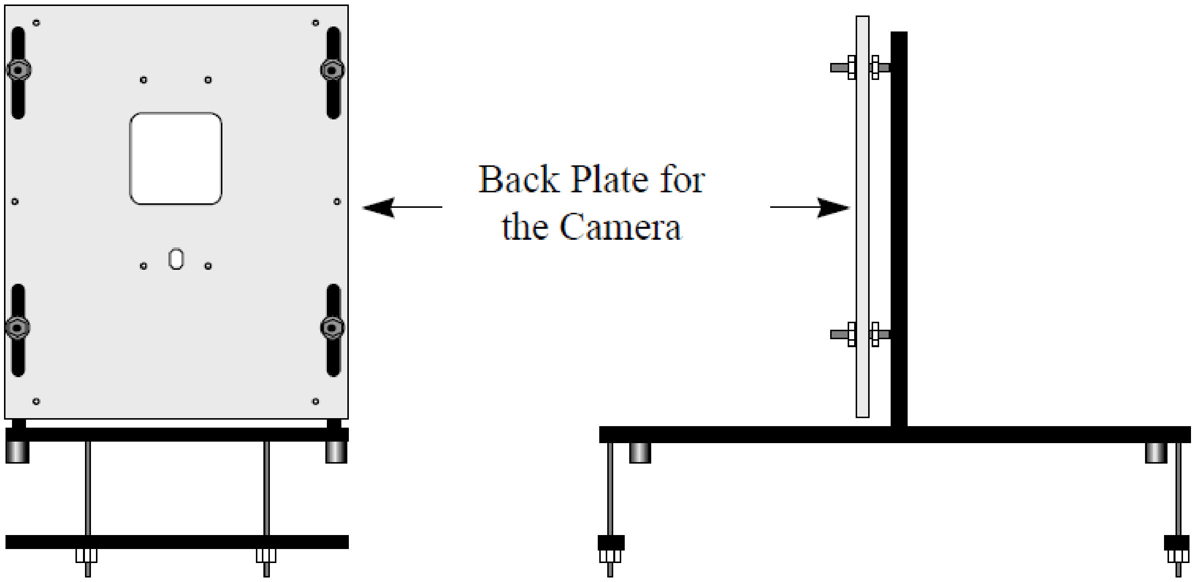

Figure 4.45. The high speed camera frame.

A mirror holder is used with a mirror placed at 45^o to the tube axis and adjacent to the viewing window. The image of the flow was thus reflected at 90^o towards the camera which was too voluminous to mount directly in line with the test section. The section with the mirror is shown in Figure 4.46. The section with the mirror holder is attached behind the back of the air distributor as illustrated in Figure 4.47.

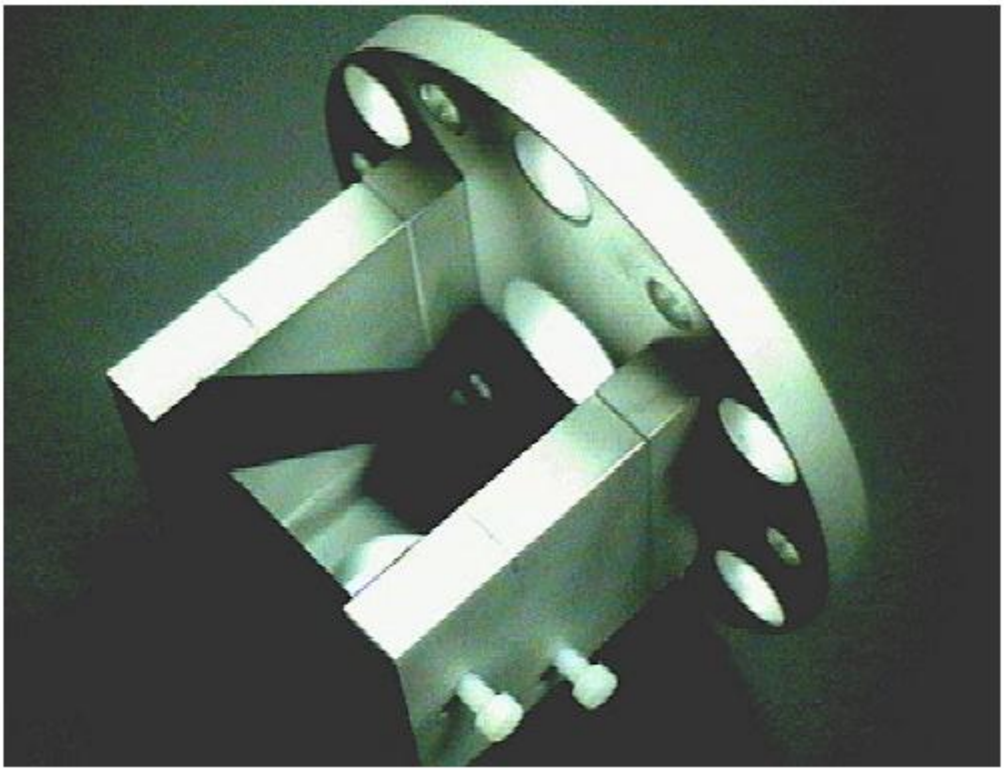

Figure 4.46. The mirror holder.

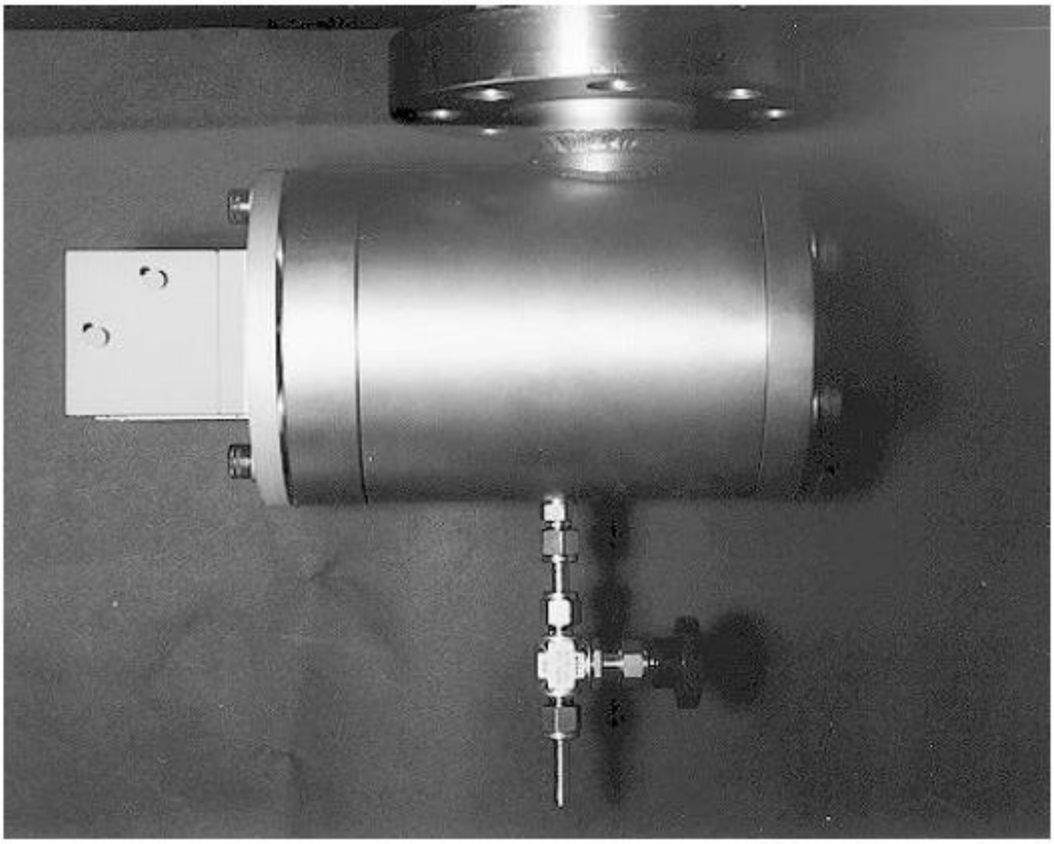

Figure 4.47. The air distributor and the 90^{o} reflecting system.

The different pieces used to assemble the complete viewing system are shown in the photo graphs in Figure 4.48 (side view) and in Figure 4.49 (view from above).

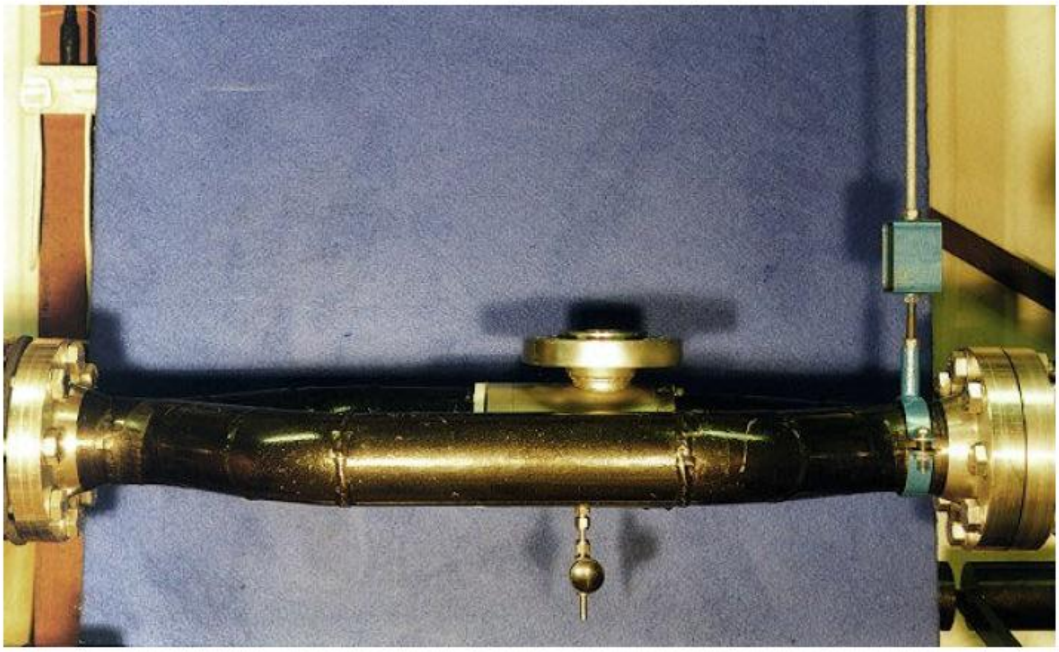

Figure 4.48. The axial viewer.

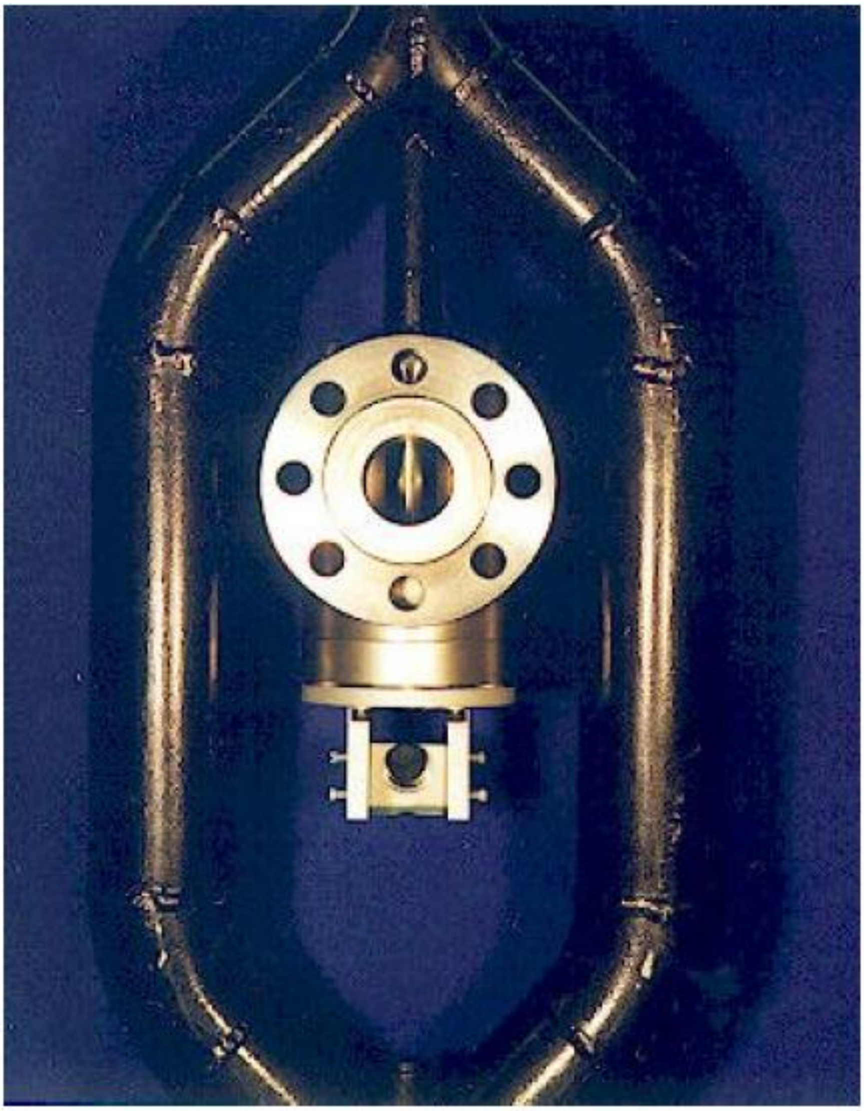

Figure 4.49. The axial viewer view from above.

A photograph of the complete axial viewing system in which are assembled the axial viewer, the camera frame, the air purge line and the camera is illustrated is Figure 4.50.

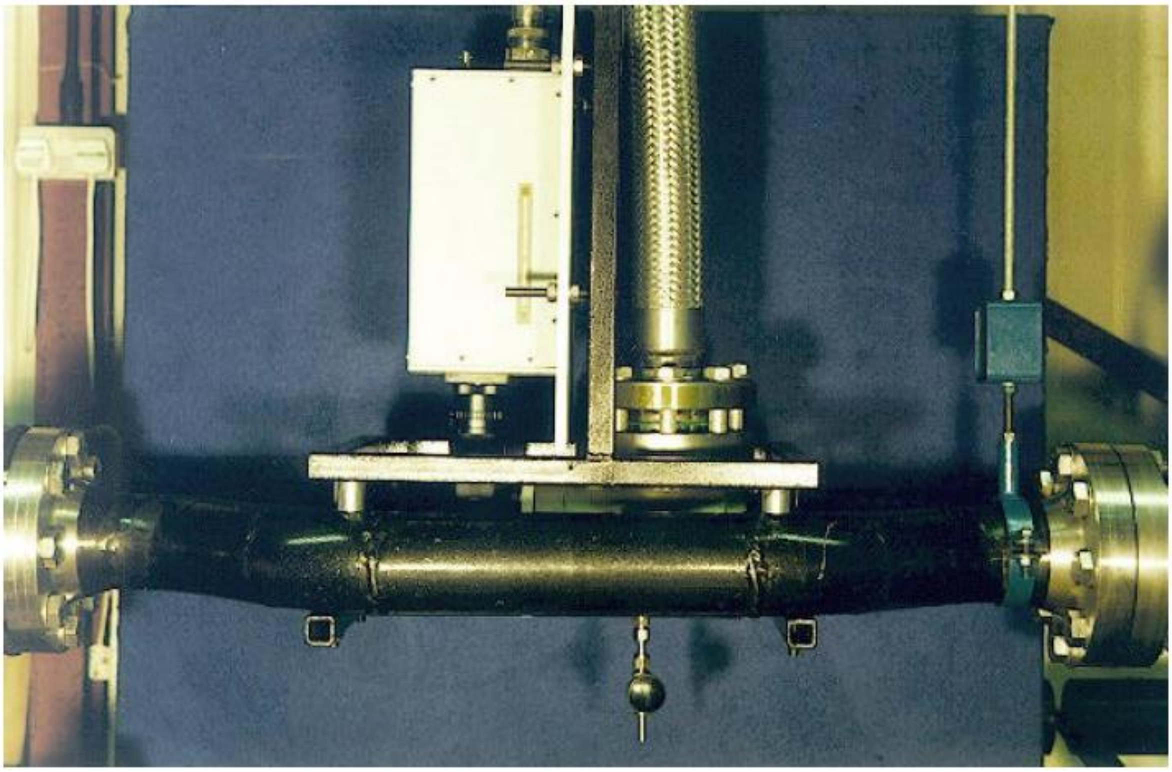

Figure 4.50. The complete axial viewing system showing the camera in position.

The axial viewing system is placed between the end of the test section and the slug catcher as shown in Figure 4.51. It is connected with a rotating flange to the gamma densitometer. The rotating flange is here to give more flexibility allowing the user to orientate the viewer along the pipe axis.

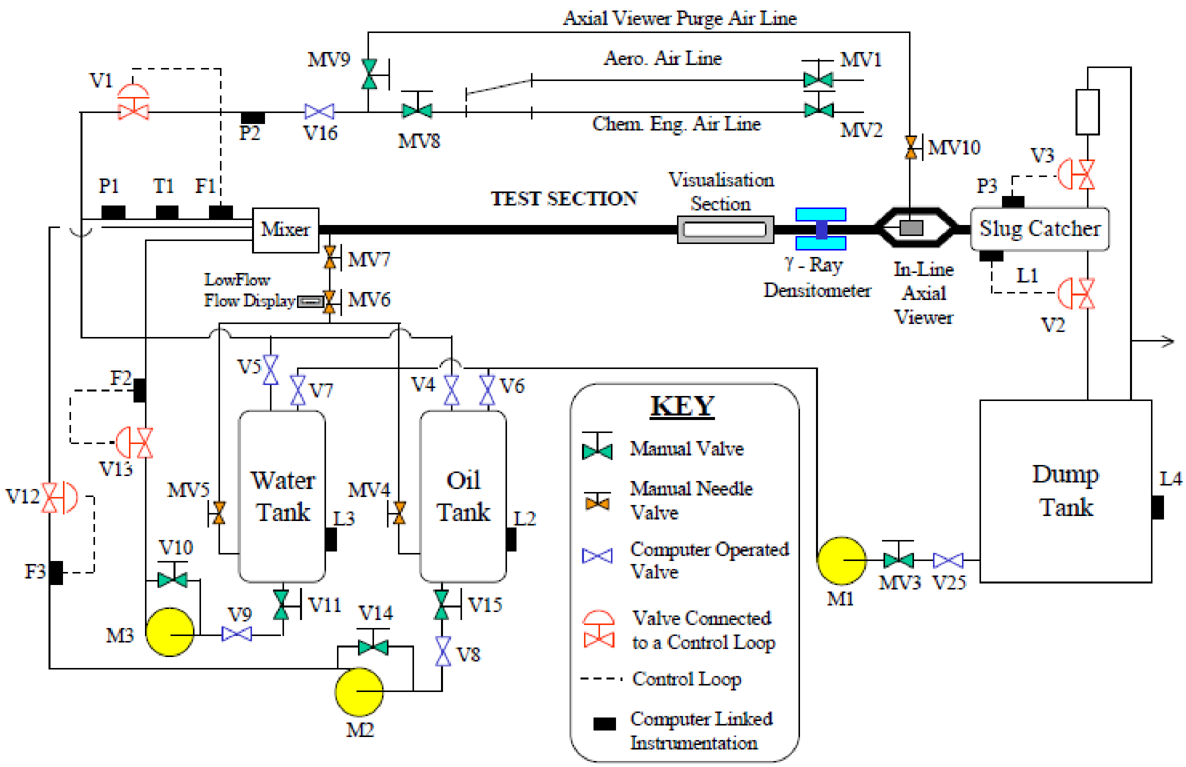

Figure 4.51. Schematic diagram of the WASP facility showing axial viewing device in position.

Two 500W halogen lamps were used to illuminate the test section for the axial view photography test. The 1 meter transparent Perspex visualisation section is 1.5 meters upstream the viewing window, giving a useful flexibility in terms of the position and the thickness of the illuminated plane. It is important to note that the ring of light obtained with the halogen lamps is not perfectly uniform due to presence of the metal guard around the Polycarbonate section, the large slits on either side of it being of different size, thus different amount of light can pass though the viewing section.

The image acquisition system is shown in Figure 4.52. It is composed of a high speed camera a memory card and a computer. Once the conditions are set and the steady state is reached, the flow is recorded at a pre-set framing rate with the Olympus high speed camera. The data are then downloaded from the camera onto a memory card and can be played back using a computer.

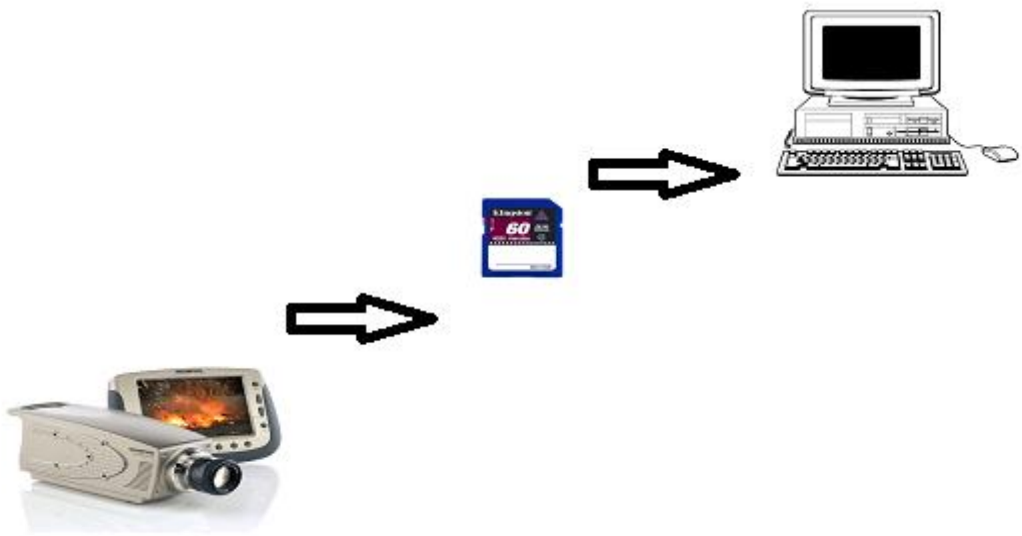

Figure 4.52. The image acquisition system.

4.3.2.7. Liquid film flow rate distribution. An important new measurement made in the present work was that of circumferential distribution of liquid film flow rate. Though limitations of time and the unavailability of the WASP facility restricted the number of such measurements which could be made, a limited range of data were obtained for comparison with the modelling methods (see Chapter 8). The principle used in this measurement was to separate a known sector of the film and to measure the flow rate in this sector by extracting it through a porous sinter wall section. The design of the device constructed for application in the WASP facility is shown in Figure 4.53. The device is composed of interchangeable fins, a sinter section, a mounting section and an extraction chamber.

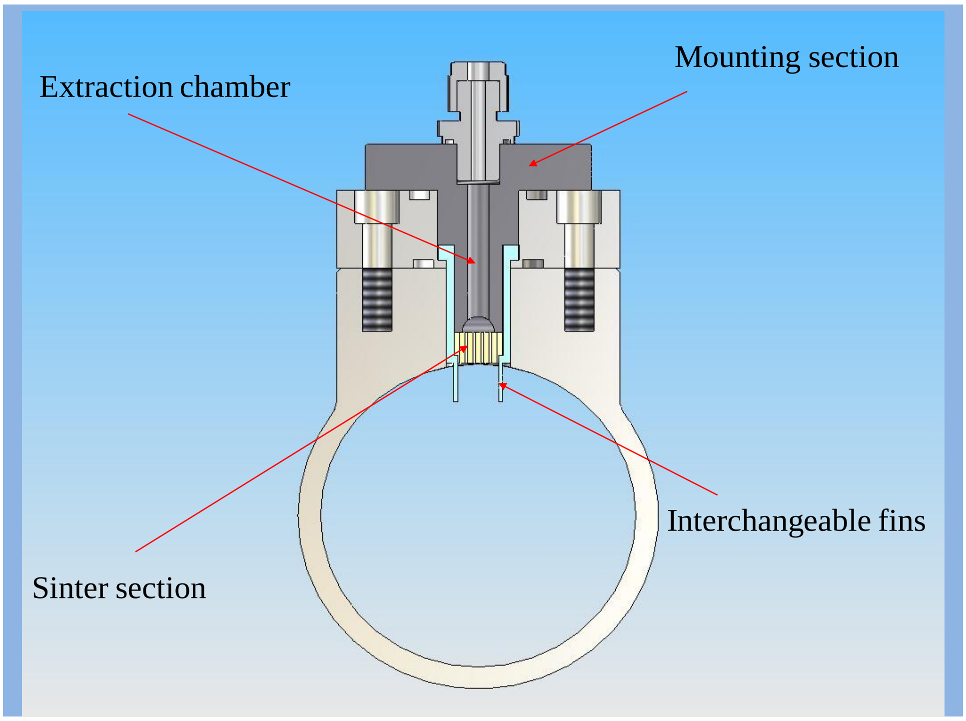

Figure 4.53. Film extraction section.

The distributions of entrained liquid film flow rate around the tube periphery are of great importance in horizontal annular flows. The film flow varies with circumferential position and it is therefore necessary to use localised measurements. The local film flow rate device used was based on one developed for a much smaller diameter (32 mm) tube by Butterworth and Pulling (1973) (see Figure 4.54).

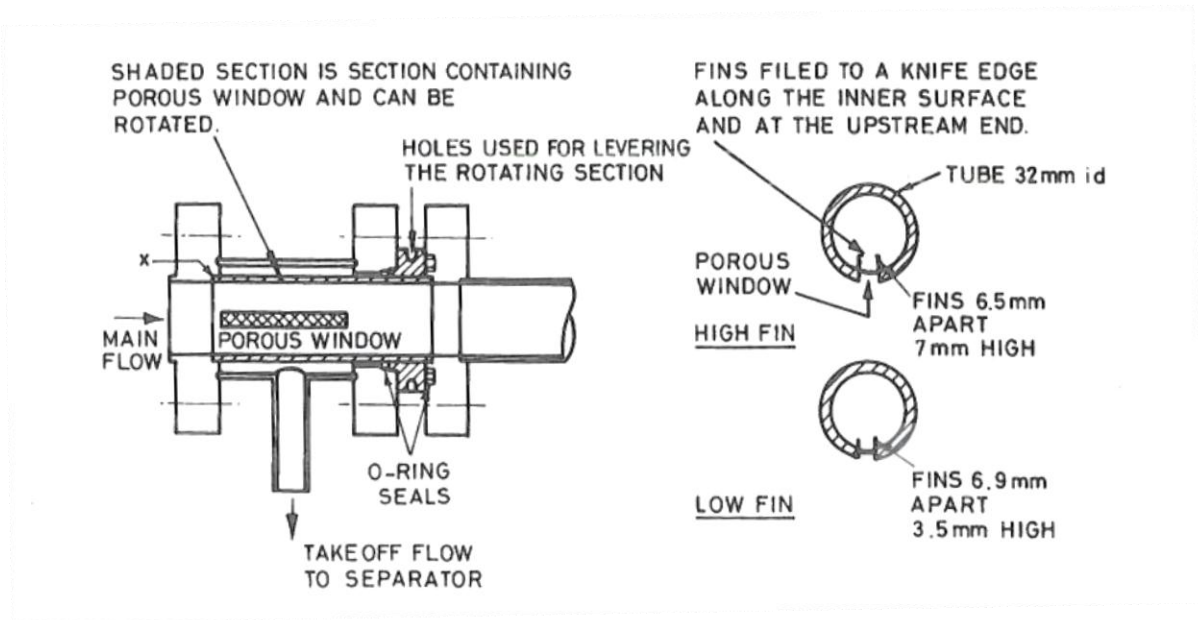

Figure 4.54. Film extraction device for measurement of film flow rate distribution (Butterworth & Pulling, 1973).

A segment of the film flow is separated by fins so that adjacent portions of liquid film are blocked. The separated film segment is removed through a porous wall section using a suction method. Fins of 6.5 mm ("high fin") and 3.5 mm ("low fin") height were used and Figure 4.55 shows results for local film flow rate as measured using the device with these two respective fin heights. As will be seen, there is some sensitivity to the fin height near the top of the tube, but the effect is rather small.

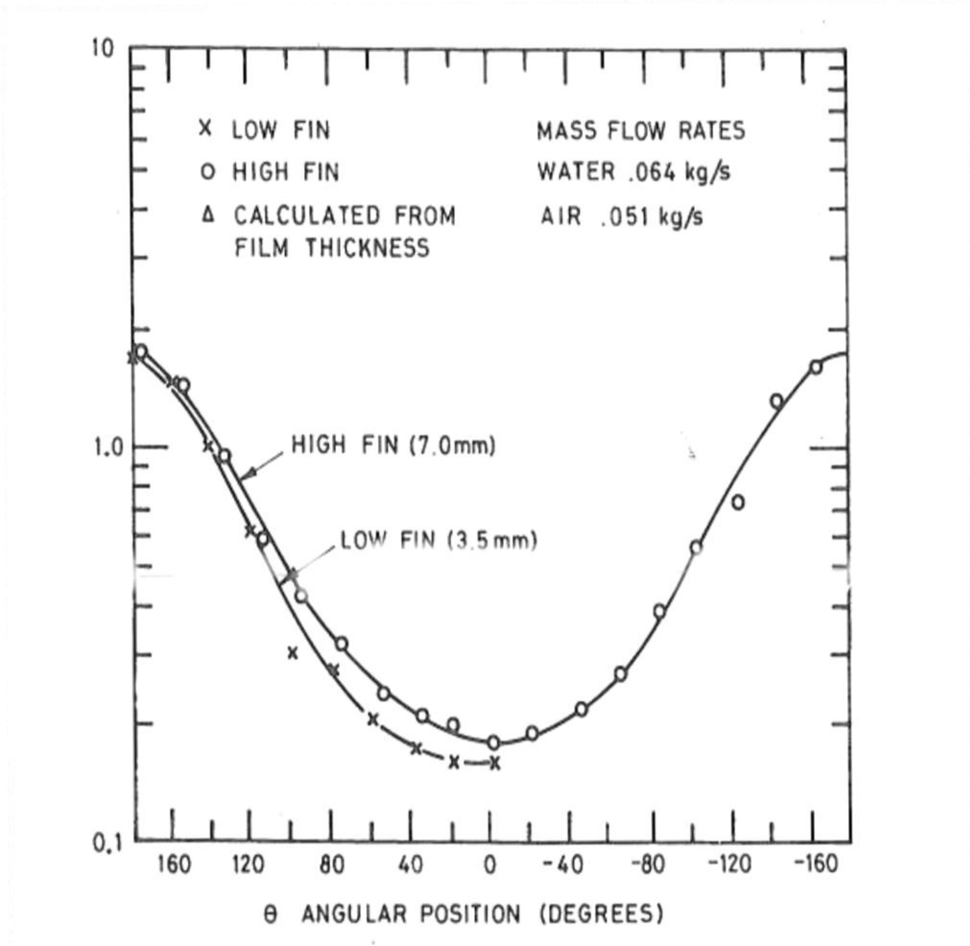

Figure 4.55. Variation of peripheral film flow rates around tube for low water flow conditions. (Butterworth & Pulling, 1973).

The original schematic of the film extraction device for the WASP facility is illustrated in Figure 4.56. This design needed some alteration because in the original sizing the slot was too long and thin and there were some problems for the welding. There also existed some stagnation zones because of the extraction cavity dimensions.

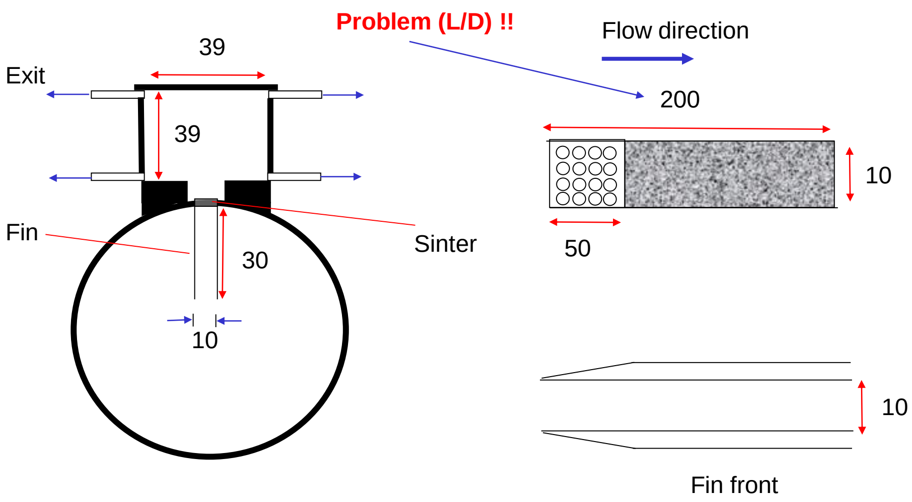

Figure 4.56. Original schematic of the film extraction device for the WASP facility.

A new design for the extraction device was constructed as shown in Figure 4.57. In the new design, the slot was shorter and slightly wider. The extraction cavity dimensions were smaller, with a lower holdup of liquid. This new design was found to perform much better. Note that the film collection is over an equivalent 14.7 degrees around the periphery.

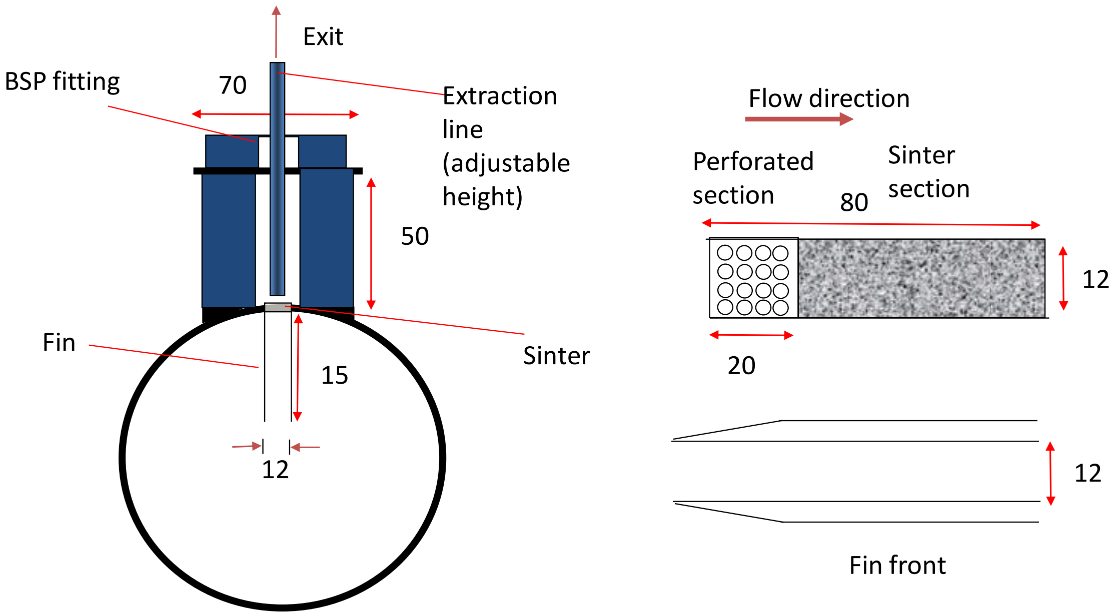

Figure 4.57. Schematic of the film extraction device for the WASP facility.

Illustrations of the film flow rate device are shown in Figures 4.58, 4.59 and 4.60 respectively.

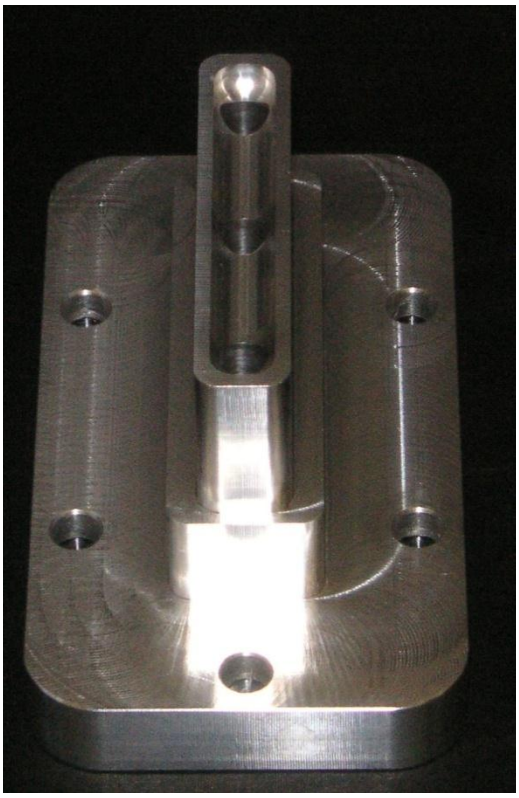

Figure 4.58. Photograph of the mounting section for the film flow rate distribution device (top view).

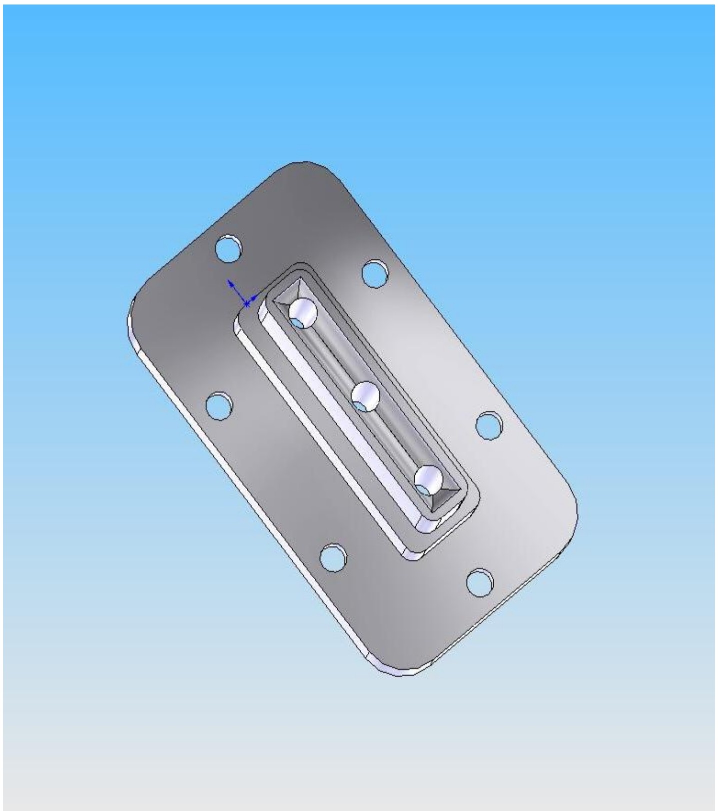

Figure 4.59. Schematic of the top view of the mounting section.

Figure 4.60. Photography of the extraction section device mounted on the test section.

The experimental setup for the liquid film flow rate measurements is illustrated in Figure 4.61. The liquid that was originally in the separated segment of film flows (together with a small amount of air) into a gas-liquid separator (a simple vessel) where the gas and liquid streams are separated and monitored. The arrangement shown in Figure 4.61 is for a three-phase flow where two liquid phases (oil and water) can be separated and measured; however, the experiments described in this thesis were restricted to one liquid phase (i.e. water).

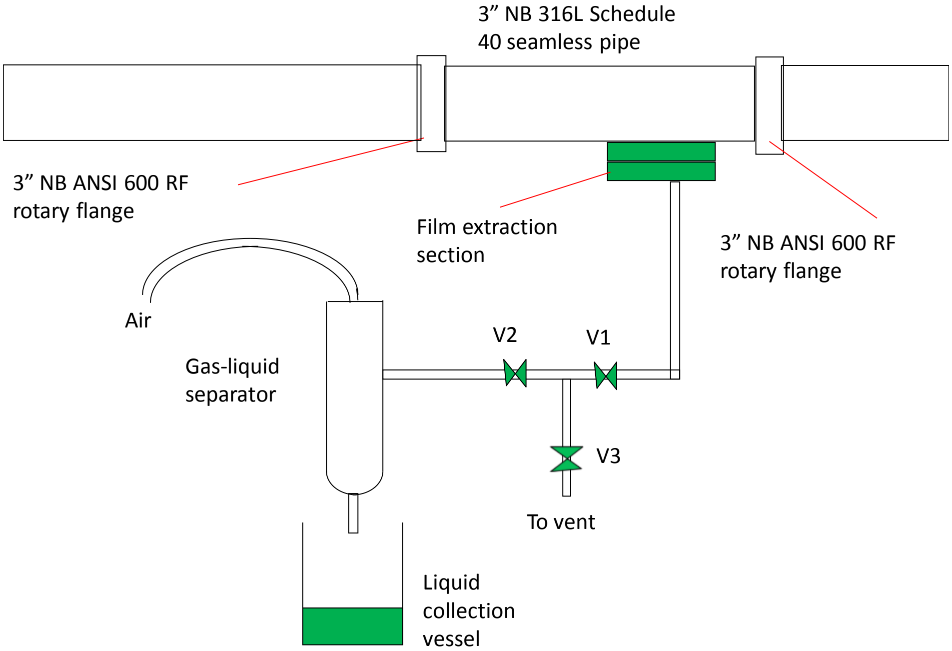

Figure 4.61. Experimental setup for the liquid film flow rate measurements.

The film flow rate device mounted on the test section is illustrated in Figure 4.62.

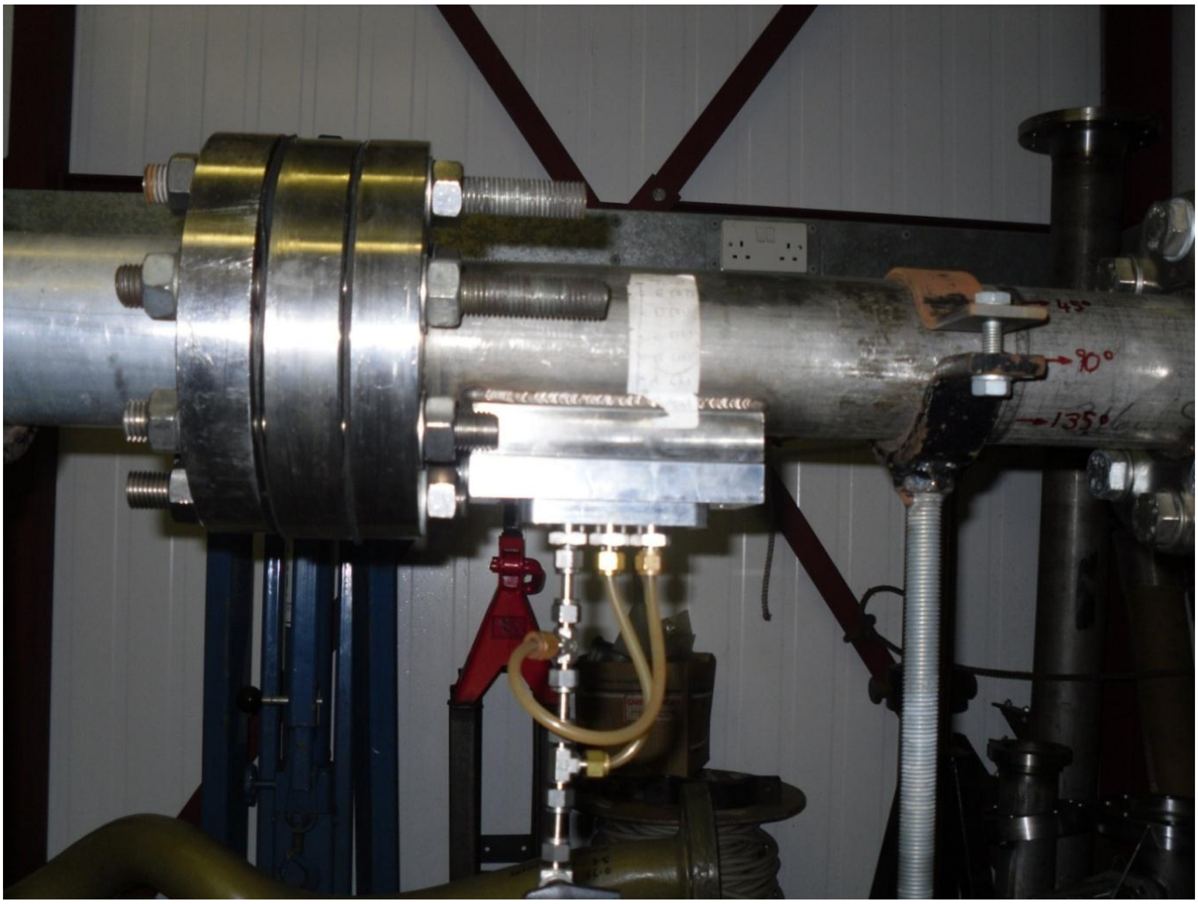

Figure 4.62. Photograph of film flow rate device mounted on the test section.

The liquid film flow rate in the measurement sector (see Figure 4.56) was determined by adjusting the gas flow rate through the sector. Thus, with valve V1 (see Figure 4.61) open and V3 closed, the effluent flow rate to the gas-liquid separator was adjusted by turning valve V2. The flow rate of the liquid separated from the effluent was determined by measuring the amount collected in the liquid collection vessel in a given time (typically around 2 minutes). The liquid flow rate was measured as a function of the number of turns of V2 as is exemplified in Figure 5.25. When the valve is opened sufficiently, the liquid flow rate collected becomes independent of valve position.

4.3.2.8. Accuracy of the measurements on WASP

Table 4.2 lists the experimental measurements made on WASP with estimates of the measurement error.

Measurement	**Error ±**
Superficial Gas Velocity	0.2 $m.s^{-1}$
Superficial Liquid Velocity ($u_{L,S}$ < 0.05 $m.s^{-1}$)	0.0001 $m.s^{-1}$
Superficial Water Velocity ($u_{L,S}$ > 0.05 $m.s^{-1}$)	0.001 $m.s^{-1}$
Superficial Oil Velocity ($u_{L,S}$ > 0.05 $m.s^{-1}$)	0.001 $m.s^{-1}$
Pressure Gradient	1 $Pa.m^{-1}$
Mean Holdup	0.0025
Temperature	0.1°C
Local Entrainment Flow rate	0.04 $g.min^{-1}$
Liquid Film Flow rate	0.0001 $g.min^{-1}$

Table 4.2. Accuracy of the experimental measurements.

CHAPTER 5

Experimental results

The facilities and techniques used in the experimental work are described in Chapter 4. In this present Chapter, the results obtained are presented. Section 5.1 describes the results obtained in the visualization studies on the LOTUS facility (see Section 4.1) and Section 5.2 describes those obtained on the LOWPRESS facility (see Section 4.2). The largest body of experimental work (described in Section 5.3) was carried out on the WASP facility and included studies of stratifying annular flows using axial and side view photography (Section 5.3.1) and film flow rate measurements (Section 5.3.2). The WASP facility is described in Section 4.3 which also contains detailed descriptions of the experimental methods.

5.1 Results from work on the LOTUS facility

Table 5.1 summarizes the 31 tests carried out on the LOTUS (see Section 4.1) facility.

Campaign	Number of runs	Range Superficial Air Velocity (m.s-1)	Superficial Water Velocity (m.s-1)	Frame per second
1	11	5.26-27.93	0.021	500
2	9	5.88-14.64	0.031	500
6	11	8.26-40.05	0.01-0.041	1000

Table 5.1. Tests carried out on the LOTUS facility (32.8 mm diameter tube).

Videos of side views of stratified and stratifying-annular flows in a 32.8 mm diameter pipe were recorded for several superficial gas velocities at a given superficial liquid velocity. The transition between stratified and annular flows is illustrated in a series of snapshots from of a selection of videos obtained and is shown in Figure 5.1. These videos can be found in the CD attached to this thesis (Videos 5.1.a, 5.1.b, 5.1.c and 5.1.d). It was observed that the frequency of interfacial waves increases with an increase of the superficial gas flow rate.

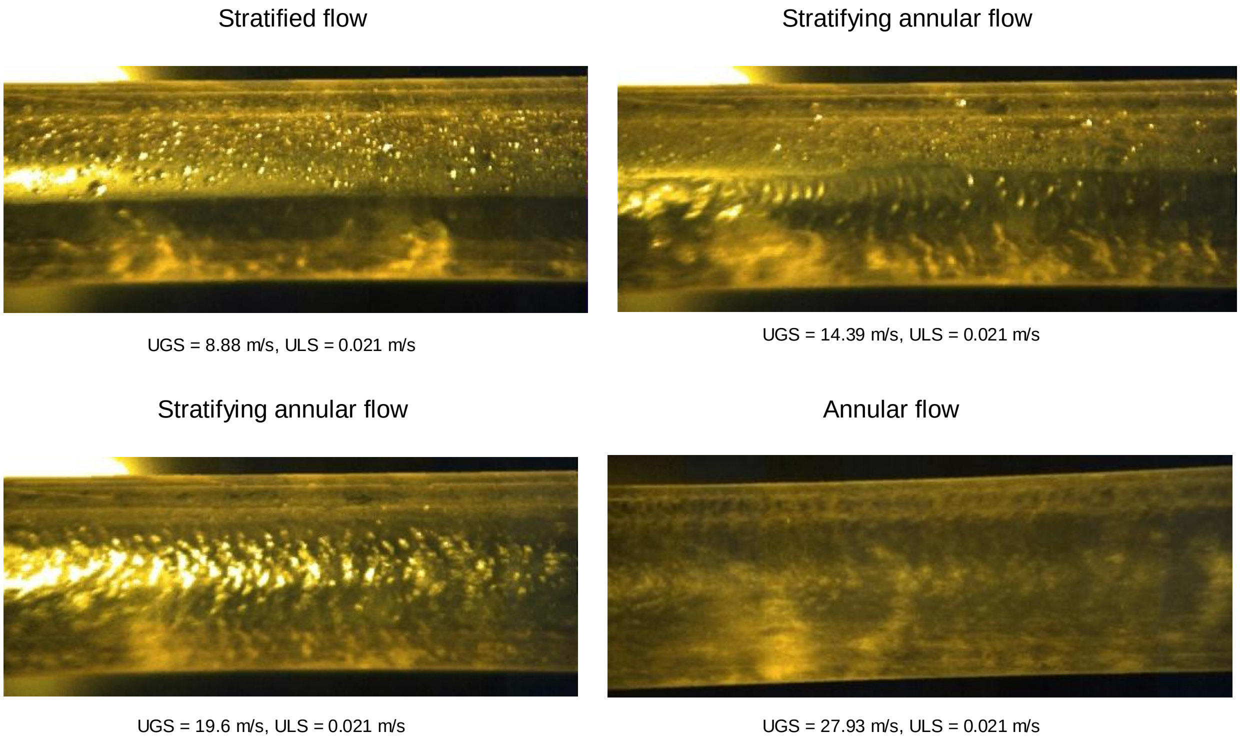

Figure 5.1. Videos of 32 mm experiments: Stratified and stratifying-annular flows. Side views in the LOTUS facility (32.8 mm tube).

5.2 Results from work on the LOWPRESS facility

Using the LOWPRESS facility (see Section 4.2), air-water flows were studied in a 76 mm internal diameter tube. The structure of liquid films in stratified flows for a 76 mm diameter pipe was visualized with the FEP technique using an ultra violet light (see Section 4.2 for details of the experimental arrangements). Very high quality detailed videos and pictures were obtained using this method and are exemplified in Figures 5.2a and 5.2b. Because of restrictions in the available gas velocity, it was not possible to obtain the required conditions in this facility to create significant liquid entrainment. The observations were limited to smooth and wavy stratified flow. To obtain significant droplet entrainment it was necessary to use the WASP facility (see below). However, the use of refractive index matching (FEP tubing) and UV-induced fluorescence is a very promising avenue for future research. Videos obtained using this technique are given in the CD appended to this thesis (videos 5.2.a and 5.2.b).

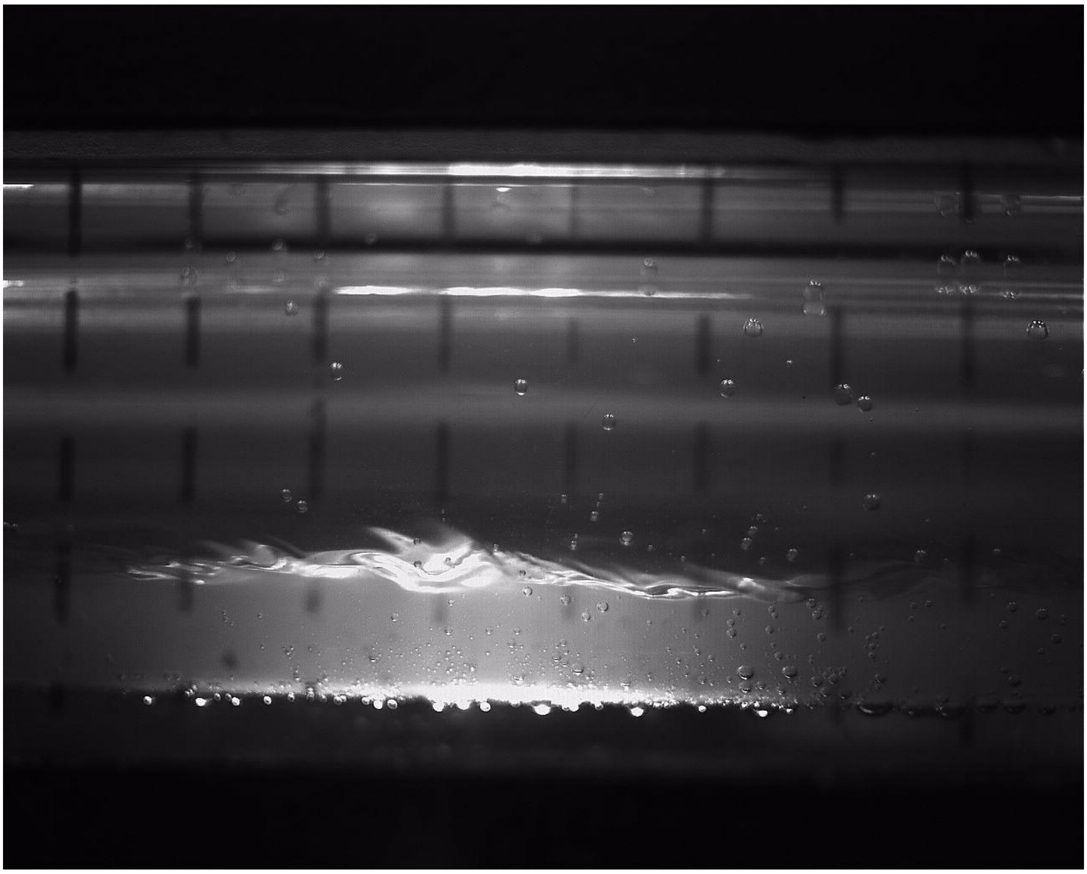

Figure 5.2a. Interfacial structure in a stratified flow observed using FEP tube and UV fluorescence (thick liquid layer).

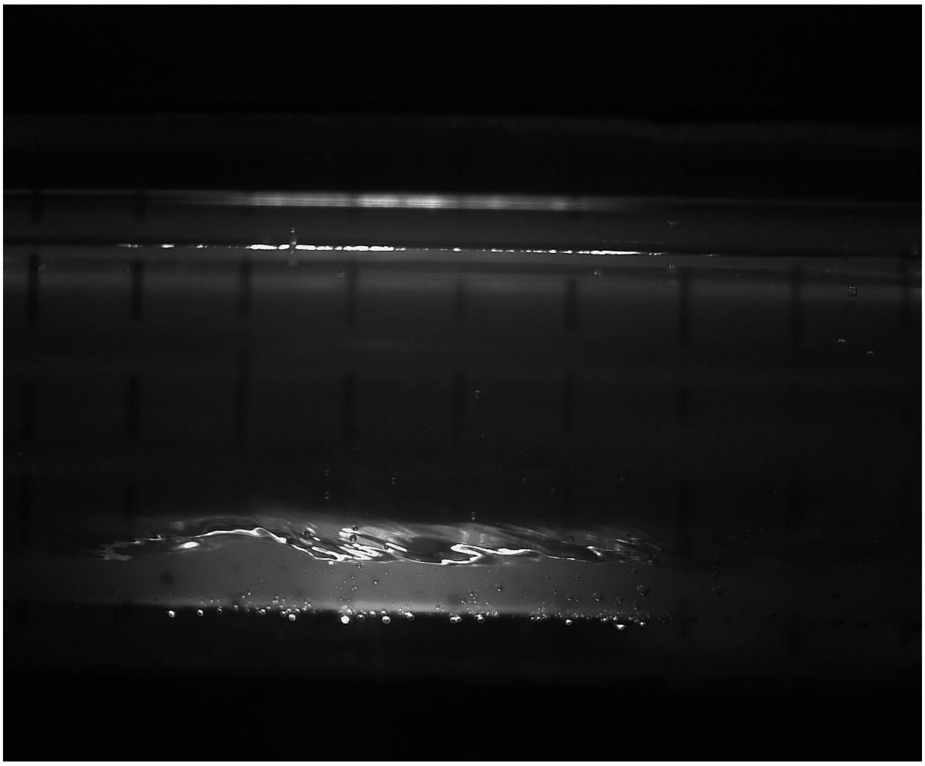

Figure 5.2b. Interfacial structure in a stratified flow observed using FEP tube and UV fluorescence (thinner liquid layer).

5.3 Results from work on the WASP facility

The major part of the experimental work described in this thesis was carried out on the WASP facility (see Section 4.3) and was focused on two main areas, namely axial view and related visualization studies (Section 5.3.1) and measurements of film flow rate (Section 5.3.2). A limited number of pressure gradient measurements were also made (Section 5.3.3). In all the studies, the emphasis was on the stratifying annular flow regime.

5.3.1 Axial view and related studies

The axial view studies carried out using the 78 mm diameter tube on the WASP facility were carried out in 5 "campaigns" as listed in Table 5.2. Here the word "campaign" is used to describe a set of experiments on the facility.

Campaign	Number of runs		Range Superficial Air Velocity (m.s-1)	Superficial Water Velocity (m.s-1)	Pipe Diameter (mm)	Side view	Axial view	Frames per second
3	14	5	5.4 - 15	0.04	79		X	500
		7	10.6-16	0.036	79		X	500
		2	17-18.5	0.033	79		X	500
4	1		7.5	0.046	79		X	2000
5	7		7.3-13.1	0.018	79		X	2000
7	7		5 – 14.8	0.03	79	X	X	1000
8	4		9.98-25	0.02-0.12	79	X	X	1000

Table 5.2. Summary of the runs carried out.

As will be seen from Table 5.2, simultaneous side and axial view video recordings were taken in campaigns 7 and 8.

Images of air-water stratified and stratifying-annular flows at constant superficial liquid velocity are presented in Figure 5.3. These pictures show the effect of the superficial gas velocity. Picture 5.3.a represents a smooth stratified flow with a flat liquid pool. Picture 5.3b shows a wavy stratified flow with a wavy liquid pool and Picture 5.3c represents a stratifying-annular flow with a wavy liquid pool, a liquid film around the circumference of the pipe and liquid droplets entrained into the gas core. At low gas velocities, an equilibrium stratified flow is obtained (Picture 5.3.a) but when the superficial gas velocity is above a given value, the gas shear stress makes unstable the liquid flow by creating some turbulence and then some waves (see Picture 5.3b). When the superficial gas velocity is increased further, the gas shears the waves, generating some droplets entrained into the gas core which may be transported to the upper part of the tube (see Picture 5.3c).

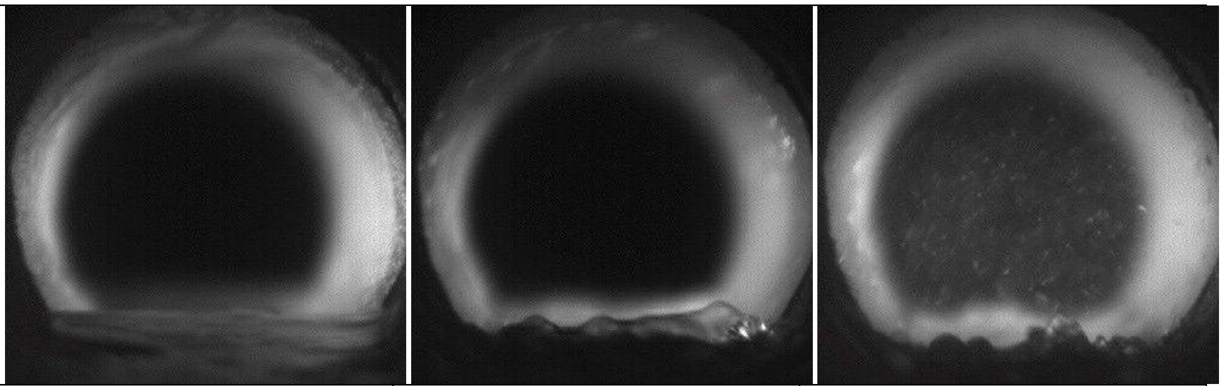

(a) $U_{G,S}$=5.4m.s^{-1} $U_{L,S}$=0.04 m.s^{-1}	**(b) $U_{G,S}$=9.6 m.s^{-1} $U_{L,S}$=0.04 m.s^{-1}**	**(c) $U_{G,S}$=15 m.s^{-1} $U_{L,S}$=0.04 m.s^{-1}**

Figure 5.3. Frames from videos of WASP (78 mm tube) experiments: Stratified and stratifying-annular flows Axial view.

We report here on the visualization of the detailed processes whereby droplets are entrained from a liquid layer by a highly turbulent gas flow in horizontal stratifying-annular flow. Key results obtained from videos of the cross sectional views of a stratifying-annular air-water flow in 78 mm diameter pipeline using axial viewing technique are presented in this Section.

Different types of droplet entrainment are identified, including ligament and bag-type breakup, as well as intermediate events, all under the same flow conditions. Results will also be presented on the subsequent motion of entrained droplets (also obtained with the axial viewing technique), including droplet deposition at the top of the pipe cross section after the droplets follow a ballistic trajectory directly after entrainment.

A typical bag breakup sequence is shown in Figure 5.4. A perturbation is formed on the interface and this is undercut by the gas to form a bag. This bag has a thick filament of liquid around its base and, when the bag bursts, this filament breaks into an arc of droplets. The bag is initiated by the gas phase undercutting a large wave on the interface. Thus, the pressure in the bag is higher than the pressure above it and this leads to bag growth. Eventually, the bag bursts and this leads to radial release of the air in the bag and the acceleration away from the interface of the arc of droplets formed from the filament.

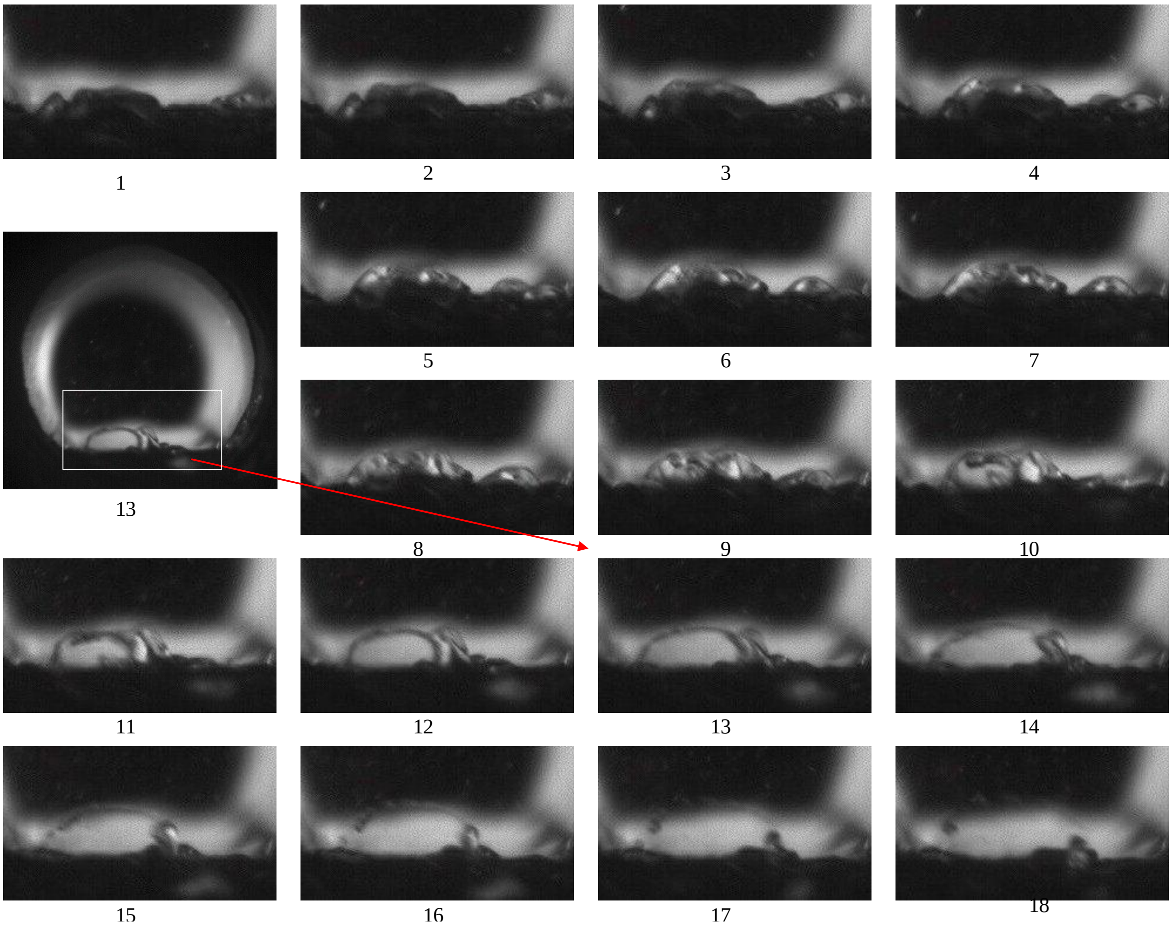

Figure 5.4. Images of air-water flows with Superficial gas velocity = 11.6 m.s^{-1} and Superficial liquid velocity = 0.036 m.s^{-1}, 500fps - Filament.

Another bag type break up leasing to a filament bursting into droplets is presented in Figure 5.5. The liquid extends as a thin film around the pipe. Some very thin varicosities can be observed on the thin plane circle quarter. The varicosities are in the same direction as the normal of the right corner of the pipe, and are thus diagonal. The plane extends, the thin parallel varicosities are then abruptly projected towards the top of the pipe, but the droplets are too small to reach the top of the pipe, and there remains a circular filament similar to that observed in the previous case (Filament (I)) which extends and breaks up into droplets. Picture 18 has been enlarged and is shown in Figure 5.6.

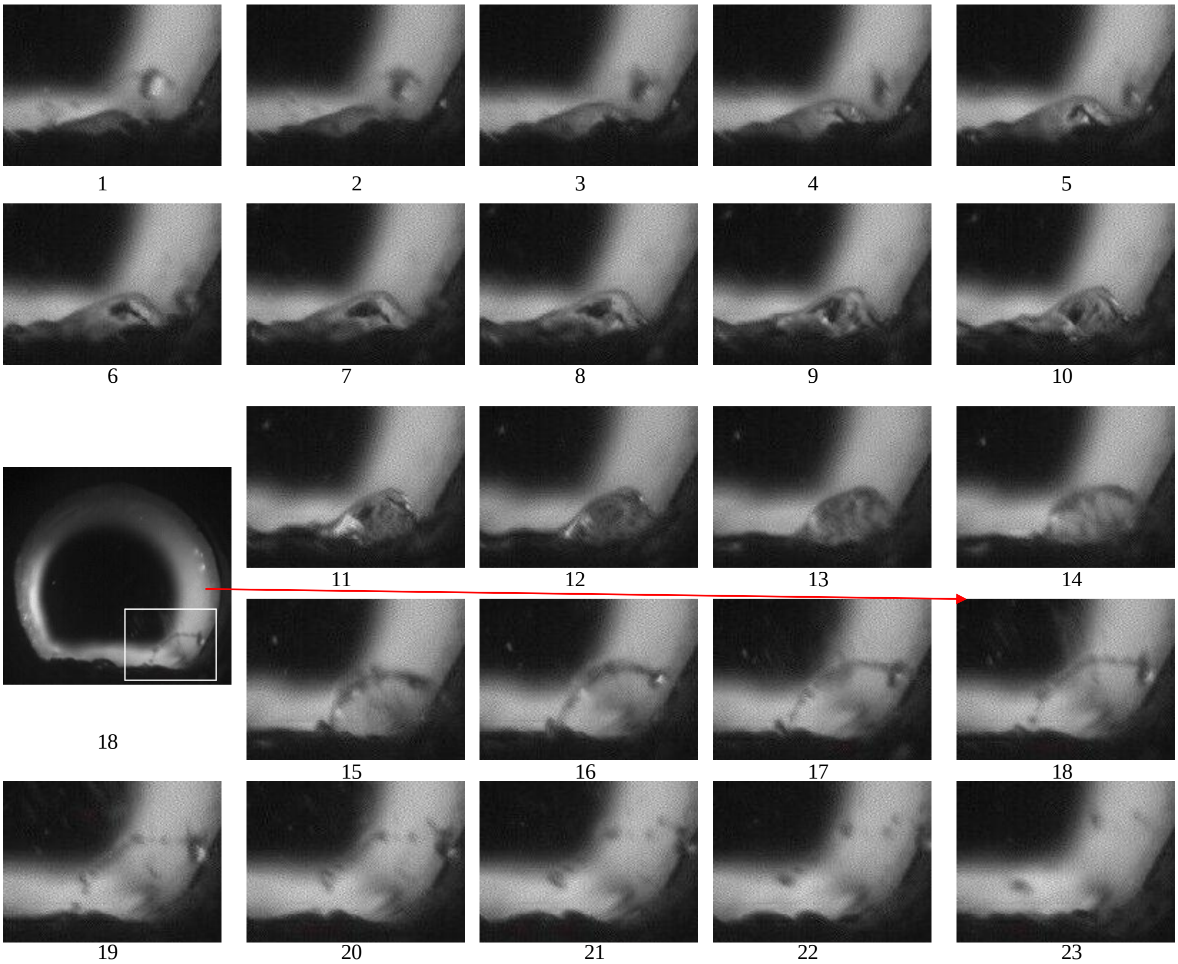

Figure 5.5. Images of air-water flows with Superficial gas velocity = 10.6 $m.s^{-1}$ and Superficial liquid velocity = 0.035 $m.s^{-1}$, 500fps - Bag break-up and filament.

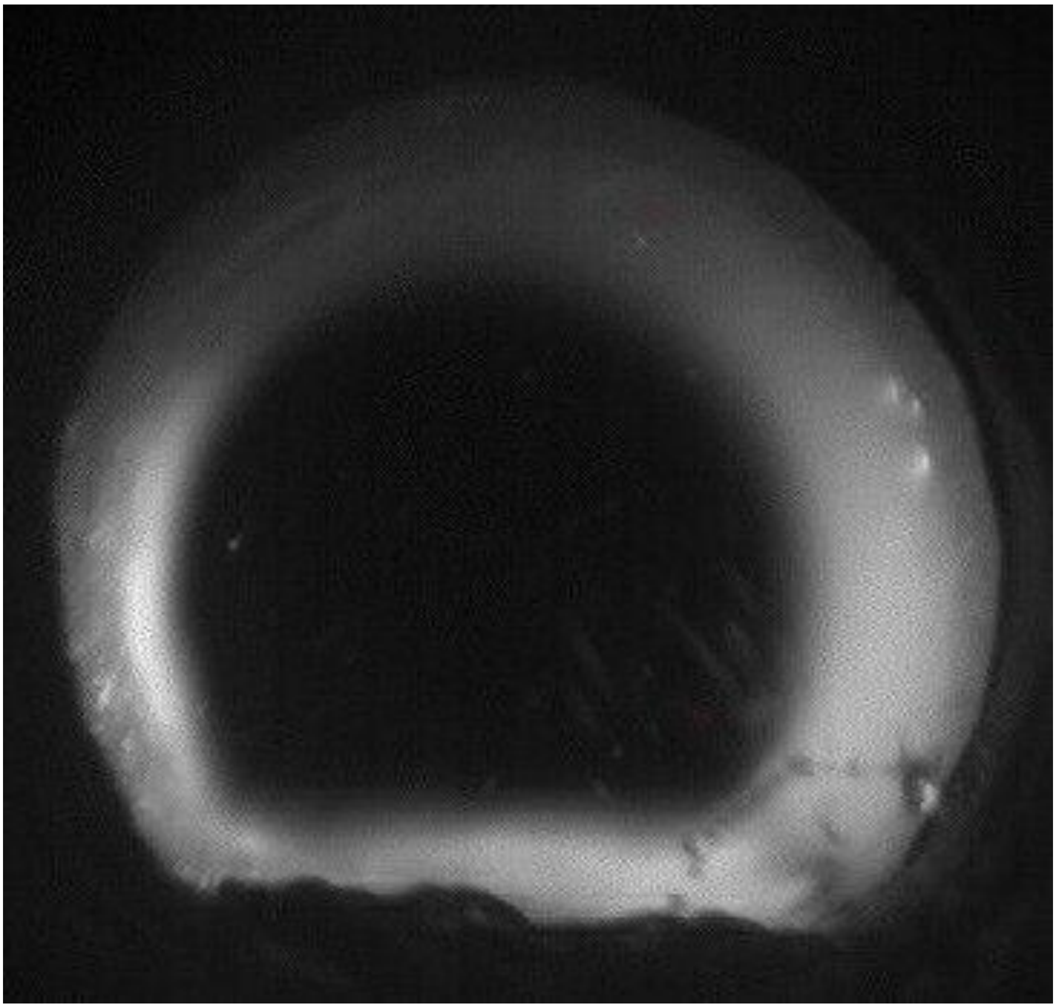

Figure 5.6. Images of air-water flows with Superficial gas velocity = 10.6 m.s^{-1} and Superficial liquid velocity = 0.035 m.s^{-1}, 500fps - Bag break-up and filament.

Some of the bag breakup events observed involve a complex evolution and breakup of multiple bags. Such a sequence is illustrated in Figure 5.7. The process starts with the appearance of several deformations of the interface and these develop to form the complex bag whose outer limit consists of thick ring of water (a “strap”) but which has a series of compartments separated by filaments whose source was the original deformations of the interface. For the case shown in Figure 5.7, five compartments in the bag are visible during the growth of the bag. The compartments break, in succession with the compartment nearest the wall being ruptured first. The last remaining remnants of the bag are formed from the strap that delineated the outside of the compound bag. The strap ruptures into quite large droplets. One node on the right of the bag evolves as a ring, which extends to break up into droplets. One of the droplets formed from this ring reaches the top of the pipe.

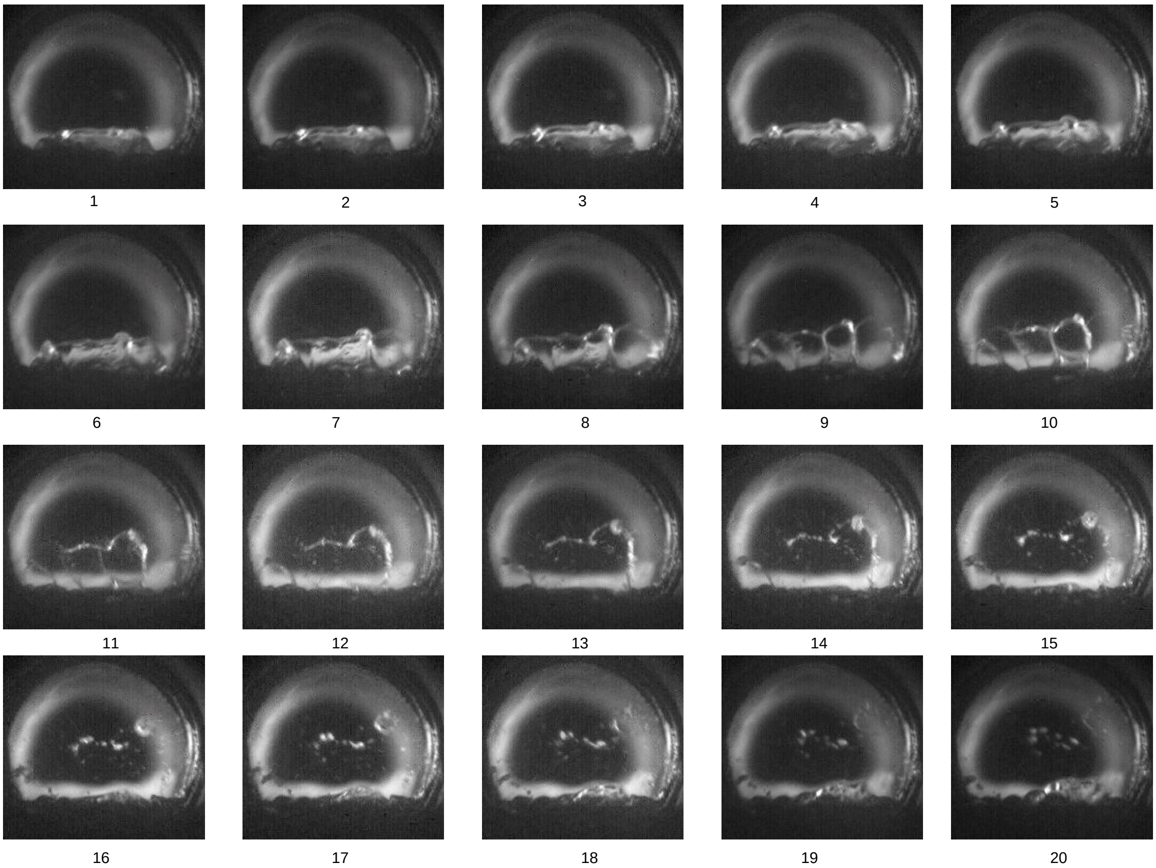

Figure 5.7. Images of air-water flows with Superficial gas velocity = 11.6 m.s^{-1} and Superficial liquid velocity = 0.036 m.s^{-1}, 500fps - Bag break-up.

Figures 5.8 and 5.9 show cases of *ligament* rather than bag breakup. In Figure 5.8, we can observe a ligament on the left hand side of the pipe and from this ligament is created a droplet which has a large initial radial velocity allowing it to be projected ballistically. The ligament is formed from a small perturbation on the interface. The proximity of the perturbation to the wall is an important factor in ligament formation and breakup. The nearer the perturbation to the wall, the more likely are the ligament and its droplet daughters to be projected upwards.

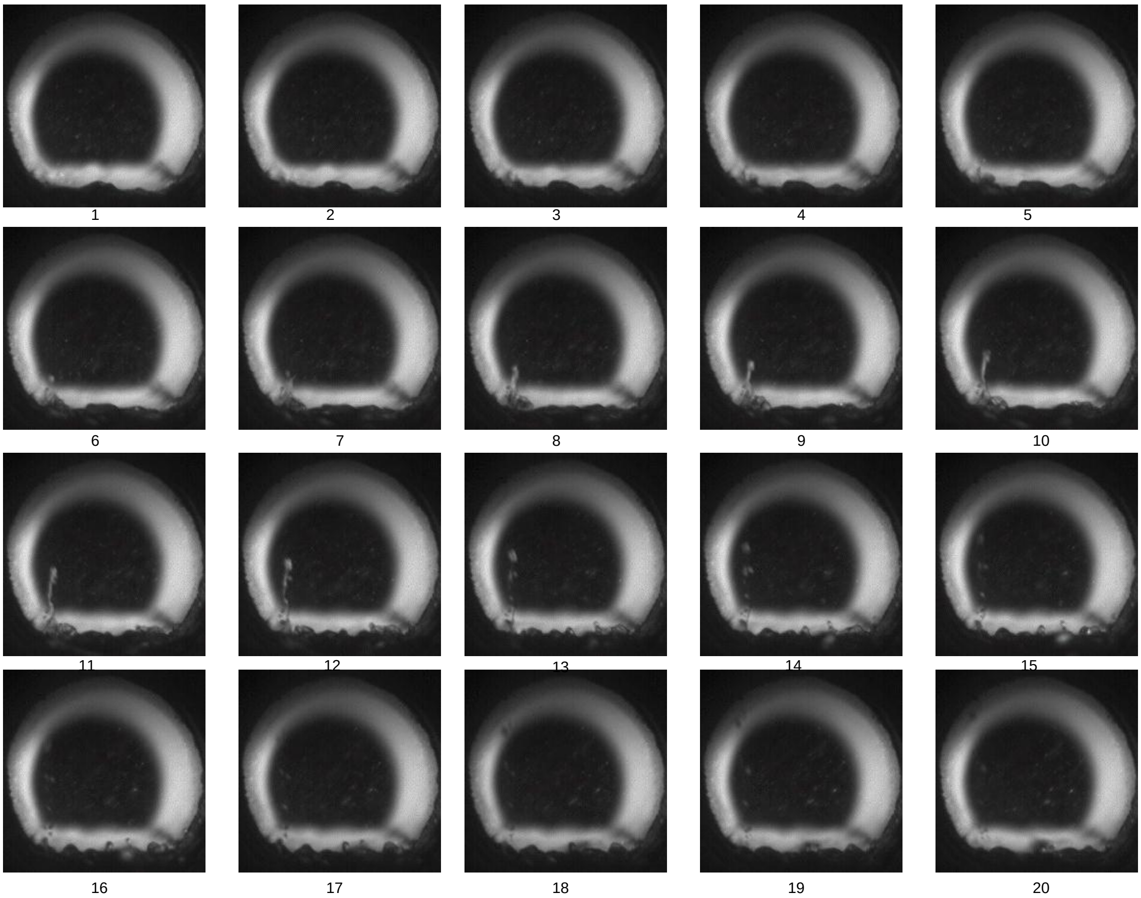

Figure 5.8. Images of air-water flows with Superficial gas velocity = 13 m.s^{-1} and Superficial liquid velocity = 0.036 m.s^{-1}, 500fps - Ligament.

Figure 5.9 shows the formation of multiple ligaments, again arising from independent small perturbations. In this particular case, the drops formed from the ligaments did not have sufficient upwards momentum to reach the top of the pipe.

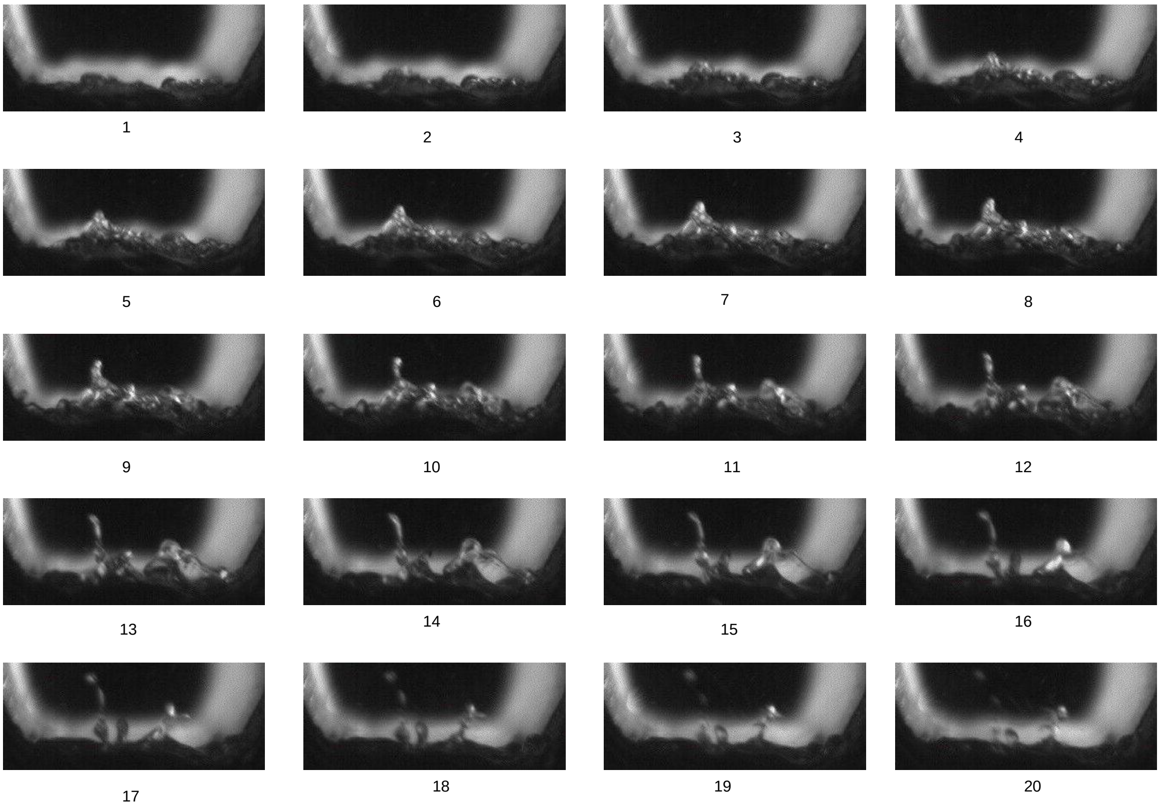

Figure 5.9. Images of air-water flows with Superficial gas velocity = 11.6 m.s^{-1} and Superficial liquid velocity = 0.036 m.s^{-1}, 500fps - Ligament.

In the above, we have made a distinction between bag breakup (Figures 5.4, 5.5 and 5.6) and ligament breakup (Figures 5.8 and 5.9). However, events may occur which demonstrate the characteristics of both types of drop formation, as exemplified by the sequences shown in Figures 5.10 and 5.11. Figure 5.10 shows the formation of ligaments arising from perturbations formed at the top of a breaking bag. The ligament thus formed then breaks up leading to the entrainment of at least three droplets, one of which reaches the top of the pipe.

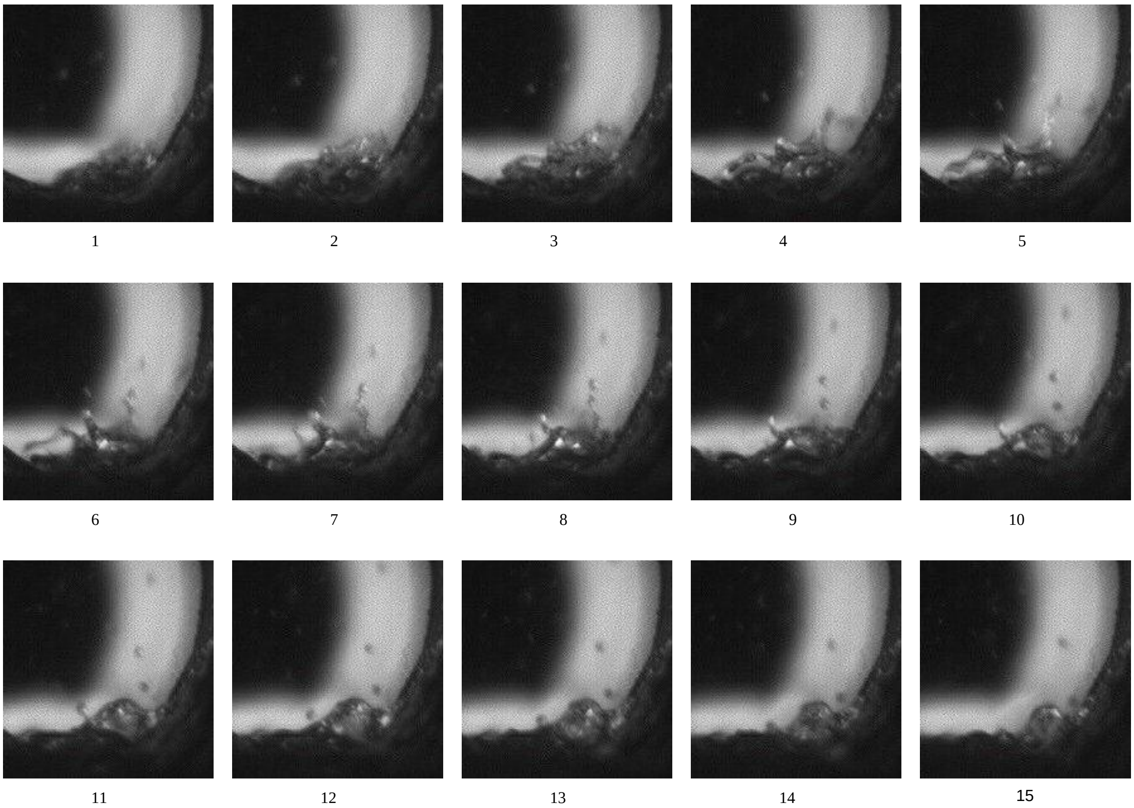

Figure 5.10. Images of air-water flows with Superficial gas velocity = 11.6 m.s^{-1} and Superficial liquid velocity = 0.036 m.s^{-1}, 500fps - Ligament formed from growing bag and breaking up into droplets which may reach the top of the pipe.

Figure 5.11 presents successive frames illustrating a mechanism of droplet entrainment which may also lead to droplet deposition at the top of the pipe. Two “lumps” of liquid are seen. The liquid lumps have small perturbations on them and collide as shown. A ligament extends from the first lump and the second lump undergoes bag breakup with the formation of a ring filament. The ring filament then breaks up to form two ligaments, one of which has sufficient kinetic energy to retain its ligament shape and extend again. This ligament then splits into droplets, the largest droplet being located at the top end of the ligament. This droplet is released with sufficient vertical velocity to reach the top of the pipe. The radial velocity of this ballistic droplet was around 1 m.s^{-1}. Here, one may speculate that the energy acquired by the droplet emitted from the ligament is due to the collision of the two lumps.

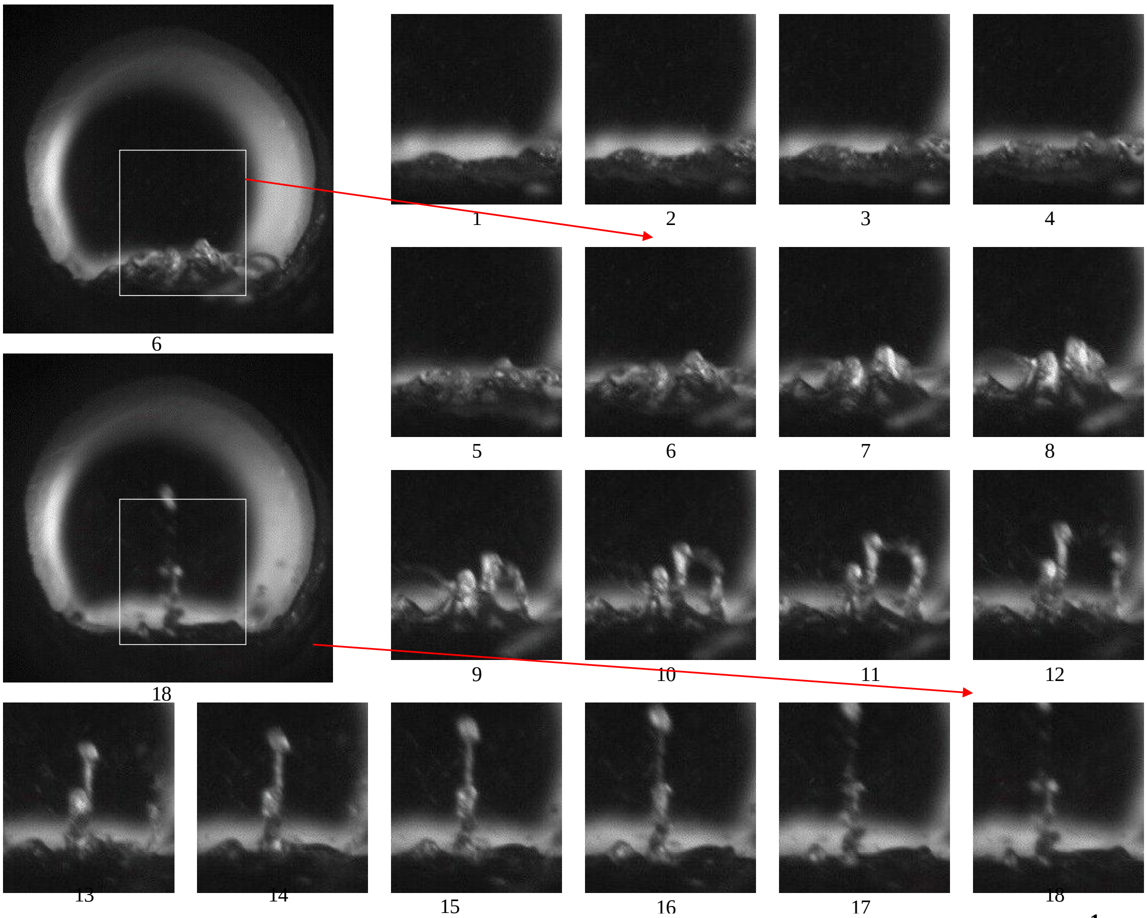

Figure 5.11. Images of air-water flows with Superficial gas velocity = 11.6 m.s^{-1} and Superficial liquid velocity = 0.036 m.s^{-1}, 500fps - Droplets entrainment at the top of the pipe.

Figure 5.12 shows the cross sectional views of the phenomenon shown in Figure 5.11 and Figure 5.13 shows a magnification of Image 15 appearing in Figure 5.11.

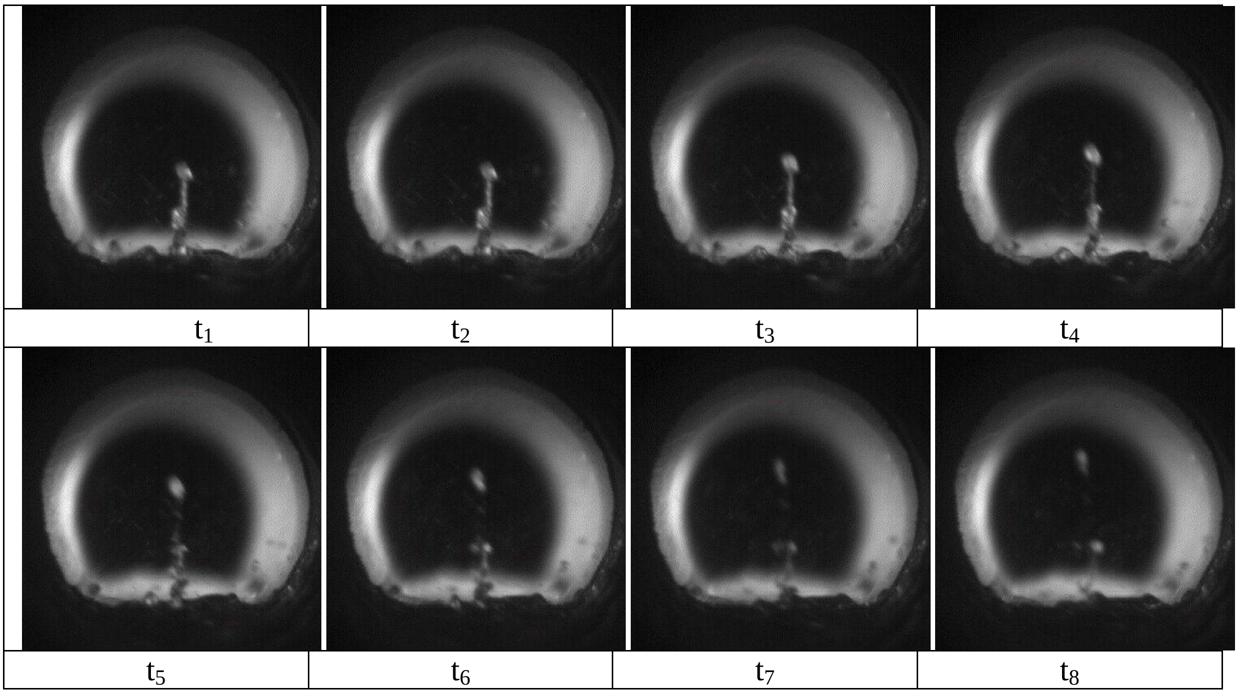

Figure 5.12. Videos of experiments: ligament type break-up ($t_{i+1}=t_i+\Delta t$ with $\Delta t=2.10^{-3}$s).

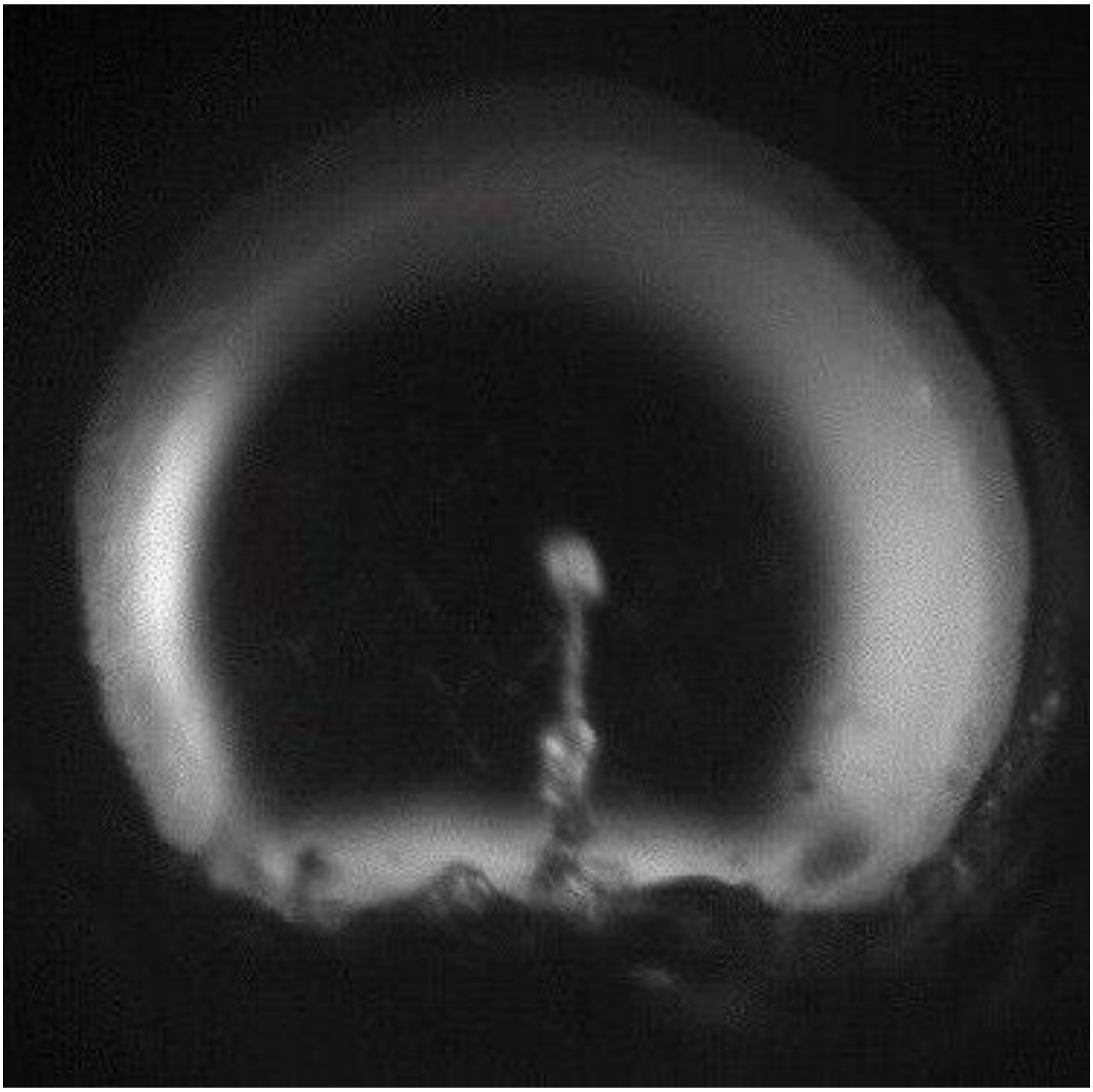

Figure 5.13. Images of air-water flows with Superficial gas velocity = 11.6 m.s^{-1} and Superficial liquid velocity = 0.036 m.s^{-1}, 500fps - Droplets entrainment at the top of the pipe.

The video of this phenomenon named “video 5.3. Ligament” can be found in the CD attached to this thesis.

Ligament and bag break up - Summary

Azzopardi (1983) postulates that ligament occurs at higher gas and liquid flow rates and that bag break up occurs at lower gas and liquid flow rates. Ligament and bag breakup have both been observed in the present work, as well as intermediate mechanisms. Typically, all mechanisms (see Figures 5.14, 5.15 and 5.16) are present in each flow wherein entrainment occurs.

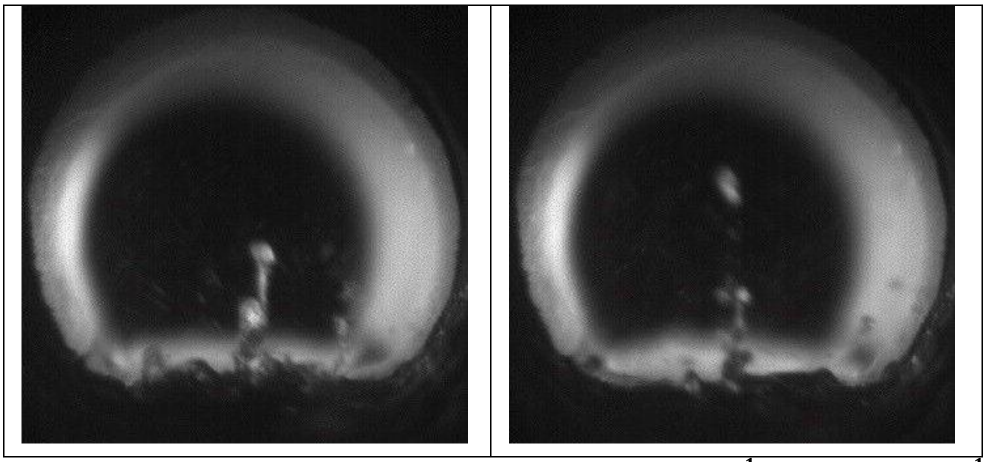

Figure 5.14. Big droplet reaching the top (U_{SG}=11.6 m.s^{-1}, U_{SL}=0.036 m.s^{-1}).

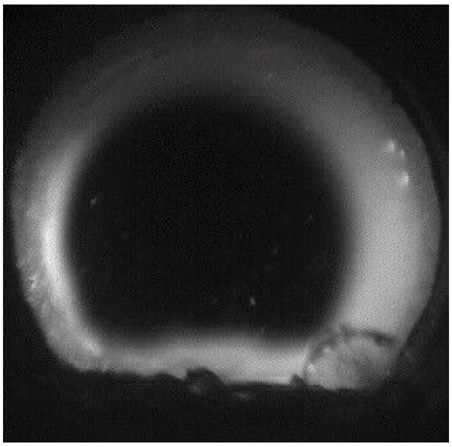

Figure 5.15.Very thin droplets inside the filament moving rapidly and diagonally (U_{SG}=10.6 m.s^{-1}, U_{SL}=0.035 m.s^{-1}).

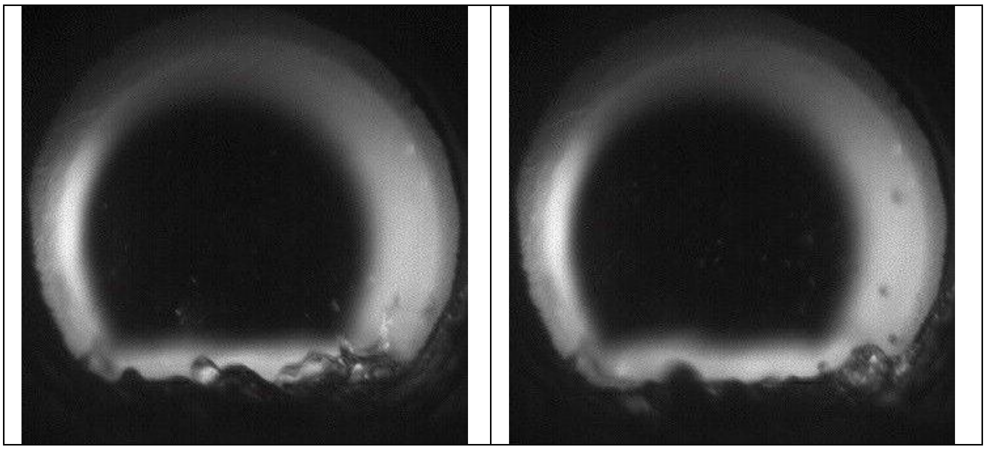

Figure 5.16. Very rapidly moving droplet from ligament on a bag (U_{SG}=11.6m.s^{-1}, U_{SL}=0.036 m.s^{-1}).

Simultaneous axial and side views on the WASP facility

Simultaneous axial and side views of stratifying-annular flow in a 78 mm diameter pipeline have been recorded using the WASP facility (see Chapter 4 for details of the experimental arrangement). The main sets of conditions studied are summarized in Table 5.3.

Superficial Gas Velocity (m.s-1)	**Superficial Liquid Velocity (m.s-1)**	**Notes**
9.92	0.05	Mass flow rate of water passing vertical through the centre line of the channel available. (Bin & Hale)
11.90	0.12	Variation of droplet flow rate with position in a vertical line through the centre line of the pipe available. (Bin & Hale)
21.00	0.02	Centre Line liquid mass flux available. (Badie)
25.00	0.02	Distribution of droplet flow across horizontal mid-plane of the pipe. Also pressure gradient data. (Badie)

Table 5.3. Conditions studied in simultaneous axial and side view experiments.

Pictures taken from the video sequences of the axial and side views are shown in Figures 5.17 to 5.20. The superficial phase velocities are given in the Figure headings and copies of the video sequences are given in the CD appended to this thesis. The respective video sequences are as follows:

Figure 5.17: Axial view: “video 5.4-Case0-axial”. Side view “video 5.4-Case0-side”
Figure 5.18: Axial view: “video 5.4-Case1-axial”. Side view “video 5.4-Case1-side”
Figure 5.19: Axial view: “video 5.4-Case2-axial”. Side view “video 5.4-Case2-side”
Figure 5.20: Axial view: “video 5.4-Case3-axial”. Side view “video 5.4-Case3-side”

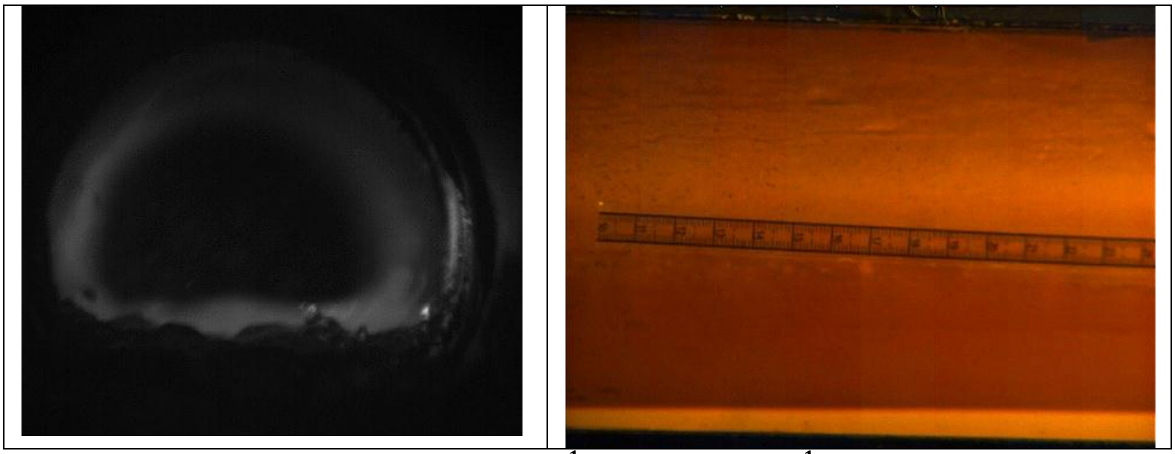

Figure 5.17. Air-water flow U_{SL}=0.03m.s^{-1}; U_{SG} = 9.4 m.s^{-1}-Pipe diameter = 0.078 m, Frames per second = 500.

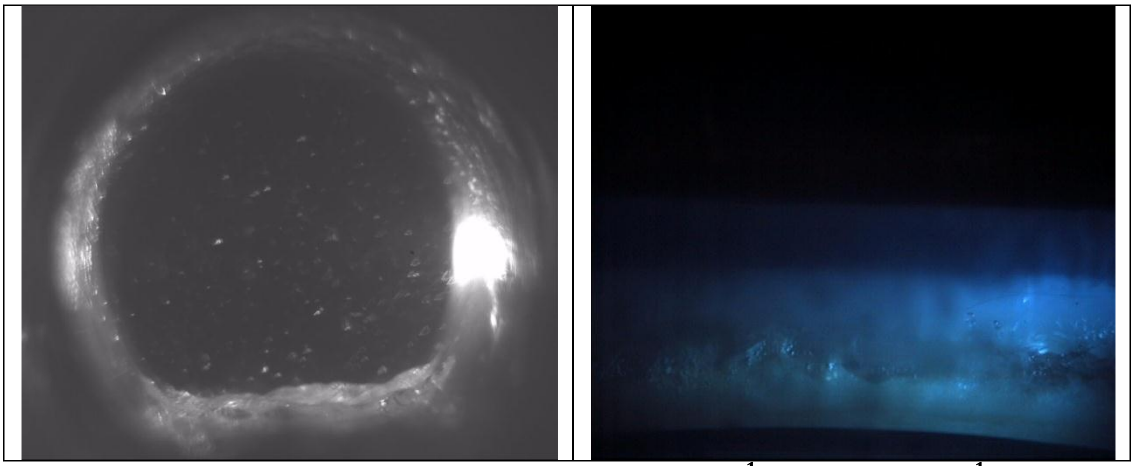

Figure 5.18. Flow Condition: U_{SG} = 9.92 m.s^{-1}, U_{SL} = 0.05 m.s^{-1}.

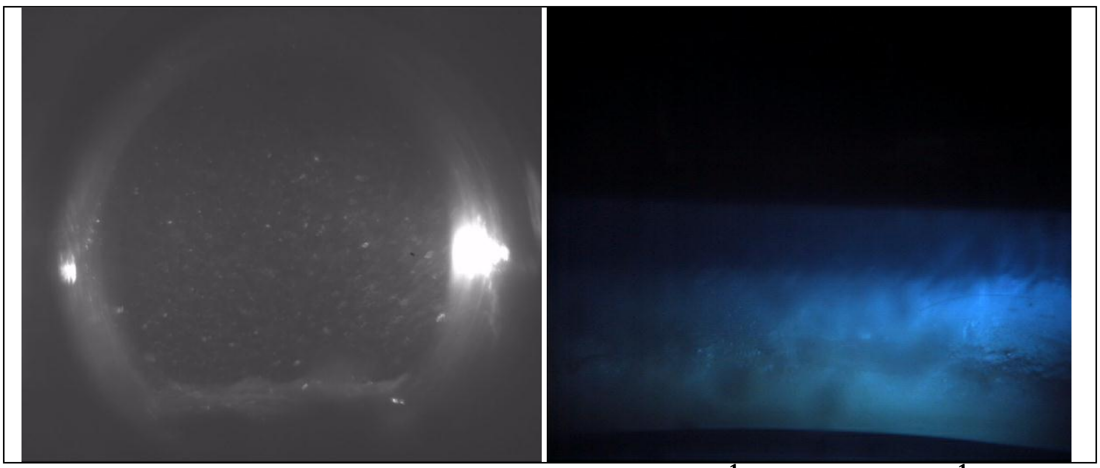

Figure 5.19. Flow Condition: U_{SG} = 11.9 m.s^{-1}, U_{SL} = 0.12 m.s^{-1}.

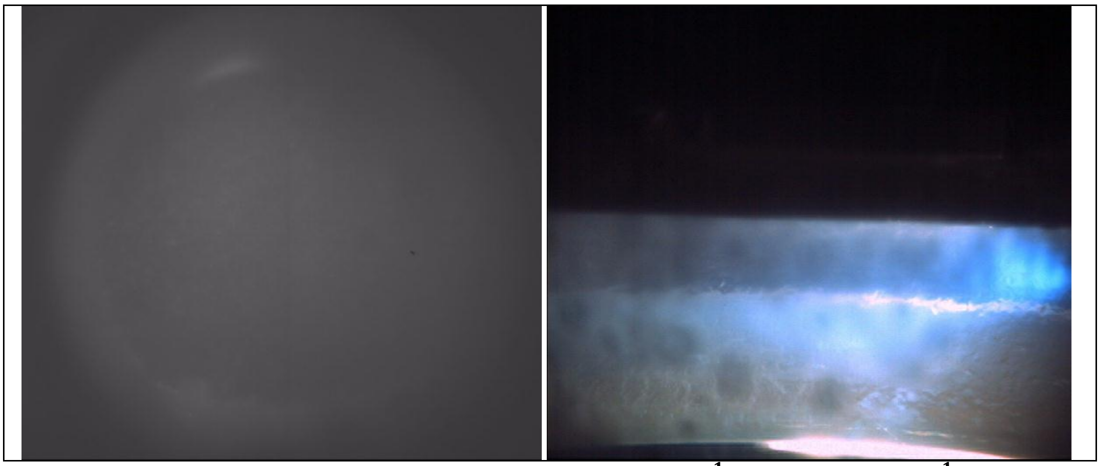

Figure 5.20. Flow Condition: U_{SG} =21 m.s^{-1}, U_{SL} = 0.02 m.s^{-1}.

Study of the simultaneous axial and side view videos of the flow allows one to draw the following important conclusions:

-Droplets are travelling axially at a very high speed.

The wetting of the pipe in the top half is essentially due to droplets entrained in the gas core and trapped into it, travelling for some distance and some of them eventually deposit when they are close enough to the wall. These droplets are thus moving at a very high axial speed before being deposited. While the radial speed of the droplet is in the order of 1m.s-1, the axial speed is far higher, approaching the speed of the superficial gas velocity.

-More droplets are entrained when the superficial gas velocity is higher.

There are more droplets wetting the top of the pipe in the case of very high superficial velocities because more droplets have been entrained into the gas core when the superficial velocity is higher. The higher the superficial gas velocity, the larger is the number of droplets entrained into the gas core and the higher they can reach; in particular, many drops reach the top of the pipe and deposit there.

-Droplets are the consequence of the liquid phase (and in particular waves) sheared by the phase gas and the frequency of waves increase with gas velocity.

The droplets are the product of shearing of the liquid phase by the gas phase. The shearing off of droplets is more significant at the tips of the waves formed at the interface. The increase in the superficial gas velocity also induces an increase in the frequency of waves which increases the droplet entrainment rate into the gas core. So many droplets are present in the gas core on the axial view in Figure 5.20 that visualization is impaired due to the scattering of the light by the droplets.

-Breaking waves play an important role in droplet entrainment.

Waves formed on the liquid pool at the bottom of the pipe may break under the influence of high speed gas flow. The breaking waves may themselves be broken up by the high speed gas flow to form droplets but, also, the impact of the breaking waves on the pool surface may also enhance entrainment.

Frequency of entrainment events

The frequency of entrainment events at a given gas velocity was measured by counting entrainment events on the video recordings. The frequency of observed entrainment events (which include both bag and ligament breakups) is shown as a function of gas velocity in Figure 5.21.

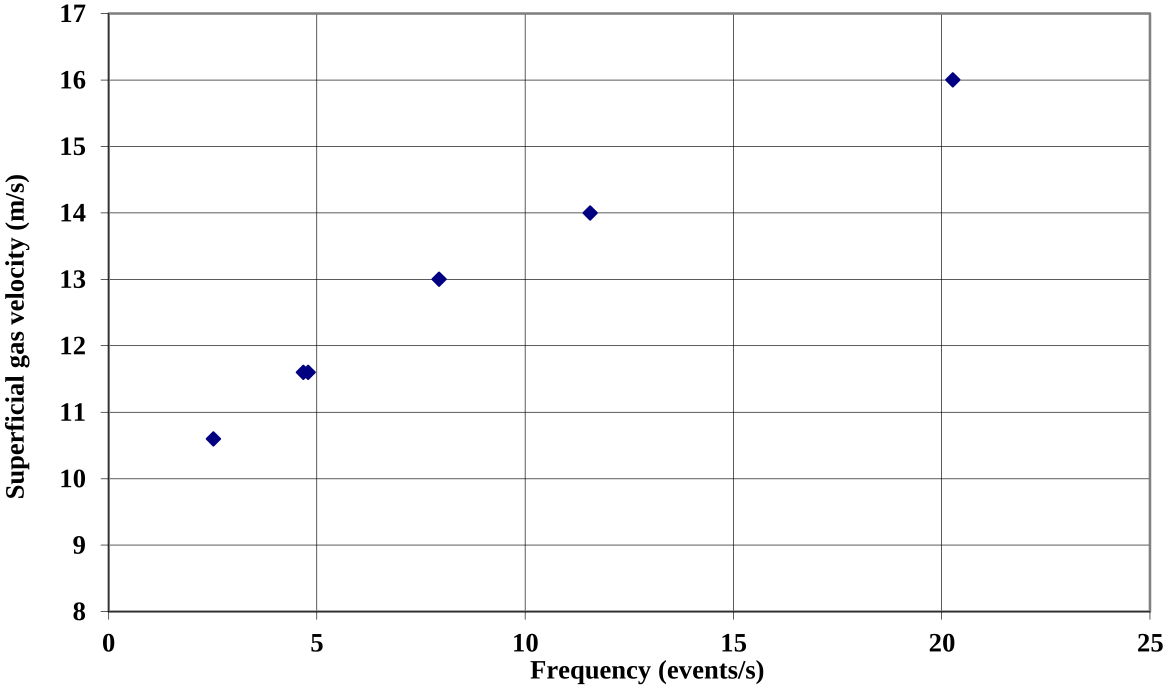

Figure 5.21. Frequency of entrainment.

Droplet sizes

Droplet size ranges and amount of droplets in the gas core are investigated for three sets of conditions: the first set of conditions is a) superficial gas velocity U_{SG}=11.6 m.s^{-1} and superficial liquid velocity U_{SL}=0.036 m.s^{-1}, the second set is b) U_{SG}=14 m.s^{-1}, U_{SL}=0.036 m.s^{-1} and the third set is c) U_{SG}=17 m.s^{-1}, U_{SL}=0.033 m.s^{-1}. Pictures taken from the videos for these three conditions are shown in Figure 5.22.

For conditions a) we can observe the presence of rare large droplets with an average diameter of 500 microns and several small droplets with a diameter range of about 100 microns and below.

For conditions b) we can note the presence of several large droplets with a diameter of about 700 microns and also a large amount of small droplets with a diameter range of 100 microns and below. Some large and some small droplets are seen reaching the top of the pipeline by direct impaction for the largest (ballistic drops) and by turbulent diffusion for the smallest (diffusional droplets)

For conditions c) The presence of a higher number of large droplets (100-500 microns) is observed. A higher amount of small droplets (100 microns and below) is also seen. The pipe is practically completely wetted. Light is scattered to in this case due to the large number of droplets present in the gas core (hence the “cloudy” appearance of the image.

Videos corresponding to the conditions shown in Figure 5.22 are given on the CD attached to this thesis (Video 5.5a_Droplets size, 5.5b_Droplets size and 5.5c_Droplets size).

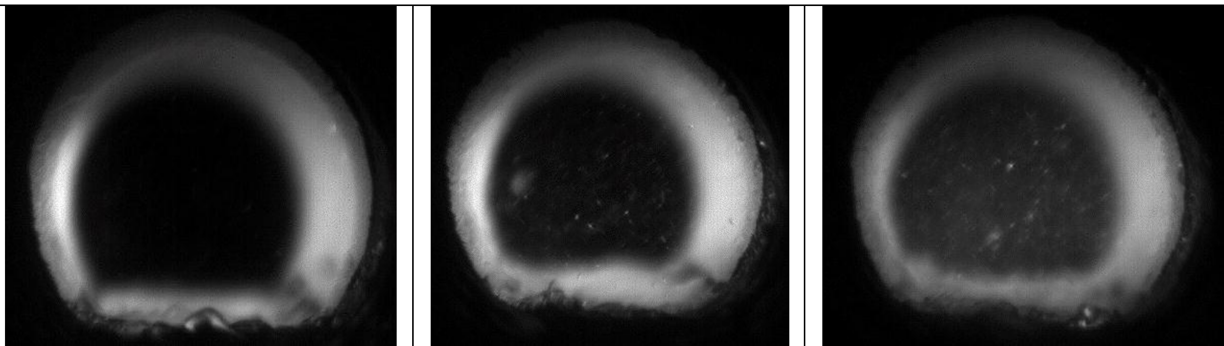

a) U_{SG}=11.6m.s^{-1}, U_{SL}=0.036m.s^{-1}	**b) U_{SG}=14m.s^{-1}, U_{SL}=0.036m.s^{-1}**	**c) U_{SG}=17m.s^{-1}, U_{SL}=0.033m.s^{-1}**

Figure 5.22. Amount of droplets and droplets size range.

Droplet diameter distribution

In order to determine the droplet size distribution in the gas core in horizontal pipes at several conditions, snapshots from the videos were analysed with the software package Image J (Image Processing and Analysis) available in the Java package. Figures 5.23 and 5.24 show the plots obtained for the conditions of superficial gas velocity and superficial liquid velocity respectively 1) U_{SG}=9.98 m.s^{-1}, U_{SL}= 0.05 m.s^{-1} and 2) U_{SG}=11.2 m.s^{-1}, U_{SL}=0.12 m.s^{-1}.

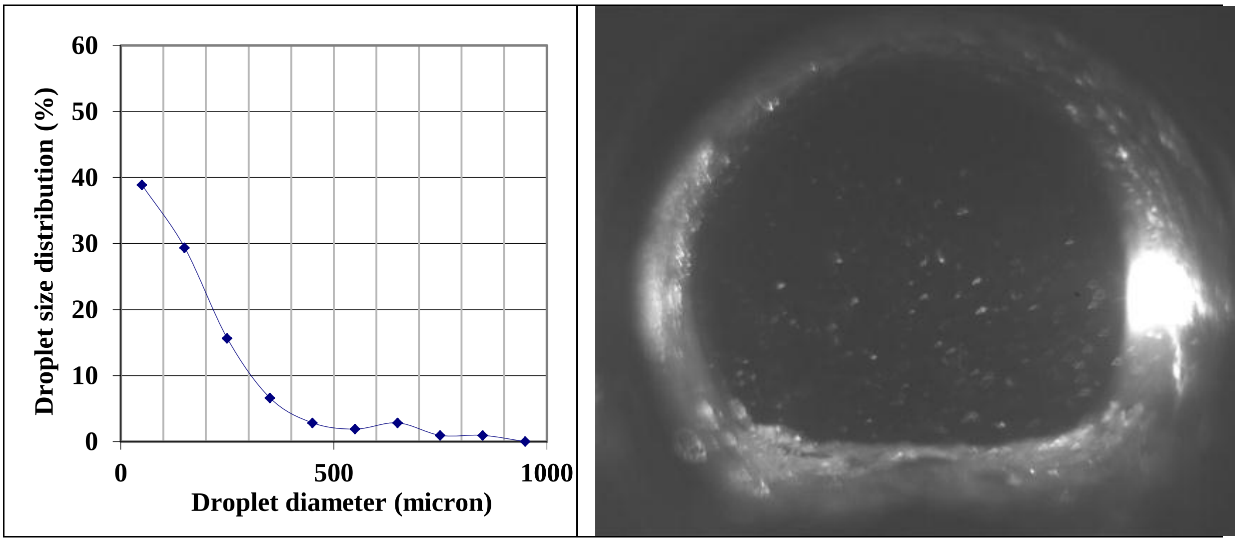

Figure 5.23. Droplet diameter distribution - U_{SG}=9.98 m.s^{-1}, U_{SL}=0.05 m.s^{-1}.

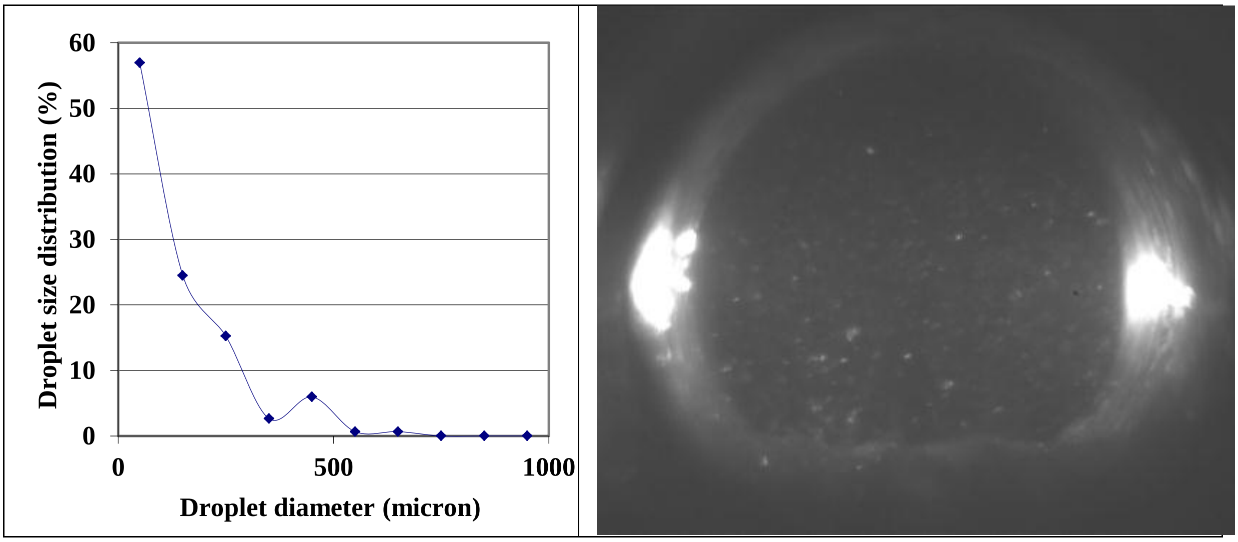

Figure 5.24. Droplet diameter distribution - U_{SG}=11.2 m.s^{-1}, U_{SL}=0.12 m.s^{-1}.

The comparison between both results showed that in the case of higher superficial gas and liquid velocities, a larger amount of small droplets were found in the gas core.

5.3.2 Liquid film flow rate measurements

The distribution of the film flow rate around the pipe perimeter is very important in pipeline operation. It may be essential, for instance, to keep the top of the pipe wet in order to minimize corrosion. A new methodology was developed to measure local film flow rate (see Chapter 4) but it was only possible to carry out a very limited tests. These were for an angle of 45º from the top of the tube (i.e. the film suction device was midway between the top of the pipe and the centerline). Further tests are clearly desirable but could not be performed due to the lack of availability of the WASP facility caused mainly by problems with the gas supply.

The matrix of conditions for the film flow rate measurements is given in Table 5.4. The conditions were similar to those used for the simultaneous axial and side view experiments (see Table 5.3).

Superficial Gas Velocity ($m.s^{-1}$)	**Superficial Liquid Velocity ($m.s^{-1}$)**	**Notes**
9.92	0.05	Mass flow rate of water passing vertical through the centre line of the channel available. (Bin & Hale)
11.90	0.12	Variation of droplet flow rate with position in a vertical line through the centre line of the pipe available. (Bin & Hale)
21.00	0.02	Centre Line liquid mass flux available. (Badie)
25.00	0.02	Distribution of droplet flow across horizontal mid-plane of the pipe. Also pressure gradient data. (Badie)

Table 5.4. Conditions at which film flow rate measurements were made.

An essential step in measuring the local film flow rate is to plot the rate of liquid extraction through the device as a function of the rate of gas extraction. Figure 5.25 presents such a plot obtained for superficial gas and liquid velocities of U_{SG}=9.92 $m.s^{-1}$ and U_{SL}=0.05 $m.s^{-1}$. Because of the unsteady (wavy) nature of the film flow, it is necessary to extract a certain amount of gas to ensure that the film flow rate associated with the waves is collected. Once all the waves are collected, then collection rate becomes independent of gas flow rate over a “plateau” range and it is this plateau rate of collection which characterises the film flow rate.

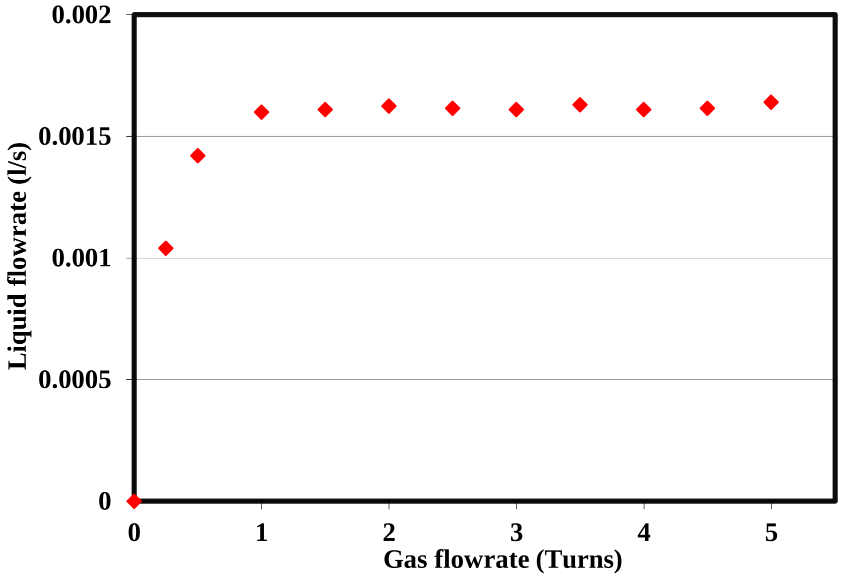

Figure 5.25. Film Extraction: 45° from top,

U_{SG} = 9.92 m.s^{-1}, U_{SL} = 0.05 m.s^{-1}

At 45° (this angle representing the position of the centre of the porous section around the circumference of the pipe, 0° being the top of the pipe), the results found are reported in Table 5.5.

U_{SG}-U_{SL}	Liquid film flow rate
9.92-0.05	0.0016 l/s
11.8-0.12	0.0048 l/s
20.6-0.02	0.0035 l/s

Table 5.5. Liquid film flow rate with the porous section at 45°.

5.3.3. Pressure gradient measurements

Measurements of pressure gradient in the rig have been carried out for each test. The pressure gradient data is exemplified by that shown in Figure 5.26 where pressure gradient is plotted against the superficial air velocity for a superficial liquid velocity equal to 0.035m.s^{-1}.

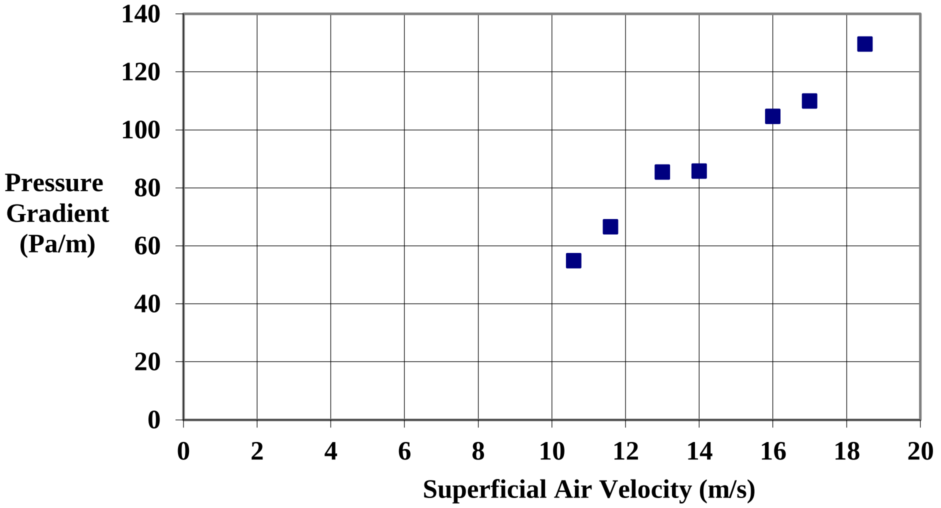

Figure 5.26. Pressure gradient for air-water flows (superficial water velocity =0.035m.s^{-1}).

The results for film flow rate are presented and compared with predictions in Chapter 7. It is estimated that the accuracy of film flow rate measurements is approximately $\pm 10^{-4}$ g/min.

CHAPTER 6

Modelling of liquid transport in stratifying annular flow

In this Chapter, the background to the modelling studies carried out as part of this project is described. The main focus has been on the computational simulation of the processes involved in liquid transport (droplets and liquid film) and an approach has been adopted which combines Computational Fluid Dynamics (CFD) and phenomenological modelling. In the mid-2000's, Imperial College and Cranfield University collaborated in carrying out a study for ConocoPhillips related to stratifying annular flow in an industrial pipeline system and a description of the non-proprietary aspects of this work is given by Brown et al (2009). The paper by Brown et al has guided the present work and many of the same relationships have been employed (see Section 6.4 below for details). However, there are important differences between the present work and the study reported by Brown et al (2009). These include:

1. The CFD calculations were carried out with a different commercial CFD code, namely CFX rather than the code FLUENT used in the joint Imperial College/Cranfield University study reported by Brown et al (2009). The choice of CFX in the present work was dictated partly by the availability of licenses and background experience but also by the range of modelling options available.
2. The present study was focussed on the prediction of the results for stratifying annular flow obtained on the WASP facility, notably by Badie (2000) and in the present work (see Chapter 5).
3. A study has been made in the present work of the applicability of Reynolds Averaged Navier Stokes (RANS) models to the stratifying annular flow case. Such models have been used in both the FLUENT-based calculations summarised by Brown et al (2009) and the present CFX-based calculations the results from which are described in Chapter 7. The question naturally arises as to whether the droplet/turbulence interactions represented by the Lagrangian tracking methods used in these commercial RANS codes (i.e. describing local turbulence with random functions) are realistic. It could be argued that the structural aspects of the turbulence can be important. Such structures can be predicted using Large Eddy Simulation (LES) models and comparisons of the performance of LES models and RANS models are discussed in Chapter 8.

In the modelling of stratifying annular flow, it is important to note that large droplets emitted from the bottom pool of liquid are often emitted with sufficient velocity (see Chapter 5) that their motion is essentially ballistic and is not significantly affected by the turbulence. On the other hand, very small droplets diffuse in a manner dictated by their interaction with turbulent eddies. It is convenient to model liquid transport in stratifying annular flow in terms of these two types of interaction. A “two-group” analytical model for stratifying annular flow is described by Brown et al (2009) in which separate expressions are derived for *ballistic* and *diffusional* droplet transport. However, in reality, there is a continuous spectrum in the nature of the interaction between the turbulence and the droplets as the drop size changes and this is recognised in the CFD calculations described by Brown et al (2009) and in the present work as described in Chapter 7.

In what follows in this Chapter, Section 6.1 discusses the empirical, semi-empirical and phenomenological models which have been used for two-phase flows in general and stratifying annular flows in particular. Issues relating to the CFD modelling are discussed in Sections 6.2, 6.3 and 6.4. Thus, Section 6.2 reviews the different available turbulence models and Section 6.3 describes the codes (CFX and TransAT) which have been employed in the present RANS and LES work respectively. Section 6.4 gives a description of the problem being solved and Section 6.5 gives details of the data processing methodology.

6.1. Empirical and semi-empirical modelling

Empirical correlations are still the most widely used approach to predict pressure gradient in multiphase flows. The extensive work on empirical correlations is typified by the studies of Lockart & Martinelli (1949), Chisholm (1973), Friedel (1979). Laurinat at al (1984), Hart et al (1989) and Badie (2000).

Four main categories of approach have been used to predict liquid hold-up and pressure gradient: the homogeneous approach, the separated flow methods, the two fluid models and the phenomenological models.

The homogeneous approach

In the homogenous approach, the gas-liquid mixture is considered as a single fluid with suitably averaged properties. The gas and liquid velocities are considered as being equal. The mixed fluid is treated as a single phase fluid with a mixture density given by a linear average relationship:

$$\rho_M = \frac{\rho_G \rho_L}{x\rho_L + (1-x)\rho_G} = (1-\varepsilon_{NL})\rho_G + \varepsilon_{NL}\rho_L \qquad (6.1)$$

where x is the flow quality and ε_{NL} is the non-slip (or input) liquid hold-up.

$$\varepsilon_{NL} = \frac{u_{L,S}}{u_{L,S} + u_{G,S}} \qquad (6.2)$$

$$x = \frac{\dot{m}_G}{\dot{m}_G + \dot{m}_L} \qquad (6.3)$$

The viscosity is typically given by:

$$\eta_M = (1-\varepsilon_{NL})\eta_G + \varepsilon_{NL}\eta_L \qquad (6.4)$$

The separated flow technique

In this approach, the gas and liquid are considered to be in separate fields, with different velocities. Equations (for instance momentum equations) can be written for each phase and combined to produce separated flow equations (for instance the separated flow momentum equations for pressure gradient). For the stratifying-annular flows considered in the present work, this dominant term in pressure gradient is the frictional pressure gradient $\frac{dp_f}{dz}$. Empirical and semi-empirical correlations are used in which the term $\frac{dp_f}{dz}$ is related to the pressure gradient in single phase flows of the individual phases in the channel. The two phase pressure gradient is calculated using a multiplier. For example, ϕ_L^2 is a pressure gradient multiplier applied to the liquid phase pressure gradient.

$$\left(\frac{dp_f}{dz}\right)_M = \phi_L^2 \left(\frac{dp_f}{dz}\right)_L \qquad (6.5)$$

where

$\left(\frac{dp_f}{dz}\right)_L$ is the single phase pressure gradient given by:

$$\left(\frac{dp_f}{dz}\right)_L = \frac{4}{D}\tau_{WL} \tag{6.6}$$

where τ_{WL} is the liquid wall shear stress and given by:

$$\tau_{WL} = f_L \frac{\rho_L u_L^2}{2} \tag{6.7}$$

where u_L is the liquid phase velocity and f_L the friction factor calculated from standard single phase correlations.

Two-fluid models

In this model, the equations for the (separated) phases are not combined but, rather, are retained. The momentum equations are solved by introducing relationships for interface and wall friction, leading to predictions of holdup and pressure gradient.
However, it is difficult to specify generic relationships for interfacial friction and wall friction. This method also has a strong element of empiricism except for some special cases such as laminar flows (Ng, 2002).

Phenomenological modelling: Badie's model (2000)

In phenomenological modelling, modelling strategies are developed based on observations and physical insights. An example of such a model for stratifying annular flow is that of Badie (2000) which is described in Section 2.2.2.

6.2. Computational fluid dynamics (CFD) and turbulence models

A major objective of this work has been to model droplet transport in stratifying annular flows using Computational Fluid Dynamics (CFD).

Basically, droplets are numerically tracked within the turbulent gas core by using Lagrangian tracking through the turbulent field, the latter being characterised using a turbulence model. The background to such turbulence modelling is given in what follows.

Turbulence modelling

The complexity of turbulence arises from the facts that it is a three dimensional phenomenon, it is unsteady and it contains many scales. Turbulent flows occur at high Reynolds numbers when the inertia forces in the fluid become predominant in comparison with the viscous forces.

The Reynolds number is an a dimensionless number defined by:

$$\mathrm{Re} = \frac{\rho U D}{\mu} \tag{6.8}$$

where ρ is the density, μ is the dynamic viscosity, D the diameter of the pipe and U the velocity of the fluid.

The transition to turbulent flow occurs for single-fluid flows at a critical value of a Reynolds number, which depends on the various parameters such as the geometry and wall roughness. Not much appears to be known about the corresponding transition in two-phase flows such as stratified flows.

The Navier-Stokes equations describe the flow of incompressible laminar and turbulent fluids. These equations are for the conservation of mass and the conservation of momentum. The equation for the conservation of mass is:

$$\nabla . u = 0 \tag{6.9}$$

and that for the conservation of momentum is:

$$\rho\left(\frac{\partial u}{\partial t} + u.\nabla u\right) = -\nabla p + \mu \nabla^2 u + \rho g \tag{6.10}$$

In principle, all flows (including turbulent flows) can be represented in terms of these equations which can be solved either analytically or numerically. Thus, at limited Reynolds numbers, even turbulent flows can be predicted directly by numerical solutions of the Navier-Stokes equations (DNS: Direct Numerical Simulation). Unfortunately, turbulence contains such a large range of length and time scales at realistic Reynolds numbers that DNS would require an unrealistic computational effort. Two alternative methods are available to reduce the computational effort, at the expense of resolution of the simulations.

A first alternative method is the use of turbulence models. These models are statistical turbulence models based on the Reynolds averaged Navier-Stokes equations (RANS). The numerical solution of the RANS equations requires far less computational effort than DNS. The basic idea behind the RANS equations is to split the instantaneous velocity u into a mean velocity $\overline{U}$ and a fluctuating velocity u' (the "Reynolds' decomposition"):

$$u = \overline{U} + u' \tag{6.11}$$

u is substituted by this expression into the equation of momentum (6.10). The equation is then averaged. This results in momentum equations for $\overline{U}$ that are very similar to the usual Navier-Stokes equations, but with a new term involving the so-called Reynolds stresses, $\rho\overline{u_i^{'}u_j^{'}}$. Effectively, rather than solving the actual fluctuating velocity field u', only the averaged velocity field $\overline{U}$ is solved in these methods.

For this purpose the new term in the Reynolds equation, $\rho\overline{u_i^{'}u_j^{'}}$, called the Reynolds stress tensor, must somehow be expressed in terms of $\overline{U}$. Hence each component of this tensor is an unknown that needs to be modelled by additional closure relations. Reynolds stresses act as additional stresses in the fluid. Different methods exist to solve these stresses and the turbulence models are classified as eddy-viscosity models or Reynolds stress models, according to the method used.

In eddy viscosity models, turbulence is assumed to be formed by small eddies continuously forming and dissipating. The Reynolds stresses are taken to be proportional to the mean velocity gradients, the proportionality constant being the turbulent or eddy viscosity.

Based on these assumptions, the $k - \varepsilon$ turbulence model is the most common model. Here, k is the turbulence kinetic energy. It is defined as the variance of the fluctuations in velocity. ε is the turbulence eddy dissipation and is defined as the rate at which the velocity fluctuations dissipate. In this model, the Reynolds stresses are proportional to the mean velocity gradients and the turbulent viscosity is the product of a turbulent velocity and a turbulent length scale. This eddy viscosity model offers good predictions of most flows. However, there are important cases where the basic assumption of the $k - \varepsilon$ model that the turbulent viscosity is isotropic breaks down and more sophisticated models are required.

RSM

A fundamental assumption in the k-ε model is that the turbulent diffusivity is isotropic. Though this is often a reasonable approximation when the flow is uniform (as in single phase flow in round tubes), significant problems arise when the geometry is non-uniform (as in the case, for example, of flows in rectangular channels where corner vortices occur which are not predicted by the k-ε model). In the case studied here, the flow zone for the gas is non-circular because of the liquid layer at the bottom of the pipe (see Figure 2.5). The non-uniformity of the geometry can cause secondary flows, particularly in the corners where the liquid layer meets the draining film (see Figure 2.5). These secondary flows may have a considerable influence on the droplet motion in the gas core and it is important to capture them. In order to do this, a more complex model (namely the Reynolds Stress Model RSM) is used. In this model, the Reynolds stresses are not assumed isotropic and it is possible to predict secondary flow (including corner vortices). Modelling these extra complexities of the turbulence does necessitate additional empirical constants in fitting the empirical data. Two main types of RSM have been adopted in commercial CFD codes, namely those by Launder, Reece and Rodi (1975) (CRR) and Speziale, Sarkar and Gatski (1991) (SSG). In the present work, the SSG model has been used within the framework of CFX.

LES

A compromise between RANS-based models and DNS is Large Eddy Simulation (LES). It may be deduced from the Kolmogorov (1941) theory, that large eddies in the flow are dependent on the flow geometry, while smaller eddies are self similar and have a universal character. In LES only the large-scale turbulent structures are modelled directly. The effect of the smaller and more universal eddies on the larger ones is modelled. Thus, in LES the large scale motions of the flow are calculated, whilst the effect of the smaller universal scales (the so-called sub-grid scales) is modelled using a sub-grid scale (SGS) model.

The “filtered” Navier-Stokes equations for the large-scale flow contains an additional sub-grid scale stress term, similar to that arising in the RANS approaches. The most commonly used SGS model is the Smagorinsky model. This compensates for the unresolved turbulent scales through the addition of an "eddy viscosity" into the governing equations.

Naturally, LES requires less computational effort than direct numerical simulation (DNS) but more effort than those methods that solve the Reynolds-averaged Navier-Stokes equations (RANS).

Another advantage of LES is the increased level of details it can deliver. While RANS methods provide "averaged" results, LES is able to predict instantaneous flow characteristics and resolve turbulent flow structures. While the "averaged" values may be too low to trigger a phenomenon, instantaneously there can be localised areas of high turbulence in which the process will occur.

6.3. CFD codes used in present work

A wide variety of general purpose CFD codes are now available commercially (including CFX, STAR-CD, FLUENT) and, in addition, there are a number more specialised codes. In the present work, the CFX code was employed for the main series of calculations on droplet transport using a RANS approach. In addition, a more specialised code (TransAT developed by Ascomp in Switzerland with the specific aim of calculating multiphase flows) was used for the LES calculations (see Chapter 8). In what follows, the CFX and TransAT codes will be described in more detail.

CFX

The deposition of the droplet entrained from the liquid pool contributes to the formation of a liquid film. In order to study the movement of a droplet, namely from its entrainment from the liquid pool to its deposition around the circumference of the pipe, a commercially available CFD code is used: CFX® 13.0. Using this code the droplets were tracked using a Lagrangian tracking method based on a turbulence field calculated using a RANS (RSM) model.

The CFX codes (distributed by ANSYS Ltd.) combine solving power and friendly interfaces. They comprise three main components, the pre-processor, the solver and the post-processor. The pre-processor is used to define the details of the model: geometry of the region, the mesh of volume elements into which the domain is divided, the fluid properties, the physical phenomena and the boundary conditions. In this part are also defined the solution method (discretisation schemes and convergence criteria.) The solver implements the calculation from the details entered in the pre-processor. It gives a discretisation of the equations describing the flow problem and then an algebraic approximation to these equations. The flow is then solved for each variable at each grid point in the domain by an iterative solution technique until the criteria of convergence is fulfilled. The post-processor provides tools to analyse and interpret the results as vector plots or in terms of particle tracking.

TransAT

The Computational Multi-Fluid Dynamics (CMFD) code TransAT© is a code developed at ASCOMP GmbH in Zurich, Switzerland. It is a multi-physics, finite-volume code based on solving single-phase and multi-fluid Navier-Stokes equations. This code uses structured multi-block meshes. MPI (Message Passing Interface) parallel based algorithm is utilised in connection with multi-blocking. High-order time marching and convection schemes can be employed. Multiphase flows are studied using interface tracking techniques for both laminar and turbulent flows. Specifically, both the Level-Set and the Volume-of-Fluid methods can be employed. Static or dynamic angle treatment is possible. Turbulent multiphase flows can be tackled within both the RANS and LES frameworks, with specific near interface treatments. The application of the TransAT code in a numerical experiment to determine the effect of turbulence model (RANS or LES) on predictions of droplet transport is described in Chapter 8.

6.4. Prediction of WASP data using RANS Lagrangian droplet tracking with the CFX code

In this Section, the application of Lagrangian droplet tracking using the CFX code to the prediction of stratifying annular flow, and specifically to the conditions studied in the WASP facility, is described. The methodology is similar to that described by Brown et al (2009) but with the important differences that CFX was used in the present study (as distinct from the use of FLUENT in the Brown et al study) and that the present study was focused on the prediction of data from the WASP facility (as described in Chapter 5).

6.4.1. Introduction

The CFD calculations with CFX used a Reynolds stress (RSM) model (i.e. the SGS model) to describe the turbulence field within the gas core of the flow. Within this turbulence field, the droplets emitted from the pool surface were tracked using the CFX Lagrangian tracking procedure. Thus, they were subject to random fluctuations in the velocity of the surrounding gas, these fluctuations being consistent with the calculated turbulence field. The track of the position of the droplet from the time of its emission to the time of its deposition on the tube wall could be calculated. Due to the randomness imposed in the turbulent field, the trajectory of a droplet could vary from case to case even if the conditions of the emission of the droplet were the same. It would be expected that the size of the emitted drops would vary over a range as would their initial velocity and direction. The objective of the calculation is to establish the total equilibrium rates of deposition of drops as a function of circumferential position and the mass flux of droplets as a function position in the gas core. These deposition rates and mass fluxes represent the sum of the rates for drops of all sizes and initial emission conditions. In the present work, the initial direction of emission of the droplets was calculated on the same basis as that described by Brown et al (2009) and described in more detail in Section 6.4.3 below.

The components of the model implemented in CFX are defined below:

1. Mathematical Model : SSG (Speziale, Sarkar, Gatski, 1991) Reynolds Stress Model
2. Discretisation method : Finite Volume (FV) Method
3. Coordinate system : Cartesian coordinates
4. Numerical grid : Structured
5. Finite difference approximations : High resolution scheme for advection
6. Solution method : AMG (Algebraic Multigrid) solver (Default)
7. Convergence criteria : Maximum number of iterations=1000, Residual type=RMS (Root Mean Square): Residual Target = 10^{-6}.

6.4.2. Geometry

The geometry of the model used in CFX is illustrated in Figure 6.1 and Figure 6.2.

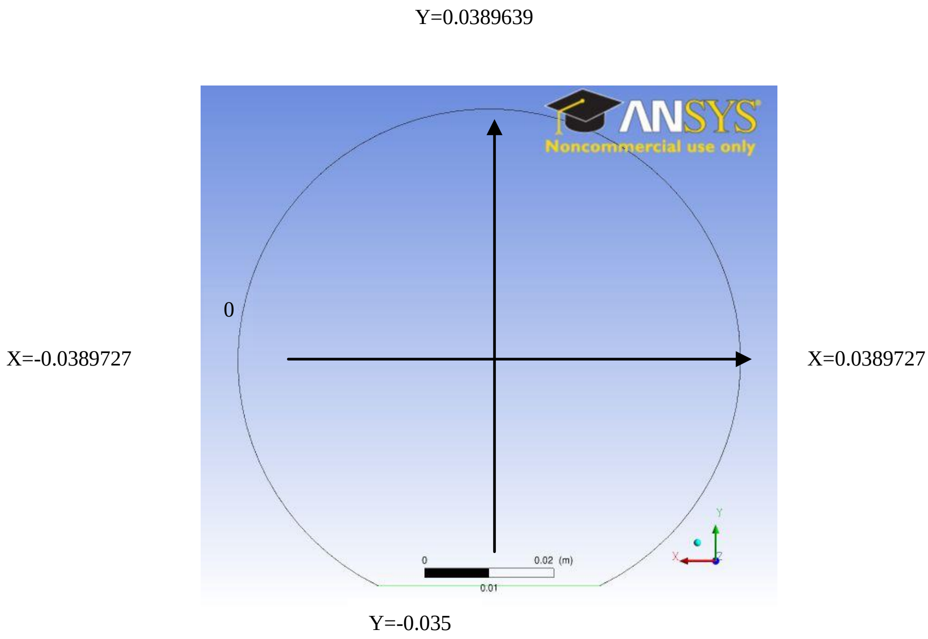

Figure 6.1. Geometry (with CFX).

The height of the liquid pool in the model is 3.96 mm

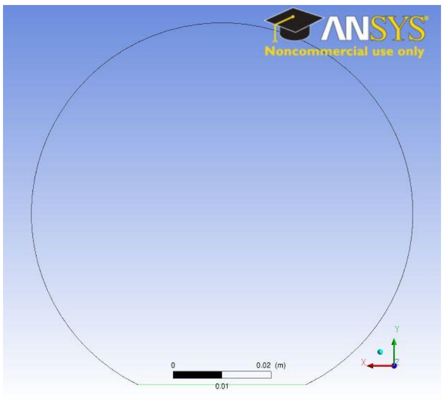	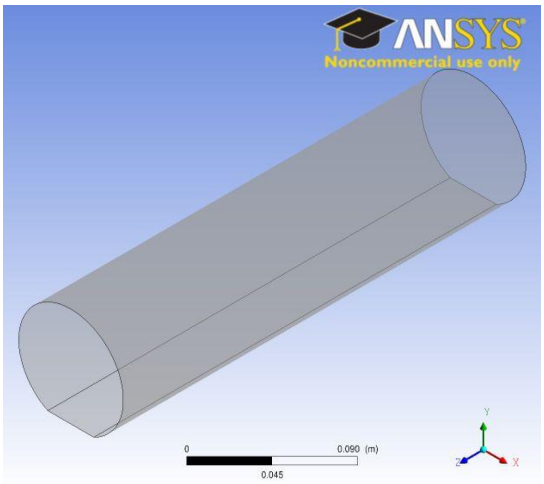
Cross section view	**Perspective view**

Figure 6.2. Geometry (perpective view).

Essentially, the flow channel used is cylindrical with a segment cut out at the bottom to represent the liquid pool from which the droplets are entrained.

6.4.3. Boundary conditions and initial conditions

Flow conditions

The principal aim here was to predict the data from the WASP facility described in Chapters 4 and 5. From the previous measurements of droplet mass flux by Badie (2000) and Hale (2006) four conditions were selected for air water stratifying annular flow as described in Section 4,3.2.7. These conditions were all for air-water flows in WASP and were as follows (see Section 4.3.2.7 for more details):

Condition 1 (Hale, 2006): U_{SG}=9.92 m.s^{-1} and U_{SL}=0.05 m.s^{-1}. Here, the droplet mass flux was measured as a function of position on a vertical line through the tube centre.

Condition 2 (Hale, 2006): U_{SG}=11.9 m.s^{-1} and U_{SL}=0.12 m.s^{-1}. Here, the droplet mass flux was measured as a function of position on a vertical line through the tube centre.

Condition 3 (Badie, 2000): U_{SG}=21 m.s^{-1} and U_{SL}=0.02 m.s^{-1}. Here, the droplet mass flux on the channel centre line was measured.

Condition 4 (Badie, 2000): U_{SG}=25 m.s^{-1} and U_{SL}=0.02 m.s^{-1}. Here, the droplet mass flux on the channel centre line was measured.

Initial random angle of ejection, diameter, position and velocity.

A flow simulation and a particle simulation with a Fortran file for particle injection were used in the CFX case. The procedure for simulation of the emission of droplets from the liquid pool at the bottom of the pipe was similar to that described by Brown et al (2009) and is illustrated in Figure 6.3. The observations by Badie (2000) indicated that the droplets left the surface at a velocity of around 1.5 m.s^{-1} normal to the wall and this velocity was assumed for all of the droplets emitted. It is important to also consider the *direction* of the emission in addition to the velocity. In the model, it is assumed that the emission angles α and β are independent random variables distributed uniformly in the ranges $(-\beta_0, \beta_0)$ and $(0, \alpha_0)$ where α_0 and β_0 are the maximum vertical and horizontal angles of emission. It is assumed (following Brown et al, 2009) that, on emission, the axial velocity of the droplet instantaneously becomes equal to the gas core velocity U_{GC}. From this assumption, and using Badie's value of 1.5 m.s^{-1} for the velocity normal to the surface, it follows that:

$$\alpha_0 = \arctan\left[\frac{1.5}{U_{GC}}\right]$$

It is further assumed that $\alpha_0 = \beta_0$.

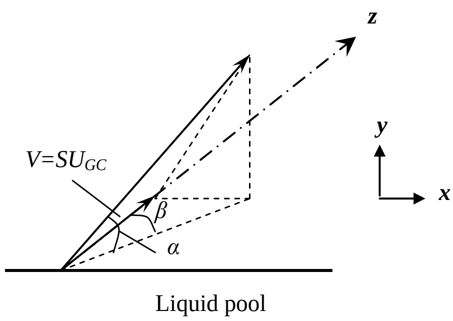

Figure 6.3. Angle of ejection of droplets.

This leaves two other variables relating to the emission of the droplets:

1. The location of the emission. Here it is assumed that the droplet is emitted from a location which is uniformly and randomly distributed across the width of the pool at the point of droplet initiation.
2. The size of the droplet. Here, the log normal distribution of drop size as given by Al-Sarkhi and Hanratty (2002) as shown in Figure 6.4 was assumed. This distribution was divided into N segments, each representing an equal volume of liquid and each with a characteristic mean drop size. Typically, N was set to 10. Calculations were then done for droplets of the segmental characteristic mean size and the deposition rate and mass flux distribution for each case was estimated. It was then a simple matter to sum the results to give the total deposition rate and the total gas core mass flux distribution.

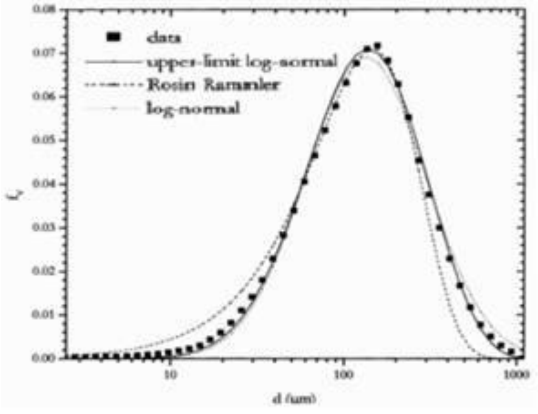

Figure 6.4. Log-normal distribution of drop sizes (Al-Sarkhi and Hanratty, 2002)

Droplet trajectory data obtained from the simulation are post-processed. Theory of the post-processing are summarized in Section 6.5 and results are presented in Chapter 7.

Periodic boundary conditions (PBCs)

The pipe studied in this research has a length of 37 meters. To simplify, we chose a representative unit length set to 0.5 meters and we use periodic boundary conditions under a specified pressure drop. The flux of the flow variables at the outlet periodic boundary and the flux entering the domain at the inlet periodic boundary are then set equal. This is shown in Figure 6.5.

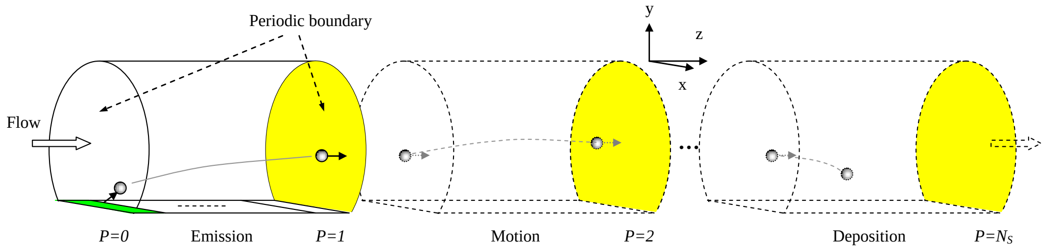

Figure 6.5. Schematic of the simulation processes (Brown et al. (2009)).

The pressure gradient –ΔP/L

The defined pressure drop shown in Figure 6.6 was calculated assuming that the interfaces were smooth using a standard Moody plot given the Reynolds number of the flow. Φ represents any intensive property of the flow.

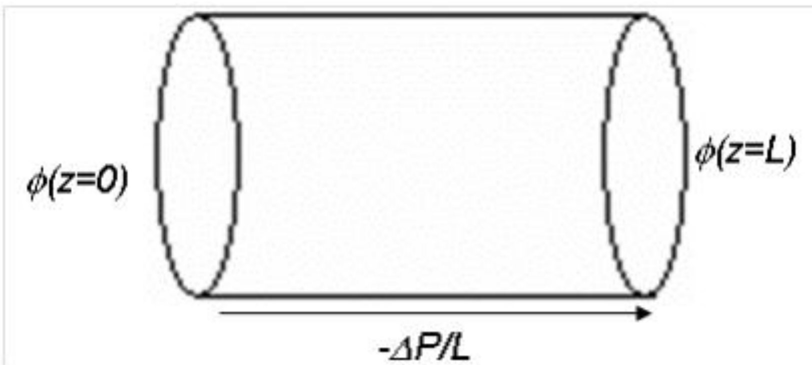

Figure 6.6. Schematic of section of pipe under PBC's.

Mesh

The flow domain was represented by a structure of hexahedra elements.

The mesh has been optimized to meet the two objectives: a reasonable computational time and a good accuracy of the solution. At the beginning of the calculations, the sensitivity -of the calculated velocity profile to the number of mesh elements was established by increasing the number of mesh points until the velocity profiles became continuous and independent of the number of mesh elements. For a section of tube which was 0.3 m in length, this mesh sensibility was achieved with a mesh specified as shown in Table 6.1.

Number of nodes	197960
Number of elements	191900
Hexahedra	191900
Max edge length ratio	409.829
Volume (m^3)	0.00139825

Table 6.1. Mesh details for the 78 mm diameter tube.

Pictures of the mesh structure used for the 78 mm tube are given in Figures 7.1 and 7.2. Similarly, pictures of the mesh for a 965 mm diameter tube are given in Figure 7.3 and 7.4.

One way coupling

In this study, we make the assumption of one way coupling between the fluid and particles. It means that the fluid flow affects the movement of the particles but the particles do not affect the fluid flow.

6.5. Steps of the post-processing

This Section describes the steps used for the post-processing of the output droplet trajectory data file. A schematic diagram of the model of a stratifying-annular flow is illustrated in Figure 6.7.

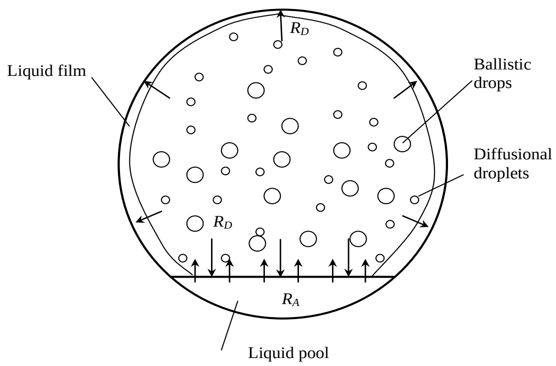

Figure 6.7. Schematic diagram of a stratifying-annular flow.

Atomisation rate

The atomisation rate R_A (kg/m^{2}s) is given by the Equation (Pan & Hanratty, 2002) for entrainment rate of liquid droplets at the surface of the liquid pool.

$$R_A = \frac{K_A^{"} U_G^2 (\rho_G \rho_L)^{1/2}}{\sigma} \left(\frac{\dot{M_{LP}}}{S_I}\right) \tag{6.12}$$

with U_G is the gas velocity, ρ_L and ρ_G are the liquid and gas density respectively, σ is the surface tension, S_I is the interfacial periphery and $\dot{M_{LP}}$ (kg/s) is the mass flow rate of liquid phase in the stratified layer.

In horizontal pipes a value $K_A^{"}$ =3.0×10^{-6} has been suggested (Pan & Hanratty 2002) and this value has been used in the present study.

The parameter S_I used to calculate this expression is illustrated on the schematic diagram in Figure 6.8.

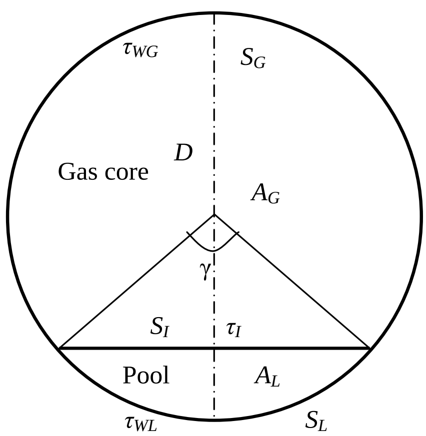

Figure 6.8. Schematic of the stratified flow.

6.5.1. Droplet deposition rate distribution around periphery

This paragraph gives the different steps to determine the deposition rate.

1) Firstly due to symmetry reasons, only the half of the circumference is considered. This part is decomposed in j partitions as illustrated in Figure 6.9. The probability of an emitted droplet of diameter di being deposited at partition j is calculated.

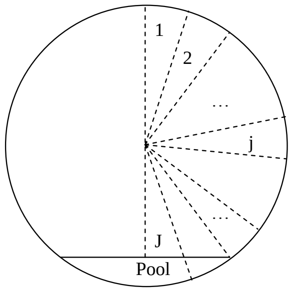

Figure 6.9. Decomposition of the circumference of the pipe in element 1 to j.

$$P_i(j) = \frac{C_i(j)}{C_i} \tag{6.13}$$

With C_i is the total number of drops with a diameter d emitted from the source plane and $C_i(j)$ is the number of droplets deposited at partition j summed on the N group of planes pn parallel to the cross section (See Figures 6.10 and 6.11).

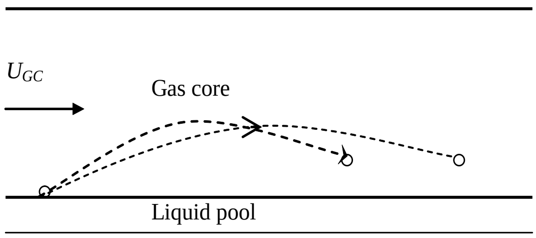

Figure 6.10. Droplets depositing at angle θ at various locations (side view of the circular pipe).

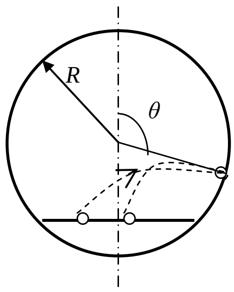

Figure 6.11. Droplets depositing at angle θ at various locations (cross sectional view of the horizontal pipe).

2) The circumferential probability is then used to establish the local deposition rate of drops at partition j.

$$R_{D_i}(j) = \frac{2R_A S_I}{(\pi D/J)N} P_i(j) \tag{6.14}$$

Where J is the number of partitions into which the pipe wall is split, R_A the atomisation rate, D the pipe diameter, S_I is the width of the interface, N is the number of equal volume increments into which the drop size spectrum has been split.

3) The distributions of film thickness and film flow rate are then obtained from the deposition rate by the analysis of Butterworth (1973). The Butterworth model is aimed at obtaining the film thickness δ(θ) at angle θ measured from the top of the pipe. The model of Butterworth (1973) leads to the following equation:

$$\beta\psi\sin\theta\frac{d\delta^+}{d\theta}+\beta\varphi\cos\theta+\varphi\sin\theta\frac{d\beta}{d\theta}=R_D^+-R_A^+ \tag{6.15}$$

with $\delta^+=\rho_L u^*\delta/\mu_L$, $R_D^+=R_D R/\mu_L$ and $R_A^+=R_A R/\mu_L$, $\beta=g\mu_L(\rho_L-\rho_G)/(\rho_L^2 u^{*3})$ and $u^*=\sqrt{\tau_o/\rho_L}$

where τ_o is the wall shear stress, R_A and R_D are the atomization and deposition rate (kg/m^2s) and *R* is the pipe radius. No entrainment is assumed to occur on the liquid film thus R_A=0. The turbulence is assumed to be isotropic in the liquid film. The following functions for φ and ψ are derived:

$$\phi=\begin{cases}\frac{1}{3}\delta^{+3} & \delta^+\le 5\\ 5\left(5\delta^+ +\delta^{+2}\left(\ln\frac{\delta^+}{5}-\frac{1}{2}\right)-\frac{25}{6}\right) & 5<\delta^+\le 30\\ 5\left(\frac{1325}{6}-25\delta^+ +\delta^{+2}\left(\frac{1}{4}+\ln 6+\frac{1}{2}\ln\frac{\delta^+}{30}\right)\right) & \delta^+>30\end{cases} \tag{6.16}$$

$$\psi=\begin{cases}\delta^{+2} & \delta^+\le 5\\ 5\left(5+2\delta^+\ln\frac{\delta^+}{5}\right) & 5<\delta^+\le 30\\ 5\left(\delta^+\left(2\ln 6+\ln\frac{\delta^+}{30}+1\right)-25\right) & \delta^+>30\end{cases} \tag{6.17}$$

For the top of the pipe (i.e. θ=0) Equation (6.15) becomes

$$\beta\phi(\delta^+)=R_D^+ \tag{6.18}$$

Knowing the deposition rate, Equation (6.18) can predict the initial film thickness at the top of the pipe $\delta(0)$. The film thickness profile can therefore be deduced using Equation (6.15).

In contrast to Butterworth's model which takes account of the axial turbulence into the film drainage, a laminar film drainage model has been developed by Baik & Hanratty (2002) which formulates the following expression for $\delta(0)$.

$$\delta(0) = \left(\frac{3R_D D \mu_L}{2g\rho_L^2} \right)^{1/3} \tag{6.19}$$

However, to be consistent with film drainage model employed in the calculation, Equation (6.18) was used in this study.

The deposition rate at a series of positions around the pipe, $R_D(\theta)$, and the local shear rate, $\tau_o(\theta)$, are fed in to the model so that the film thickness and film flow rate distributions are estimated.

6.5.2. Droplet mass flux distribution

The axis of the pipe is discretised and the outlined cell shown in Figure 6.12 represents the atomisation source cells.

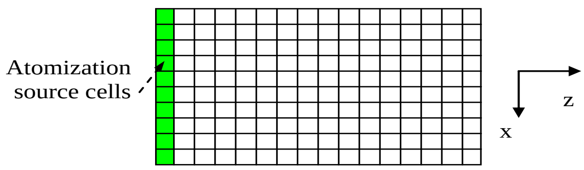

Figure 6.12. Discretisation of the axis of the pipe

The elements of areas used in calculating droplets count distribution are shown in Figure 6.13. The core cross section has been divided into JxK (72 elements). These elements have areas A(j,k) and they are truncated at the edges. The areas of the truncated elements are calculated by standard geometrical methods.

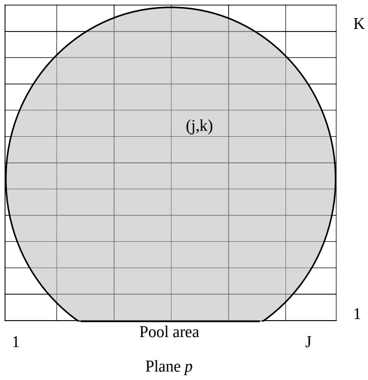

Figure 6.13. Discretisation of the axial plane of the pipe.

The steps to obtain the droplet mass flux distribution are detailed below:

1) Note pn the sum of all the parallel plane p: $\left(\mathrm{pn} = \sum_{\mathrm{p}=1}^{\mathrm{N}} \mathrm{p}\right)$

   The cumulative probability of a droplet emitted at z=0 passing through the sum of areas A(j,k) of each plane p of the group of parallel plane pn is defined by:

$$\mathrm{P_i(j,k)} = \frac{\mathrm{C_i(j,k)}}{\mathrm{C_i}} \tag{6.20}$$

2) The volumetric emission rate of droplets of diameter di

$$\dot{V}_i = R_A S_I L_p / (\rho_L N) \tag{6.21}$$

   With R_A the atomisation rate, S_I is the width of the interface, L_p the length of the periodic elements with J is the number of partitions into which the pipe wall is split, and N is the number of equal volume increments into which the drop size spectrum has been split.

3) The number of droplets of diameter di emitted per unit time from the defined element is written:

$$\dot{n}_{d_i} = \frac{\dot{V}_i}{\pi d_i^3/6} = \frac{R_A S_I L_p}{\rho_L N\left(\frac{\pi d_i^3}{6}\right)} \tag{6.22}$$

$$\left(\dot{n}_{d_i}(j,k,-N) = \dot{n}_{d_i} P_i(j,k,-N)\right)$$

4) The total number of droplets of diameter di passing through the sum of parallel areas A(j,k) per unit time is equal to the expression below:

$$(\dot{n}_{d_i}(j,k) = \dot{n}_{d_i} \sum_{p=-N}^{p=-1} P_i(j,k,p) = \dot{n}_{d_i} \sum_{p=1}^{p=N} P_i(j,k,p) = \dot{n}_{d_i} P_i(j,k))$$

$$\dot{n}_{d_i}(j,k) = \dot{n}_{d_i} P_i(j,k) \tag{6.23}$$

5) The mass flux of droplet of diameter di passing through area A(j,k) is then written:

$$\dot{m}_i(j,k) = \frac{\dot{n}_{d_i}(j,k)\rho_L(\pi d_i^3)}{6A(j.k)} = \frac{\dot{n}_{d_i} P_i(j,k)\rho_L(\pi d_i^3)}{6A(j.k)} = \frac{R_A S_I L_p P_i(j,k)}{A(j.k)N} \tag{6.24}$$

6) The expression of the total local drop mass flux through area A(j,k) is therefore:

$$\dot{m}(j,k) = \frac{R_A S_I L_p}{A(j.k)N} P_i(j,k) \tag{6.25}$$

Where R_A is the total liquid atomization rate (kg/m^{2}s), S_I is the width of the interface, L_P is the length of the periodic elements and N is the number of equal increments into which the drop size spectrum has been split.

7) The total droplet mass flux in the gas core

$$\dot{m} = \sum_{j,k} \dot{m}(j,k) \tag{6.26}$$

CHAPTER 7

Results from CFX-RANS modelling studies and comparisons with experiments

CFX (RANS) calculations were carried out (using the methodology outlined in Chapter 6) for stratifying annular flow in a 78 mm (3 inch nominal) diameter pipe and were compared with data obtained on the WASP facility. Calculations were also carried out for stratifying annular flow in a much larger pipe (namely for a 0.965 m, 38 inch pipe) to gain some insights into the differences in flow behaviour between small and large pipes. It should be noted that, in both cases, liquid transport to the top of the pipe would still be dominated by droplet transport.

In what follows, Section 7.1 presents the results obtained for the continuous phase flow distribution. The results are presented for the 78 mm WASP pipe cross section and also (for comparison) with what would be obtained in a much larger (0.965 m, 38 inch) pipe. Section 7.2 gives results for droplet trajectories for droplets injected at the centre of the pool and Section 7.3 gives results for droplet trajectories for droplets injected at random positions across the width of the pool. Section 7.4 gives the distributions for a 3 inch diameter pipe of the following quantities: deposition rate, liquid film flow rate, liquid film thickness and droplets mass flux. Comparisons are made in Section 7.5 and finally a conclusion is given in Section 7.6.

7.1 Flow distribution in the continuous phase

Calculations were carried out for the reference case of a 78 mm diameter pipe as used in the WASP facility, and also (for comparison) for a pipe with a diameter of 965 mm (38 inches). The direct influence of the liquid phase droplets on the continuous phase behaviour has been assumed to be negligible.

The first step in modelling the continuous phase is to create a mesh to discretise the core flow region. Typical meshes are shown in Figures 7.1 and 7.2 for the 78 mm pipe and, in Figures 7.3 and 7.4, for the 965 mm pipe. The main characteristics of the meshes used are given in Tables 7.1 and 7.2. Of course, the actual detailed shape and behaviour of the core region depends on the dimensions of the wall liquid layer and this is part of the overall calculation.

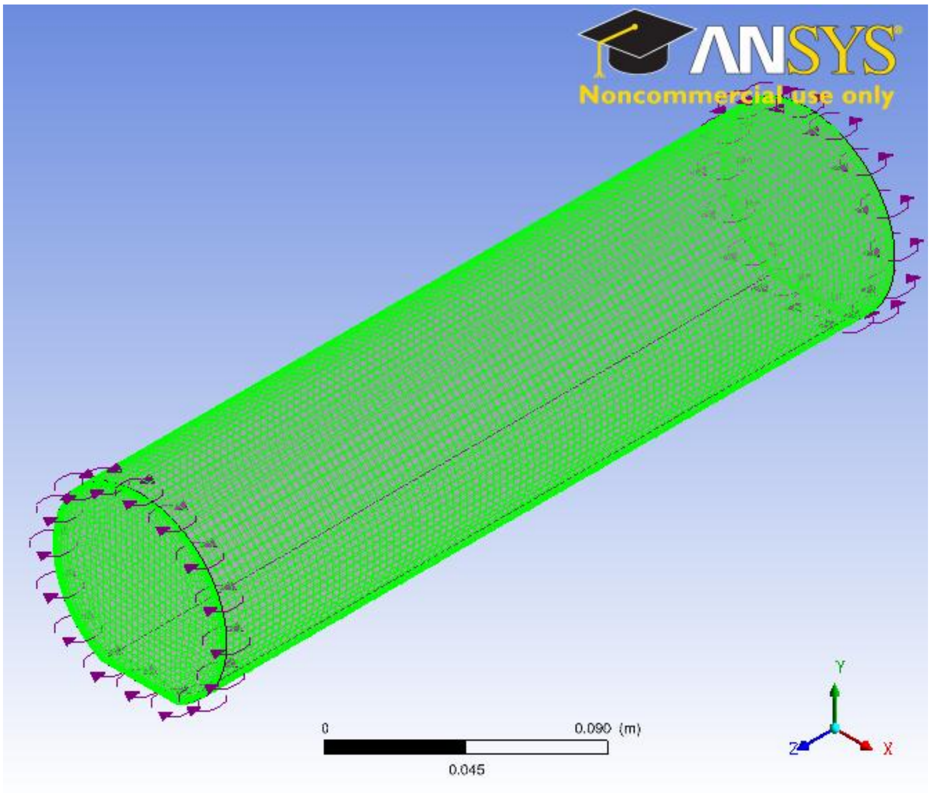

Figure 7.1. Mesh used for 78 mm diameter pipe.

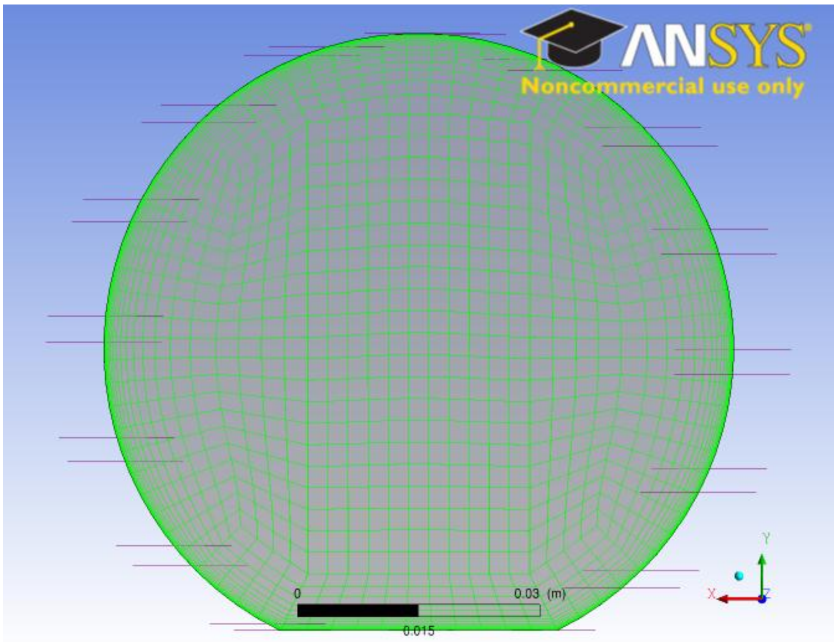

Figure 7.2. Cross-sectional view of mesh used for 78 mm diameter pipe.

Selected Region:	Assembly
Number of Nodes:	197960
Number of Elements :	191900
Hexahedra :	191900
Extents: min x max x : min y max y : min z max z :	-0.0389727 [m], 0.0389727 [m] -0.035 [m], 0.0389639 [m] 0 [m], 0.3[m]
Max Edge Length Ratio:	409.829
Volume :	0.00139825[m^3]

Table 7.1. Mesh Statistics for 78 mm diameter pipe.

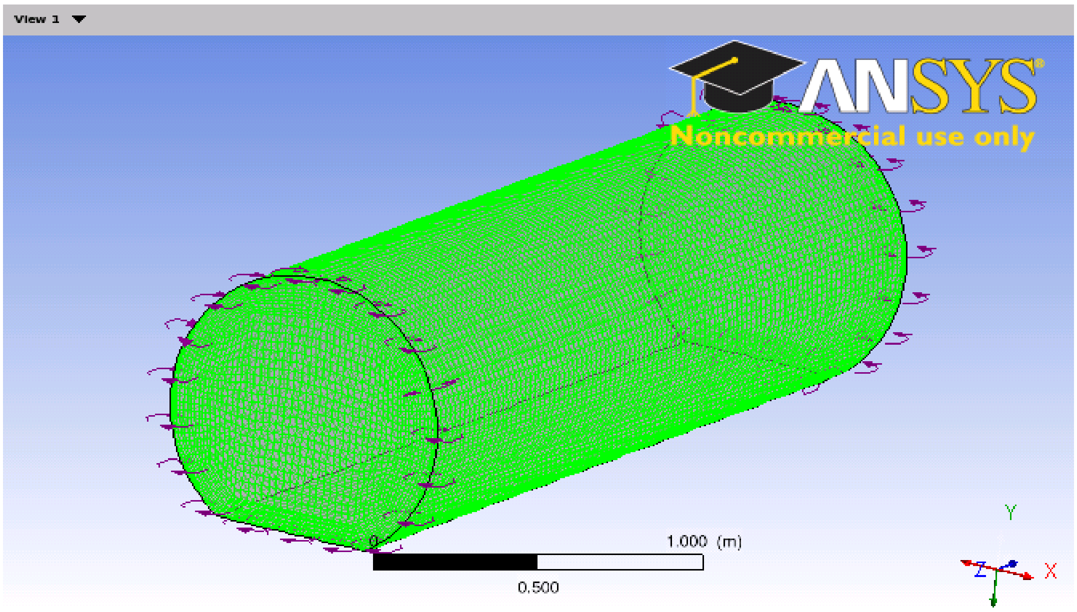

Figure 7.3. Mesh used for 965 mm (38 inch) diameter pipe.

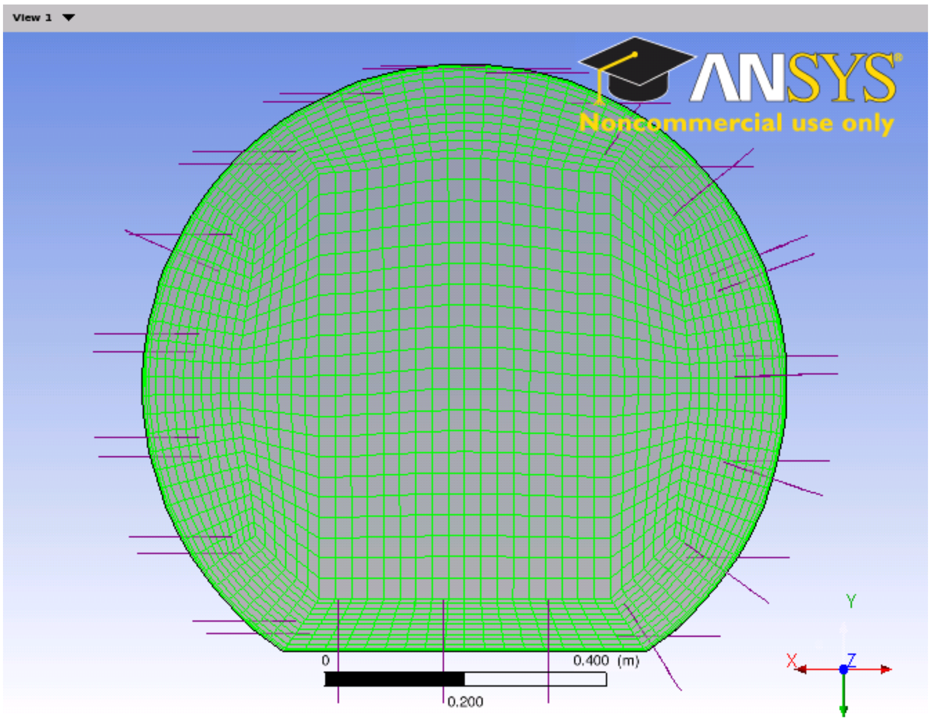

Figure 7.4. Cross-sectional view of mesh used for 965 mm diameter pipe.

Selected Region:	Assembly
Number of Nodes:	223412
Number of Elements :	216000
Hexahedra :	216000
Extents: min x max x : min y max y : min z max z :	-0.458587 [m], 0.458587 [m] -0.3788 [m], 0.4588 [m] -4.13571e-09 [m], 3.00006 [m]
Max Edge Length Ratio:	181.731
Volume :	1.89261 [m^3]

Table 7.2. Mesh Statistics for the 965 mm diameter pipe.

Figures 7.5 and 7.6 show end views of the pipe for the 78 mm and 965 mm cases respectively with the magnitude of the axial component of velocity indicated by the color code. Figures 7.7 and 7.8 show the components of axial velocity (again color coded) in a horizontal plane passing through the tube axis, again for the 78 mm and 965 mm pipes respectively.

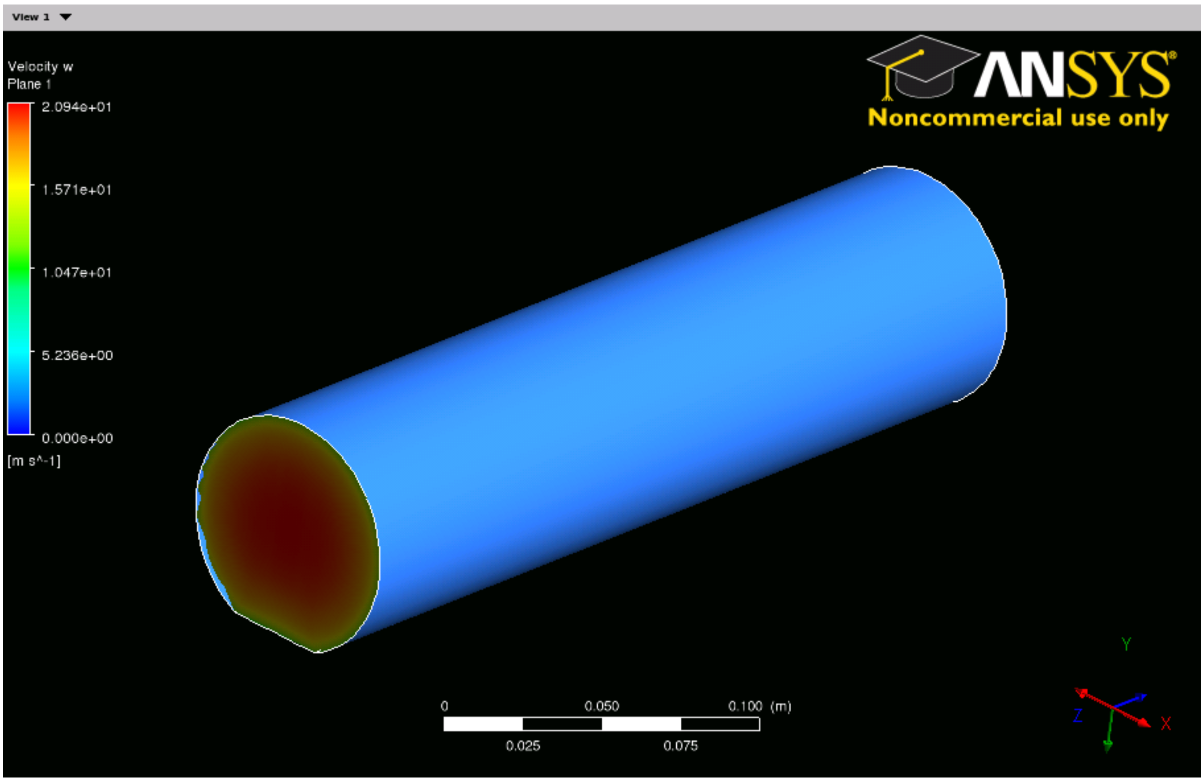

Figure 7.5. CFX-RANS results showing axial component of velocity for the 78 mm pipe.

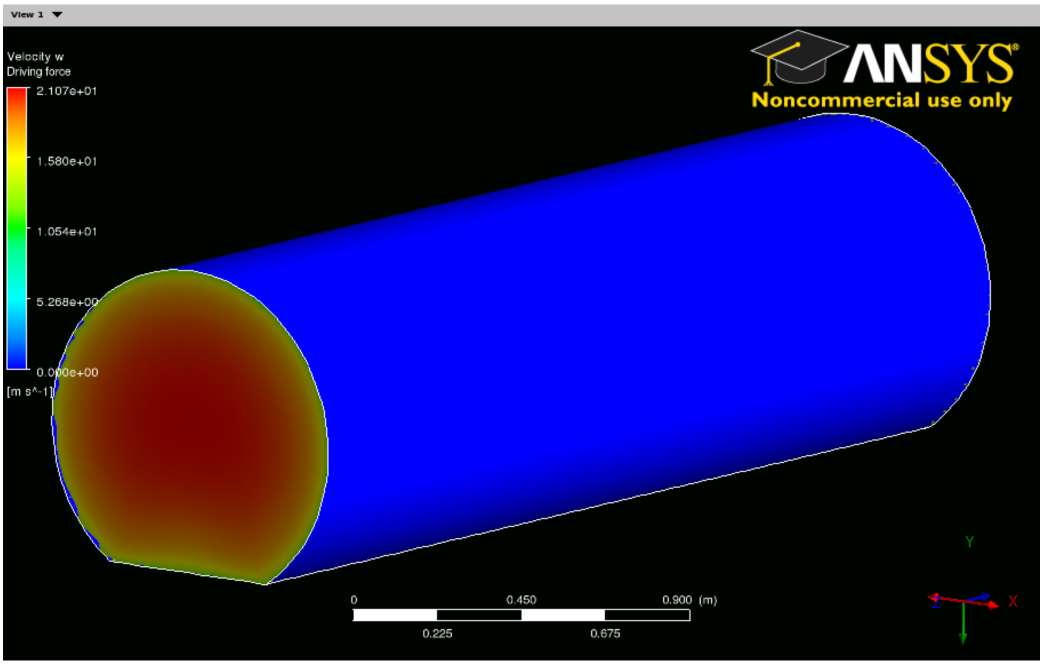

Figure 7.6. CFX-RANS results showing axial component of velocity for the 965 mm pipe.

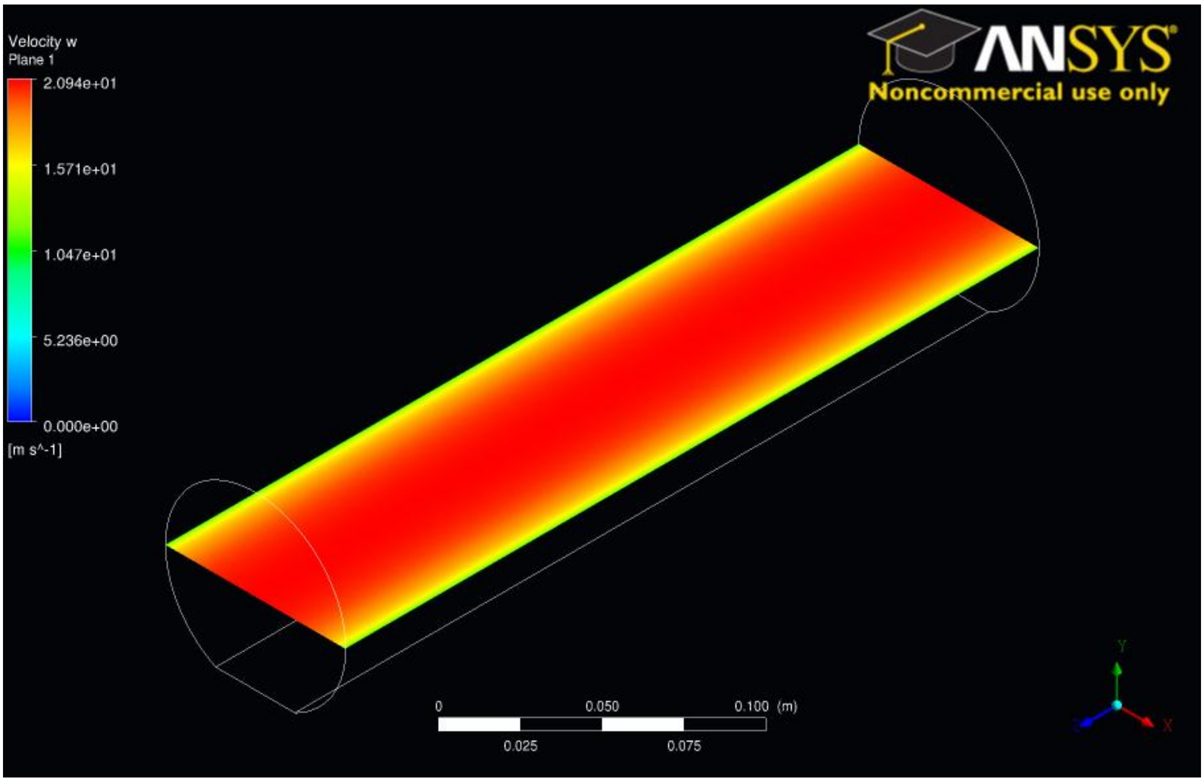

Figure 7.7. Axial velocity distribution in a horizontal plane passing through the tube centre line. 78 mm diameter tube.

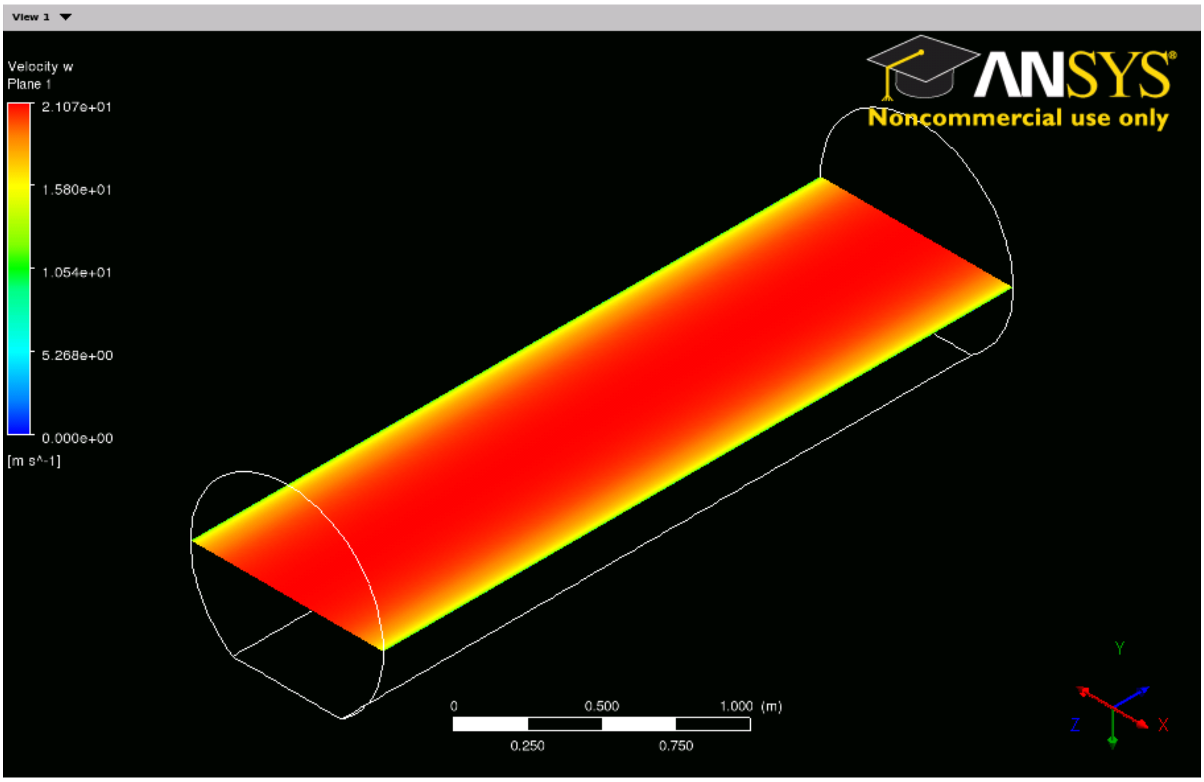

Figure 7.8. Axial velocity distribution in a horizontal plane passing through the tube centre line. 965 mm diameter tube.

7.2. Calculated droplet trajectories for droplets introduced at the centre of the pool

Using the Lagrangian tracking methodology incorporated into CFX, it was possible to calculate the motion of droplets of a given size being emitted from the centre position across the liquid pool. Ultimately, the droplets deposit on the tube wall and it is useful (following Brown et al, 2009) to plot the distribution function for drop deposition position based on the partitions illustrated in Figure 7.9; in the present work, the channel circumference was split into 10 such equal partitions. The probabilities of deposition for a sample of droplets are presented here for both a 3 inch and a 38 inches diameter pipes. The aim is to give an overview of the path followed by the droplets and to evaluate their deposition behaviour.

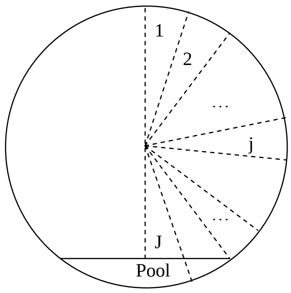

Figure 7.9. Element of pipe periphery for droplet deposition (Brown et al, 2009).

The results obtained for the 78 mm diameter pipe are given in Tables 7.3 and 7.4 for superficial gas velocities of 21 m.s^{-1} and 25 m.s^{-1} respectively. The droplet diameters investigated were 10, 50,100 200, 500 and 1000 microns. The trajectories of 1000 droplets in the cross section of the pipe and the probability of deposition in a partition (as defined above) are given for each droplet size.

D(μm)	Visualisation of the droplet motion in the cross section, **78 mm (3 inch) pipe, U_{SG}=21m.s^{-1}**	Probability of deposition at angle θ measured from the top of the pipe
10	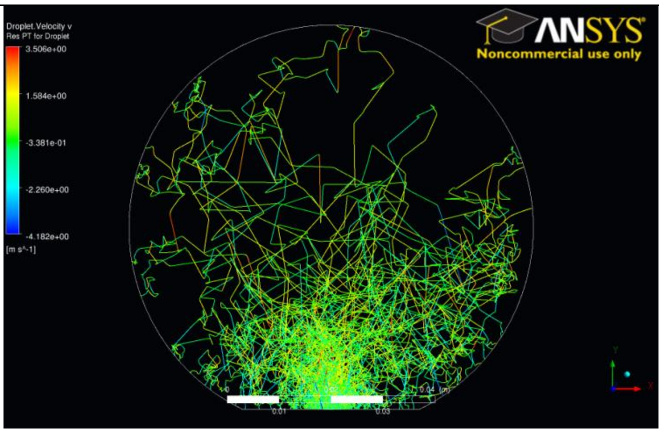	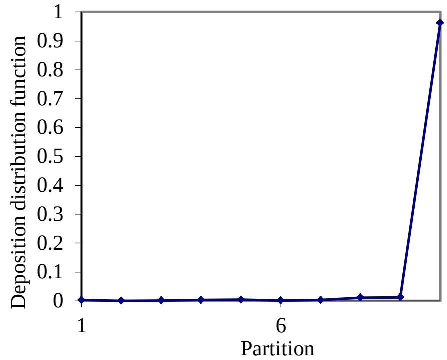
50	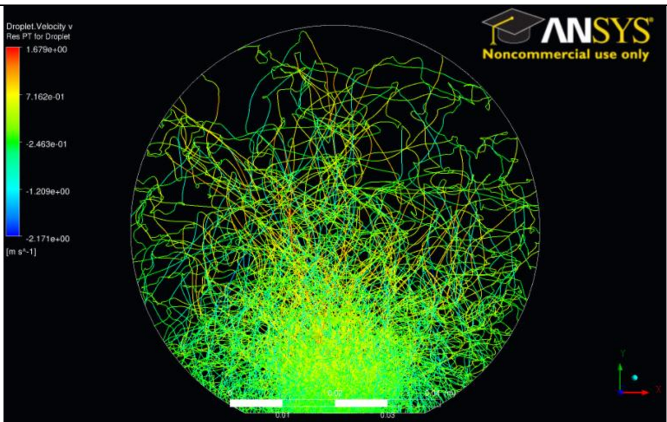	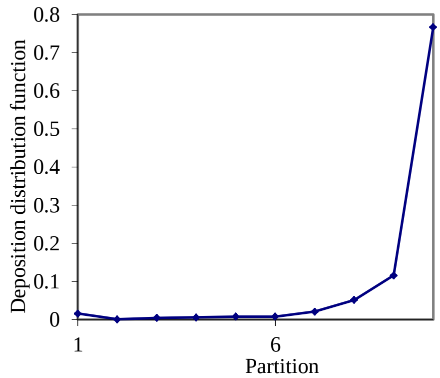
100	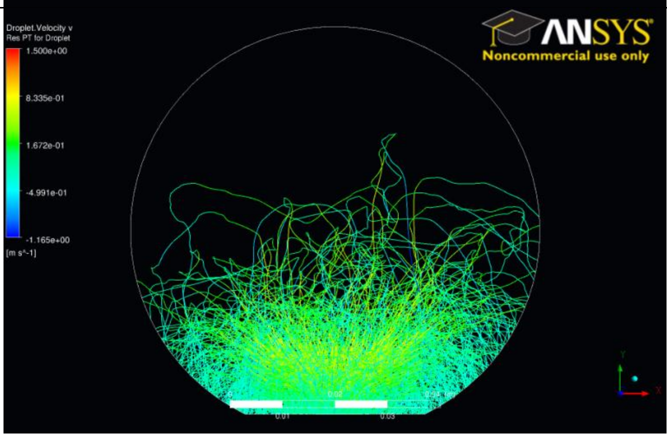	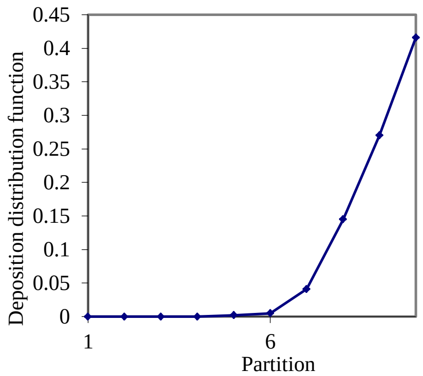
200	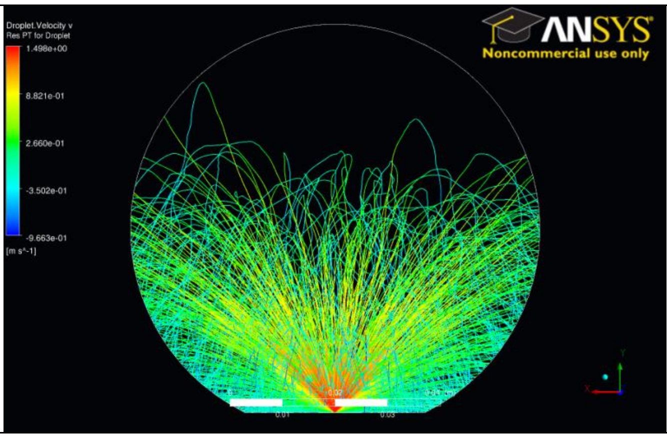	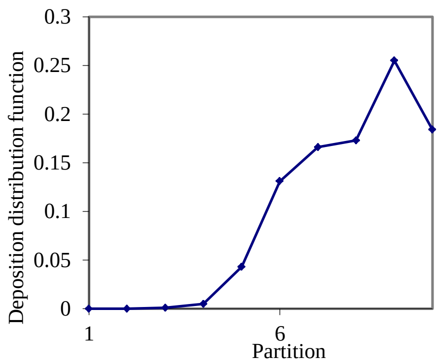

500	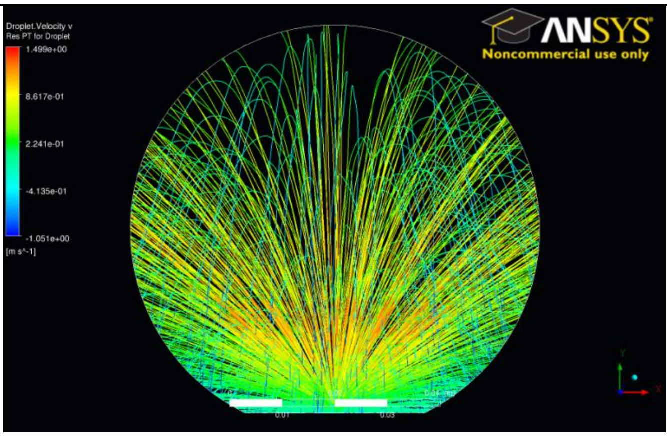	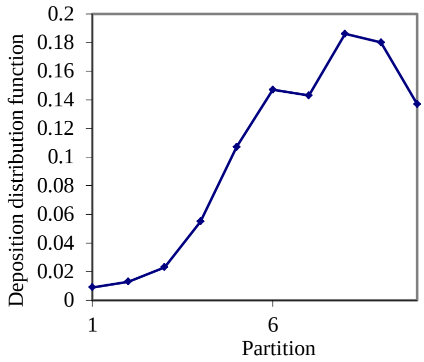
1000	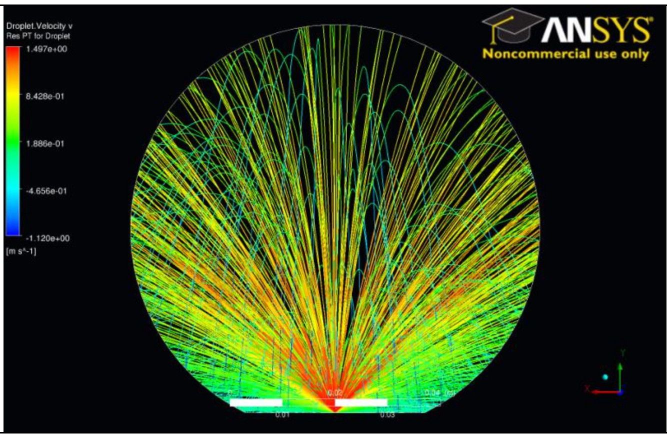	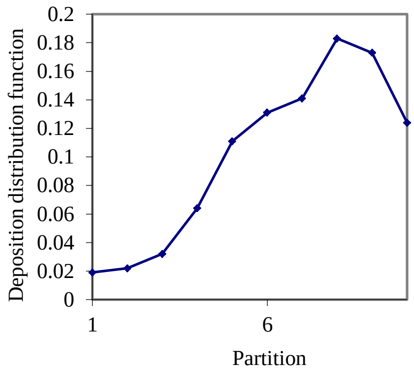

Table 7.3. Droplet trajectories and probability of deposition in each partition: 78 mm diameter tube, U_{SG}=21 m.s^{-1}, droplets injected at centre of pool.

<table>
<tr><th>D (µm)</th><th>Visualisation of the droplet motion in the cross section,
<u>78 mm (3 inch) pipe, U_{SG}=25 m.s^{-1}</u></th><th>Probability of deposition at angle θ measured from the top of the pipe</th></tr>
<tr><td>10</td><td>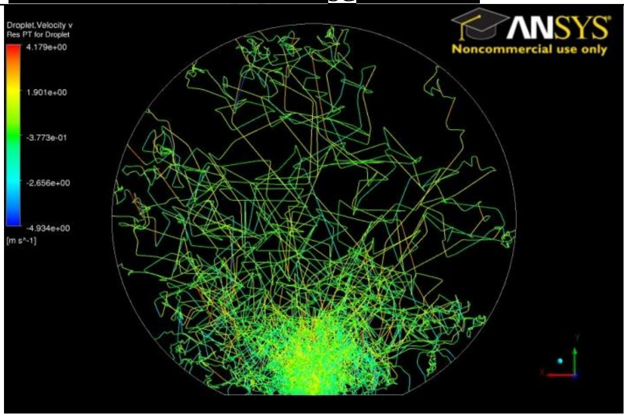
</td><td>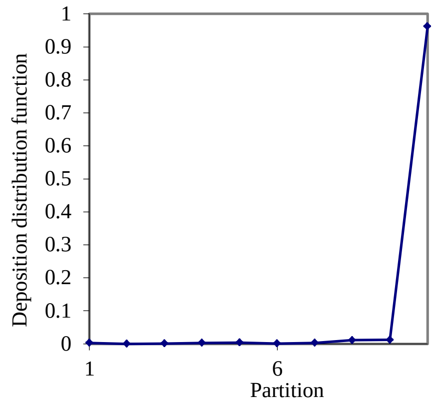
</td></tr>
<tr><td>50</td><td>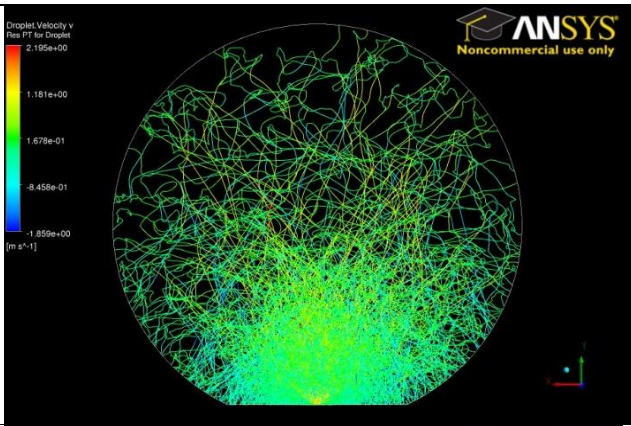
</td><td>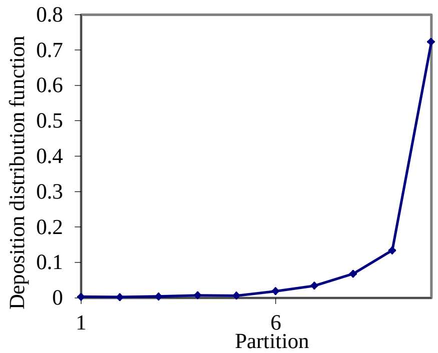
</td></tr>
<tr><td>100</td><td>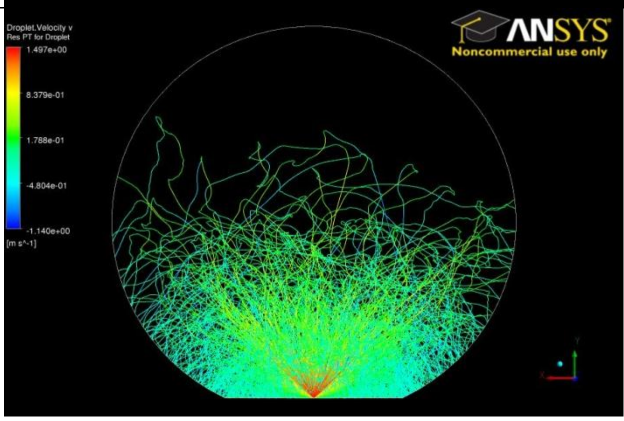
</td><td>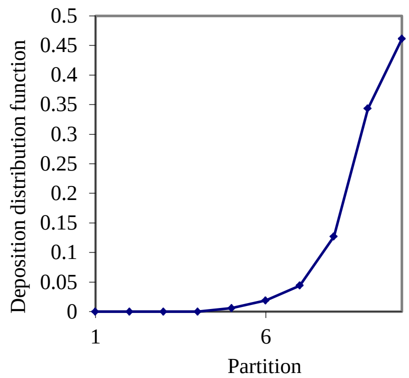
</td></tr>
</table>

200	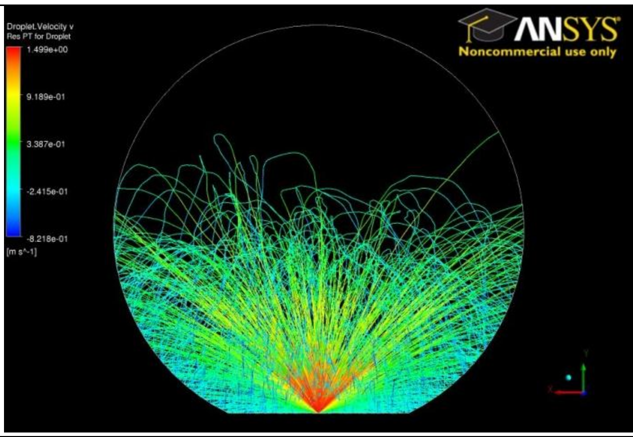	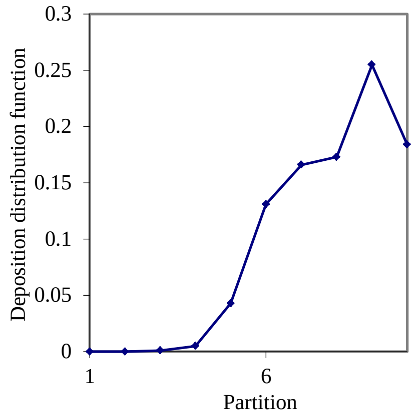
500	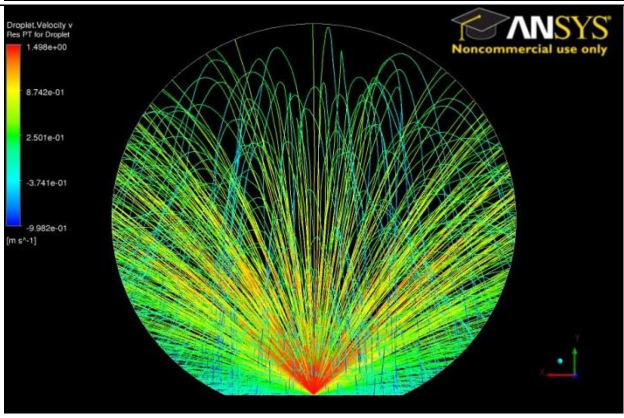	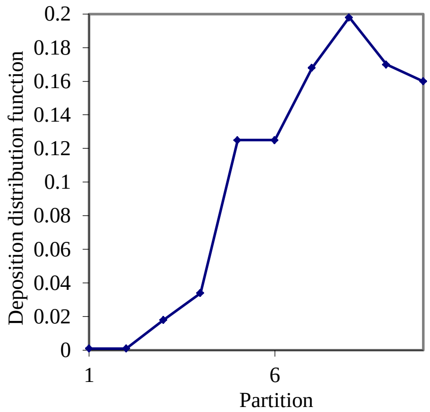
1000	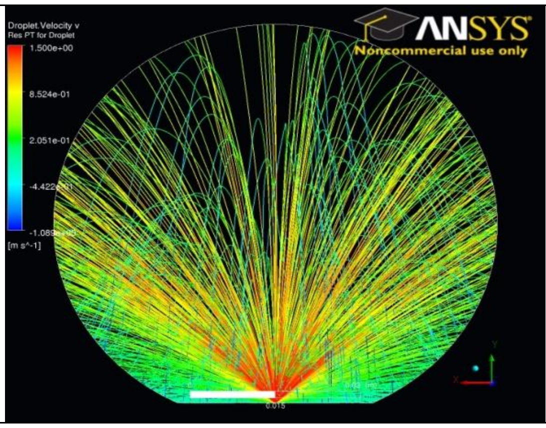	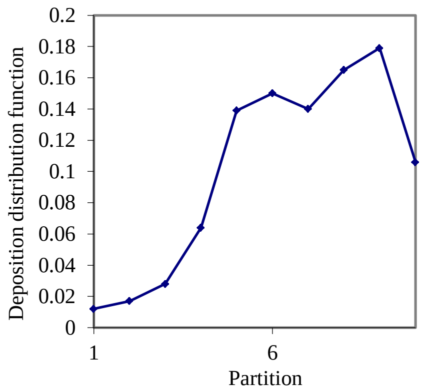

Table 7.4. Droplet trajectories and probability of deposition in each partition: 78 mm diameter tube, U_{SG}=25 m.s^{-1}, droplets injected at centre of pool.

The deposition distribution functions for both gas velocities show that the probability of touching the top of the tube is higher for droplets of size greater than 200 microns which indicates that (for the 78 mm diameter tube), the droplet deposition process is dominated by the ballistic effect.

It is perhaps clearer to consider the motion of a smaller number of droplets, though a large number of trajectories are required to obtain statistically satisfactory quantitative data. Table

7.5 shows the droplets trajectories for 10 droplets in the case of the 78 mm diameter tube for several droplet sizes. It can be clearly seen that the trajectory is dominated by gravity and that turbulent diffusion is negligible for the larger droplets (greater than 100 micron diameter), the small drops following a fluctuating path which indicates the influence of turbulence.

D=10 microns	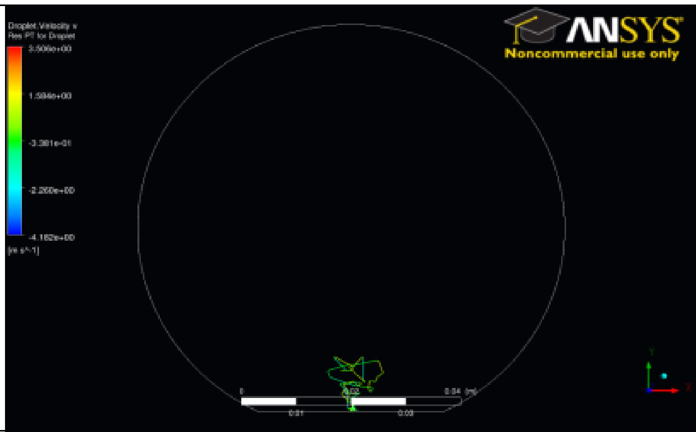
D=50 microns	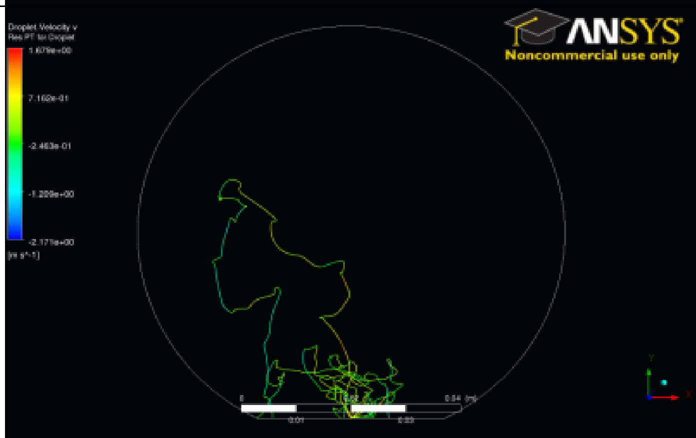
D=100 microns	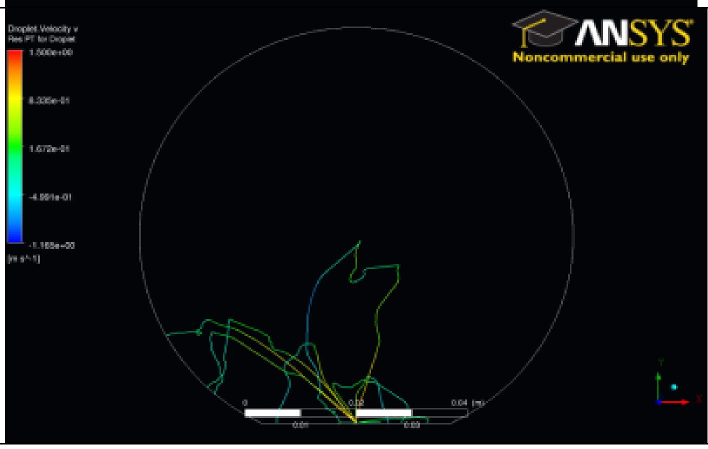

D=200 microns	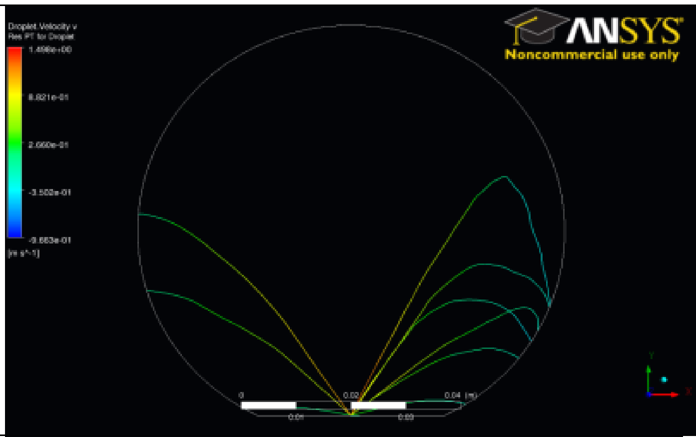
D=500 microns	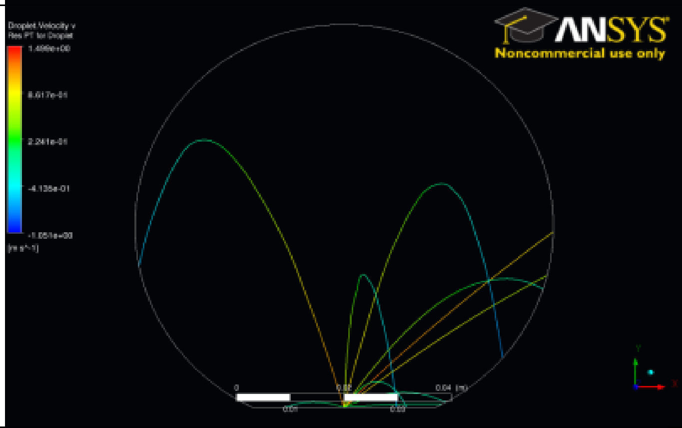
D=1000 microns	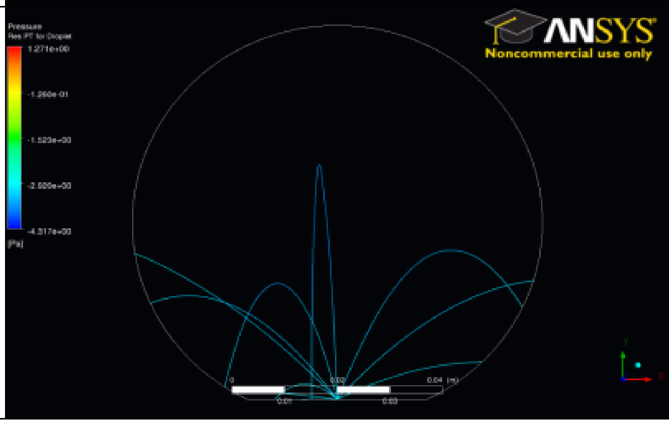

Table 7.5. Droplet trajectories at 21 m.s^{-1} superficial gas velocity for the 78 mm pipe.

Tables 7.6 and 7.7 show the results obtained for a 965 mm (38 inch) diameter pipe for velocities of 21 and 25 m.s^{-1} respectively. The drop sizes considered were 10, 50,100 200, 500 and 1000 microns. For each drop size and gas velocity, the trajectory of 1000 droplets in the cross section of the pipe and the probability of deposition at angle θ measured from the top of the pipe are represented, again with the droplets injected at the central position across the pool.

<table>
<tr><th>D (µm)</th><th>Visualisation of the droplet motion in the cross section,
965 mm (38 inches) pipe, U_{SG}=21 m.s^{-1}</th><th>Probability of deposition at angle θ measured from the top of the pipe</th></tr>
<tr><td>10</td><td>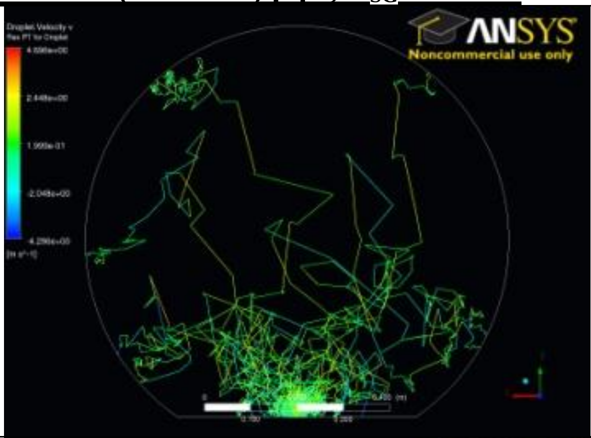</td><td>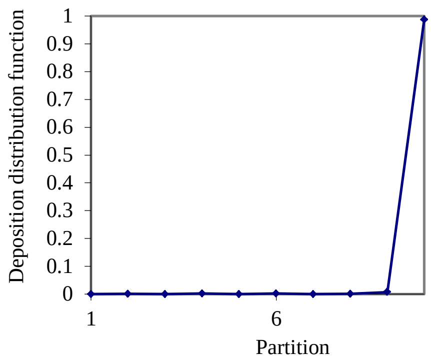</td></tr>
<tr><td>50</td><td>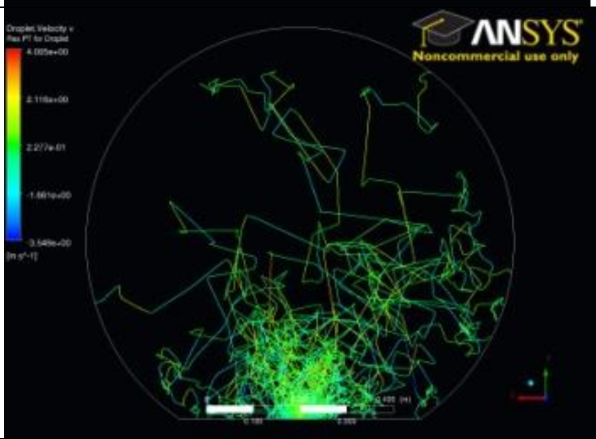</td><td>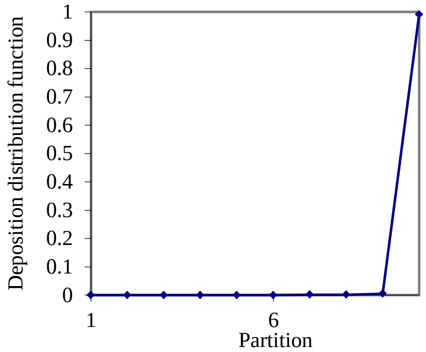</td></tr>
<tr><td>100</td><td>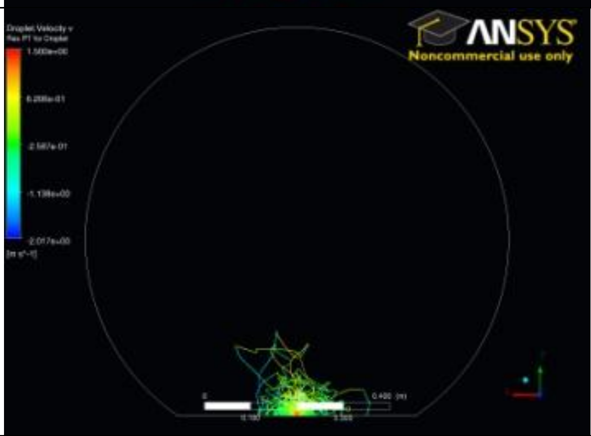</td><td>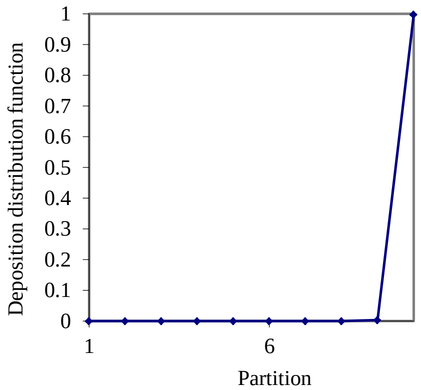</td></tr>
<tr><td>200</td><td>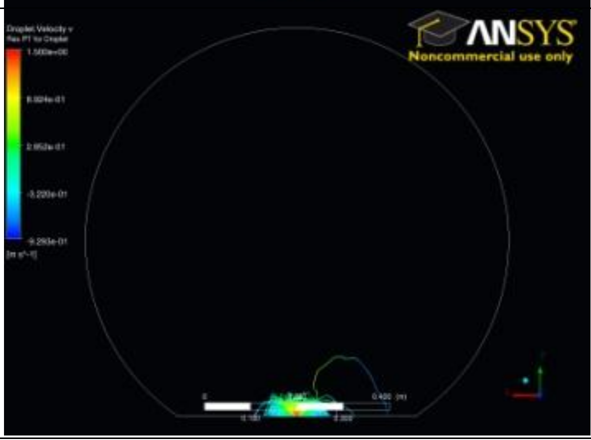</td><td>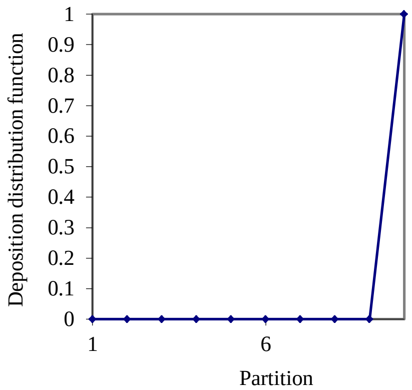</td></tr>
</table>

500		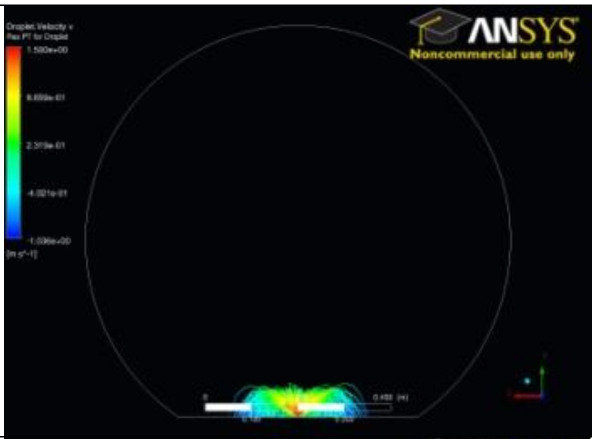		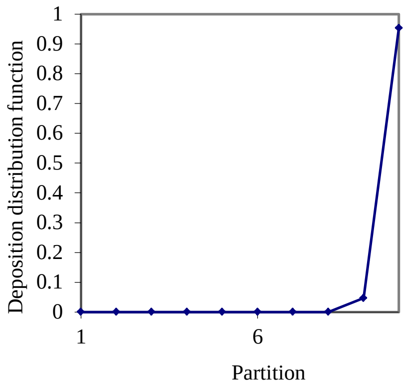
1000		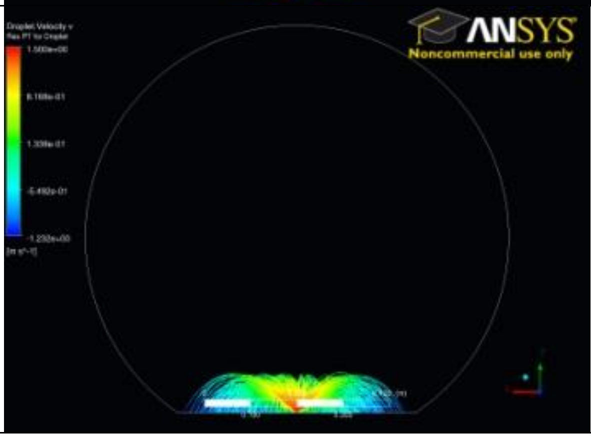		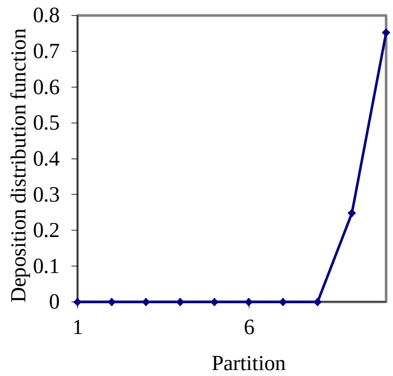

Table 7.6. Droplet trajectories and probability of deposition in each partition: 965 mm (38 inch) diameter tube, U_{SG}=21 $m.s^{-1}$, droplets injected at centre of pool.

38inch D (µm)	1000 droplets	10000 droplets	100000 droplets
10	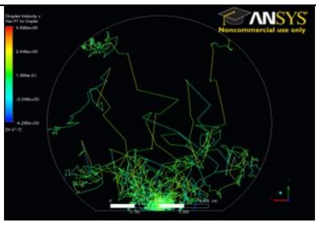	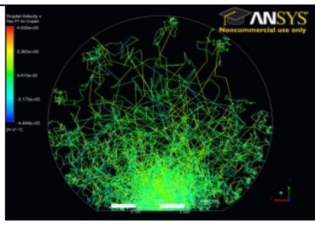	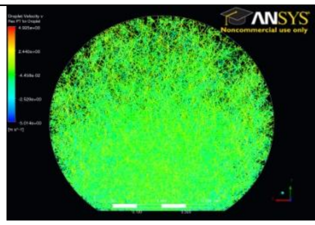
100	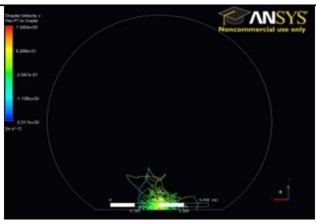	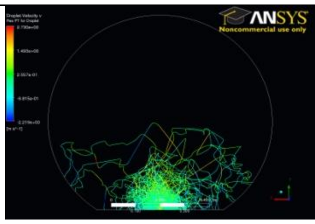	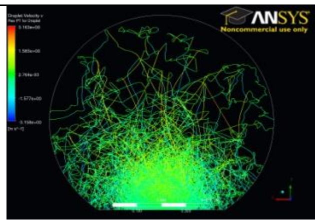
200	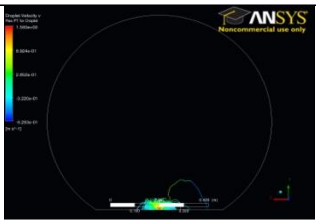	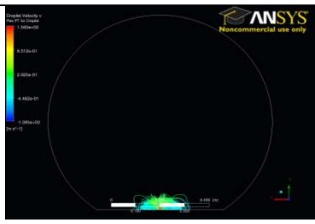	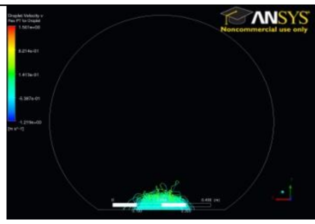
500	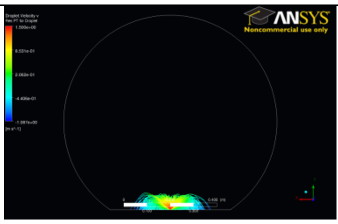	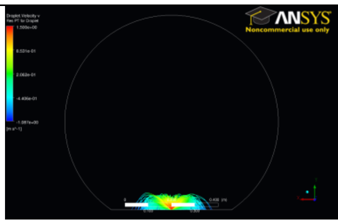	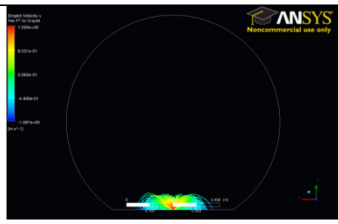
1000	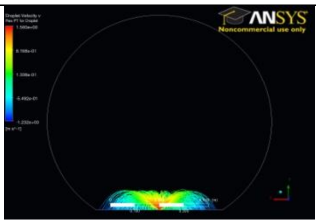	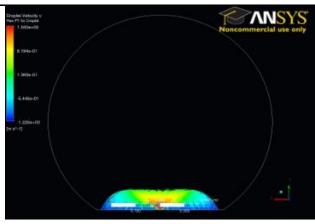	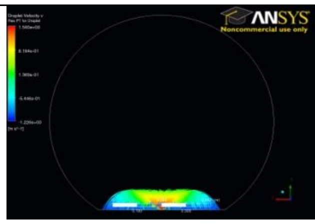

Table 7.7. Droplet trajectories and probability of deposition in each partition: 965 mm (38 inch) diameter tube, U_{SG}=25 m.s^{-1}, droplets injected at centre of pool.

As can be seen from Tables 7.6 and 7.7, the larger drops do not penetrate beyond a fraction of the diameter in the direction of the upper surface of the pipe. On the other hand, the smaller droplets undergo random motions induced by the turbulence and have a small but significant chance of being deposited in the upper regions. Thus, for this larger pipe diameter, wetting of the upper surface of the pipe is possible only by turbulent diffusion of the smaller drops. In contrast, the larger ("ballistic") drops play a dominant role in deposition on the upper surface of the pipe in the case of the 78 mm pipe. However, they do not have sufficient initial velocity to reach the top of the larger pipe. For this latter case, the (small rate) deposition in the upper region of the pipe is dominated by transport by turbulent diffusion of the smaller ("diffusional") droplets.

Again, it is probably easier to see the influence of droplet size by showing fewer drops. Thus, Table 7.8 shows the droplets trajectories for 100 droplets in the case of the 965 mm (38 inch) pipe for several droplet sizes. The trajectory is dominated by gravity for the biggest ("ballistic") droplets and by the turbulent diffusion for the smallest ("diffusional") droplets.

D=10 microns	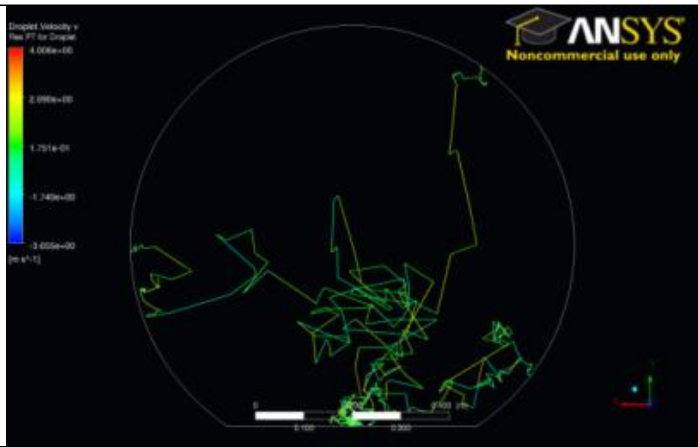
D=50 microns	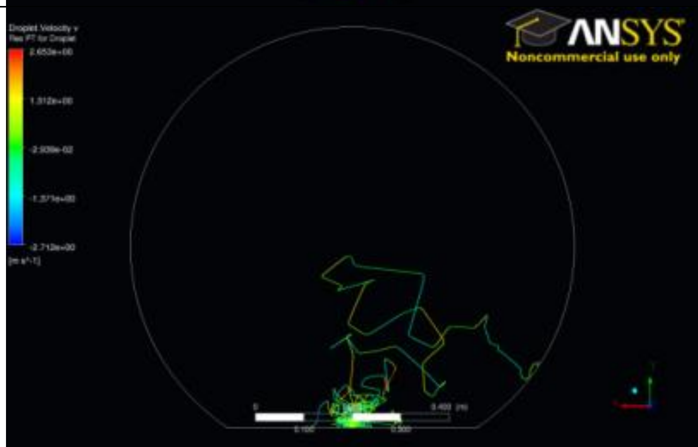
D=100 microns	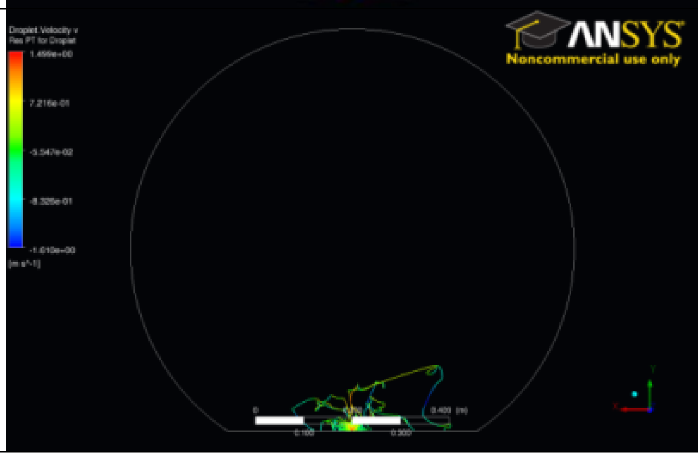

D=200 microns	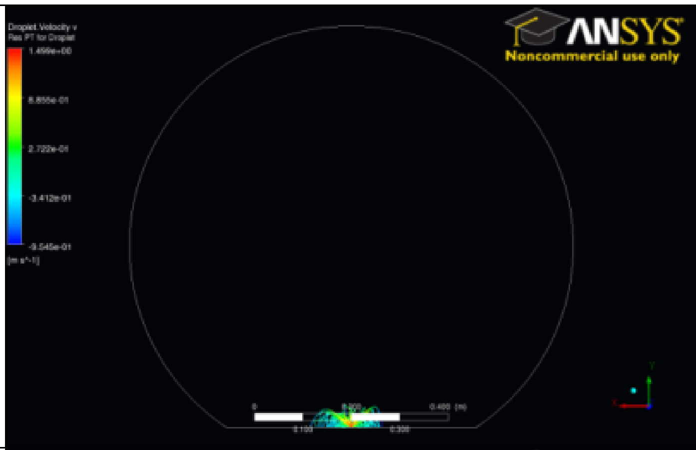
D=500 microns	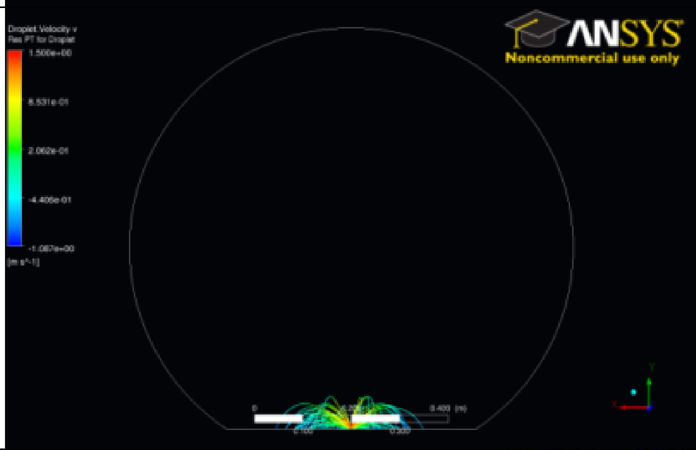
D=1000 microns	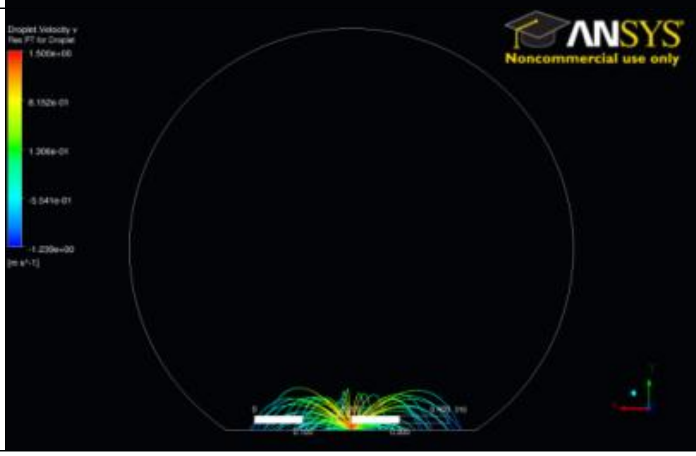

Table 7.8. Droplet trajectories in a 965 mm (38 inch) pipe with U_{SG}= 21 $m.s^{-1}$.

7.3. Calculated droplet trajectories for droplets introduced at a random position across the liquid pool

Though it is interesting to model the case of injection of the droplets from a central position in the liquid pool, it is necessary, for the purpose of comparison with experimental data, to consider the more physically realistic case of droplet injection at a random position across the liquid pool. Table 7.9 presents results obtained for the 78 mm diameter tube at a gas superficial velocity of 21 $m.s^{-1}$. We can see that the probability to touch the top of the pipe is high not only for 50 microns diameter droplets but also for droplets with sizes superior to 500 microns. Nevertheless, the dominant effect acting on the droplets to help them to touch the top is different according to their sizes. The influence of the turbulent diffusion is dominant in case of smaller droplets and it is the gravity and thus the initial injection velocity with a ballistic effect that is preponderant in the case of bigger droplets as shown by the ballistic path followed by the droplets in this case.

D=10 microns	D=50 microns	D=100 microns
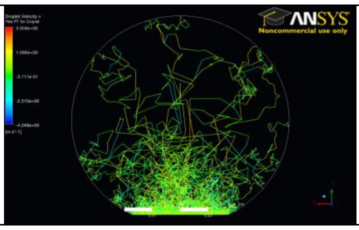	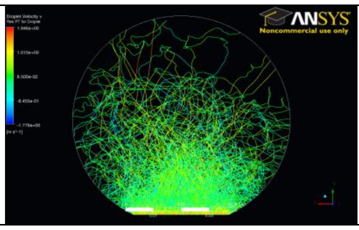	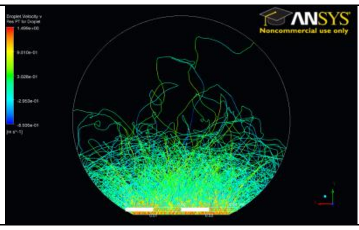
D=200 microns	D=500 microns	D=1000 microns
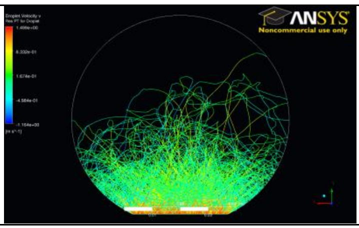	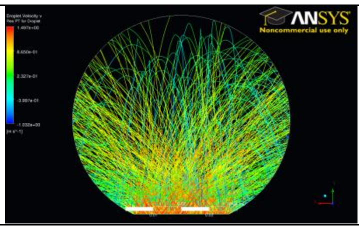	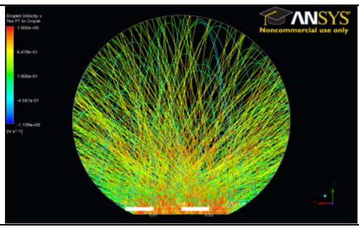

Table 7.9. Trajectories for 1000 droplets injected into the gas core from a random position across the pool for a range of drop sizes. 78 mm pipe, U_{SG}=21 m.s^{-1}.

Table 7.10 presents the results obtained when the droplets are injected at random positions on the liquid pool for a 965 mm diameter pipe with an air superficial velocity of 25 m.s^{-1}. The probability to wet the top of the pipe is very small but remains possible for small droplets with a range of size of 10-50 microns.

D=10 microns	D=50 microns	D=100 microns
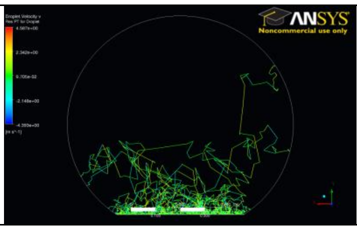	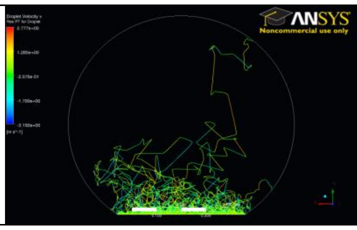	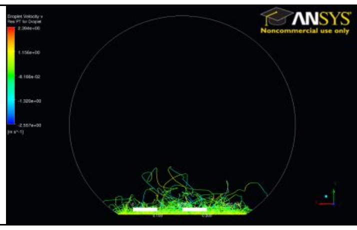
D=200 microns	D=500 microns	D=1000 microns
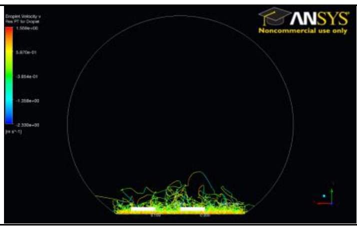	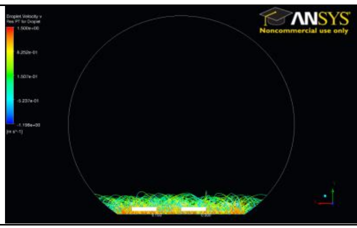	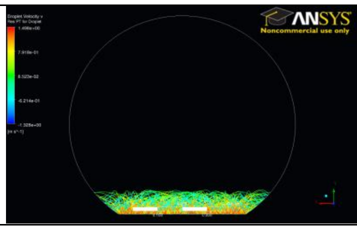

Table 7.10. Trajectories for 1000 droplets injected into the gas core from a random position across the pool for a range of drop sizes. 965 mm pipe, U_{SG}=25 m.s^{-1}.

Table 7.11 presents the results obtained for the 965 mm diameter pipe when the droplets are injected at random positions on the liquid pool in an air flow with a superficial velocity of 25 m.s^{-1} and with a random droplet diameter. The probability to wet the top of the pipe exists and is due to the contribution of the smallest droplets under the effect of the turbulent diffusion as shown previously.

Visualisation of the droplet in the cross section (U_{SG}=25m.s^{-1}) : Random Position and diameter		
1000 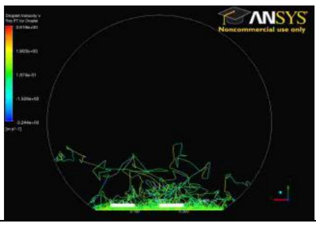	10000 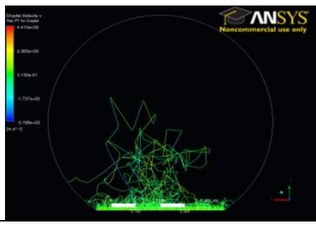	100000 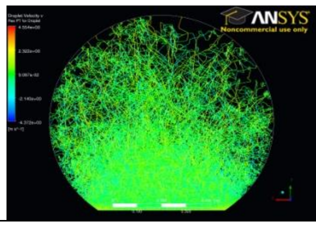

Table 7.11. 1000, 10000 and 100000 trajectories for droplets injected into the gas core from a random position across the pool for randomly selected drop sizes - 965 mm pipe, U_{SG}=25 m.s^{-1}.

7.4. Calculations for 78 mm tube and comparisons with experiments

It is of interest to consider in more detail the predictions from the CFX-RANS model for the case studied experimentally (namely in the WASP facility with a 78 mm diameter tube) and (where possible) to make quantitative comparisons between measured and calculated results. The computational results have been analysed (in the manner described in Chapter 6) to produce predictions of deposition rate of droplets (Section 7.4.1), distribution of liquid film flow rate (Section 7.4.2), distribution of liquid film thickness (Section 7.4.3) and droplet mass flux distrbution (Section 7.4.4). The calculations were carried out for the 4 standard conditions described in Chapters 4 and 6. Comparisons with limited experimental data were possible in the cases of film flow rate and droplet mass flux.

7.4.1. Deposition rate calculations

The deposition rate has been determined as a function of angle for the four sets of conditions for the superficial gas velocity and the superficial liquid velocity listed in Section 4.3.2.5. The results are illustrated in Figure 7.10.

The deposition rate distributions are almost identical for the superficial gas velocities of 9.98 $m.s^{-1}$ and 11.8 $m.s^{-1}$. Moreover, the plots for high gas velocities i.e. for superficial gas velocities of 21 $m.s^{-1}$ and 25 $m.s^{-1}$ are also very close. The deposition rate is higher at high superficial gas velocities in comparison with the one obtained at low superficial gas velocities.

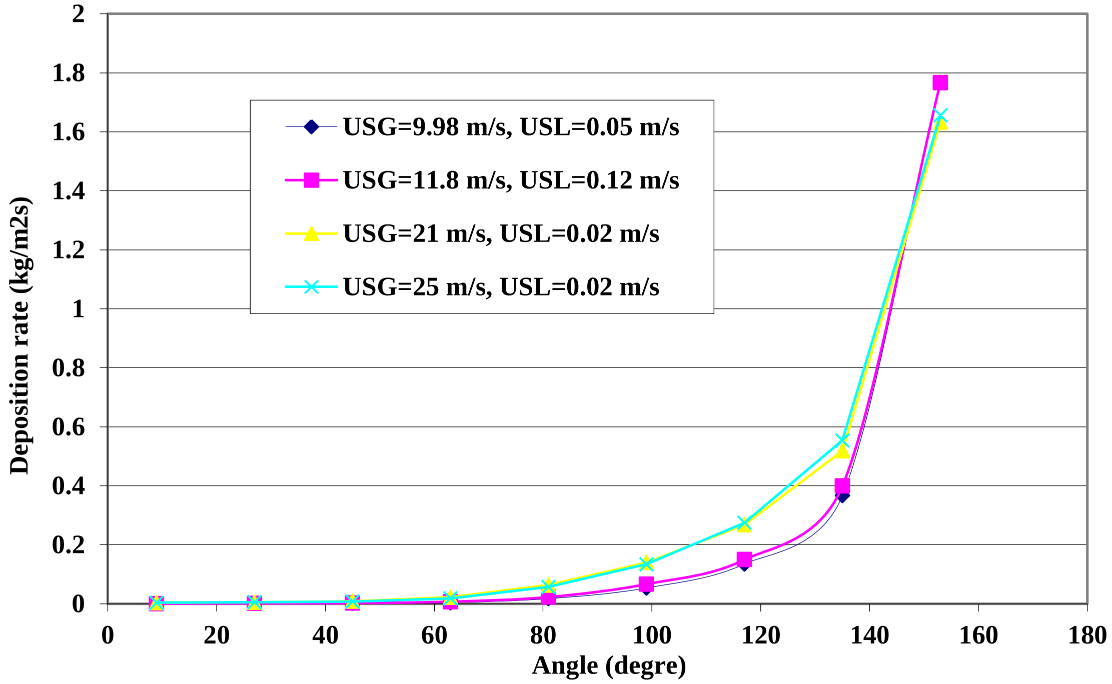

Figure 7.10. Deposition rate distribution; 78 mm diameter tube.

7.4.2. Film flow rate distribution

Application of the method of Butterworth (1973) (as described in detail in Chapter 6) allows the film flow rate to be determined from the deposition rate distribution. The results are illustrated in Figure 7.11. The curves for the film flow rate distributions at high gas velocities are quite similar and it is the same for the curves at low gas velocties. The liquid film flow rate is higher at high superficial gas velocities than at low superficial gas velocities.

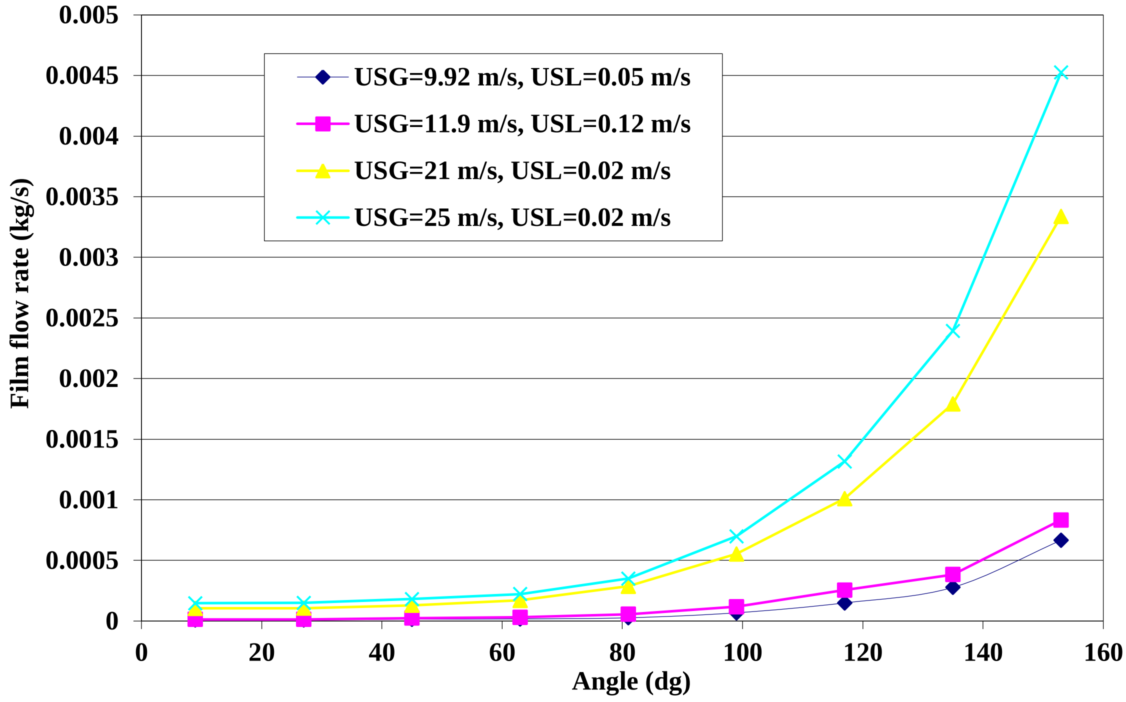

Figure 7.11. Film flow rate distribution-Comparisons of 4 different conditions. 78 mm tube.

Figures 7.12, 7.13 and 7.14 show comparisons between the calculated film flow rate and the results given in Chapter 5, measured by the technique described in Chapter 4.

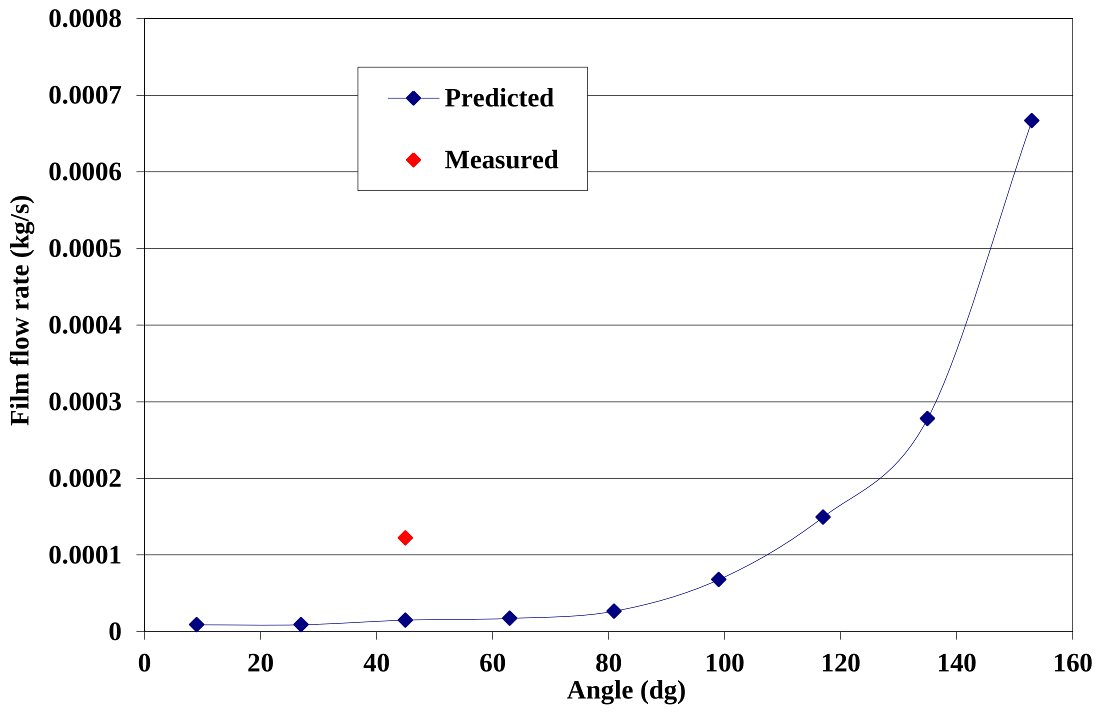

Figure 7.12. Comparison of measured and calculated film flow rates for experiments in the WASP facility (tube diameter 78 mm, U_{SG}=9.98 m.s^{-1}, U_{SL}=0.05 m.s^{-1}).

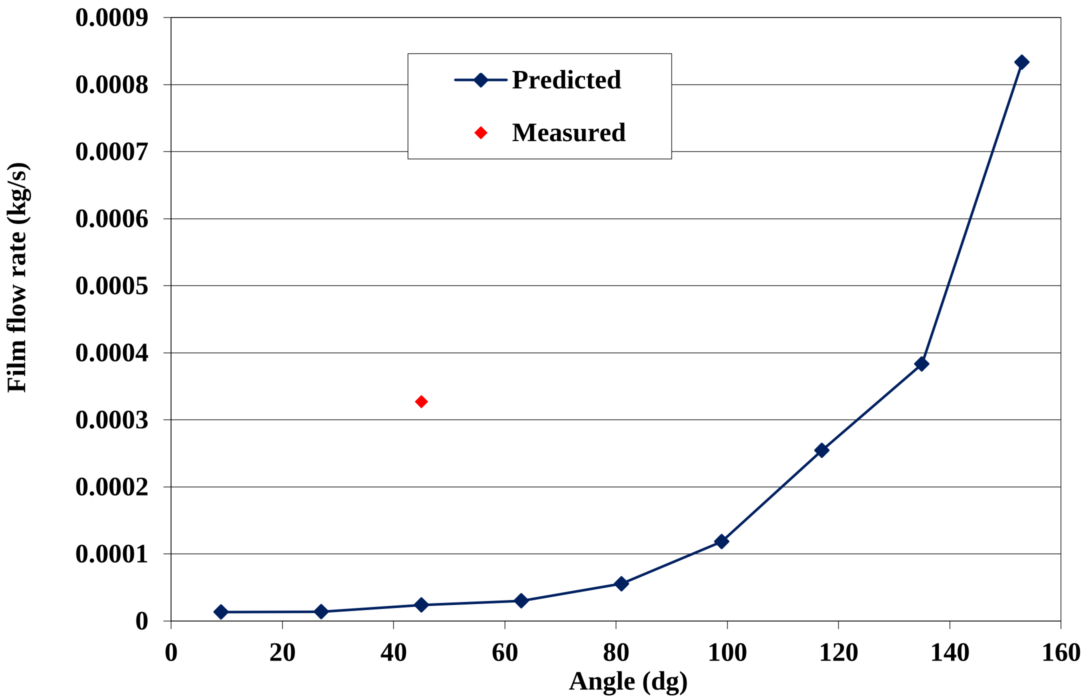

Figure 7.13. Comparison of measured and calculated film flow rates for experiments in the WASP facility (tube diameter 78 mm, U_{SG}=11.9 m.s^{-1}, U_{SL}=0.12m.s^{-1}).

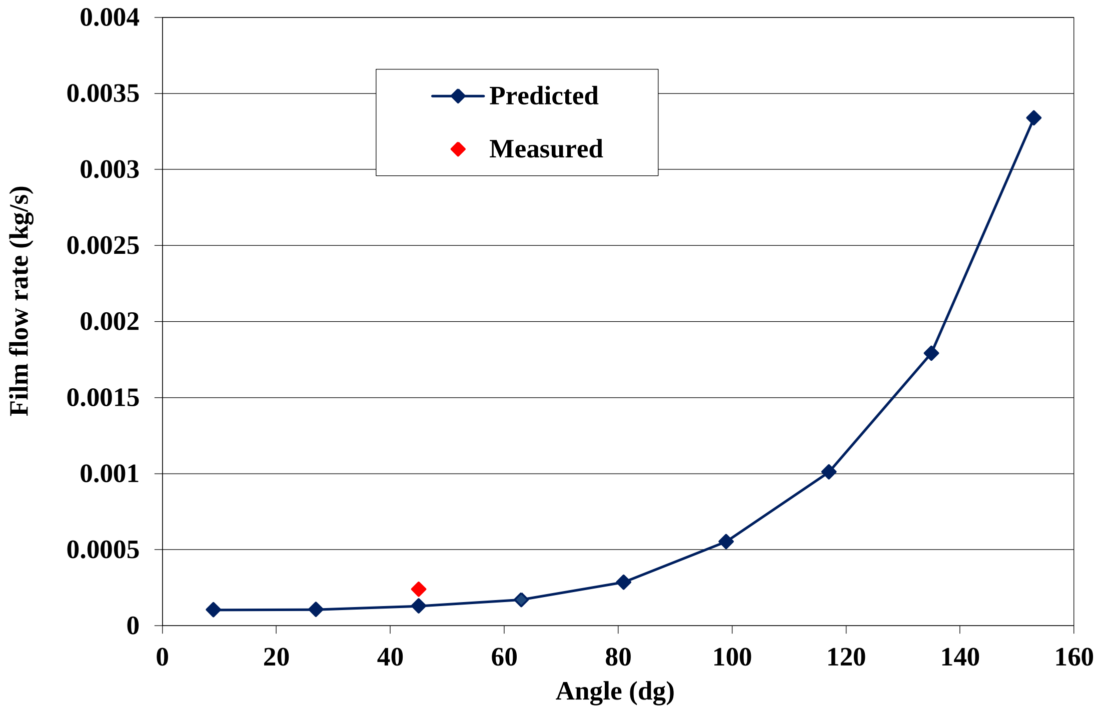

Figure 7.14. Comparison of measured and calculated film flow rates for experiments in the WASP facility (tube diameter 78 mm, U_{SG}=21 m.s^{-1}, U_{SL}=0.02 m.s^{-1}).

As will be seen from Figure 7.12 to 7.14, the measured film flow rate (kg/s.degree) is much higher than the predicted are for low gas superficial velocities (9.98 m/s and 11.92 m/s), see Figures 7.12 and 7.13 but agrees quite closely at high gas superficial velocities (21 m/s). The discrepancy at low gas velocity is much higher than would be expected from the assessment of errors given in Table 4.2. Much more data on film flow rate covering a wider range of conditions would be required to reach definitive conclusions from these results. A tentative conclusion might be drawn that the equation for entrainment rate (Equation 6.36) is predicting too high values at low gas velocity.

7.4.3. Film thickness distributions

It is also possible to determine the film thickness distribution via the butterwoth code entering the deposition rate distribution. The result is shown in Figure 7.15. Again we can draw the same conclusion, the curves at high gas velocities are similar and the curves at low superficial gas velocities are close to each other. According to the results, the films for high gas velocities are thicker than the films we would have at low gas velocities.

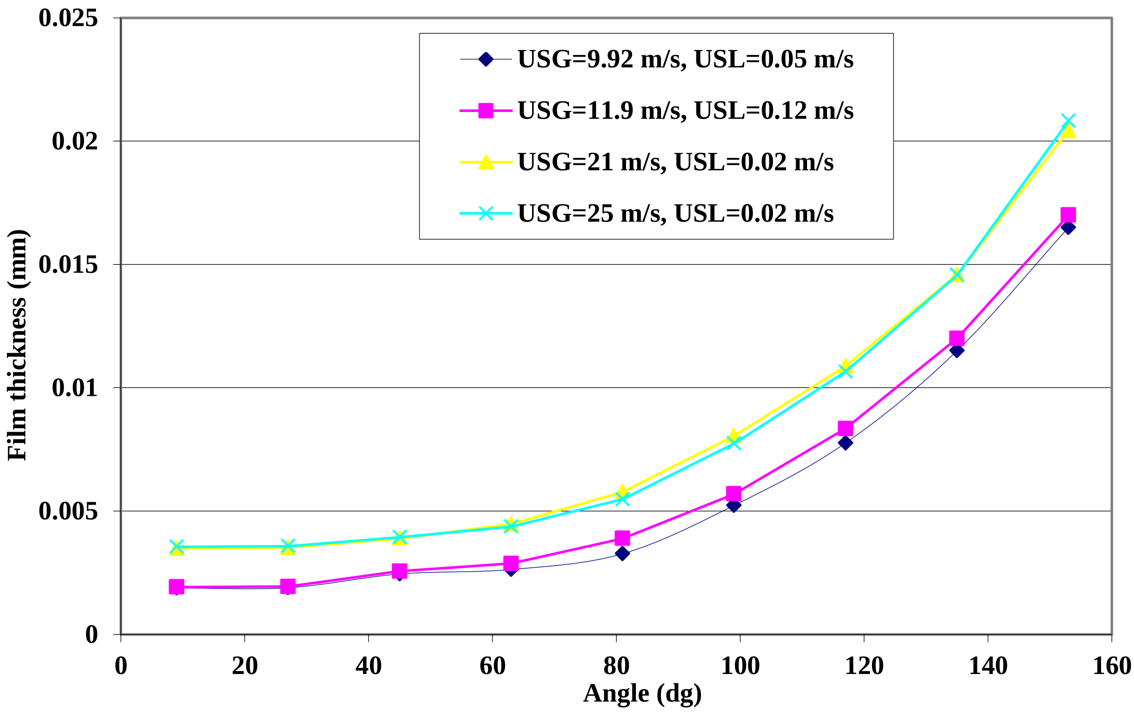

Figure 7.15. Film thickness distribution - Comparisons of 4 different conditions. 3 inch.

7.4.4. Droplet mass flux calculations

The droplet mass flux distribution at the vertical centreline is calculated from the CFX results and shown in Figures 7.16 and 7.17 for two standard conditions. As would be expected, the droplet mass flux decreases with distance from the bottom of the pipe and generally increases with increasing gas superficial velocity.

The calculated values for droplet mass flux are compared with those measured by Badie (2000) using a sampling probe and such comparisons are shown in Figures 7.16. and 7.17.

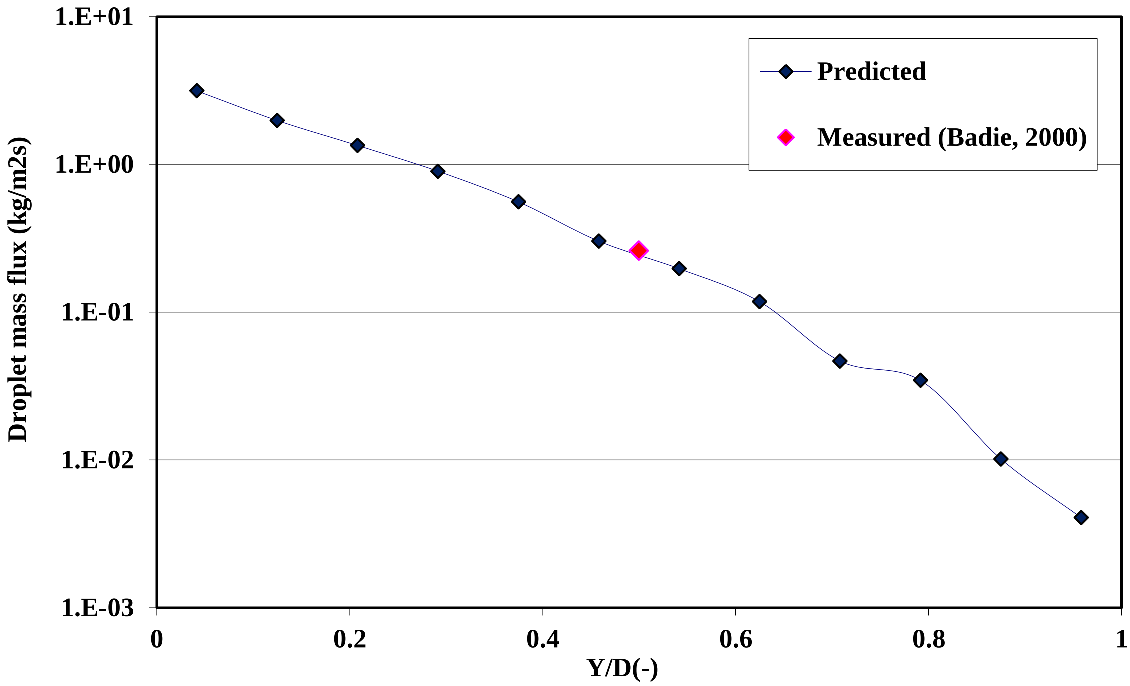

Figure 7.16. Droplet mass flux - U_{SG} =21m.s^{-1}, U_{SL} =0.02m.s^{-1} - Diameter pipe=3inches.

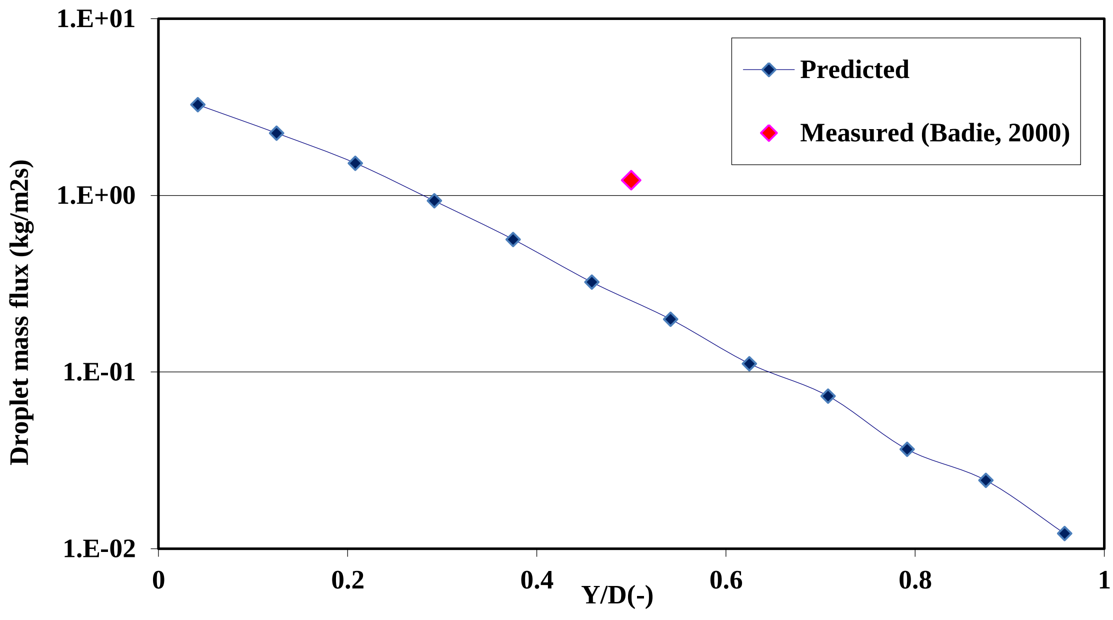

Figure 7.17. Droplet mass flux - U_{SG} =25 m.s^{-1}, U_{SL} =0.02 m.s^{-1} - Diameter pipe=3inches.

The results obtained in the present predictions are in reasonable agreement with the values obtained by Badie (2000). However the comparisons were made for high gas superficial velocity (21 and 25 m/s) and are thus consistent with the film flow rate data shown in Figure 7.14. It would seem probable that greater discrepancies would appear (with under predictions of the data) at lower velocities.

7.5. Conclusion

A model for droplet transport in stratifying annular flow has been implemented in CFX and gives qualitatively reasonable results.

The results have been compared with film flow rate data obtained in the present work and with gas core droplet mass flux data obtained by Badie (2000). The predictions are in reasonable agreement with the data at high gas superficial velocity. However, the model tends to underpredict film flow rates at lower gas velocity and thus may reflect some inadequacies in the expressions used (Pan and Hanratty, 2002, Equations 6.36) for entrainment rate from the liquid pool.

CHAPTER 8

Droplet transport in a tube: A numerical experiment to compare the RANS and LES turbulence models

The main focus of the work described in this thesis was on the application of RANS models (through the vehicle of the CFX code) to the prediction of stratifying annular flows. The main aim was to compare predictions with experimental data obtained on the WASP facility for a 78 mm diameter pipe. In the RANS model, the turbulence is represented statistically based on the local parameters of the flow. In reality, however, the turbulence field contains *structures* which may not be adequately represented by the RANS statistical approach and the interaction of the droplets with these structures may not be adequately represented by the RANS models. An increasingly used approach to account for such structures is that of *Large Eddy Simulation (LES)* in which the larger eddies in the main flow are captured specifically. The small eddies are represented by *sub-grid models* and the wall region is represented with *wall functions.* In this Chapter, a numerical experiment is descibed whose objective was to explore the differences in droplet deposition behaviour between RANS and LES models. The aim was to focus on the differences between the turbulence models so the influences of gravity and secondary flows were not included.

The work described in this Chapter formed part of an ongoing collaboration with ASCOMP GmbH of Zurich, Switzerland. ASCOMP have developped a powerful and versatile code (TransAT) for the simulation of turbulent multiphase flows and it was convenient to use this code for the numerical experiment described in this Chapter. The assistance of Dr. Chidambaram Narayanan in setting up this experiment is gratefully acknowledged. The calculations were performed on the Imperial College cluster.

In the numerical experiment, the following assumptions were made:

(1) The gas velocity was fixed at 21 m/s

(2) Gravity was ignored

(3) The initial condition was with particles of a range of sizes placed in the gas continuum. The particule size distributions matched that used for the droplet/gas case in the previous calculation (see Table 8.1 and Figure 8.2.)

In the main series of calculations (Chapter 7) a Reynolds Stress Model (RSM) was used to allow for the non-circular geometry. In the numerical experiment, gravitational separation was ignored and circular geometry was assumed. For the RANS part of the calculations, it was thus adequate to use ordinary RANS (a simple k-ε model).

Basically, in the numerical experiment, a “cloud” of droplets with a selected size range was set up in a 78 mm tube and the surrounding turbulence field is characterised by either RANS or by LES. The droplet cloud travels along the pipe and the droplets deposit on the tube wall. The rate of deposition calculated by RANS and LES respectively can be determined and compared.

In what follows, the modelling set-up is described in Section 8.1 and the results are presented in Section 8.2. Finally, Section 8.3 gives some concluding remarks.

8.1. Modelling Setup

The model is summarized below:

A 78 mm (3 inch) diameter pipe is studied with as an initial condition an axial air velocity equal to 21 $m.s^{-1}$ at the inlet of the pipe. To model the 37 meter long WASP facility, periodic boundary conditions were used.

The Immersed Surfaces Technique for meshing (IST) and a cartesian grid containing 300000 cells are used. The mesh is shown in Figure 8.1.

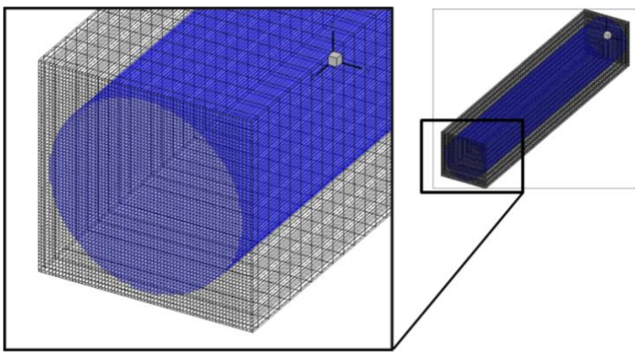

Figure 8.1. Schematic of the geometry and mesh.

Basically, two models were used in the numerical experiment:

(1) A k-ε type model (URANS, Unsteady Reynolds Averaged Navier Stokes) was used to give RANS-type predictions. A filtered equation was used for each droplet and 1-way coupling assumed.

(2) An LES (Large Eddy Simulation) model built into TransAT was employed. The LES model used the WALE (Wall-Adapting Local Eddy-Viscosity Model). The Subgrid-Scale Stress Model of Nicoud and Ducros, 1999) was used as the subgrid model.

8680 particles are injected in the flow field. One particle represents the statistics of a cloud of particles, with all the particles of the same size. The size of the particles is divided into 5 groups from 10 to 200 micrometers. The particle distribution is assumed to be log normal following the log normal distribution given by Al-Sarkhi & Hanratty, (2002) illustrated in Figure 8.2.

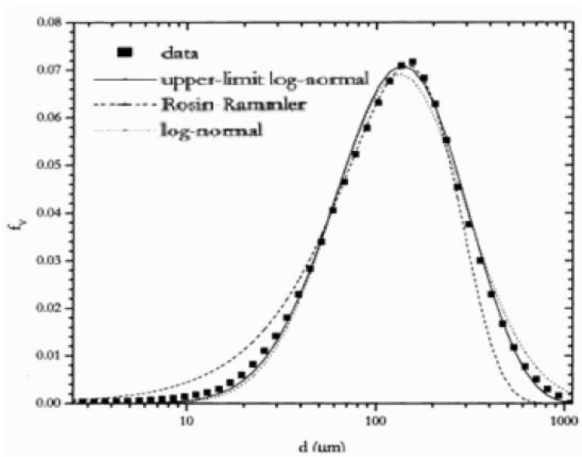

Figure 8.2. Log-normal distribution ofdrop sizes (Al-Sarkhi & Hanratty, 2002).

This log normal distribution is given by equation (8.1).

$$n(d_p) = \frac{1}{\sqrt{2\pi}} \frac{1}{a_0 d_p} \exp\left[-\left(\frac{\log d_p^+ - \log D_{nm}^+}{\sigma_0} \right)^2 \right] \tag{8.1}$$

The sizes of the particles are shown in Table 8.1.

Range	Droplet diameter (micrometer)
1	10-48
2	49-85
3	86-123
4	124-161
5	162-200

Table 8.1. Droplet sizes ranges.

A third order Quick for space and a third order Runge Kutta for time are set.
The convergence criteria of the model are the residue criterion explicit which is equal to 1.0E-3 and the number of iterations to run which is 20000.

In LES, the smallest length scale corresponds to the local grid size which is typically 0.142mm for the conditions investigated. This compares with the investigated particle size range of 0.01 to 0.2 mm. Thus, the particles are generally smaller than the LES grid. However, additional turbulence (with length scales smaller than the LES grid) is introduced via the sub-grid model. No attempt has been made to calculate the interaction of the drops with this sub-grid scale turbulence but it is expected that this interaction would be small.

The steps in the modelling involve:
Firstly, the flow field is set up in a zone of the pipe using periodic boundary conditions. Secondly droplets of a range of sizes are injected into random positions in the flow field. Thirdly, the motion of drops in flow field using periodic boundary conditions is then studied and, finally, the number of droplets remaining as a function of distance and drop size is determined.

8.2. Results

The results files were calculated by running the TransAT code with the solver for the required amount of time.

Videos are made from the post processing of the results files for the continuous and the dispersed phases for both RANS and LES. Snapshots of the videos are shown below. The actual videos are given in the CD attached to this thesis.

The turbulent flow field of the continuous phase with the RANS turbulent model is recorded on Video 1. Figure 8.3 shows a snapshot of this Video. The RANS model is seen to produce a symmetric flow field.

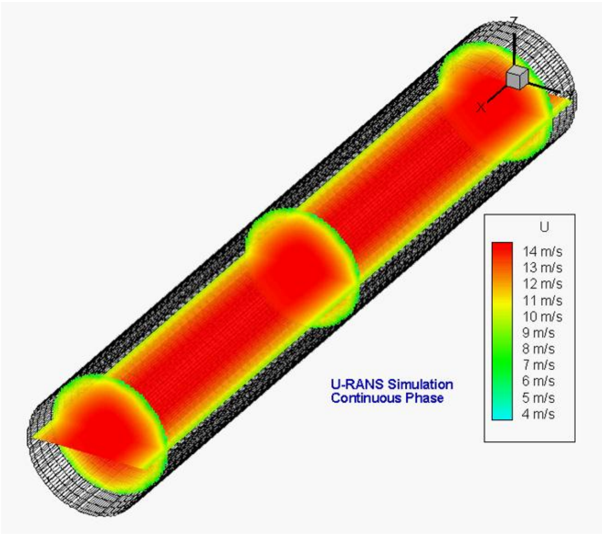

Figure 8.3. URANS Continuous Phase (from Video 1).

The turbulent flow field of the continuous phase with the LES turbulent model is recorded on Video 2. Figure 8.4. shows a snapshot of this Video. The LES model is seen to produce temporal and spatial evolutions of this highly unsteady flow.

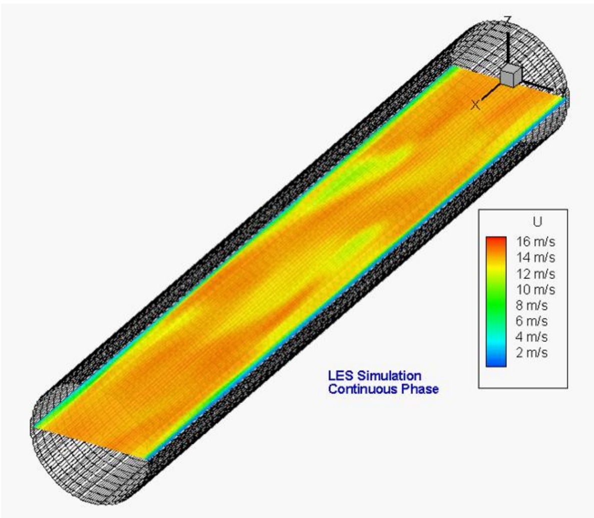

Figure 8.4. LES Continuous Phase (from Video 2).

The colour coding for the various drop sizes is shown in Table 8.2:

Colour	Drop diameter (microns)
1 Red	200
2 Green	100
3 Turquoise	50
4 Dark Blue	20
5 Light Blue	10

Table 8.2. Colour coding.

The droplet motion in the flow field is visualized for both the RANS and the LES turbulent models respectively on Video 3 and Video 4. Figure 8.5 and Figure 8.6 show snapshots of these Videos.

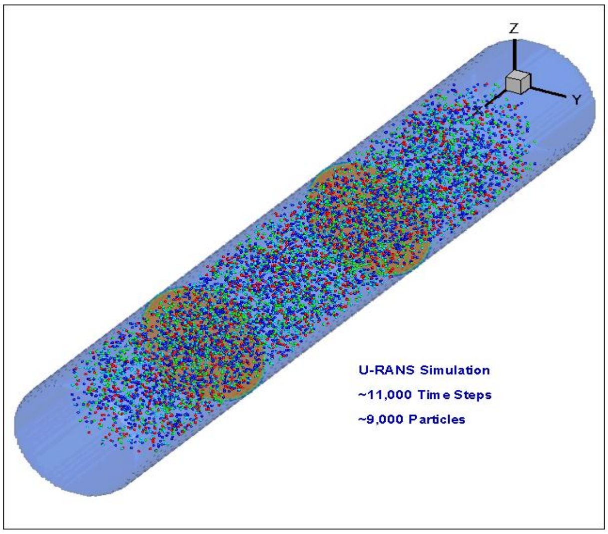

Figure 8.5. URANS Dispersed Phases (from Video 3).

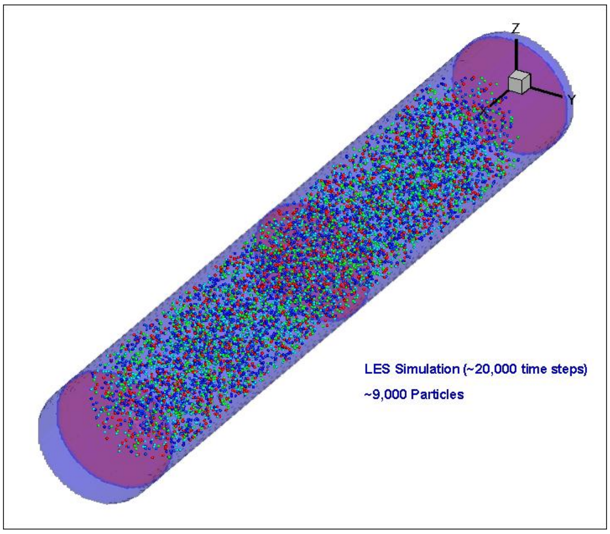

Figure 8.6. LES Dispersed Phase (from Video 4).

It is interesting to visualize the flow from the inside of the pipe. Axial views of the dispersed phase for all ranges of droplets sizes considered in the scope of this study, for both RANS and LES turbulent flow models, are presented respectively in Figure 8.7.and 8.8 and can be viewed on Videos 5 and 6.

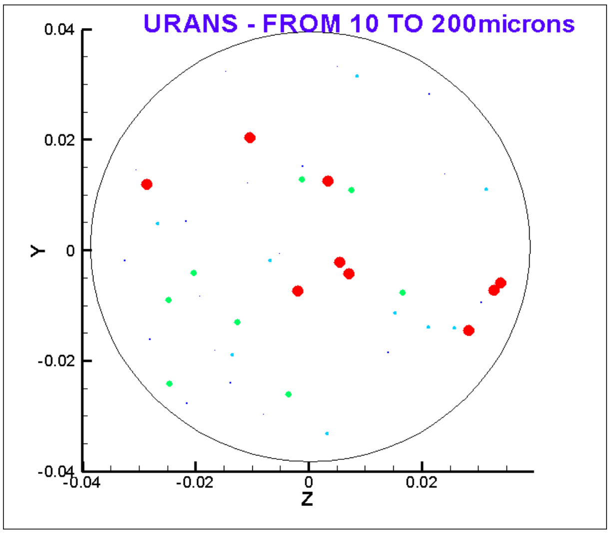

Figure 8.7. Axial view of Droplet motion in the flow field (RANS model) (from Video 5).

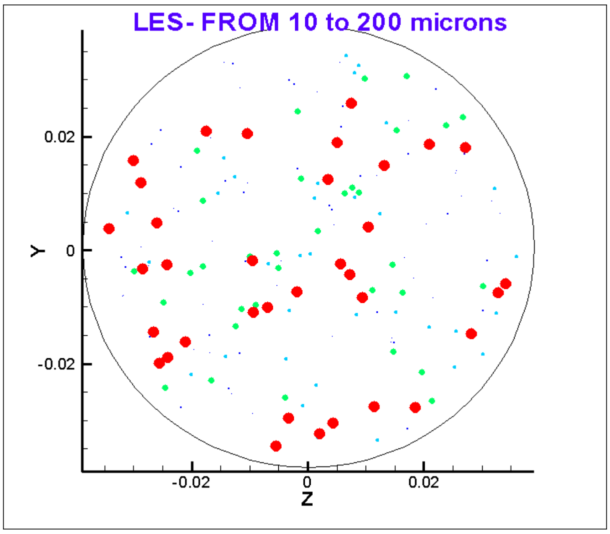

Figure 8.8. Axial view of Droplet motion in the flow field (LES model) (from Video 6).

The number of droplets remaining in the gas core is shown as a function of two parameters (axial distance travelled in the pipe and the size of the droplets) for both the RANS and the LES models in Figures 8.9 and 8.10.

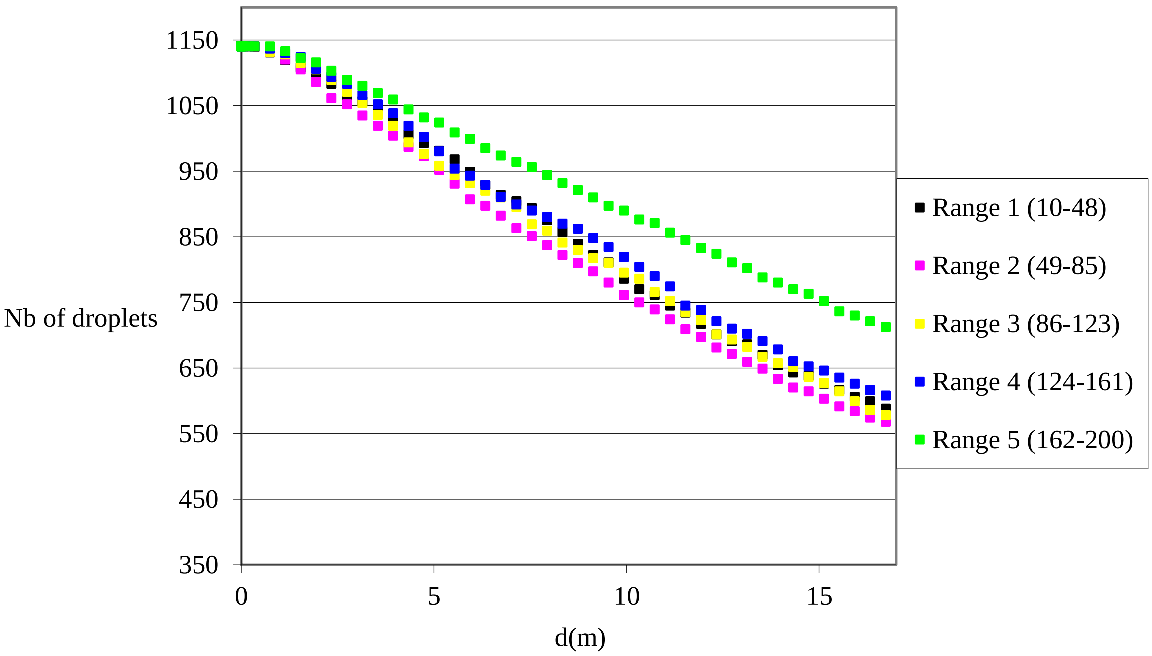

Figure 8.9. Variation of number of droplets remaining as function of drop size range and distance along the tube (d) for the RANS model.

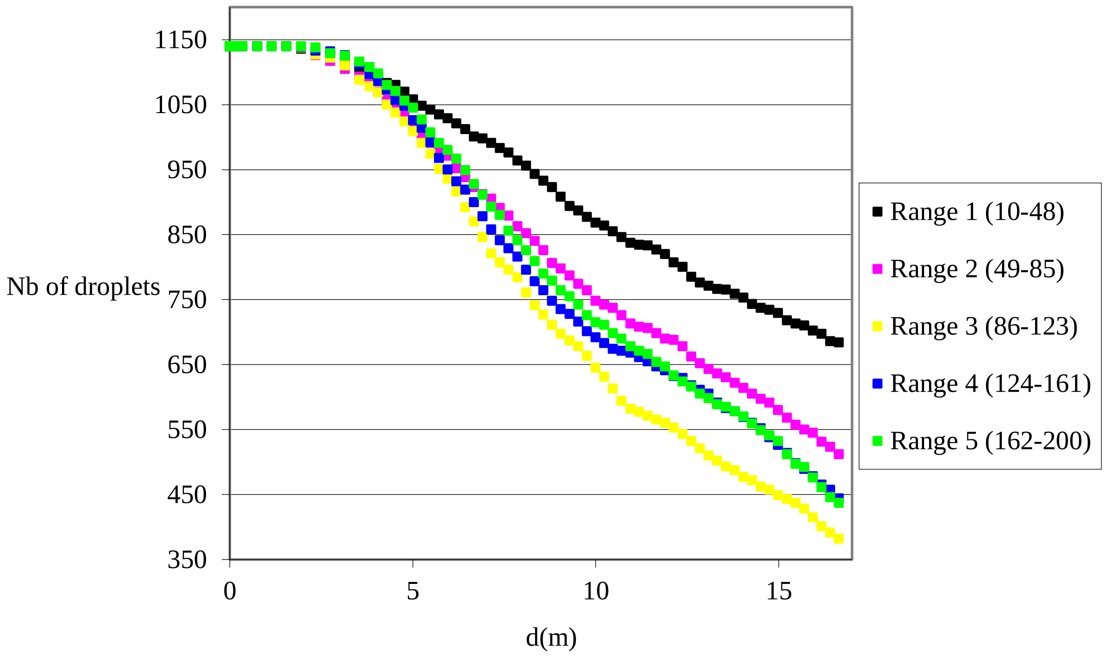

Figure 8.10. Variation of number of droplets remaining as function of drop size range and distance along the tube (d) for the LES model.

The results obtained show important discrepancies between the two turbulence models. The droplet size has a more important effect on the LES simulation than on the RANS simulation. The larger droplets deposit quicker than the smaller with LES. For the smallest droplets, they deposit quicker with RANS.

The number of droplets remaining in the gas core is shown as a function of the axial distance travelled in the pipe for both the RANS and the LES models and for several droplet sizes in Figures 8.11 and 8.12.

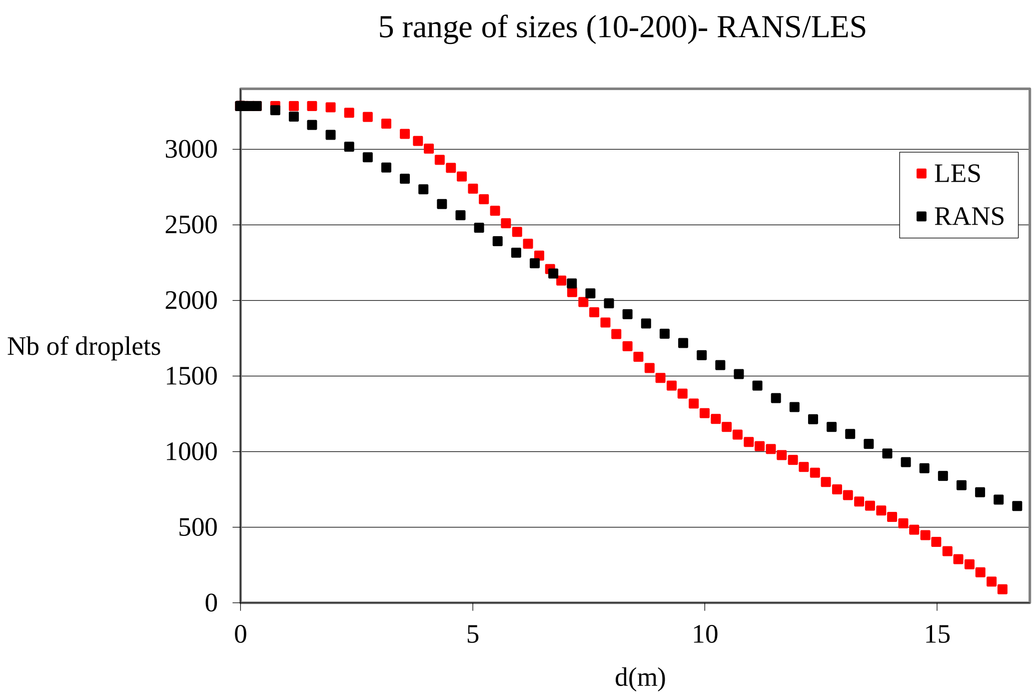

Figure 8.11. Comparison RANS model with LES model.

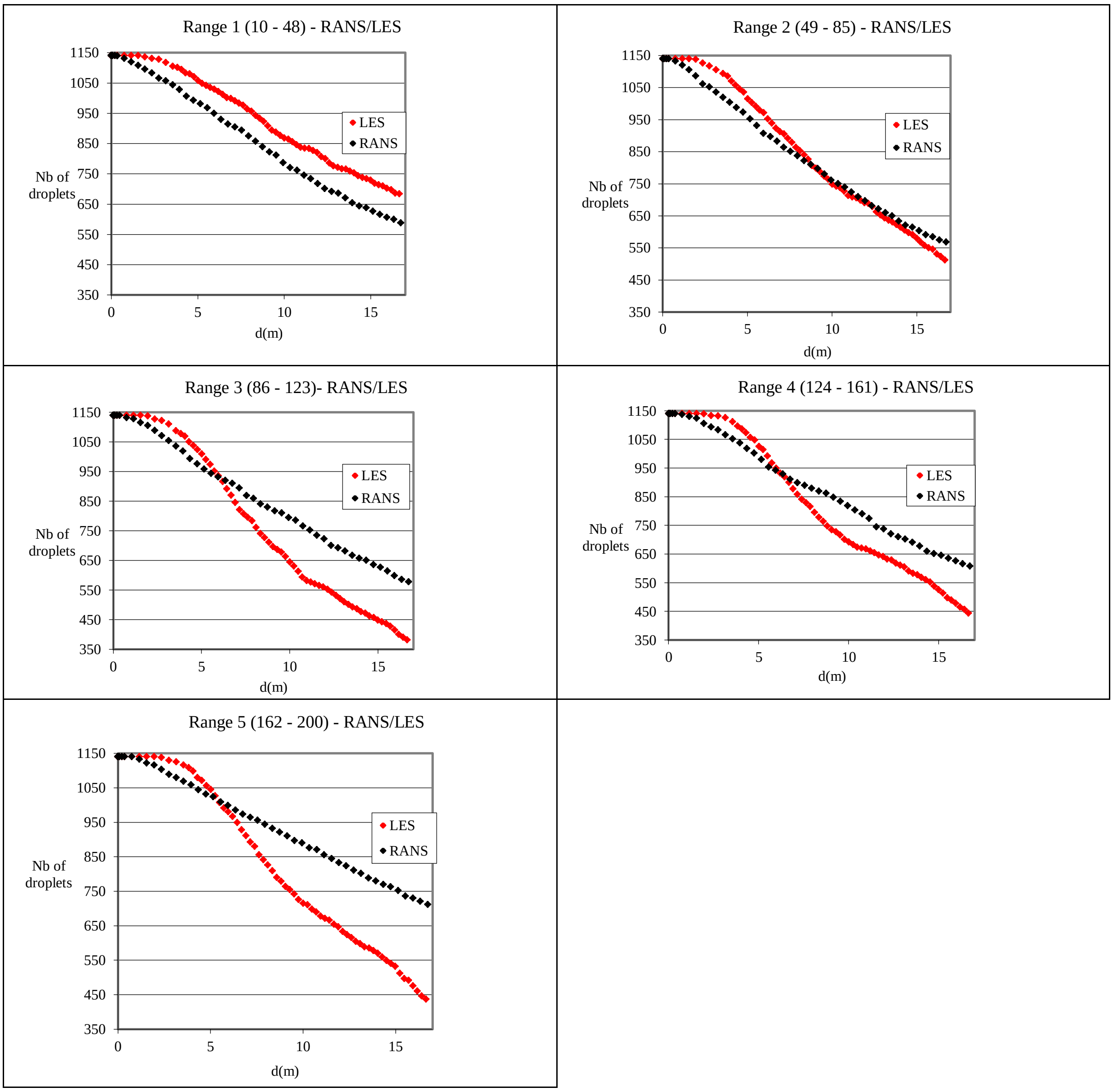

Figure 8.12. Comparison RANS model with LES model for several ranges of sizes.

According to these graphs, in most of the case, the LES model predicts a slower deposition than the RANS model in the first part of the simulation and a quicker deposition of droplets around the periphery of the pipe than the RANS model in the second part of the simulation. For the smallest range (range 1) of droplets, RANS always predicts a quicker deposition than for the LES model. Range 2 shows the LES above at the beginning and then below the RANS curve but the curves being close to each other. Range 4 and 5 shows a net difference between both plots, the LES droplets depositing quicker. The difference between LES and RANS in the total range of size is due to the fact that the biggest droplets deposit quicker with LES. In the RANS model, unsteady turbulence is artificially created but the model has a much lower range of eddy length scales that does the LES model. This means that the larger particles respond to these larger length scales and this causes them to deposit.

8.3. Conclusion

Models for droplet transport in a tube have been set up in the TRANSAT code using RANS and LES models respectively for the turbulence. The carrier fluid flow was assumed symmetrical (no secondary flows) and gravity was set to zero (no gravitational - “ballistic” - effects).

With the LES model, the larger droplets were found to deposit much more rapidly than with the RANS model.

In droplet tracking, it can be concluded that the model chosen for the continuous phase turbulence is of considerable significance. It could be argued that the LES model would be closer to the physical reality, but much wider investigations of this matter are needed.

Calculation of much more complex situations (e.g. that of horizontal annular flow) using both the RANS and LES approaches would appear to be a useful aim for future work.

CHAPTER 9

Conclusions and recommendations

In this chapter, the main conclusions from the work are summarized in Section 9.1 and recommendations for further work are given in Section 9.2.

9.1. Conclusions

The main conclusions from the work described in this thesis are as follows:

1. An examination of published information on annular and stratifying annular flow in horizontal tubes (see Chapter 2) leads to the conclusion that such flows are maintained mainly by wave action in smaller diameter tubes but that, for medium and large tube diameters, the processes of droplet entrainment and deposition are essential in maintaining a liquid film in the upper part of the tube. The study of these processes has been the main focus of the present work.
2. Studies of the droplet entrainment and transport using the axial view photography technique (see Chapter 5) indicate that droplet entrainment from the lower pool in stratifying annular flow occurs by the "bag breakup" and "ligament breakup" processes. In many cases, both mechanisms of breakup occur simultaneously. The axial view pictures also show that (in the 78 mm pipe studied), the droplets could be emitted with a significant velocity in the cross sectional plane. Sometimes, this velocity was sufficient to carry the emitted droplet to the top of the tube.
3. It was possible to analyze the pictures obtained using the axial viewing technique to produce drop size distribution data. The results obtained were consistent with classical drop size distribution spectra.
4. A new apparatus was successfully commissioned on the 78 mm WASP facility for the measurement of local film flow rate in stratifying annular flow. A limited set of data were obtained using this apparatus.
5. A model for droplet transport and deposition was set up using the commercial CFD code Ansys-CFX. The motion of the droplets in the gas core was tracked from the time of their emission from the lower "pool" of liquid to the time of their deposition. Lagrangian tracking of the droplets was carried within the gas core turbulent field. This turbulent field was calculated using a Reynolds Stress (RANS) Model with the droplets being exposed to

random fluctuations in velocity within the field consistent with the RANS model. A periodic boundary condition was used in order to follow the motion of droplets along the tube from the time of their emission to the time of their deposition. Repeating the calculations (up to thousands of times) with a range of particle sizes and emission angles, it was possible to estimate the rate of deposition as a function of circumferential position.

6. Liquid deposited on the tube surface forms a liquid film which drains downwards under the influence of gravity whilst, at the same time, being transported axially by the influence of shear from the moving gas core. This situation is analogous to that of turbulent film condensation in a horizontal tube and a model for such condensation by Butterworth (1973) has been applied here to the prediction of film flow rate distribution in stratifying annular flow.
7. Droplet trajectories were calculated for both a tube of the diameter used in the experiments (78 mm) and for a tube of a size typical of some industrial applications (965 mm, 38 inches). A wide range of droplet sizes was covered in these calculations. It was found that, for the smaller tube, the initial velocity of the larger droplets was often sufficient to carry them directly to the upper surfaces of the tube where they deposited. The rate of deposition of liquid was dominated in this case by the deposition of these larger droplets. These larger droplets are displaying, therefore, the “ballistic” behaviour described in the paper by Brown et al (2009). For the larger tube, the behaviour is quite different. The larger droplets fall back under gravity to the pool and cannot reach the upper part of the tube. On the other hand, the smaller droplets are strongly influenced by the gas phase turbulence and are able to undergo turbulent diffusion which may carry them to the upper surface of the tube. Thus, for the larger tube the deposition of liquid at the upper part of the tube is dominated by these “diffusional” droplets. This diffusion process also occurs in the smaller diameter pipe but its contribution to deposition at the upper part of the tube is small compared to the direct transfer (“ballistic”) mechanism.
8. The droplet mass fluxes and film flow rates predicted by the model are lower than the values observed in the experiments. It seems likely that this under-prediction is at least partly due to uncertainties in the correlation used for entrainment rate (Equation 6.36).
9. A numerical experiment (Chapter 8) indicates that there may be significant differences in calculated droplet motion between the RANS model and a model (LES) which takes account of the local turbulent structures.

9.2. Recommendations for further work

The problem studied in the work described here is an important one, affecting the viability of industrial pipeline systems. Though progress has been made on a number of aspects in the present work, there seems to be a good case continuing the work to address the still-outstanding issues. The following recommendations are therefore made:

1. That the air-water experiments on the WASP facility be extended to cover a wider range of flow rates and pressures. In particular, a wider range of film flow rate measurements is suggested and it would also be of interest to include measurements of film thickness.
2. That experiments be carried out with non-aqueous liquids. Thus, the experiments could be carried out with mixtures of air and the lubricating oil (Shell Tellus) already available on the WASP facility. In many practical applications, there are two liquid phases (water and oil) and experiments on stratifying annular flow could be carried out for three-phase (air/water/oil) flow in the WASP facility. Some preliminary results have been obtained for droplet mass flux (see Figure 4.28) and the experiments could be extended to include film flow rate measurements and axial view photography. Of course, modelling such three-phase systems would be an even greater challenge!
3. That work be pursued in the application of the side view visualization described in Sections 4.2.2 and 5.2. i.e. with the use of matched refractive index and UV illumination. This system might usefully be adopted in the WASP facility and combined with axial view photography.
4. That the CFD-RANS methodology be further explored in the prediction of stratifying annular flow over a wider range of cases. Obviously, the relationship for entrainment rate needs to be improved. Another area for improvement might be the representation within the model of liquid-gas interfacial roughness. Alternative RANS turbulence models might also be explored.
5. The numerical experiment reported in Chapter 8 gives some indication that the use of RANS and LES turbulence models to represent droplet motion in a turbulent field can give somewhat different results in some ranges. This probably reflects the fact that the droplet motion is, in some cases, sensitive to the actual structure of the turbulent eddies and it could be argued that LES could give a better representation of this. However, the re-casting of the full model into an LES framework would not be a straightforward task. This topic could be a useful one to follow in future work.

BIBLIOGRAPHY

Adechy, D. & Issa, R.I. (2004). Modelling of annular flow through pipes and T-junctions. Int. J. Multiphase Flow, Vol 33, pp 289-313.

Altunbas, A, Hills, J.H. & Azzopardi, B.J. (1999). Liquid phase controlled mass transfer in gas-liquid annular horizontal flow. Two-phase Flow Modelling and Experimentation, 533-538.

Al-Sarkhi, A. & Hanratty, T. J. (2002). Effect of pipe diameter on the drop size in a horizontal annular gas-liquid flow, Int. J. Multiphase Flow, Vol.28, pp 1617-1629.

Al-Sarkhi, A. & Hanratty, T. J. (2001). Effect of pipe diameter on the performance of drag-reducing polymers in annular gas-liquid flows. Trans IChemE, part A, Vol.79, pp 402-408.

Al-Sarkhi, A. & Hanratty, T. J. (2001). Effect of drag-reducing polymers on annular gas-liquid flow in a horizontal pipe. Int. J. Multiphase Flow, Vol 27, pp 1151-1162.

Anderson, R.J. & Russell, TWF. (1970). Film formation in two-phase annular flow. AIChE J. Vol 16, pp 626-633.

Arnold, C.R. & Hewitt, G.F. (1967). Further development of the photography of two-phase gas-liquid flow. J. Photographic Sci. Vol 15, p 97

Azzopardi, B.J. (1983). Mechanisms of entrainment in annular two phase flow. AERE R 11068, UKAEA, Harwell, UK.

Azzopardi, B.J. (1987). Observation of drop motion in horizontal annular flow. Chem. Eng. Sci., Vol.42(8), pp 2059-2062.

Azzopardi, B.J. (1988). The role of drops in annular gas-liquid flow: Drop sizes and velocities. Jap. J. Multiphase Flow, Vol. 2, pp 15-35.

Azzopardi, B.J., Zaidi, S.H. & Jepson, D.M. (1997). Entrained fraction in inclined annular gas/liquid flow. Proceedings of the ASME Fluids Engineering Division, Vol. 244, pp 69-76.

Azzopardi, B.J. (1997). Drops in annular two-phase flow, *Int. J. Multiph. Flow* **23** (Suppl.): 1-53.

Azzopardi, B.J. (1999). Turbulence modification in annular gas/liquid flow. Int. J. Multiphase Flow, Vol. 25, pp 945-955.

Badie, S. (2000). Horizontal stratifying/annular gas-liquid flow. PhD Thesis, University of London, London, UK.

Badie S., Lawrence, C. J, and Hewitt, G. F., Axial viewing studies of horizontal gas-liquid flows with low liquid loading, *Int. J. Multiphase Flow*, vol. 27, pp. 1259–1269, 2001.

Baik, S. & Hanratty, T. J. (2003). Concentration profiles of droplets and prediction of the transition from stratified to annular flow in horizontal pipes. Int. J. Multiphase Flo, Vol. 29, pp 329-338.

Baker, O (1954). Simultaneous flow of oil and gas. Oil Gas J. Vol. 53, p185.

Beggs, H. D. & Brill J. P. (1973) A study of two phase flow in inclined pipes. *Trans. J. Petroleum Technology*, **255**, p. 607.

Bennett, A. W., Hewitt, G. F., Kearsey, H. A., and Keeys, R. K. F. (1967) Studies of burnout in boiling heat transfer. Trans. Instn. Chem. Engrs., Vol. 45, ppT319 – T333.

Binder, J. L. & Hanratty, T. J. (1991). A diffusion model for droplet deposition in gas/liquid annular flow. Int. J. Multiphase Flow, Vol. 17, pp 1-11.

Binder, J. L. & Hanratty, T. J. (1992). Use of Lagrangian methods to describe drop deposition and distribution in horizontal gas--liquid annular flows. Int. J. Multiphase Flow, Vol. 18: pp 803-820.

Brown L., Hewitt G.F., Hu Bin, Thompson C.P. & Verdin P. (2009). Predictions of droplet distribution in low liquid loading, stratified flow in a large diameter pipeline. 14th International Conference on Multiphase Production Technology, BHR Group, Cannes, France: 17th–19th June 2009.

Butterworth, D. (1968). Paper presented at the National Symposium on Research of Co-Current Gas Liquid Flow, University of Waterloo, Ontario, 1968.

Butterworth, D. (1969). Note on fully-developed, horizontal, annular two-phase flow. Chem. Eng. Sci., Vol.24(12), pp 1832-1834.

Butterworth, D. (1974). An analysis of film flow and its application to condensation in a horizontal tube. Int. J. Multiphase Flow, Vol.1, pp 671-682.

Butterworth, D. (1973). An analysis of film flow for horizontal annular flow and condensation in a horizontal tube. AERE R 7575, UKAEA, Harwell, UK.

Butterworth, D. & Pulling, D.J. (1973). Film flow and film thickness measurements in horizontal annular air-water flow. UKAEA Report AERE-R7576.

Butterworth, D. & Pulling, D.J. (1972). A visual study of mechanism in horizontal, annular, air-water flow. AERE M2556, October 1972, UKAEA, Harwell, UK.

Butterworth, D. & Pulling, D.J. (1974). Further visual studies of horizontal, annular, air-water flow. AERE R 7574, UKAEA, Harwell, UK.

Charron, Y. & Whalley, P.B. (1995). Gas-liquid annular flow at a vertical Tee junction – part I. flow separation. Int. J. Multiphase Flow, Vol.21(4), pp 569-589.

Chen, X. T., Cai, X. D. & Brill, J. P. (1997) Gas-liquid stratified-wavy flow in horizontal pipelines. *J. Energy Resources Technology*, **119**, p. 209.

Chisholm, D. (1973). Pressure gradients due to friction during the flow of evaporating two-phase mixtures in smooth tubes and channel. Int. J. Heat Mass Transfer, Vol. 16, pp 347-348.

Coney, M. W. E. and Fisher, S. A., Instrumentation for two-phase flow in use or under devel- opment at the Central Electricity Research Laboratories, European Two-Phase Flow Group Meeting, Erlangen, 1976.

Cousins, L. B. & Hewitt, G. F. (1968) Liquid phase mass transfer in annular two- phase flow radial liquid mixing. UK AEA Report, AERE - R5693.

Dallman, J. C., Laurinat, J. E. & Hanratty, T. J. (1984). Entrainment for horizontal annular gas-liquid flow. Int. J. Multiphase Flow, Vol.6:, pp 677-689.

Darling, R.S. & McManus, H.N. (1969). Flow patterns in circular ducts with circumferential variation of roughness: a two-phase analogue. Developments in Mechanics, Vol (5). Ohio State University Press.

De Sampaio P.A.B., Faccini J. L.H., Su J., Modelling of stratified gas–liquid two-phase flow in horizontal circular pipes, International Journal of Heat and Mass Transfer 51 (2008) 2752–2761.

Dorao C.A., Fernandino M., Patruno L.E., Dupuy P.M., Jakobsen H.A., Svendsen H.F. Macroscopic description of droplet–film interaction for gas–liquid systems Applied Mathematical Modelling 33 (2009) 3309–3318.

Eck, B. (1973). Technische Stromunglehre, Springer, New York.

Fernandes, P.L.J., Jutte, B.M. & Rodriguez, M.G. (2004). Drag reduction in horizontal annular two-phase flow. Int. J. Multiphase Flow, Vol. 30, pp 1051-1069.

Fisher, S.A. & Pearce, D.L. (1978). A theoretical model for describing horizontal annular flows. Presented at Int. Semin. On Momentum, Heat and Mass Transfer in Two-phase Energy and Chemical Systems, Dubrovnik, Yugoslavia.

Fisher, S. A., Harisson, G. S. and Pearce, D. L. (1978) Instrumentation for localised measurements with fast response in liquid/vapour flows. *Symposium on Measurements on Polyphase Flows, ASME Winter Annual Meeting*, San Francisco, California, USA.

Fisher, S. A. and Yu, S. K. W., Dryout in serpentine evaporators, *Int. J. Multiphase Flow*, vol. 1, no. 6, pp. 771–791, 1975.

Flores, A.G. & Crowe, K.E., Griffith, P. (1995). Gas-phase secondary flow in horizontal, stratified and annular two-phase flow. Int. J. Multiphase Flow, Vol. 21(2), pp 207-221.

Friedel, L. (1979). Improved friction pressure drop correlations for horizontal and vertical two-phase pipe flow. European Two-Phase Flow Group Meeting, Ispra, Italy, paper E2.

Fukano, T., Ousaka, A., Morimoto, T. & Sekoguchi, K. (1983). Air-water annular two-phase flow in a horizontal tube. Bulletin of the JSME, Vol. 26(218), pp 1387-1396.

Fukano, T., Itoh, A. & Ousaka, A. (1985). Breakdown of a liquid film flowing concurrently with gas in horizontal line. PhysicoChemical Hydrodynamics, Vol.6(1/2), pp23-47.

Fukano, T. & Ousaka, A. (1989). Prediction of the circumferential distribution of film thickness in horizontal and near-horizontal gas-liquid annular flows. Int. J. Multiphase Flow, Vol. 15(3), pp 403-419.

Fukano, T., Nakagawa, H., Mori, Y. & Watanabe, M. (1997). Liquid film formation on the inner surface of the horizontal channel. Nuclear Engineering and Design, Vol.175, pp 3-13.

Fukano, T. & Inatomi, T. (2003). Analysis of liquid film formation in a horizontal annular flow by DNS. Int. J. Multiphase Flow, Vol. 29, pp 1413-1430.

Galbiati, L. & Andreini, P. (1992). The transition between stratified and annular regimes for horizontal two-phase flow in small diameter tubes. Int. Comm. Heat Mass Transfer, Vol. 19, pp185-190.

Govan, A. H., Hewitt, G. F., and Ngan, C. F., Particle motion in a turbulent pipe flow, *Int. J. Multiphase Flow*, vol. 15, no. 3, pp. 471–481, 1989.

Hamersma, P. J. & Hart, J. (1987) A pressure drop correlation for gas/liquid flow with a small liquid holdup. Chem. Eng. Sci., Vol. 42, pp 1187-1196

Harms, T.M., Li, D., Groll, E.A. & Braun, J.E. (2003). A void fraction model for annular flow in horizontal tubes. Int. J. Heat and Mass Transfer, Vol. 46, pp 4051-4057.

Hart, J., Hamersma, P.J. & Fortuin, M.H. (1989). Correlations predicting frictional pressure drop and liquid holdup during horizontal gas-liquid pipe flow with a small liquid holdup. Int. J. Multiphase Flow, Vol.15(6), pp 947-964.

Hart, J., Hamersma, P.J. & Fortuin, J.M.H. (1991). A model for predicting liquid route preference during gas-liquid flow through horizontal branched pipelines. Chem. Eng. Sci., Vol. 46(7), pp 1602-1622.

Hewitt, G.F., King, R.D. & Lovegrove, P.C. (1962). Techniques for liquid film and pressure drop studies in annular two-phase flow. UKAEA Report AERE-R3921.

Hewitt, G.F. & Lacey, P.M.C. (1965). The breakdown of the liquid film in annular two-phase flow. Int. J. Heat Mass Transfer. Vol. 8, pp 781-791.

Hewitt, G.F. & Roberts, D.N. (1969). Investigation of interfacial phenomena in annular two-phase flow by means of axial view technique. UKAEA Report AERE-R6070.

Hewitt, G.F. & Govan, A.H. (1990). Phenomena and prediction in annular two-phase flow. Advances in Gas-Liquid Flows, ASME, FTD, Vol. 99: HTD-155.

Hewitt, G. F., Jayanti, S. & Hope, C. B. (1989) Structure of the thin liquid films in gas-liquid horizontal flow. UKAEA Report AERE-R13643

Hewitt, G.F., Jayanti, S. & Hope, C.B. (1990). Structure of thin liquid films in gas-liquid horizontal flow. Int. J. Multiphase Flow, Vol. 16(6), pp 951-957.

Hewitt, G. F. and Jayanti, S., Prediction of film inversion in 2-phase flow in coiled tubes, *J. Fluid Mech.*, vol. 236, pp. 497–511, 1992.

Hewitt, G.F. & Whalley, P.B., (1980). Advanced optical instrumentation method. Int. J. Multiphase Flow, Vol. 6, pp 139-156.

Hewitt, G.F. (2000). Frictional pressure gradient in adiabatic flows of gas-liquid mixtures in horizontal pipes: Prediction using empirical correlations and database. Engineering Sciences Data Unit (ESDU), Data Item 01014 (ISBN 1 862 46 171 6).

Hu, B.. Stewart, C., Hale, C.P., Lawrence, C.J., Hall, A.R.W., Zwiens, H. and Hewitt, G.F. (2005). Development of a X-ray computed tomography (CT) system with sparse sources: Application to three-phase pipe flow visualisation. Experiments in Fluids, Vol. 39, pp 667-678.

Hubbard M.G. & Dukler A.E. (1968), Paper presented at AIChE National Meeting, Tampa, Florida, USA, 1968.

Hurlburt, E.T. & Newell, T.A. (2000). Prediction of the circumferential film thickness distribution in horizontal annular gas-liquid flow. Transaction of the ASME, Journal of Fluids Engineering, Vol. 122, pp 396-402.

Hurlburt, E.T. & Hanratty, T.J. (2002). Measurement of drop size in horizontal annular flow with the immersion method. Experiments in Fluids Vol. 32, pp 692-699.

Jacowitz, L.A. & Brodkey, R.S. (1964). An analysis of geometry and pressure drop for the horizontal, annular, two-phase flow of water and air in the entrance region of a pipe. Chem. Eng. Sci., Vol. 19, pp 261-274.

Jamari, S. (2006). Experimental study of stratified/slug-annular flow regime transition in two-phase (air-liquid) flow in a horizontal pipe. PhD Thesis, University of London, London, UK.

James, P.W. & Hutchinson, P. (1979). Droplet deposition in an annular geometry. Int. J. Multiphase Flow, Vol. 5(2), pp 103-112.

James, P.W., Wilkes, N.S., Conkie, W. & Burns, A. (1987). Developments in the modelling of horizontal annular two-phase flow. Int. J. Multiphase Flow, Vol. 13(2), pp 173-198.

Jayanti, S., Wilkes, N.S., Clarke, D.S. & Hewitt, G.F. (1989). The prediction of turbulent flows over roughened surfaces and its application to interpretation of mechanisms of horizontal annular flow. AERE R 13697, UKAEA, Harwell, UK.

Jayanti, S., Hewitt, G.F. & White, S.P. (1990a). Time-dependent behaviour of the liquid film in horizontal annular flow. Int. J. Multiphase Flow, Vol. 16 (6), pp 1097-1116.

Jayanti, S., Hewitt, G.F.& White, S.P. (1989). Time-dependent behaviour of the liquid film in horizontal annular flow. AERE R 13487, UKAEA, Harwell, UK.

Jayanti, S., Cliffe, K.A. & Hewitt, G.F. (1990b). Investigation of interface wave structure using time-series analysis techniques. AEA D&R 0035, UKAEA, Harwell, UK.

Jayanti, S. & Hewitt, G.F. (1991). Structure of interfacial waves in air-water horizontal annular flow. Phase-interface phenomena in multiphase flow, Hemisphere Publishing Corporation, New York.

Jayanti, S. & Hewitt, G.F. (1996). Response of turbulent flow to abrupt changes in surface roughness and its relevance in horizontal annular flow. Appl. Math. Modelling, Vol. 20, pp 244-251.

Jayanti, S. & Hewitt, G.F. (1997). Hydrodynamics and heat transfer in wavy annular gas-liquid flow: a computational fluid dynamics study. Int. J. Heat and Mass Transfer, Vol.40(10) pp 2445-2460.

Joseph, D.D., Bannwart, A.C. & Liu, Y.J. (1996). Stability of annular flow and slugging. Int. J. Multiphase Flow, Vol. 22(6), pp 1247-1254.

Kadambi, V. (1982). Stability of annular flow in horizontal tubes. Int. J. Multiphase Flow, Vol. 8(4), pp 311-328.

Langner, H., Studies of entrainment behaviour in steady and transient two-phase annular flow, Thesis T. U. Hannover, Germany, 1978.

Langner, H. and Mayinger, F., Entrainment mass flow measurements in annular two-phase flow, International Seminar on Momentum, Heat and Mass Transfer in Two-Phase Energy and Chemical Systems, Dubrovnik, Yugoslavia, 1978.

Laurinat, J. E., Hanratty & T. J., Dallman, J. C. (1984). Pressure drop and film height measurements for annular gas-liquid flow. Int. J. Multiphase Flow, Vol. 10, pp 341-356.

Laurinat, J.E., Hanratty & T.J., Jepson, W.P. (1985). Film thickness distribution for gas-liquid annular flow in a horizontal pipe. PhysicoChemical Hydrodynamics, Vol. 6(1/2), pp 179-195.

Lee, M. M., Hanratty, T. J., and Adrian, R. J., An axial viewing photographic technique to study turbulence characteristics of particles, *Int. J. Multiphase Flow*, vol. 15, no. 5, pp. 787–802, 1987.

Lee, M. M. & Hanratty, T. J. (1988). The inhibition of droplet deposition by the presence of a liquid wall film. Int. J. Multiphase Flow, Vol. 14, pp 129-140.

Lin, T.F., Murase, M. Jones, O.C., Jr., Lahey, R.T. & Block, R.C. (1983). Annular two-phase flow measurements in a horizontal pipe using the pulsed photon activation (PPA) technique. Trans. Am. Nucl. Soc., Vol 45, pp 837-838.

Lin ,T.F., Block, R.C., Jones, O.C., Jr., Lahey, R.T. & Murase, M. (1983). Two-phase flow measurements using a pulsed-photon-activation (PPA) technique. Proc. Symp. On Measuring Techniques in Gas-liquid Two-Phase Flows. I.U.T.A.M., Nancy, France.

Lin, T.F., Jones, R.T., Lahey, R.T., Block, R.C. & Murase, M. (1985). Film thickness measurements and modelling in horizontal annular flows. PhysicoChemical Hydrodynamics, Vol. 6(1/2), p97-206.

Lockhart, R.W. & Martinelli, R.C. (1949). Proposed correlation of data for isothermal two-phase, two-component flow in pipes. Chem. Eng. Prog., Vol. 45, pp 39-48.

Lu G., Wang J. Jia Z., Experimental and numerical investigations on horizontal oil-gas flow, Journal of hydrodynamics, Ser.B, 2007,19(6):683-689.

Mandhane, J.M., Gregory, G.A. & Aziz, K.A. (1974). A flow pattern map for gas-liquid flow in horizontal pipes. Int. J. Multiphase Flow, Vol. 1, pp 537-553.

Marmottant, P. (2001). Atomization of a liquid by a gas jet. *Phd Thesis,* Institut National Polytechnique de Grenoble, France

McQuillan, K. W., Whalley, P. B., and Hewitt, G. F., Flooding in vertical two-phase flow, *Int. J. Multiphase Flow*, vol. 11, no. 6, pp. 741–760, 1985.

Mayinger, F., Advanced optical instrumentation, *Two-Phase Flow and Heat Transfer in the Power and Process Industries*, Bergles, A. E., Collier, J. G., Delhaye, J. M., Hewitt, G. F., and Mayinger, F. (eds.), Hemisphere Publishing, New York, p. 489, 1981.

Meng, W., Chen, X.T., Kouba, G.E., Sarica, C. and Brill, J.P. (1999) Experimental study of low liquid loading gas-liquid flow in near-horizontal pipes. SPE Annual technical Conference and Exhibition, Houston, October, 1999.

Mito, Y. & Hanratty, T. J. (2003). A stochastic description of wall sources in a turbulent field. Part 1: Verification. Int. J. Multiphase Flow, Vol. 29, pp 1373-1394.

Mito, Y. & Hanratty, T. J. (2004). A stochastic description of wall sources in a turbulent field: part 2. Calculation for a simplified model of horizontal annular flows. Int. J. Multiphase Flow, Vol. 30, pp 803-825.

Mito, Y. & Hanratty, T. J. (2006). Effect of feedback and inter-particle collisions in an idealized gas-liquid annular flow. Int. J. Multiphase Flow, in press.

Mols, B. & Oliemans, R.V.A. (1998). A turbulent diffusion model for particle dispersion and deposition in horizontal tube flow. Int. J. Multiphase Flow, Vol. 24(1), pp 55-75.

Mols, B., Mittendorff, I., & Oliemans, R.V.A. (2000). Results from a two-dimensional turbulent diffusion-model for dispersion and deposition of droplets in horizontal annular dispersed gas/liquid flow. Int. J. Multiphase Flow, Vol. 26, pp 949-975.

Ng, T.S.(2002). Interfacial Structure of stratified pipe flow. *Phd Thesis*, University of London, London, UK.

Nicoud F., Ducros F., Subgrid-Scale Stress Modelling Based on the Square of the Velocity Gradient Tensor, Flow , Turbulence and Combustion 62: 183-200, 1999.

Owen, D.G. & Hewitt, G.F. (1987). An improved annular two-phase flow model. Proc. 3rd Int. Conf. Multiphase Flow, Netherlands, paper C1.

Pan, L. & Hanratty, T. J. (2002). Correlation of entrainment for annular flow in horizontal pipes. Int. J. Multiphase Flow, Vol. 28, pp385-408.

Paras, S.V. & Karabelas, A.J. (1991a). Properties of the liquid layer in horizontal annular flow. Int. J. Multiphase Flow, Vol. 17(4), pp 439-454.

Paras, S.V. & Karabelas, A.J. (1991b). Droplet entrainment and deposition in horizontal annular flow. Int. J. Multiphase Flow, Vol. 17(4), pp 455-468.

Paz, R.J. & Shoham, O. (1999). Film-thickness distribution for annular flow in directional wells: horizontal to vertical. SPE Journal, Vol. 4(2), pp 83-91.

Pearce, D.L. (1979). Film waves in the horizontal annular flow: space-time correlator experiments. Central Electricity Research Laboratories Report RD/L/N 111/79.

Pearce, D.L. & Fisher, S.A. (1976). Theoretical and experimental investigation of dryout in horizontal annular flows: preliminary report. Central Electricity Research Laboratories Report RD/L/N 193/75.

Raynal, L. (1997a). Instability and entrainment at the interface of a gas-liquid mixing layer. *Phd Thesis,* Institut National Polytechnique de Grenoble, France.

Ribeiro, A.M., Bott, T.R. & Jepson, D.M. (2001). The influence of a bend on drop sizes in horizontal annular two-phase flow. Int. J. Multiphase Flow, Vol. 27, pp 721-728.

Rodriguez, D.J. & Shedd, T.A. (2004). Entrainment of gas in the liquid film of horizontal, annular, two-phase flow. Int. J. Multiphase Flow, Vol. 30, pp 565-583.

Roberts, P.A., Azzopardi, B. & Hibberd, S. (1995). The split of horizontal semi-annular flow at a large diameter T-junction. Int. J. Multiphase Flow, Vol. 21(3), pp 455-466.

Roberts, P.A., Azzopardi, B. & Hibberd, S. (1997). The split of horizontal annular flow at a T-junction. Chem. Eng. Sci., Vol. 52(20), pp 3441-3453.

Sarica, C. & Brill, J.P. (1999). Experimental study of low-liquid-loading gas-liquid flow in near-horizontal pipes. SPE paper 56466.

Schubring D., Shedd T.A., Wave behaviour in horizontal annular air–water flow, International Journal of Multiphase Flow 34 (2008) 636–646.

Schubring D., Shedd T.A., Prediction of wall shear for horizontal annular air–water flow International Journal of Heat and Mass Transfer 52 (2009) 200–209.

Schubring D., Shedd T.A., Critical friction factor modelling of horizontal annular base film thickness, International Journal of Multiphase Flow 35 (2009) 389–397.

Schubring D., Shedd T.A., A model for pressure loss, film thickness, and entrained fraction for gas–liquid annular flow, International Journal of Heat and Fluid Flow 32 (2011) 730–739.

Scott D.S. (1963). Properties of cocurrent gas-liquid flow, in Advances in Chemical Engineering, Vol. 4, Academic Press, New York

Sekoguchi, K., Ousaka, A., Fukano, T. & Morimoto, T. (1982). Air-water annular two-phase flow in a horizontal tube. Bulletin of the JSME, Vol. 25(208), pp 1559-1566.

Shaha, J. (2000). Phase interactions in transient stratified flow. *PhD Thesis*, Imperial College of Science, Technology and Medicine, University of London.

Shibata, Y., Katuyama, A., and Kaminaga, F., The generation and behaviour of entrained droplets in an annular countercurrent two-phase flow in a vertical tube, *Two-Phase Flow Modelling and Experimentation*, Begell House, Redding, CT, p. 873, 1999.

Sidi-Ali K., Gatignol R., Interfacial friction factor determination using CFD simulations in a horizontal stratified two-phase flow. Chemical Engineering Science 65 (2010) 5160–5169.

Simmons, M. J. H. & Hanratty, T. J. (2001). Droplet size measurements in horizontal annular gas-liquid flow. Int. J. Multiphase Flow, Vol. 27, pp 861-883.

Skartlien R., A droplet transport model for channel and pipe flow based on particle kinetic theory and a stress–w turbulence model, International Journal of Multiphase Flow 35 (2009) 603–616.

Sun, G., Chan, W.H.G.T. & Hewitt, G.F (1996). A general heat transfer model for two-phase annular flow. Convective Fluid Boiling (Ed JC Chen, Taylor and Frances, 1996)

Sutharshan, B., Kawaji, M. & Ousaka, A. (1995). Measurement of circumferential and axial liquid film velocities in horizontal annular flow. Int. J. Multiphase Flow, Vol. 21(2), pp 193-206.

Suzuki, S. and Ueda, T., Behaviour of liquid films and flooding in counter-current two-phase flow—Part 1. Flow in circular tube, *Int. J. Multiphase Flow*, vol. 3, no. 6, pp. 517–532, 1977.

Taitel, Y. & Dukler, A.E. (1976). A model for predicting flow regime transitions in horizontal and near-horizontal gas-liquid flow. A.I.Ch.E.J., Vol. 22, pp 47-55.

Tso, C.P. & Sugawara, S. (1990). Film thickness prediction in a horizontal annular two-phase flow. Int. J. Multiphase Flow, Vol. 16(5), pp 867-884.

Vames, S. & Hanratty, T.J. (1988). Turbulent dispersion of droplets for air flow in a pipe. Experiments in Fluids, Vol. 6, pp 94-104.

Van't Westende J.M.C., Belt R.J., Portela L.M., Mudde R.F., Oliemans R.V.A., Burgerscentrum J.M. Effect of secondary flow on droplet distribution and deposition in horizontal annular pipe flow, International Journal of Multiphase Flow 33 (2007) pp 67–85.

Vlachos, N. A., Paras, S. A. & Karabelas, A. J. (1999) Prediction of holdup, axial pressure gradient and wall shear stress in wavy stratified and stratified/atomisation gas/liquid flow. *Int. J. Multiphase Flow*, **25**, p. 365.

Wallis, G.B. (1975). The terminal speed of simple drops or bubbles in an infinite medium. Int. J. Multiphase Flow, Vol. 1, pp 491-511.

Whalley, P. B., Azzopardi, B. J., Pshyk, L. and Hewitt, G. F., Axial view photography in annular two-phase flow, European Two-Phase Flow Group Meeting, Grenoble, June, 1977a.

Whalley, P. B., Hewitt, G. F., Azzopardi, B. J., and Pshyk, L., Axial view photography of waves in annular two-phase flow, UK AEA Report No. AERE-R8787, 1977b.

Whalley, P. B., Hewitt, G. F., and Terry, J. W., Photographic studies of two-phase flow using a parallel light technique, UK AEA Report No. AERE-R9389, 1979.

Whalley, P.B. & Hutchinson, P. (1973). A possible characterization of entrainment in annular flow, Chem. Eng. Sci. ,Vol 28 pp 974-975.

Wilkes, N.S., Conkie, W. & James, P.W. (1980). A model for the droplet deposition rate in horizontal annular two-phase flow. AERE R 9691, Harwell, UK.

Williams, L. R., Dykhno, L. A. & Hanratty, T. J. (1996). Droplet flux distributions and entrainment in horizontal gas-liquid flows. Int. J. Multiphase Flow, Vol. 22, pp 1-18.

Zeng, Y., Flow and heat transfer in pressurised water reflood, PhD thesis, Imperial College London, 2010.

Zeng, Y., Hale, C. P., Walker, S. P., and Hewitt, G. F., Design of a high temperature axial viewing system for experimental studies of single tube reflood. 7th International Conference on Multiphase Flow, ICMF 2010, Tampa, May 30–June 4, 2010.

Zhang H.-Q., Sarica C., Low liquid loading gas/liquid pipe flow, Journal of Natural Gas Science and Engineering 3 (2011) 413-422.

Zhou, L., Ahmed, R.M., Miska, S.Z., Takach, N.E, Yu, M. & Pickell, M.B. (2005). Measurement of in-Situ cuttings concentrations using nuclear densitometers in a horizontal annulus at simulated downhole conditions. SPE paper 94261.

Zimmerman, R., Gurevich, M., Mosyak, A., Rozenblit, R. & Hetsroni, G. (2006). Heat transfer to air-water annular flow in a horizontal pipe. Int. J. Multiphase Flow, Vol. 32, pp 1-9.

I am the author of this thesis and all publications by other authors, used to write this thesis have been referenced.

APPENDIX 1

A summary of axial viewing techniques

REPORTS	TEST SECTION	FLOWS	VIEW	TECHNIQUE	OBSERVATION / INVESTIGATION
Arnold and Hewitt (1967)	Fitted on top of a vertical Perspex tube (32mm ID)	Annular air-water	Vertical top viewing,	Still photography and high speed filming (frame rates 2000-4000 frames/s)	• the motion of disturbance waves • the entrainment of the droplets • radial motion of the droplets in gas stream
Hewitt and Roberts (1969)	Same device as Arnold and Hewitt (1967)	Annular air-water	Vertical top viewing, straight through	Single-shot flash photography; high speed cine filming (frame rates: up to 4000 frames/s)	• the interface and the motion of droplets in annular two-phase flow
Fisher and Yu (1975)	• based on original idea by Hewitt and Roberts (1969) • could be placed at any point in a bank of horizontal tubes • 50 mm ID exp. facility.	Air-water	Horizontal; straight through	High speed cine technique	• detailed descriptions of flow patterns in horizontal flows

REPORTS	TEST SECTION	FLOWS	VIEW	TECHNIQUE	OBSERVATION / INVESTIGATION
Suzuki and Ueda (1977)	Installation of a high speed camera directly at the bottom of a 28.8 mm ID vertical tube. 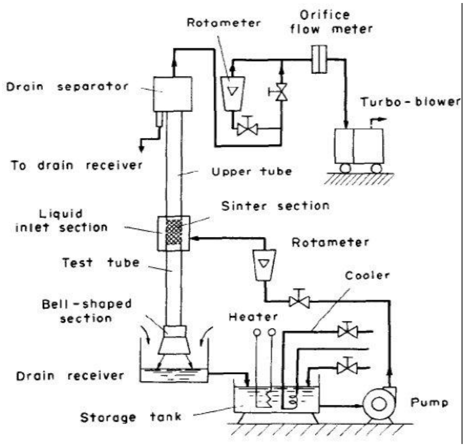 Fig. 1. Schematic of the experimental apparatus of Suzuki & Ueda (1977)	Air-water	Vertical, straight through	Axial viewing photographs taken by a high speed camera, 40 millisecond intervals between successive frames	An investigation of flooding phenomena in vertical counter-current two-phase flow to observe the state of the wavy liquid surface and the process of flooding

REPORTS	TEST SECTION	FLOWS	VIEW	TECHNIQUE	OBSERVATION / INVESTIGATION
Whalley et al. (1977)	Same basic facility as Arnold and Hewitt (1967); changes: 1) an 8° tilt of camera, 2) a longer illumination length (100 mm), 3) a stereoscopic axial viewing technique has also been developed. 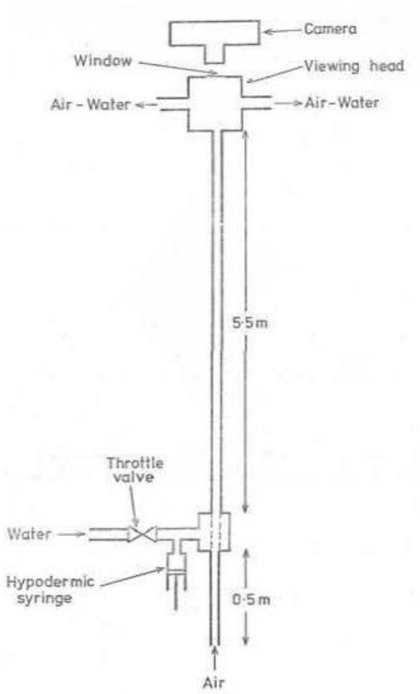 Fig. 2. Schematic of the test section of Whalley et al. (1977)	Annular air-water	Vertical, top viewing, straight through	Still photography and high speed cine films (frame rates: 4000 frames/s); still and high speed cine stereo photography	• wave phenomena in annular two-phase flow • most of the liquid droplets in the annular flow are entrained from disturbance waves

REPORTS	**TEST SECTION**	**FLOWS**	**VIEW**	**TECHNIQUE**	**OBSERVATION / INVESTIGATION**
Fisher et al. (1978)	New axial viewer, for a 32mm ID facility for use with Freon-12 at pressures up to 40 bar	Air-water	Horizontal, straight through	High speed cine photography (frame rates up to 2500 frames/s)	• to observe and then describe two-phase flow patterns; • to determine the boundaries between different flow patterns (latter study).
Whalley et al. (1979)	Same facility as Whalley et al. (1977)	Air-water	Vertical, top viewing, straight through	Parallel-light technique in photographic studies	• the motion of droplets; • the estimation of the droplet velocities
Hewitt and Whalley (1980)	———	———	———	———	A **review** of the optical methods developed at Harwell, involving the various axial view systems

REPORTS	TEST SECTION	FLOWS	VIEW	TECHNIQUE	OBSERVATION / INVESTIGATION
McQuillan et al. (1985)	Annulus apparatus: Central stainless steel tube (38 mm OD, wall thickness of 9 mm) inside a Perspex tube. 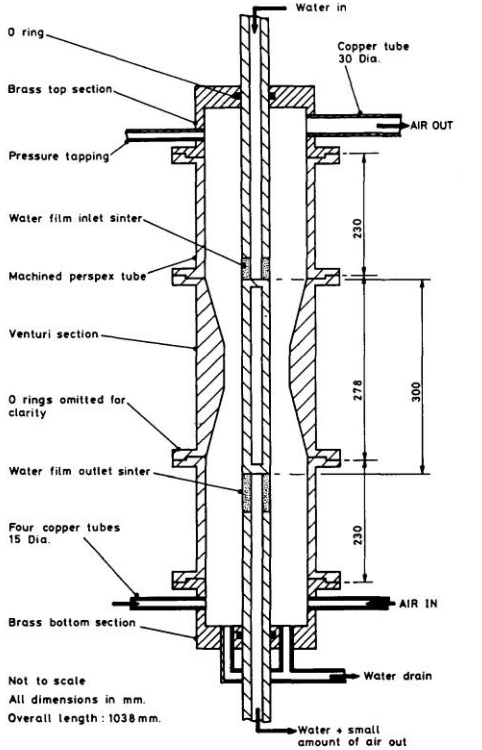 Fig. 3. Schematic of the test section of McQuillan et al. (1985)	Air-water	Vertical, top viewing, through 45° prism	Parallel light beam axial view method (using a local illumination combined with a parallel laser beam). A recording rate of 500 frames/s was chosen as a compromise between two conflicting requirements: • High speed to give a slow motion view of the events; • Low speed to give a reasonably long running time and to enable a small aperture to be used, thus giving a large depth of field.	• Demonstration of upward wave transport during the flooding process • Using transparent tube with bands of different colour side illuminations

REPORTS	TEST SECTION	FLOWS	VIEW	TECHNIQUE	OBSERVATION / INVESTIGATION
Azzopardi (1987)	Technique developed by Whalley et al. (1979); test section mounted with the tube axis horizontal 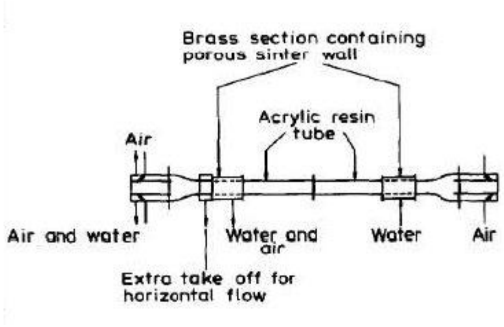 Fig. 4. Schematic of the test section of Azzopardi (1987)	Air-water	Horizontal, straight through (the parallel beam of light from the laser passes through the windows)	**Parallel-light technique; high-speed cine films** were taken using the visualization technique (camera speed of 4000 frames/s)	Drop motion • mean ejection velocities of the drops show no trends with gas and liquid flow rates. (cf. vertical annular flow: the velocity depends on both gas and liquid flow rates) • gas density effects the velocity

REPORTS	TEST SECTION	FLOWS	VIEW	TECHNIQUE	OBSERVATION / INVESTIGATION
Govan, Hewitt and Ngan (1989)	Test section: 32 mm in diameter, 1 m in length. Study of the motion of particles in a gas stream. Glass spheres of 110, 250 and 550 µm diameters.	Air-particles Particles glass spheres, density: 2600 kg/m^3	Vertical, prism	**Laser** (5 mW He-Ne laser) **axial-viewing technique. High-speed ciné photography** (4000 frames/s).	• The experiments showed the possibility of tracking such particles over many frames of the ciné films and to calculate particle velocities from them. • Lagrangian measurements, in the form of velocity time-histories.

REPORTS	TEST SECTION	FLOWS	VIEW	TECHNIQUE	OBSERVATION / INVESTIGATION
Lee, Hanratty and Adrian (1989)	• Downward air flow in a 5.08 cm pipe; • Droplets injected into the centre of the pipe at a velocity approx equal to that of air 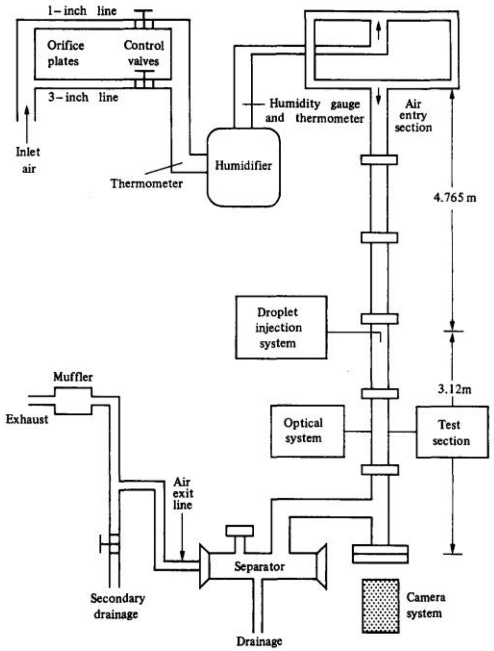 Fig. 5. Schematic of the apparatus of Lee et al. (1987)	Air-water: Air 60-70% humidity Water deionised water droplets of uniform sizes; 50, 90, and 150μm	Vertical, straight through. An optically flat quartz window was used for the viewing of the camera, which was situated on a 3D traversing mechanism at the bottom of the pipe.	**Axial viewing photographic technique** (Kodax Tri-X ASA 400 black-and-white film); **Laser-Doppler velocimetry**: 5 parallel light sheets formed by an electronic flash unit (Nissin 4000 GW with thyristor auto.bounce double reflector and xenon tubes) and a spherical copy lens.	The study of the random motion of particles or droplets contained in a fluid flowing turbulently in a vertical pipe under the influence of the turbulent velocity fluctuations. Through the synchronization of the flashes with the mean translation of the drops, images of the same particles were obtained as they move down the pipe → radial and tangential components of the particles velocities.

REPORTS	TEST SECTION	FLOWS	VIEW	TECHNIQUE	OBSERVATION / INVESTIGATION
Shibata et al. (1999)	Vertical test section, 100 mm in diameter	Air-water	Top viewing, straight through	A **high speed video camera** placed above test section	Interesting images showing the generation of droplets from the film layer and break-up of large drops in the gas core region
Badie (2000)	Based on the axial viewing system used by Fisher and Yu (1975). The flow from a 3 inch (77.92 mm) nominal bore WASP (Water, Air, Sand and Petroleun) high pressure multiphase flow facility is horizontally diverted into two 3-inch tubes to provide space for the viewing and purge system. Test section was set up so that the transparent visualisation section was ~1.5 m upstream of viewing window allowing the illumination (provided by two 500 W halogen lamps) to take place in the 1 m Perspex section.	Air-water	Horizontal. The viewing tube inserted at the junction (purge air blowing against the direction of the main flow) *Initial*: straight through; *later tests*: viewing via a 45° mirror adjacent to the viewing window.	**In-Line Axial View System** <u>Axial view</u> of the flow observed on a Sony EVM-9010PG Trinitron colour video monitor. <u>Initial tests</u> at 24 frames/s with a *miniature camera* (Panasonic WV-KS152) and a lens (Tarcus TV Zoom Lens 1:2/[11.5 – 90]) were fixed to the back of the distributor allowing a *direct view* down the viewing tube. <u>Later tests</u>: *high speed video recording system*: a Kodak EktaPro HG Imager – Model 2000 high speed digital camera to capture images at framing rates up to 2000/s.	• series of experiments carried out to measure and record flow behaviour in the low liquid loading region • measurement of flow parameters, incl. pressure gradient and holdup • the flow was observed and recorded axially: - the bulk of the liquid travels in the film at the bottom of the pipe, but a significant portion is entrained as droplets within the gas core; - waves on the liquid layer were observed to converge and break up into rapidly moving spray droplets.

REPORTS	TEST SECTION	FLOWS	VIEW	TECHNIQUE	OBSERVATION / INVESTIGATION
Govan, Hewitt and Ngan (1989)	Glass spheres of 110, 250 and 550 μm dia, test section: 32 mm diameter, 1 m length.	Air-particles (glass spheres, ρ_p: 2600 kg/m^3)	Vertical, prism	**Laser** (5mW He-Ne laser) **axial-viewing technique**. **High-speed ciné photography** (4000 frames/s) 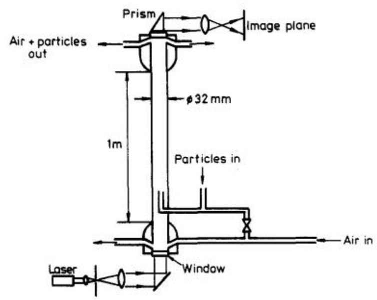 Fig. 6. Schematic of the apparatus of Govan et al. (1989)	The experiments showed the possibility of tracking such particles over many frames of the ciné films and to calculate particle velocities from them.

REPORTS	TEST SECTION	FLOWS	VIEW	TECHNIQUE	OBSERVATION / INVESTIGATION
Lee, Hanratty and Adrian (1989)	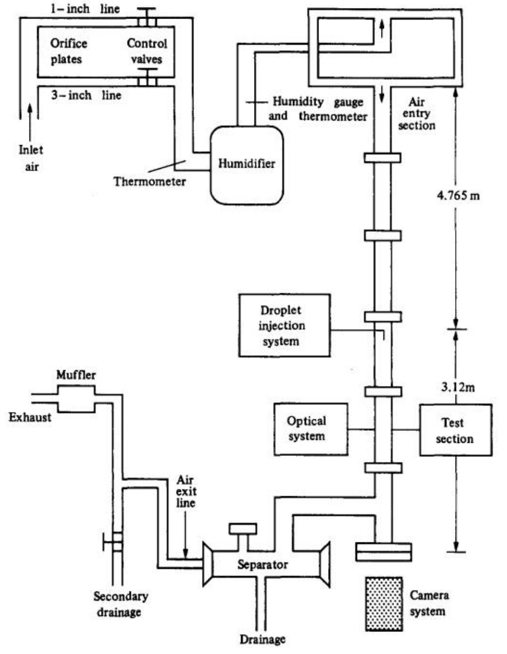 Fig. 7. Schematic of the apparatus of Lee et al. (1987)	**Air** (60-70% humidity to minimise droplets evaporation)-deionised **water** droplets (50, 90, 150 μm)	Vertical, straight through. An optically flat quartz window was used for the viewing of the camera, which was situated on a 3D traversing mechanism at the bottom of the pipe.	**Axial viewing photographic technique** (Kodax Tri-X ASA 400 black-and-white film); **Laser-Doppler velocimetry**: 5 parallel light sheets formed by an electronic flash unit (Nissin 4000 GW with thyristor auto.bounce double reflector and xenon tubes) and a spherical copy lens.	The study of the random motion of particles or droplets contained in a fluid flowing turbulently in a vertical pipe under the influence of the turbulent velocity fluctuations. Through the synchronization of the flashes with the mean translation of the drops, images of the same particles were obtained as they move down the pipe → radial and tangential components of the particles velocities.

REPORTS	TEST SECTION	FLOWS	VIEW	TECHNIQUE	OBSERVATION / INVESTIGATION
Shibata et al. (1999)	Vertical test section, 100 mm in diameter	Air-water	Top viewing, straight through	A **high speed video camera** placed above test section	Interesting images showing the generation of droplets from the film layer and break-up of large drops in the gas core region
Badie (2000)	Based on the axial viewing system used by Fisher and Yu (1975) though alterations made. The flow from a 3 inch (77.92 mm) nominal bore WASP (Water, Air, Sand and Petroleun) high pressure multiphase flow facility is horizontally diverted into two 3-inch tubes to provide space for the viewing and purge system. Test section was set up so that the transparent visualisation section was ~1.5 m upstream of viewing window allowing the illumination (provided by 2 500 W halogen lamps) to take place in the 1 m Perspex section. 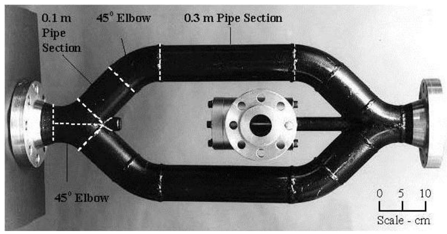 Fig. 8. The in-line axial viewing system (Badie 2000)	Air-water	Horizontal. The viewing tube inserted at the junction (purge air blowing against the direction of the main flow to keep it clear) *Initial*: straight through; *later tests*: viewing via a 45° mirror adjacent to the viewing window.	**In-Line Axial View System** <u>Axial view</u> of the flow observed on a Sony EVM-9010PG Trinitron colour video monitor. <u>Initial tests</u> at 24 frames/s with a *miniature camera* (Panasonic WV-KS152) and a lens (Tarcus TV Zoom Lens 1:2/[11.5 – 90]) were fixed to the back of the distributor allowing a *direct view* down the viewing tube. <u>Later tests</u>: *high speed video recording system*: a Kodak EktaPro HG Imager – Model 2000 high speed digital camera to capture images at framing rates up to 2000/s. 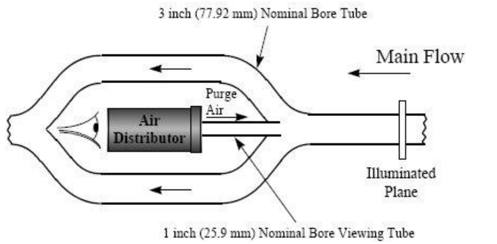 Fig. 9. The basic design of the in-line axial viewing system (Badie, 2000).	• series of experiments carried out to measure and record flow behaviour in the low liquid loading region • measurement of flow parameters, incl. pressure gradient and holdup • the flow was observed and recorded axially: - the bulk of the liquid travels in the film at the bottom of the pipe, but a significant portion is entrained as droplets within the gas core; - waves on the liquid layer were observed to converge and break up into rapidly moving spray droplets.

Tables 1. A summary of axial viewing techniques.